Linear and nonlinear analysis of the acoustic response of perforated plates traversed by a bias flow

Alessandro Scarpato

To cite this version:

Alessandro Scarpato. Linear and nonlinear analysis of the acoustic response of perforated plates traversed by a bias flow. Engineering Sciences [physics]. Ecole Centrale Paris, 2014. English. NNT : 2014ECAP0038 . tel-01126834

HAL Id: tel-01126834
https://theses.hal.science/tel-01126834

Submitted on 6 Mar 2015

École Centrale Paris

THÈSE

présentée par

Alessandro Scarpato

pour l'obtention du

GRADE de DOCTEUR

Formation doctorale : Énergétique

Laboratoire d'accueil : Laboratoire d'Énergétique Moléculaire
et Macroscopique, Combustion (EM2C)
du CNRS et de l'ECP

Linear and nonlinear analysis of the acoustic response of perforated plates traversed by a bias flow

Soutenue le 10 juin 2014

Jury :

MM	Schuller	T.	Professeur, École Centrale Paris	Directeur de thèse
	Ducruix	S.	Chargé de Recherche, CNRS et ECP	Co-Directeur
	Hirschberg	A.	Professeur, TU Eindhoven	Rapporteur
	Nicoud	F.	Professeur, Université de Montpellier	Rapporteur
	Aurégan	Y.	Directeur de Recherche, LAUM	
	Schuermans	B.	PhD, Principal Engineer, Alstom	

École Centrale des Arts et Manufactures
Grand Établissement sous tutelle
du Ministère de l'Éducation Nationale
Grande Voie des Vignes
92295 Châtenay-Malabry Cedex
Tél : 33 (1) 41 13 10 00
Télex : 634 991 F EC PARIS

Laboratoire d'Énergétique
Moléculaire et Macroscopique,
Combustion (E.M2.C.)
UPR 288, CNRS et École Centrale Paris
Tél : 33 (1) 41 13 10 31
Fax : 33 (1) 47 02 80 35

Remerciements

J'aimerais tout d'abord exprimer mes remerciements les plus sincères à mes encadrants au laboratoire EM2C. Thierry Schuller et Sébastien Ducruix m'ont accueilli au labo le premier jours de thèse, et ils m'ont accompagné jusqu'à ma soutenance. Je n'oublierai jamais toutes les discussions que j'ai eues avec Thierry, avec qui j'ai énormément échangé pendant les trois ans que j'ai passés au labo. Il trouvait toujours le temps d'analyser un résultat, de relire un paragraphe, d'écrire une équation avec moi, parfois les vendredis soir ou les week-ends. Son intuition scientifique, ses connaissances théoriques et expérimentales ont été une source d'inspiration pour mes travaux de thèse et m'ont aidé à développer ma démarche scientifique. Sébastien a été mon mentor "numérique": il a suivi toute la partie "simulation" de ma thèse. J'ai beaucoup apprécié son optimisme contagieux et son approche pragmatique et rigoureuse aux problèmes rencontrés. Il a su me rassurer et en même temps m'encourager dans les moments difficiles, en restant toujours à l'écoute de mes questions et doutes. Mais ce que j'ai apprécié le plus de mes encadrants a été la confiance qu'ils m'ont accordée. J'ai toujours eu la liberté dans ma thèse de parcourir de nouvelles voies, de proposer de nouvelles idées. Cette approche m'a permis de mûrir en tant que jeune chercheur. Pour toutes ces raisons, mais surtout pour vos qualités humaines, merci Thierry et Sébastien!

Je suis très reconnaissant envers tous les membres du jury qui ont assisté à ma soutenance, et qui ont évalué ma thèse. Merci à Mico Hirschberg et Franck Nicoud d'avoir lu et examiné méticuleusement ce manuscrit. Leurs commentaires ont été très précieux et m'ont donné beaucoup de pistes de réflexion pour continuer ce travail et avancer un peu plus loin. Je souhaite également remercier Yves Aurégan d'avoir accepté d'être président de mon jury. J'ai été très heureux d'avoir eu Bruno Schuermans comme examinateur, qui a apporté un regard nouveau sur mes travaux.

Je souhaite maintenant remercier la DGA pour le financement de cette thèse, ainsi que l'École Centrale Paris et le CNRS pour leur soutien. Un grand merci à l'École Doctorale, et particulièrement à Benoît Goyeau, Géraldine Carbonel, Catherine Lhopital et Emmanuelle Coplo pour l'aide qu'ils m'ont apportée tout au long de la thèse et pour la préparation de la soutenance. Je garde aussi

d'excellents souvenirs de mes expérience d'enseignement à l'ECP, et en particulier de l'équipe TD de méca flu et de l'équipe TP au labo! Merci à Thierry, Sébastien, Laurent, Daniel et Benoît. Ayant participé pendant plusieurs années au Conseil du Labo, j'aimerais également remercier les directeurs du labo que j'ai côtoyés, en particulier Nasser Darabiha et Estelle Iacona.

Les années de thèse que j'ai passé au laboratoire EM2C ont été inoubliables. C'est vraiment un endroit spécial, où j'ai eu la chance de côtoyer des personnes incroyables. Je remercie Sébastien Candel pour ses conseils et sa disponibilité durant ma thèse, les discussions qu'on a eues dans son bureau m'ont permis de prendre du recul sur mes travaux. Je ne peux bien sûr pas oublier tous les expérimentateurs et techniciens du labo, qui m'ont beaucoup aidé dans la conception et la réalisation des expériences acoustiques: Daniel Durox, Philippe Scouflaire, Jérôme Beaunier, Yannick Le Teno, Sid Bouamama et Erika Jean-Bart. Merci aussi à Laurent Zimmer et Franck Richecoeur pour leur conseils dans le traitement d'image et l'analyse des écoulements instationnaires. Pour la partie numérique de la thèse, je souhaite remercier Matthieu Boileau, Thomas Schmitt et Denis Veynante pour les discussions très intéressantes sur les ondes acoustiques dans les simulations aux grandes échelles compressibles. Merci aussi à toute l'équipe du secrétariat du labo, Anne-Cécile, Virginie et Nathalie, pour leur soutien et leur aide, toujours avec le sourire. Un grand merci à tous les thésards et post-docs que j'ai rencontré pendant ma thèse: Vincent, Adrien, Clément, Renaud, Florent, Mélanie, Marien, Fabien, Thibault, Jef, François, Maria. J'ai des souvenirs magnifiques avec le noyau "born to burn" du labo: Benedetta, Paul, Raph, Fred, Alexis, Layal, Théo, Wenjie, PEB, Antoine. On a vécu beaucoup de beaux moments ensemble, et c'est grâce à vous tous si venir tous les jours au labo, et y passer pas mal de nuits et de week-ends, a toujours été un plaisir pour moi. Merci aussi à Deanna et Anne pour les belles discussions pendant quelques pauses café!

Je souhaite maintenant écrire un remerciement spécial à deux amis vraiment uniques: Théo et Alexis, qui m'ont accompagné depuis pas mal d'années maintenant, et qui sont toujours là à mes côtés. Je porterai toujours dans mon coeur vos sourires, vos paroles et vos encouragements. Merci infiniment!

Vorrei ora ringraziare i miei genitori, mio fratello e i miei nonni per avermi sopportato durante questi anni. Grazie di essere stati sempre al mio fianco, e di avermi dato tutte le opportunità che ho avuto nella mia vita.

Enfin, merci à mes femmes extraordinaires, mes véritables sources d'inspiration. Carole, Adele, merci d'être rentrées dans ma vie, et de me garder toujours les pieds sur terre, mais l'esprit très haut dans le ciel.

Abstract

Thermo-acoustic instabilities are of primary concern in combustion chambers for a wide range of industrial applications, from domestic boiler to gas turbines or rocket engines. They are the consequence of a resonant coupling between the flame dynamics and the acoustic modes of the combustor, and can result in strong vibrations, early aging of combustor components and structural damage. The physical mechanisms involved are complex and difficult to model, thus thermo-acoustic oscillations are not easily predictable at the design stage of a combustor. In many combustors, passive dampers are implemented to increase the acoustic energy dissipation of the system and to hinder detrimental flame-acoustics interactions. In the present work, passive damping systems based on perforated screens backed by a resonant cavity and traversed by a bias flow are investigated. The main objectives are: (i) to improve and simplify the design of these dampers by maximizing their acoustic absorption properties in the linear regime, (ii) to analyze the effect of the sound wave amplitude on the acoustic response of these systems and (iii) to develop models capable of capturing absorption at high oscillation amplitudes. First, two interesting asymptotic regimes are identified where the plate operates at low and high Strouhal numbers respectively. In these regimes the design of a damper maximizing absorption is greatly simplified, since the choice of the optimal bias flow velocity and back cavity size can be decoupled. It is shown that at low Strouhal numbers the damper behaves as a quarter-wave resonator, and features a wide absorption bandwidth. At high Strouhal numbers, the system operates as a Helmholtz resonator, featuring shorter optimal back cavity sizes but narrower absorption bandwidths. These predictions are compared to measurements in a dedicated experimental setup for the different operating regimes identified. The dependence of the acoustic properties of a perforated plate on the forcing amplitude is then examined by means of direct numerical simulations. It is shown that transition from linear to nonlinear regimes occurs when the acoustic velocity amplitude in the orifice is comparable to the mean bias flow velocity. At high amplitudes, periodic flow reversal is observed within the perforation, vortex rings are alternatively shed upstream and downstream of the hole and convected away at a velocity which is increasing with the forcing amplitude. These mechanisms greatly influence the acoustic absorption of the perforate in the nonlinear regime. Two novel models capturing this nonlinear response are then inferred based on an analysis of the vortex trajectory (VC model), and on a quasi-steady description of the flow (IDF model). Their predictions are finally compared to measurements conducted in an impedance tube, and to results from numerical simulations. The results obtained in this work can be used to ease the design of robust dampers capable of operating in harsh environments with very high sound levels, such as those found during self-sustained thermo-acoustic instabilities.

Résumé

Les instabilités thermo-acoustiques causent des problèmes récurrents dans les chambres de combustion pour une large gamme d'applications industrielles, allant des chaudières domestiques aux turbines à gaz, en passant par les moteurs fusées. Ces phénomènes résultent d'un couplage résonant entre la dynamique de la combustion et les modes acoustiques du foyer, et peuvent donner lieu à de fortes vibrations, un vieillissement prématuré des composants de la chambre, voire des dommages structurels. Les mécanismes physiques mis en jeu sont complexes et difficiles à modéliser, ainsi les oscillations thermo-acoustiques ne sont pas facilement prévisibles au stade de la conception d'une chambre de combustion. Dans de nombreux foyers, des systèmes d'amortissement passifs sont installés pour augmenter la dissipation d'énergie acoustique et empêcher le développement de ces instabilités. Dans ce travail, des systèmes d'amortissement basés sur des plaques perforées couplées à une cavité résonante et traversées par un écoulement moyen sont analysés. Les principaux objectifs sont : (i) d'améliorer et de simplifier la conception de systèmes d'amortissement robustes en maximisant leurs propriétés d'absorption acoustique en régime linéaire, (ii) d'analyser l'effet de l'amplitude des ondes sonores incidentes sur la réponse acoustique des plaques perforées et (iii) de développer des modèles capables de reproduire cette réponse aux hautes amplitudes. Tout d'abord, deux régimes asymptotiques intéressants sont identifiés où le système fonctionne à faibles et forts nombres de Strouhal respectivement. Dans ces régimes la conception d'un système d'amortissement maximisant l'absorption acoustique est grandement simplifiée, puisque les calculs de la vitesse optimale de l'écoulement et de la taille de la cavité sont découplés. Il est démontré qu'à faible nombre de Strouhal le système se comporte comme un résonateur quart d'onde, et dispose d'une bande d'absorption très large. À fort nombre de Strouhal, le système fonctionne comme un résonateur de Helmholtz, comportant une cavité de taille plus réduite, mais une bande d'absorption beaucoup plus étroite que dans le régime précédant. Ces prévisions sont confirmées par des mesures réalisées dans les différents régimes identifiés sur un dispositif expérimental dédié. L'évolution des propriétés acoustiques d'une plaque perforée lorsque l'amplitude de forçage augmente est ensuite examinée par le biais de simulations directes. Il est montré que la transition du régime linéaire au régime non linéaire se produit lorsque l'amplitude de la vitesse acoustique dans l'orifice est comparable à la vitesse de l'écoulement moyen dans les trous. Pour des amplitudes élevées, une inversion périodique de l'écoulement est observée dans l'orifice. Des anneaux tourbillonnaires sont alternativement éjectés en amont et en aval de l'orifice à une vitesse de convection qui augmente avec l'amplitude de la perturbation acoustique. Ces mécanismes influencent profondément l'absorption acoustique des plaques perforées dans le régime non linéaire. Deux nouveaux modèles décrivant la réponse non linéaire de ces systèmes sont ensuite développés en exploitant la trajectoire des vortex (modèle VC), et une approche quasi-stationnaire (modèle IDF). Les prévisions de ces modèles sont confrontées à des mesures effectuées dans le tube à impédance et aux résultats de simulations directes. Les résultats obtenus au cours de ces travaux peuvent être utilisés pour guider la conception de systèmes d'absorption robustes, capables de fonctionner dans des environnements difficiles avec des niveaux sonores élevés, comme ceux rencontrés lors d'instabilités thermo-acoustiques.

Contents

Chapter 1

General introduction

According to the International Energy Agency (www.iea.org), in 2010 more than 80 % of the global primary energy consumption was supplied by combustion [IEA (2012)], including both fuels from non-renewable sources, such as oil, natural gas and coal, and biomass fuels from renewable sources. The high energy density of hydrocarbon fuels, as well as their ease of storage and transportation, combined with a well-established distribution infrastructure, determined their dominant position on the energy markets. Today combustion technology is spread in several domains, encompassing energy production (gas turbines, coal- or oil-based thermal power plants), transportation (automotive, naval, aeronautical and aerospace propulsion), materials processing (glass and metal furnaces) and boilers (for industrial and domestic applications). Typical orders of magnitude of thermal power generated range from a few kW for a domestic boiler, up to hundreds of MW for a single stationary gas turbine for electricity production, and even a few GW for space rocket propulsion. Some applications are illustrated in Fig. 1.1.

In the case of gas turbines, their evolution has been driven in the past decades by a continuous effort to improve fuel efficiency, and more and more stringent regulations for greenhouse gases, such as CO_2, and pollutant emissions, in particular nitrogen oxides NO_x, carbon monoxide CO and unburned hydrocarbons UHC. In this perspective, lean premixed combustion technology has been developed in the past two decades. The fuel is premixed with air upstream of the combustor to obtain a more homogeneous mixture fraction field and thus a more uniform temperature distribution. Excess air reduces the flame temperature allowing the decrease of NO_x emissions without the increase of CO production that would be due to incomplete combustion. The use of lean premixed combustion technology allowed a spectacular increase of energy density in the combustor, accompanied by a reduction of NO_x emissions in gas turbines, as illustrated by Correa (1998) and Döbbeling et al. (2005) (see Fig. 1.2). However, it should be kept in mind that a compromise needs to be sought to achieve high efficiency while reducing both NO_x and CO emissions [Lefebvre and Ballal

(a) Ariane 5 space rocket. (b) Linde's burner for glass furnaces.

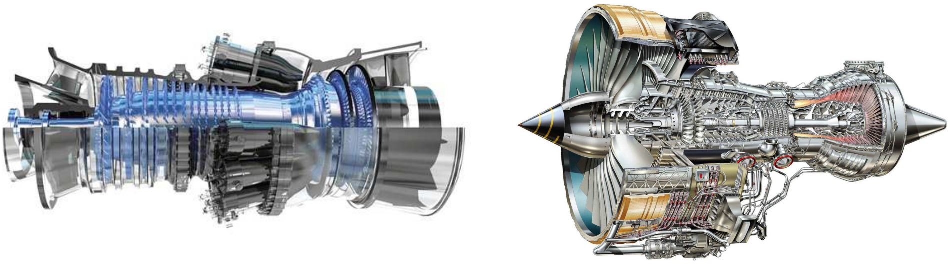

(c) General Electric's 7FA gas turbine. (d) Rolls Royce's Trent 700 turbojet.

Figure 1.1: *Examples of application of combustion technology.*

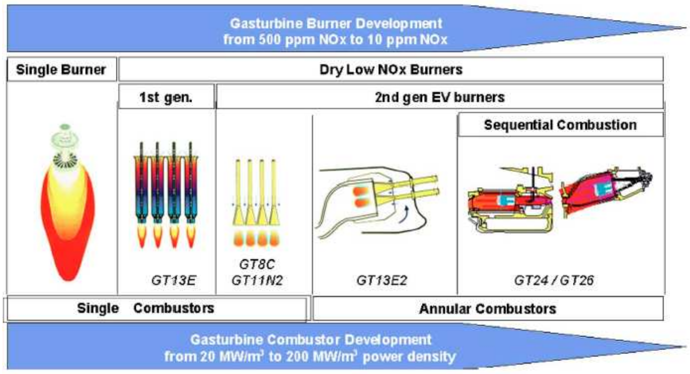

Figure 1.2: *Premix burner development in Alstom's gas turbines. Figure reproduced from Döbbeling et al. (2005).*

(2010)].

The main drawback of lean premixed combustion technologies is related to the reduced robustness of the flame with respect to flow perturbations. Flame stabilization is a challenging task, and combustion dynamics phenomena often occur in gas turbine combustors, such as flame extinction, lean blow-off, flashback and thermo-acoustic instabilities [Lieuwen and Yang (2005)]. Augmenting the stability margins of gas turbine combustors with respect to self-sustained thermo-acoustic oscillations is one of the main challenging issues for gas turbine manufacturers [Lieuwen and McManus (2003); Mongia et al. (2003); Döbbeling et al. (2005)]. These undesirable phenomena are described in the following section.

1.1 Thermo-acoustic instabilities

Thermo-acoustic instabilities are characterized by a detrimental coupling between combustion dynamics and the acoustic modes of the combustion chamber. This phenomenon is known since the early investigation of sound produced by flames by Rayleigh (1896). Some of the first combustion instabilities at industrial scale were observed in liquid propellant rocket engines and led to severe failures [Crocco and Cheng (1956); Culick (2006)]. The review articles from Keller (1995), Candel (2002), Dowling and Morgans (2005) and Huang and Yang (2009), as well as the collection of articles edited by Lieuwen and Yang (2005) and the monographs from Crocco and Cheng (1956), Yang and Anderson (1995), Culick (2006) and Poinsot and Veynante (2012) provide an extensive overview of the topic.

Many scenarios can be envisaged to describe the coupling between flames and acoustic waves propagating in a given system. For example, acoustic pressure

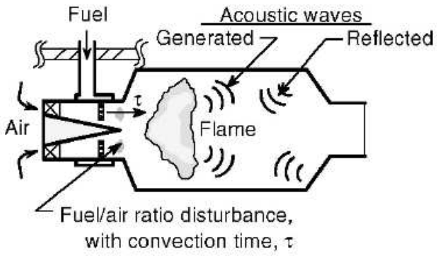

Figure 1.3: *Schematic view of unstable premix combustion. Figure reproduced from Richards et al. (2003).*

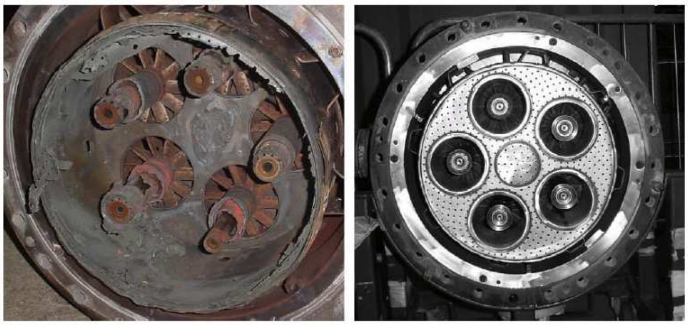

Figure 1.4: *Comparison between a multi-burner assembly damaged by a combustion instability (left) and a new multi-burner assembly (right). Figure reproduced from Huang and Yang (2009).*

oscillations p', by interacting with the boundaries of the combustion chamber, and in particular with the injection units, can induce hydrodynamic perturbations of velocity u' and equivalence ratio ϕ', leading to combustion unsteadiness [Ducruix et al. (2003)]. Interactions of the sound waves with solid elements such as the vanes used to produce the swirled flow may also lead to additional perturbations [Candel et al. (2014)]. A schematic view of unstable premixed combustion is shown in Fig. 1.3 when instabilities are triggered by perturbations of the mixture composition. The perturbed flame generally produces heat release rate fluctuations $\dot{q}'$, which act as a source term in the wave equation, constituting the feedback mechanism of unsteady combustion on the acoustic field. In gas turbines, when these heat release rate fluctuations synchronize with the acoustic perturbations, serious problems can be observed such as flame extinction, intensification of the heat fluxes to the combustor walls, and even structural vibrations due to the high sound pressure levels reached at the combustor walls. An example showing a damaged combustor is presented in Fig. 1.4.

A necessary condition for thermo-acoustic instabilities to occur is that the unsteady heat release rate $\dot{q}'$ and the pressure fluctuations in the flame region are in phase [Rayleigh (1896)]. This result can be written in the following simplified form [Putnam (1971)]:

$$\frac{1}{T_p}\int_{\mathcal{V}_f}\int_0^{T_p} p'\dot{q}' d\mathcal{V}\, dt > 0, \tag{1.1}$$

where p' denotes pressure fluctuations, $\dot{q}'$ are volumetric heat release rate perturbations. These fluctuations are integrated over the flame volume $\mathcal{V}_f$ and over the oscillation period $T_p = 1/f$. Equation (1.1) is known as the Rayleigh criterion and the left hand side term is designated in this manuscript as the Rayleigh source term. In this form, the instability criterion does not take into account physical phenomena such as volume energy losses, and also energy dissipation at the system boundaries. The latter contributions cannot generally be neglected (see for example Tran et al. (2009a)) and may be inferred from an acoustic energy budget over the combustion chamber.

Writing a rigorous acoustic energy budget in a multi-species reacting compressible flow is a difficult problem [Cantrell and Hart (1964); Myers (1986); Myers (1991)]. In many combustion systems, the Mach number of the flow is sufficiently small to neglect effects related to the mean flow except near the chamber nozzle exit where the flow is accelerated in pressurized gas turbine combustors [Nicoud and Wieczorek (2009); Motheau et al. (2014)]. An approximated expression for acoustic energy disturbances that only retain the leading combustion noise source [Strahle (1978)] can however more easily be established when the fluid is supposed to be at rest in the entire combustion chamber [Crighton et al. (1992)]:

$$\frac{\partial E}{\partial t} + \boldsymbol{\nabla}\cdot(p'\boldsymbol{u}') = \frac{\gamma-1}{\gamma\bar{p}}p'\dot{q}' \tag{1.2}$$

where $E = p'^2/(2\rho_0 c_0^2) + \rho_0 u'^2/2$ is the acoustic energy density, u' and p' denote acoustic pressure and velocity disturbances, ρ_0, c_0 and $\gamma = c_p/c_v$ are the mean density, sound speed and the heat capacity ratio. Integrated over the combustion chamber volume $\mathcal{V}$ bounded by a surface S, this yields:

$$\frac{d}{dt}\left\langle \int_{\mathcal{V}} E\, d\mathcal{V}\right\rangle = \left\langle \int_{\mathcal{V}} \frac{\gamma-1}{\gamma\bar{p}}p'\dot{q}'\, d\mathcal{V}\right\rangle - \left\langle \int_S p'\boldsymbol{u}'\cdot\boldsymbol{n}\, dS\right\rangle \tag{1.3}$$

where $\langle\cdot\rangle$ denotes the time-average over an oscillation period and $\boldsymbol{n}$ is the external unit normal vector to the surface S.

During a thermo-acoustic instability, the Rayleigh source term takes positive values and the net difference between the two right hand side contributions in Eq. (1.3) is also positive. The amplitude of the perturbations and the acoustic energy in the system increase until a limit cycle is reached [Noiray et al. (2008)]. At this point the average acoustic energy $\langle E\rangle$ remains constant, and the two terms in the right-hand side of Eq. (1.3) are in balance. An instability can therefore grow when:

$$\left\langle \int_{\mathcal{V}} \frac{\gamma - 1}{\gamma \bar{p}} p' \dot{q}' \, d\mathcal{V} \right\rangle \geq \left\langle \int_{S} p' \boldsymbol{u}' \cdot \boldsymbol{n} \, dS \right\rangle \tag{1.4}$$

This generalization of the Rayleigh criterion does not take into account dissipation phenomena taking place within the control volume. It is however admitted that it retains the main contributions to acoustic energy fluctuations in combustors and may be used to devise solutions to hinder self-sustained thermo-acoustic instabilities.
Expression Eq. (1.4) shows that an instability develops if the flame source term, i.e. the left-hand side term in Eq. (1.4), takes positive values larger than the acoustic losses at the boundaries of the combustion chamber, i.e. the right-hand side term in Eq. (1.4). As a consequence, unstable combustion regimes can be stabilized with two different strategies.

This first one consists in modifying the flame response to flow perturbations, by changing some operating parameters or the burner design [Krebs et al. (2002)]. In staged combustors, where the fuel is injected in different stages, Barbosa et al. (2009) for gaseous fuels and Providakis et al. (2012) for liquid fuels showed that the acoustic response of the flame can be modified by the staging factor. Bulat et al. (2011) also reported that the use of a pilot injection in a gas turbine for different engine loads can change the flame stabilization and thus its acoustic response. Noiray et al. (2009) show that modifying the dynamics of different injectors in a multiple-flame burner may be used to obtain a neutral system free of low frequency thermo-acoustic instabilities. There are many other examples where the response of the flame to flow perturbations is altered to reduce the Rayleigh source term in Eq. (1.4) and improve the stability margins of the combustor [Langhorne et al. (1990); Schluter (2004); Durox et al. (2013)].

The second possibility is to increase acoustic dissipation at the boundaries, for example by increasing acoustic losses [Tran (2009)] or modifying the impedance [Bothien et al. (2008)] at the inlet or outlet of the combustor, or by adding dampers to the combustor walls [Bothien et al. (2013)]. The work conducted in the present Ph.D. aims at improving this alternative strategy by passive means. This problem is discussed in the next section.

1.2 Passive acoustic damping strategies

The complexity of the combustion chamber of a gas turbine implies that the burner environment is very different from the simplified setups that can be studied at laboratory scale, and thus a thermo-acoustic analysis performed on a test rig cannot be easily transferred to engine scale. In practice this mismatch between test rigs and industrial gas turbines limits the applicability of combustion instability analyses conducted on generic systems, and alternative methods based on active or passive control are used to hinder the resonant coupling between acoustics and flame dynamics. Active methods are based on a feedback loop between a sensor and an actuator to break the resonant coupling between the acoustic modes of the combustion chamber and the response of the flame [Candel (1992); McManus et al. (1993)]. Recent examples of application of active control methods in generic configurations can be found in the works of Bothien et al. (2008) and Zhao and Morgans (2009). However these methods are difficult to implement at industrial scale, due to their high costs but also to robustness issues: in case of system failure the burner may quickly become unstable. Except rare exceptions [Hermann et al. (1998)], passive control methods are in general more reliable and more frequently used in gas turbines. They are briefly described below.

Under certain conditions, a flow can produce or absorb sound [Rienstra and Hirschberg (2003)]. Generally in external flows (free field condition), the sound level of the acoustic waves generated is too small to significantly perturb the main flow field. However in internal flows acoustic reflection can be greatly amplified by resonance phenomena or by the presence of flow constrictions that enhance compressibility effects. Most passive dampers are based on these principles, and mainly consist in the optimal placement of damping systems.

A general overview of passive control methods has been conducted by Richards et al. (2003). In rocket engines acoustic dampers have been successfully implemented to stabilize combustion and counter thermo-acoustic instabilities at frequencies in the kilohertz range. The dampers typically encountered in gas turbines are different from the ones found in rocket engines, because of the relatively low frequencies that must be damped (typically a few hundreds hertz). These low frequency instabilities require the use of larger damping volumes, which limit their placement in the combustion chamber.

Three main families of damping devices are used in stationary gas turbines: quarter-wave resonators [Richards and Robey (2008)], Helmholtz resonators [Bellucci et al. (2004); Dupere and Dowling (2005); Bothien et al. (2013)] and perforated screens [Melling (1973)]. Figure 1.5 shows a schematic view of an Helmholtz resonator and a quarter-wave tube. Their resonance frequencies are given by:

$$f_0 = \frac{c_0}{2\pi}\left[\frac{S}{V(l+\delta)}\right] \qquad \text{for an Helmholtz resonator,} \tag{1.5}$$

$$f_0 = \frac{c_0}{4(L+\delta)} \qquad \text{for a quarter-wave tube,} \tag{1.6}$$

where the notations used are defined in Fig. 1.5, and δ is an end correction length [Rienstra and Hirschberg (2003)]. Quarter-wave resonators have been

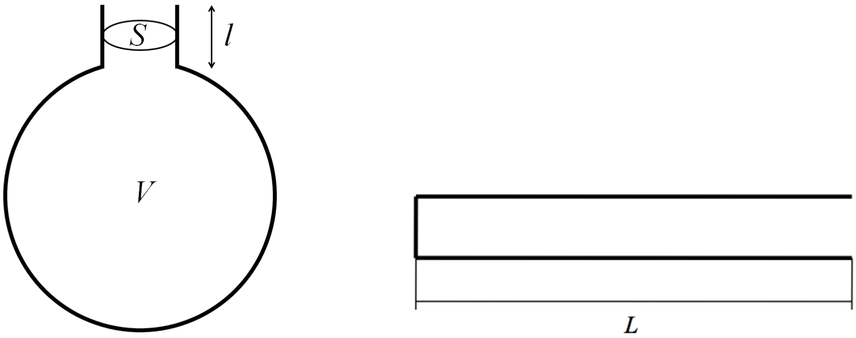

(a) Helmholtz resonator. (b) Quarter-wave tube.

Figure 1.5: *Schematic view of an Helmholtz resonator (a) and a quarter-wave resonator (b).*

used by Richards and Robey (2008) to avoid coupling between different injectors in an annular combustor due to transverse modes. These systems are often used to damp high frequency sound waves [Oschwald et al. (2008)] Helmholtz resonators are generally preferred to damp low frequency sound waves (see for example Zinn (1970) and Hersh et al. (2003)).

These dampers are typically designed to damp a single given frequency. When several acoustic modes are unstable, several dampers are needed. Each one is then designed to absorb acoustic energy at a specific frequency [Zhao and Morgans (2009)]. Their narrow frequency bandwidth is considered as a major drawback, especially in the changing environment present in a combustion chamber. Moreover, it is not uncommon that the instability frequency varies during operation. We have already mentioned that, in staged combustors, the acoustic response of the flame can be modified by the staging factor or a pilot injection at different load conditions [Barbosa et al. (2009); Bulat et al. (2011); Providakis et al. (2012)]. Bothien et al. (2013) indicated that, in gas turbines, engine-to-engine variations of pulsation frequency are expected due to, for example, different ambient conditions or the use of different fuels. In Boudy et al. (2011) a different phenomenon was observed. The frequency of the thermo-acoustic instability changed due to triggering of the first acoustic mode by a second one at a different frequency. In their review of passive acoustic dampers for gas turbine engines, Richards et al. (2003) argued that it is difficult to design acoustic resonators for a specific natural frequency, because their gas can include combustion products and purge cooling air, making the determination of the speed of sound uncertain. The effect of hot-gas ingestion has been recently analyzed by Ćosić et al. (2012).

An interesting concept to widen the absorption bandwidth of Helmholtz resonators is to couple multiple resonating volumes within a single resonator, each

Figure 1.6: *Multi-volume damper based on coupled Helmholtz resonating cavities [Bothien et al. (2013)]. Courtesy of Dr. M. Bothien.*

cavity being tuned at a different frequency [Griffin et al. (2000)]. This idea was applied by Bothien et al. (2013) to develop a new multi-volume damper capable of extending the absorption bandwidth of the equivalent single-volume Helmholtz resonator. It was then validated on a full-scale test engine. A photography of the multi-volume damper is shown in Fig. 1.6.

These works show the importance of a robust design for acoustic dampers, that must be able to absorb acoustic energy in different operating conditions and at different frequencies. Helmholtz and quarter-wave resonators can only be used to address a limited range of frequencies, and only a combination of several resonators is able to deal with different unstable modes.

Perforated screens represent an interesting alternative to the use of Helmholtz and quarter-wave resonators in gas turbines. They are widely used in aero-engine liners [Hughes and Dowling (1990)] and in car mufflers [Munjal (1987)] (see Fig. 1.7). Moreover, they are already used in combustion chambers to protect the combustor walls with film cooling, and to dilute hot combustion products before they enter the turbine. Their damping properties are examined in details in the next section as they represent the main focus of the present work.

1.3 Acoustic response of perforated plates

An important research activity has been devoted to the experimental characterization, modeling and simulation of the absorption properties of perforated screens. Early investigations of this problem were revised by Ingard and Ising (1967), Melling (1973) and Bechert (1980). The textbooks from Munjal (1987) and Howe (1998) provide a general framework for theoretical treatment of the

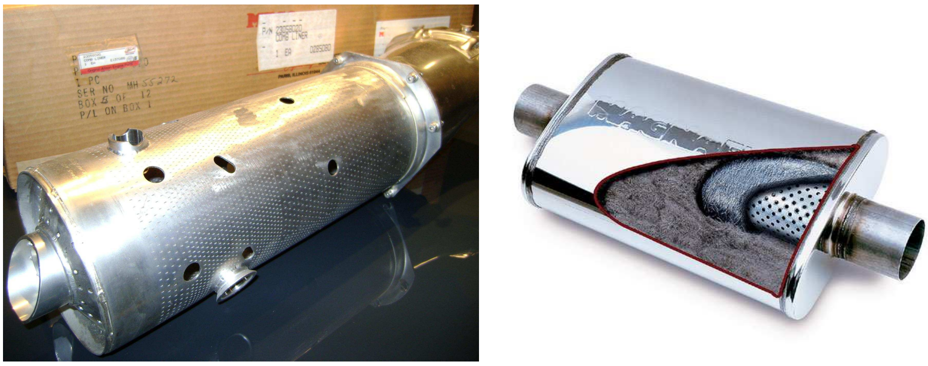

(a) Combustor liner.

(b) Car muffler.

Figure 1.7: *Photographies of a combustor liner for a gas turbine (a) and a car muffler (b).*

aero-acoustic interactions taking place within these systems illustrated by many practical applications.

In a recent study by Tran et al. (2009a), perforated screens designed using available linear models (Howe (1979) and Hughes and Dowling (1990)) and placed at the rear side of a premixing system were used to hinder longitudinal thermo-acoustic instabilities in a turbulent swirled burner. The damper was shown to operate well for small pressure disturbances in the frequency range 250 to 400 Hz and the results were consistent with the model predictions. It eventually fails when the instability oscillation level raises inside the chamber [Tran et al. (2009b)]. One of the objectives of the present work is to understand the reasons of this failure and identify the key features to improve the design of perforated screens for robust low frequency acoustic damping.

A number of parameters influences the absorption properties of perforates. The main ones are geometrical elements, and in particular the porosity, as shown by Wendoloski (1998) and Dupère and Dowling (2001), the plate thickness [Jing and Sun (2000); Peat et al. (2006)], the orifice geometry [Grace et al. (1998)], or the interspace between holes [Lee et al. (2007); Tayong et al. (2011)]. The presence of bias and grazing flows can enhance as well as lower acoustic absorption, as demonstrated by Narayana Rao and Munjal (1986); Howe (1998); Kirby and Cummings (1998); Eldredge and Dowling (2003); Dassé et al. (2008); Tonon et al. (2013). The amplitude of the incident acoustic wave can also trigger acoustic nonlinearity at the orifice, thus changing the way acoustic energy is dissipated, as analyzed for example by Ingard and Ising (1967); Cummings and Eversman (1983); Cummings (1986); Salikuddin et al. (1994); Dragan and Lebedeva (1998); Jing and Sun (2002); Bellucci et al. (2004). The design of a perforated plate used as a damper relies thus on a complex optimization procedure, involving a large number of parameters that need to be examined.

Fundamental mechanisms of sound absorption by perforated screens are revisited in the following section. The objective is to give an overview of the current understanding of this problem and give the main modeling elements that will be used later in this work to infer the damping properties of perforated plates traversed by a bias flow and subjected to normal incident acoustic waves. The analysis is voluntarily restricted to perforated screens of low porosity in absence of grazing flow. The bias flow velocity within the perforations is considered small and Mach number effects are ignored [Durrieu et al. (2001)] as well as effects of inclination of the perforations [Eldredge et al. (2007)], but the respective roles of the bias flow velocity and the presence of a resonant back cavity behind the perforate are examined. Only sound waves normal to the plate are considered. There is no difficulty to extend the following analysis to small incidence angles, but for larger incidence angles effects related to the resulting grazing flow need to be taken into account (see for example Tonon et al. (2013)). The influence of the finite thickness of the plate is also examined by taking into account the additional dissipation induced by the unsteady flow within the apertures, as shown by Melling (1973); Salikuddin et al. (1994); Jing and Sun (2000). However these additional losses due to the effects of viscous dissipation at the orifice walls are not considered in this work. These losses are related to the oscillating slug of fluid in the orifice, and increase when the frequency of the acoustic perturbation increases [Melling (1973)]. The main focus of the present work being the analysis of dampers addressing low frequency oscillations, viscous losses at the orifice walls are negligible compared to other acoustic phenomena, such as dissipation caused by flow separation and vortex generation at the orifice outlet and acoustic resonance of the cavity. This simplification also releases the need of solving the thin acoustic boundary layer in the orifice, which is very computationally demanding since it would require very fine meshes in the near-wall region.

1.3.1 Sound absorption mechanism

Sound absorption properties of perforated screens with and without bias flow significantly differ. In absence of bias flow, a perforated plate features weak absorption properties under small acoustic disturbances [Rayleigh (1896)], but absorption is notably augmented when the oscillation level is increased [Ingard and Ising (1967)]. For small disturbances, the flow remains essentially potential in the vicinity of the perforation and the conversion of acoustic energy is rather limited [Howe (1998)]. This type of behavior ceases at higher levels when flow separation takes place at the perforation edges for a certain threshold amplitude level. Acoustic energy is then converted into vortical energy and is dissipated without significant acoustic regeneration [Cummings (1984)]. This results in a net absorption of sound. The conclusion is that an orifice without a mean bias flow cannot efficiently absorb sound except at very high levels.

This issue can be circumvented using a steady bias flow through the perforations to ensure flow separation. As shown by Morfey (1971), acoustic energy can be dissipated in a vortical flow. When a bias flow passes through an orifice of a perforated plate, it separates as a jet, constituting a continuous source of vorticity produced within the jet shear layers. When sound waves interact with the jet, a fraction of the acoustic energy of the incident sound wave is thus converted into vortical energy, which is eventually dissipated by viscous losses [Bechert (1980)]. In this case, and for small acoustic perturbation amplitudes, sound absorption is a linear mechanism [Howe (1979)]. A common feature in the sound absorption mechanism of acoustic waves impinging on perforated plates with and without bias flow is that the influence of viscosity is generally insignificant, except near the edges, where flow separation takes place.

One elegant way to highlight sound absorption in an acoustically perturbed vortical flow is to derive an acoustic analogy in terms of the stagnation enthalpy from the conservation equations. In the case of a homentropic high Reynolds and low Mach number flow, where viscous dissipation is neglected and entropy is assumed to remain constant, one may write [Howe (1998)]:

$$\frac{1}{c_0^2}\frac{\partial^2 B}{\partial t^2} - \nabla^2 B = \boldsymbol{\nabla} \cdot (\boldsymbol{\omega} \times \boldsymbol{u}) \tag{1.7}$$

where $B = p/\rho_0 + u^2/2$ is the stagnation enthalpy, $\boldsymbol{u}$ is the flow velocity and $\boldsymbol{\omega}$ denotes the vorticity field. In this expression, nonlinear propagation effects and scattering of sound by vorticity are neglected. It is also assumed that the speed of sound c_0 and the density ρ_0 are constant values. Using a Helmholtz decomposition of the velocity field $\boldsymbol{u}$, one may also write:

$$\boldsymbol{u} = \boldsymbol{\nabla}\varphi + \boldsymbol{\nabla} \times \boldsymbol{\Psi} \tag{1.8}$$

where φ denotes the velocity potential and $\boldsymbol{\Psi}$ the stream function. In this description, the acoustic velocity field $\boldsymbol{u}'$ corresponds to the gradient of the unsteady component φ' of the scalar potential $\boldsymbol{u}' = \boldsymbol{\nabla}\varphi'$.

In the irrotational region of the flow ($\boldsymbol{\omega} = 0$), the stagnation enthalpy B appears thus as the natural acoustic variable. This indicates that the Coriolis force $\boldsymbol{f}_c = \rho_0(\boldsymbol{\omega} \times \boldsymbol{u})$ acts as an external force on the acoustic flow field $\boldsymbol{u}'$ [Rienstra and Hirschberg (2003)]. Neglecting wave propagation effects in the source region and mean flow convection in the wave region, the time-averaged power $\mathcal{P}$ transferred from the vorticity field to the acoustic field is given by the work performed by the Coriolis force on the acoustic field integrated over the flow region and over an oscillation period:

$$\langle \mathcal{P} \rangle = \left\langle \int_{\mathcal{V}} \boldsymbol{f}_c \cdot \boldsymbol{u}' d\mathcal{V} \right\rangle \tag{1.9}$$

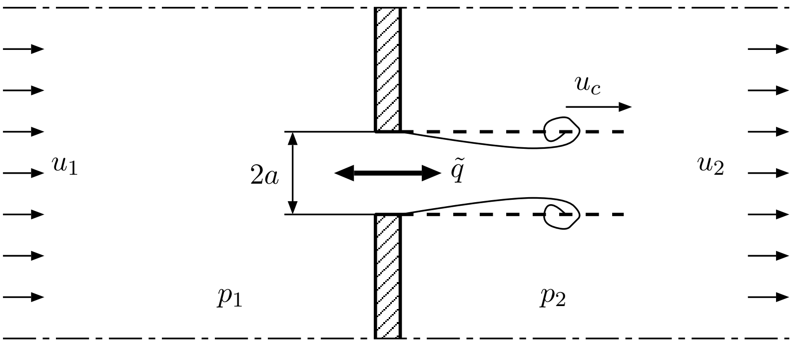

Figure 1.8: *Single orifice of diameter $2a$ traversed by a mean bias flow (from left to right), submitted to normal incident sound waves. The quantity $\tilde{q}$ is the fluctuating volume flowrate through the hole. A vortex ring is convected downstream with a velocity u_c.*

This expression shows that when the acoustic velocity differs from zero in the vorticity source region, energy transfer from the vortical to the acoustical flow takes place. This mechanism is at the origin of sound dissipation taking place in a perforation crossed by a bias flow that is submitted to acoustic forcing. By further simplifying the problem, it is possible to fully determine the acoustic properties of a perforation as shown below.

1.3.2 Rayleigh conductivity

Consider the sketch in Fig. 1.8 featuring a single perforation at $x = 0$ in a thin plate traversed by a steady bias flow. The central issue is to determine the Rayleigh conductivity linking the fluctuating volume flowrate within the perforations and the unsteady pressure difference applied to the plate [Rayleigh (1896); Howe (1998)]. Assuming harmonic disturbances, the acoustic pressure p' and velocity u' far from the perforation write:

$$p' = \Re\left\{\tilde{p}\exp(-\mathrm{i}\omega t)\right\} \tag{1.10}$$

$$u' = \Re\left\{\tilde{v}\exp(-\mathrm{i}\omega t)\right\} \tag{1.11}$$

$$\tag{1.12}$$

where $\omega = 2\pi f$ is the angular frequency, and $\Re\{\cdot\}$ denotes the real component of a complex quantity. Using these notations, the Rayleigh conductivity of the aperture is given by:

$$K_R = \frac{\mathrm{i}\omega\rho_0\tilde{q}}{\tilde{p}_2 - \tilde{p}_1} = \frac{\tilde{q}}{\tilde{\varphi}_2 - \tilde{\varphi}_1} \tag{1.13}$$

where $\tilde{q}$ denotes the volume flowrate fluctuation through the aperture and $\Delta\tilde{p} = \tilde{p}_2 - \tilde{p}_1$ is the fluctuating pressure difference applied to the plate that may also be replaced by the velocity potential difference $\mathrm{i}\omega\rho_0\Delta\tilde{\varphi} = \Delta\tilde{p}$ of the uniformly perturbed flow away from the perforation.

As indicated previously, the Reynolds number within the perforation is assumed to be large enough $\mathrm{Re} \gg 1$ to neglect viscous effects except near the perforation edges where flow separation takes place. The Rayleigh conductivity of a circular aperture of radius a in which a steady jet emerges irrotationally and is separated from the ambient fluid by an infinitely thin vortex sheet has been determined by Howe (1979). In Fig. 1.8, vortices created at the aperture edges are swept away by the bias flow with a velocity u_c along a straight vortex tube of radius a. In this case, Howe showed that for linear perturbations, the dominant contribution to the right hand side term in Eq. (1.7) is related to the perturbed vorticity field $\boldsymbol{\omega}' = \tilde{\boldsymbol{\omega}} \exp(-\mathrm{i}\omega t)$ transported by the mean flow $\bar{\boldsymbol{u}}$:

$$\nabla^2 \tilde{B} = -\boldsymbol{\nabla} \cdot (\tilde{\boldsymbol{\omega}} \times \bar{\boldsymbol{u}}) \tag{1.14}$$

where $\tilde{\boldsymbol{\omega}} = \tilde{\omega} \boldsymbol{e}_\theta$ is the perturbed vorticity in the azimuthal direction $\boldsymbol{e}_\theta$ and $\bar{\boldsymbol{u}} = u_c \boldsymbol{e}_x$ is the velocity of this vortical disturbance in the axial direction $\boldsymbol{e}_x$. If Ω denotes the amplitude of the circulation of the shed vorticity per unit axial length of the jet, the fluctuating vorticity field may be modeled as:

$$\tilde{\omega} = \Omega H(x) \delta(r-a) \exp(\mathrm{i} k_c x) \tag{1.15}$$

where $k_c = \omega / u_c$ is the wavenumber of this aerodynamic perturbation, H is the Heaviside function and δ is the Dirac function.

For a uniform harmonic stagnation enthalpy perturbation $\tilde{B} = \mathrm{i}\omega \Delta\tilde{\varphi}$, the perturbation amplitude is given by [Howe (1979)]:

$$\Omega = \tilde{\Delta}\varphi \left(a \int_0^\infty \frac{x \mathcal{H}_1^{(1)}(x) \cos(x)}{x^2 + (k_c a)^2} \right)^{-1} \tag{1.16}$$

where $\mathcal{H}_1^{(1)}(x) = J_1(x) + \mathrm{i} Y_1(x)$ denotes the Hankel function of the first kind, $J_1(x)$ and $Y_1(x)$ being the Bessel functions of the first and second kinds respectively. This expression can then be used to determine the volume flowrate fluctuation $\tilde{q}$ through the aperture. The relatively long and technical derivation is not reproduced here since it is fully described by Howe (1979). It finally yields an expression for the Rayleigh conductivity of the aperture:

$$K_R = 2a(\gamma - \mathrm{i}\delta) \tag{1.17}$$

where the γ and δ are positive functions of the Strouhal number $\mathrm{St} = ka = \omega a / u_c$ only, calculated with the convection velocity u_c of the vortex sheet:

$$\gamma - \mathrm{i}\delta = 1 + \frac{(\pi/2) I_1(\mathrm{St}) \exp(-\mathrm{St}) - \mathrm{i} K_1(\mathrm{St}) \sinh(\mathrm{St})}{\mathrm{St}\left[(\pi/2) I_1(\mathrm{St}) \exp(-\mathrm{St}) + \mathrm{i} K_1(\mathrm{St}) \cosh(\mathrm{St})\right]} \tag{1.18}$$

where I_1 and K_1 are the modified Bessel functions of the first and second kinds.

The convection velocity u_c of vortical disturbances has to be specified to determine K_R with Eq. (1.17). It is generally admitted that this velocity scales with the mean bias flow velocity: $u_c = C\bar{u}_0$, where C is a constant. One difficulty is to identify the correct scaling factor C. For quasi-steady operating conditions, Howe (1979) proposed to use a vorticity convection velocity u_c equal to half the jet velocity u_j in the *vena contracta* section $u_c = (1/2)u_j$, but u_j is not easy to determine. Hughes and Dowling (1990) found experimentally that $u_c = \bar{u}_0$, where $\bar{u}_0$ is the bias flow velocity, yields a good collapse on their experimental data. This assumption was then adopted in the more recent theoretical analysis of Luong et al. (2005). The correct value of the scaling factor depends on the geometry of the orifice and the structure of the flow in this region. For the sake of simplicity, the same assumption as in [Hughes and Dowling (1990); Luong et al. (2005)] is made in the present study and the convection velocity u_c is assumed to be equal to the bias flow velocity $\bar{u}_0$: $u_c = \bar{u}_0$. A detailed analysis of the convection velocity of vortices shed at the orifice edges is conducted in chapter 5.

Different models were derived based on the original expression Eq. (1.17), including effects of ducting [Wendoloski (1998)], hole shape [Dowling and Hughes (1992)] or plate thickness [Jing and Sun (2000); Luong et al. (2005); Jing and Sun (1999)]. Equation (1.18) is valid for infinitely thin plates. Jing and Sun (2000) proposed a model taking into account the additional dissipation due to the finite thickness h of the plate. In this case, the function $\gamma - \mathrm{i}\delta$ should be replaced by $\gamma' - \mathrm{i}\delta'$, where:

$$\frac{1}{\gamma' - \mathrm{i}\delta'} = \frac{1}{\gamma - \mathrm{i}\delta} + \frac{2h}{\pi a} \tag{1.19}$$

It is now interesting to examine the limits taken by the Rayleigh conductivity of the aperture K_R at small and large Strouhal numbers. For an infinitely thin plate, Eq. (1.17) reduces to:

$$K_R \simeq 2a\left(\frac{1}{3}\mathrm{St}^2 - \mathrm{i}\frac{\pi}{4}\mathrm{St}\right), \ \mathrm{St} \ll 1 \tag{1.20}$$

$$K_R \simeq 2a\left(1 - \frac{\mathrm{i}}{\mathrm{St}}\right), \ \mathrm{St} \gg 1 \tag{1.21}$$

These relations will be used later in the manuscript. Figure 1.9 compares the γ and δ functions from Eq. (1.18) with the asymptotical expressions in Eqs. (1.20) and (1.21). The agreement between the general expression and the low Strouhal approximation is good as long as $\mathrm{St} \leq 0.5$ for both the real γ and imaginary δ components of the Rayleigh conductivity K_R. The high Strouhal approximation collapses on the general expression when $\mathrm{St} \geq 4$.

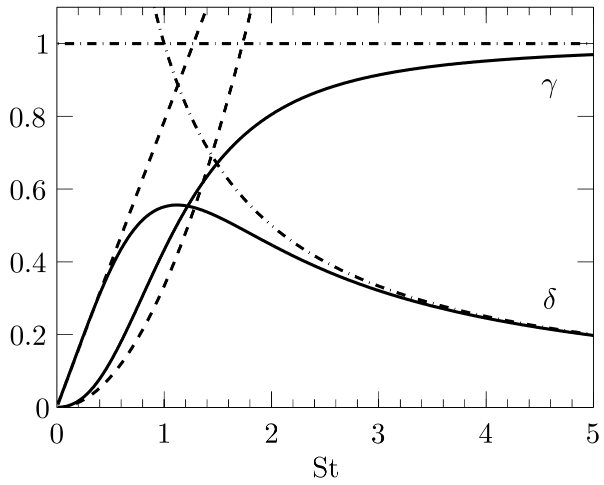

Figure 1.9: *Comparison between the functions γ and δ from Eq. (1.18) (solid lines) and their asymptotical approximations at small Strouhal number Eq. (1.20) (dashed lines) and large Strouhal number Eq. (1.21) (dashed dotted lines).*

1.3.3 Absorption without resonant back cavity

It is now possible to link the Rayleigh conductivity K_R to the absorption coefficient α of a perforated plate of porosity $\sigma = \pi a^2/d^2 \ll 1$. Consider a collection of circular holes of radius a regularly spaced over a plate with a square pattern of elementary size d, as shown in Fig. 1.10. Interactions between holes can be neglected for plates featuring a small porosity when $\sqrt{\sigma} \leq 0.2$ [Melling (1973)]. The flow in the vicinity of the perforations is unsteady, but low frequency fluctuations remain incompressible because they are compact with respect to the acoustic wavelengths considered $\lambda/a \gg 1$. Compressibility effects thus only modify the pressure field away from the perforations $z/a \gg 1$ where plane waves propagate.

Continuity of the fluctuating volume flowrate $\tilde{q}$ in the vicinity of the perforation implies:

$$\tilde{q} = \tilde{u}_1 d^2 = \tilde{u}_0 \pi a^2 = \tilde{u}_2 d^2, \tag{1.22}$$

where $\tilde{u}_1$ and $\tilde{u}_2$ indicate the acoustic velocities upstream and downstream the perforated plate. The Rayleigh conductivity Eq. (1.13) is now used to express the momentum balance of sound waves across the plate:

$$\mathrm{i}\rho_0\omega\tilde{u}_1 = \mathrm{i}\rho_0\omega\tilde{u}_2 = \frac{K_R}{d^2}\left[\tilde{p}_2 - \tilde{p}_1\right] \tag{1.23}$$

Let R and T denote the respective complex amplitudes of the reflected and transmitted plane waves away from the aperture (Fig. 1.10), for an incident

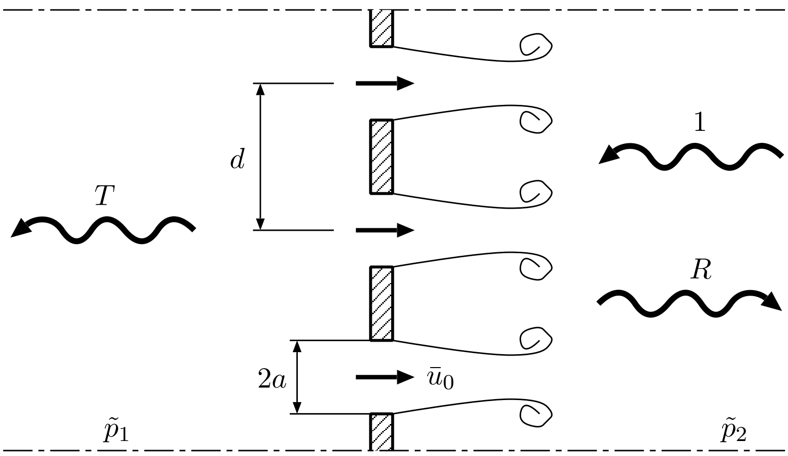

Figure 1.10: *Perforated plate traversed by a bias flow and submitted to normal incident pressure waves. Circular holes of diameter* $2a$ *are regularly spaced with a square pattern of size* d*. The complex amplitudes of the reflected and transmitted waves are denoted* R *and* T*, respectively. The dash-dotted lines indicate symmetry axes.*

wave of amplitude equal to unity:

$$\tilde{p}_2(x) = R\exp(\mathrm{i}kx) + \exp(-ikx) \qquad \text{for } x \geq 0 \tag{1.24}$$

$$\tilde{p}_1(x) = T\exp(-\mathrm{i}kx) \qquad \text{for } x \leq 0 \tag{1.25}$$

where $k = \omega/c_0$ is the acoustic wavenumber. This wavefield must comply with Eqs. (1.22) and (1.23) at the plate location $x = 0$ yielding a general expression for the reflection and transmission coefficients:

$$R = \frac{\mathrm{i}kd^2}{2K_R}\left(\frac{\mathrm{i}kd^2}{2K_R} - 1\right)^{-1} \tag{1.26}$$

$$T = -\left(\frac{\mathrm{i}kd^2}{2K_R} - 1\right)^{-1} \tag{1.27}$$

From the definition of the absorption coefficient $\alpha = 1 - |R|^2 - |T|^2$, one finally obtains [Howe (1998)]:

$$\alpha = -\frac{4kd^2\Im\{K_R\}}{|\mathrm{i}kd^2 - 2K_R|^2} \tag{1.28}$$

where $\Im\{K_R\}$ denotes the imaginary component of the Rayleigh conductivity. If the motion in the aperture remained ideal, the conductivity $K_R = 2a$ would be a real number and there would be no absorption of acoustic energy through the perforation [Rayleigh (1896); Hirschberg (2001)].

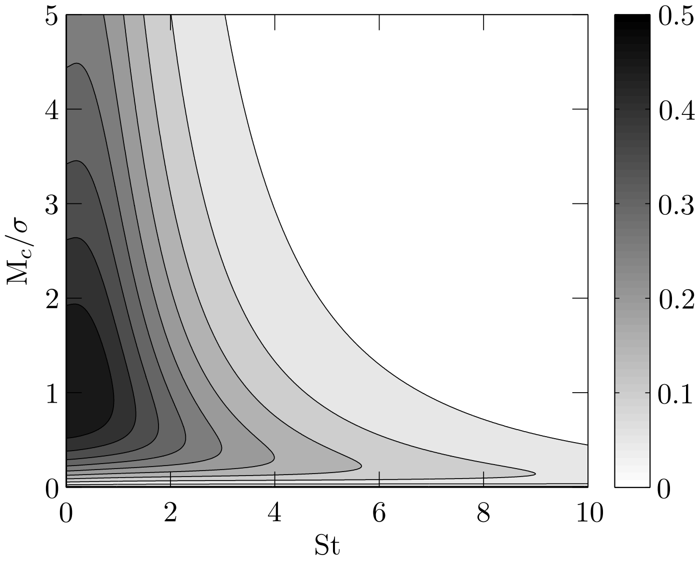

Figure 1.11: *Evolution of the absorption coefficient* α *of a thin perforated plate as a function of the Strouhal number* St *and the ratio* M_c/σ*.*

For an infinitely thin plate, replacing the expression for the Rayleigh conductivity, given by Eq. (1.17), in Eqs. (1.26) to (1.28) leads to:

$$R = \mathrm{i}\frac{\pi}{4}\mathrm{St}\frac{\mathrm{M}_c}{\sigma}\left[\mathrm{i}\frac{\pi}{4}\mathrm{St}\frac{\mathrm{M}_c}{\sigma} - (\gamma - \mathrm{i}\delta)\right]^{-1} \tag{1.29}$$

$$T = (\gamma - \mathrm{i}\delta)\left[\gamma - \mathrm{i}\delta - \mathrm{i}\frac{\pi}{4}\mathrm{St}\frac{\mathrm{M}_c}{\sigma}\right]^{-1} \tag{1.30}$$

$$\alpha = \frac{\pi}{2}\mathrm{St}\frac{\mathrm{M}_c}{\sigma}\delta\left|\delta + \mathrm{i}\gamma + \frac{\pi}{4}\mathrm{St}\frac{\mathrm{M}_c}{\sigma}\right|^{-2} \tag{1.31}$$

where $\mathrm{M}_c = u_c/c_0$ denotes the Mach number based on the convection velocity of vortices shed at the perforation edges and $\mathrm{St} = \omega a/u_c$ is the Strouhal number. The evolution of the absorption coefficient α given by Eq. (1.31) is plotted in Fig. 1.11. As shown by Howe (1998), the maximum attainable value for the absorption coefficient of a perforated plate is $\alpha_{\max} = 0.5$. This maximum is reached at small Strouhal numbers $\mathrm{St} \ll 1$ when $\mathrm{M}_c = \sigma$. In this regime, the optimal bias flow velocity u_c that maximizes absorption $\alpha = 0.5$ is thus solely determined by the perforated plate porosity σ. It has been further observed that this maximum does not depend on the shape of the aperture [Dowling and Hughes (1992)], which can be circular or rectangular, but it is strongly influenced by the shape of the edges [Peters et al. (1993)]. This suggests that the absorption mechanism is intimately linked to the unsteady flow dynamics near the orifice. Damping properties can be further improved by adding a

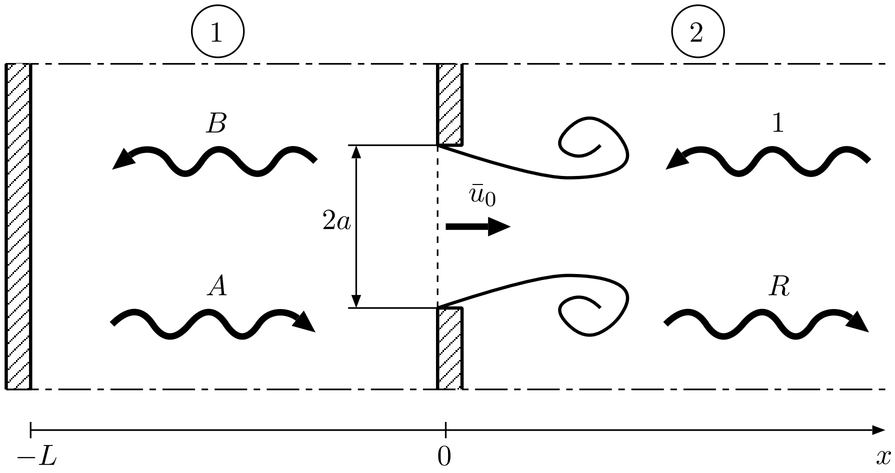

Figure 1.12: *Perforated plate traversed by a bias flow and submitted to normal incident pressure waves. Circular holes of diameter* $2a$ *are regularly spaced with a square pattern of size* d*. The plate is coupled to a resonant back cavity, of size* L*. The complex amplitude of the reflected wave is denoted* R*. The coefficients* A *and* B *denote the pressure wave amplitudes in the back cavity.*

resonant back cavity behind the perforated screen [Hughes and Dowling (1990); Dowling and Hughes (1992)], as considered below.

1.3.4 Absorption with a resonant back cavity

Consider now the presence of a back cavity located at $x = -L$ behind the perforations, as shown in Fig. 1.12. The derivation described below closely follows the analysis of Hughes and Dowling (1990), but the dimensionless numbers introduced in Eqs. (1.29) to (1.31) are used to analyze the results.

The sound field within the cavity lying between $-L \leq x \leq 0$ must now satisfy:

$$\tilde{p}_1(x) = A \exp(\mathrm{i}kx) + B \exp(-\mathrm{i}kx) \tag{1.32}$$

$$\rho_0 c_0 \tilde{u}_1(x) = A \exp(\mathrm{i}kx) - B \exp(-\mathrm{i}kx), \tag{1.33}$$

where A and B are the complex planar sound wave amplitudes in the back cavity. Outside the cavity for $x \geq 0$, one is left with:

$$\tilde{p}_2(x) = R \exp(\mathrm{i}kx) + \exp(-\mathrm{i}kx) \tag{1.34}$$

$$\rho_0 c_0 \tilde{u}_2(x) = R \exp(\mathrm{i}kx) - \exp(-\mathrm{i}kx) \tag{1.35}$$

Using Eqs. (1.22) and (1.23) together with the fact that the velocity vanishes at the back cavity rigid wall $\tilde{u}_1(-L) = 0$, one obtains an expression for the specific impedance $\zeta = \tilde{p}_2 / \rho_0 c_0 \tilde{u}_2$ at the plate location $x = 0^+$:

$$\zeta = \mathrm{i} \left[\frac{kd^2}{K_R} - \frac{1}{\tan(\mathrm{He})} \right] \tag{1.36}$$

In this expression, $\mathrm{He} = kL$ is the cavity Helmholtz number. The reflection coefficient is then given by:

$$R = \frac{\zeta + 1}{\zeta - 1} \tag{1.37}$$

The absorption coefficient can also be determined using the relation $\alpha = 1 - |R|^2$.

It is now interesting to rewrite the specific impedance and the reflection coefficient as functions of the dimensionless numbers St, M_c/σ, h/a and He. Starting from Eq. (1.36), and using Eqs. (1.17) and (1.19) for the Rayleigh conductivity K_R of a perforated plate of finite thickness h, one obtains the following expression for the specific impedance:

$$\zeta = \mathrm{i}\left[\frac{\pi}{2}\mathrm{St}\frac{\mathrm{M}_c}{\sigma}\left(\frac{1}{\gamma - \mathrm{i}\delta} + \frac{2h}{\pi a}\right) - \frac{1}{\tan(\mathrm{He})}\right] \tag{1.38}$$

where $\mathrm{M}_c = u_c/c_0$ is the Mach number based on the convection velocity of the vortex sheet, $\sigma = \pi a^2/d^2$ is the plate porosity, $\mathrm{St} = \omega a/u_c$ is the Strouhal number and h is the plate thickness. Replacing Eq. (1.38) in Eq. (1.37), one obtains a general expression for the reflection coefficient:

$$R = \frac{\mathrm{i}\left[\frac{\pi}{2}\mathrm{St}\frac{\mathrm{M}_c}{\sigma}\left(\frac{1}{\gamma - \mathrm{i}\delta} + \frac{2h}{\pi a}\right) - \frac{1}{\tan(\mathrm{He})}\right] + 1}{\mathrm{i}\left[\frac{\pi}{2}\mathrm{St}\frac{\mathrm{M}_c}{\sigma}\left(\frac{1}{\gamma - \mathrm{i}\delta} + \frac{2h}{\pi a}\right) - \frac{1}{\tan(\mathrm{He})}\right] - 1} \tag{1.39}$$

Figures 1.13(a) to 1.13(d) show the evolution of the absorption coefficient $\alpha = 1 - |R|^2$, where R is given by Eq. (1.39), for an infinitely thin perforated plate backed by a cavity, as a function of the Strouhal and the Helmholtz numbers. In each figure the absorption coefficient is computed for a set of values of the ratio M_c/σ ranging from 0.1 to 2. Acoustic absorption is a function of both the Strouhal number St and the Helmholtz number of the back cavity He. It is also possible to reach total absorption $\alpha = 1$ for certain values of the ratio M_c/σ. However, in the general case, all these parameters are strongly interrelated, and it is difficult to deduce design rules to maximize absorption. This problem will be examined in the next chapters.

It is now worth examining our current understanding of the influence of the perturbation amplitude when a perforation is subjected to incident sound waves of moderate to high amplitudes by reviewing nonlinear models.

1.4 Effects of amplitude on sound absorption

Due to the wide variety of applications, extensive research has been devoted to the experimental characterization, modeling and simulation of the absorption

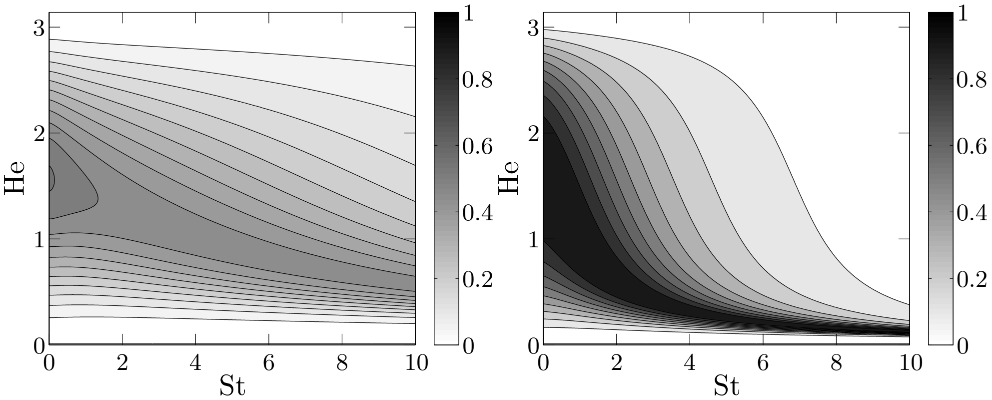

(a) $\mathrm{M}_c/\sigma = 0.1$.

(b) $\mathrm{M}_c/\sigma = 0.5$.

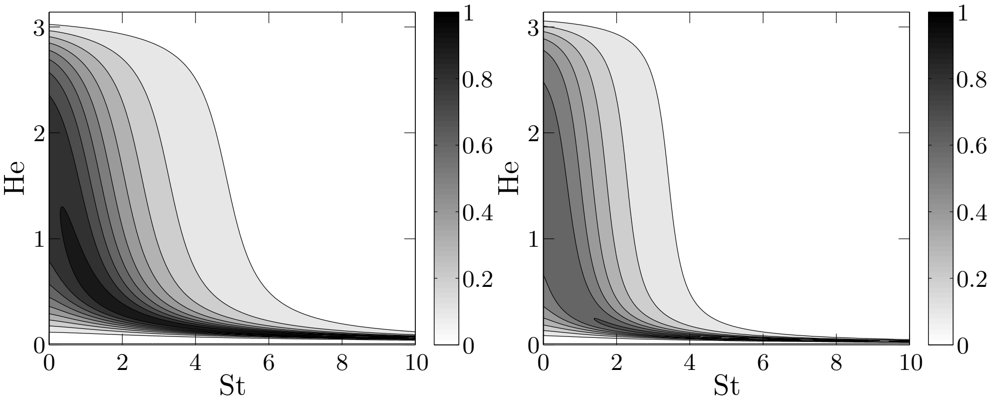

(c) $\mathrm{M}_c/\sigma = 1$.

(d) $\mathrm{M}_c/\sigma = 2$.

Figure 1.13: *Evolution of the absorption coefficient* $\alpha = 1 - |R|^2$ *(Eq. (1.39)) of a perforated plate backed by a cavity as a function of the Strouhal number* St *and the Helmholtz number* He *for* $h/a = 0$ *(infinitely thin plate), and for different values of the ratio* M_c/σ*.*

properties of perforated screens at high sound levels. Recently, Rupp et al. (2010) carried out an experimental study on the effect of excitation amplitude on acoustic absorption of a single orifice traversed by a mean bias flow. The transition between the linear and nonlinear regimes is studied using Particle Image Velocimetry (PIV). It is shown that absorption first increases when the sound level is augmented before being attenuated at higher levels. This type of response was already noted in the experiments gathered by Ingard and Ising (1967).

Numerical studies have recently been conducted to investigate the absorption properties of perforated plates traversed by a bias flow. Leung et al. (2007) studied the effects of frequency and orifice opening size on absorption by direct simulations of the Navier-Stokes equations in two dimensions. They found that absorption is improved at low forcing frequencies and for small orifices. The acoustically excited flow through a circular orifice backed by a cavity was examined with three-dimensional direct simulations by Zhang and Bodony (2012). In their work, the perforation was subjected to high amplitude sound waves at frequencies between 1.5 and 3 kHz. They analyzed the dynamics of the boundary layers within the orifice and found that the incident sound waves could affect their thickness, and thus modify in turn the discharge coefficient of the perforation. Another approach was followed by Mendez and Eldredge (2009) with the help of Large-Eddy Simulation to study the response of perforates to small acoustic disturbances. This numerical strategy captures the largest scales of the flow and the sound waves propagating in the numerical domain. It is shown to be suitable to reproduce the Rayleigh conductivity of a perforation by comparison with the predictions of the analytical model from Howe (1979). The same numerical solver is used in chapter 5 to analyze the response of an orifice to flow perturbations of increasing amplitudes.

Different analytical expressions were proposed to determine the impedance of perforated plates operating in linear and nonlinear regimes [Ingard and Ising (1967); Cummings and Eversman (1983); Cummings (1986); Bellucci et al. (2004)]. These models are presented and discussed below.

1.4.1 Ingard and Ising's model

Ingard and Ising (1967) carried out measurements of the unsteady flow in an orifice plate subjected to high amplitude sound pressure waves and backed by a cavity. The unsteady acoustic velocity in the orifice u'_0 was recorded by means of a hot-wire probe, and the driving sound pressure p'_1 was measured with a microphone in the cavity.

The amplitude of the acoustic velocity fluctuation in the perforation was compared to the amplitude of the driving sound pressure in the cavity. Their measurements are reported in Fig. 1.14. These authors identified two operating

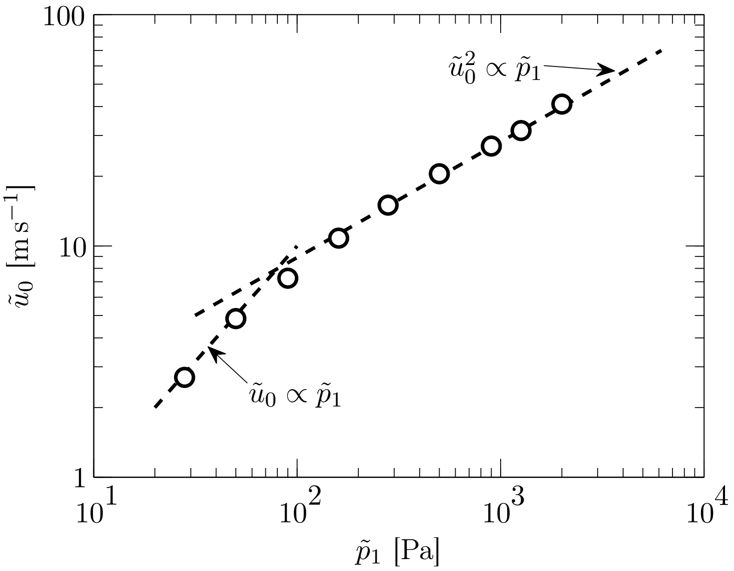

Figure 1.14: *Amplitude of the measured acoustic velocity in the orifice as a function of the unsteady pressure amplitude in the cavity, at a frequency $f = 150$ Hz. Data are reproduced from Ingard and Ising (1967).*

regimes of the orifice plate. For small acoustic amplitudes, the acoustic velocity in the orifice was found to be proportional to the unsteady sound pressure: $\tilde{u}_0 \propto \tilde{p}_1$. For higher acoustic amplitudes, the square of the acoustic velocity is proportional to the driving pressure $\tilde{u}_0^2 \propto \tilde{p}_1$. In their experiments, the transition from the linear to the nonlinear regime occurred at an acoustic velocity of approximately $u_t \simeq 10$ m s^{-1}. Using their experimental data, they obtained the following approximation, valid in the nonlinear regime:

$$\tilde{p}_1 \simeq \rho_0 \tilde{u}_0^2, \quad \tilde{u}_0 \geq u_t \tag{1.40}$$

This result can be interpreted on the basis of Bernoulli's equation, assuming that the pressure in the orifice is a certain fraction q of the pressure in the cavity. By applying Bernoulli's theorem to a streamline connecting a point in the cavity to another point situated in the orifice, one can write:

$$(1-q)\tilde{p}_1 = \frac{1}{2}\rho_0 \tilde{u}_0^2 (1-\sigma^2), \tag{1.41}$$

where $\sigma = A_0/A$ is the plate porosity, A_0 being the orifice surface area and A the section area of the back cavity. They assumed $q \simeq 1/2$, i.e. the sound pressure in the orifice is approximately the average of the sound pressures on the two sides of the perforation. Based on this consideration, the orifice resistance corresponding to the real part of the orifice impedance Z is then given by:

$$\Re(Z) = \frac{\tilde{p}_1}{\tilde{u}_0} = \rho_0 \tilde{u}_0 (1-\sigma^2) \tag{1.42}$$

This expression is in agreement with their experimental finding Eq. (1.40), neglecting the $(1-\sigma^2)$ term since in their case $\sigma \ll 1$. It is interesting to note here that predictions from their model Eq. (1.42) were only accidentally accurate, because of two errors which offset. In their work, Ingard and Ising did not consider the *vena contracta* of the orifice. Bernoulli's theorem applied to a streamline connecting the cavity to another point in the *vena contracta* section writes:

$$\tilde{p}_1 \simeq \frac{1}{2}\rho_0 \tilde{u}_j^2 = \frac{1}{2C_c^2}\rho_0 \tilde{u}_0^2, \tag{1.43}$$

where u_j is the velocity at the *vena contracta* section, and $C_c = A_j/A_0$ is the contraction ratio. A typical value for the contraction ratio of an orifice being $C_c \simeq 0.7$, Eq. (1.43) can be approximated by Eq. (1.40). We will show in paragraph 1.4.2 how Cummings and Eversman (1983) developed this approach in a more rigorous fashion.

When a mean bias flow passes through a perforation backed by a resonant cavity, Eq. (1.42) can be used to determine the specific impedance ζ:

$$\zeta = -\frac{Z}{\rho_0 c \sigma} = -\frac{\tilde{u}_0}{c}\frac{1-\sigma^2}{\sigma} - \mathrm{i}\chi = -\frac{\tilde{u}_0}{\bar{u}_0}\frac{\mathrm{M}_c}{\sigma}(1-\sigma^2) - \mathrm{i}\chi, \tag{1.44}$$

where χ is the sum of the orifice reactance and the impedance of the back cavity, $\mathrm{M}_c = \bar{u}_0/c$ is the Mach number in the aperture, and the minus sign has been introduced to be consistent with the definition of the reflection coefficient R used in the present work.

At resonance, the reactance $\chi = 0$ vanishes [Ingard and Ising (1967)], and one can use Eq. (1.44) to calculate the predicted reflection coefficient of the perforated plate. For low porosity plates $\sigma \ll 1$, one obtains:

$$R = \frac{\zeta+1}{\zeta-1} = \frac{\dfrac{\tilde{u}_0}{\bar{u}_0}\dfrac{\mathrm{M}_c}{\sigma} - 1}{\dfrac{\tilde{u}_0}{\bar{u}_0}\dfrac{\mathrm{M}_c}{\sigma} + 1}, \tag{1.45}$$

Figure 1.15 shows the nonlinear reflection coefficient of a perforated plate traversed by a mean bias flow and coupled to a resonant cavity, as a function of the ratio between the acoustic velocity $\tilde{u}_0$ and the mean bias flow velocity $\bar{u}_0$ within the aperture, as predicted by Eq. (1.45). The back cavity is operating near the resonance frequency, since its reactance is supposed to be zero. It is interesting to note that the ratio M_c/σ determines the amplitude of the incident sound wave, represented by the ratio $\tilde{u}_0/\bar{u}_0$, at which maximum absorption $|R| = 0$ takes place:

$$\left(\frac{\tilde{u}_0}{\bar{u}_0}\right)_{|R|=0} = \frac{\sigma}{\mathrm{M}_c}, \tag{1.46}$$

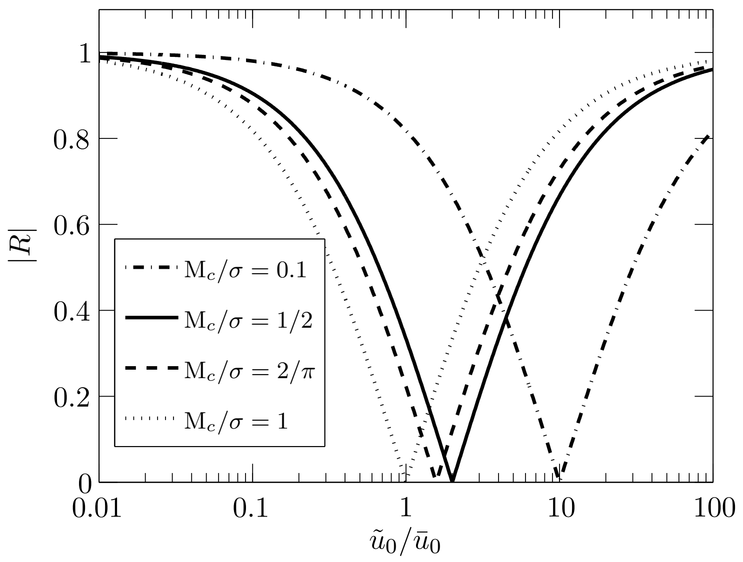

Figure 1.15: *Reflection coefficient of an orifice backed by a resonant cavity as a function of the unsteady velocity ratio in the orifice* $\tilde{u}_0/\bar{u}_0$*, for different values of* M_c/σ *(Eq. (1.45)).*

The following observations can be made:

- In the nonlinear regime, the lower the ratio M_c/σ, the higher the amplitude of the acoustic velocity at which maximum absorption occurs.
- For $M_c/\sigma = 1/2$, maximum absorption in the nonlinear regime occurs at $\tilde{u}_0/\bar{u}_0 = 2$.
- For $M_c/\sigma = 2/\pi$, maximum absorption in the nonlinear regime occurs at $\tilde{u}_0/\bar{u}_0 = \pi/2 \simeq 1.57$.
- Since Eq. (1.45) is only valid in the nonlinear regime, the reflection coefficient plotted in Fig. 1.15 is only correctly predicted for high values of the ratio $\tilde{u}_0/\bar{u}_0$. In other words, the amplitude $\tilde{u}_0$ of the acoustic velocity field near the aperture must be at least comparable to the mean bias flow velocity $\bar{u}_0$.

Interestingly, chapter 4 will demonstrate that in the linear regime, the ratios $M_c/\sigma = 1/2$ and $M_c/\sigma = 2/\pi$ are the respective optimal ratios for maximum absorption at low and high Strouhal numbers.

1.4.2 Cummings and Eversman's model

Cummings and Eversman (1983) analyzed acoustic transmission at high amplitudes through duct terminations. They examined the acoustic properties of a converging nozzle placed at the end of a circular duct, traversed by a mean bias flow and subjected to high amplitude sound waves. This problem is analogous to the study of a single orifice placed in a duct, and can be examined

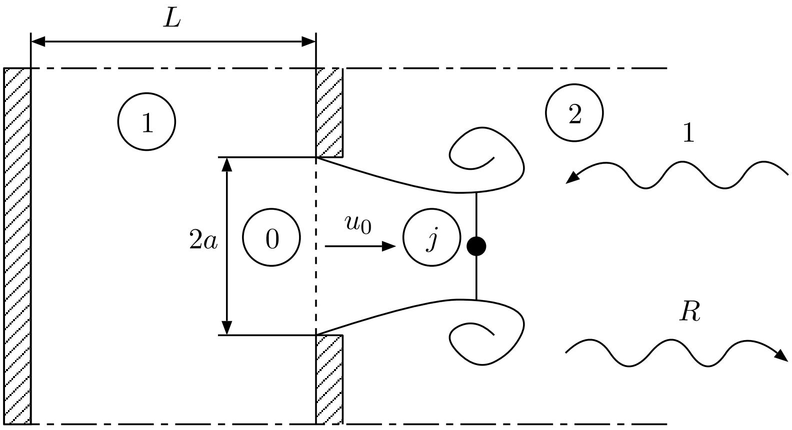

Figure 1.16: *Single orifice backed by a cavity, traversed by a mean bias flow and subjected to normal incident sound waves. The different zones considered for the application of Bernoulli's theorem are highlighted in the diagram. The* vena contracta *section is denoted by j.*

with the same approach. In this section the theory developed by Cummings and Eversman (1983) for a duct nozzle is revisited and applied to the case of a perforated plate traversed by a bias flow in a duct. Figure 1.16 shows the geometry considered in the present work.

Under the assumptions of irrotational, incompressible and inviscid flow, and if the wavelength λ is much larger than the dimensions of the orifice $\lambda/2a \gg 1$, it is possible to apply a quasi-steady approach to determine the acoustic impedance of the perforate using the analysis developed by Morse and Ingard (1986) for an aperture or by Cummings and Eversman (1983) for nozzles.

For a streamline starting upstream of the orifice (denoted 1 in Fig. 1.16) and ending at the *vena contracta* section (denoted j in Fig. 1.16), the flow is irrotational and can be treated as incompressible. The unsteady Bernoulli's theorem holds:

$$\frac{\partial}{\partial t}\left(\varphi_j - \varphi_1\right) + \frac{1}{2}\left(u_j^2 - u_1^2\right) = \frac{p_1 - p_j}{\rho_0}, \tag{1.47}$$

where φ is the velocity potential. Equation. (1.47) is used to link the unsteady pressure difference $p_2 - p_1$ applied to the plate to the velocity in the orifice u_0. First, the unsteady term can be associated with the inertial motion of a slug of fluid of length l, which is the sum of the mass end correction and the plate thickness $\partial(\varphi_j - \varphi_1)/\partial t \simeq l\partial u_0/\partial t$. The value of the end correction l depends in general on the geometry of the perforated plate [Ingard (1953)]. For a circular hole in an infinite duct, one has $l = 8a/(3\pi)$. Then, the continuity of volume flowrate yields $A_j u_j = A_0 u_0 = A_1 u_1$, where A_x indicates the cross section of the irrotational flow at locations $x = 0$, 1 or j. It is now useful to introduce the contraction coefficient C_c, defined as the ratio between the *vena contracta* cross section and the orifice section $C_c = A_j/A_0$. Thus the velocities u_1 and u_j can be expressed respectively by $u_1 = \sigma u_0$ and $u_j = u_0/C_c$, σ indicating the plate porosity. Finally the pressure in the jet p_j is assumed to be equal to the external pressure p_2. With these assumptions, Eq. (1.47) can be written as [Cummings and Eversman (1983)]:

$$l\frac{\partial u_0}{\partial t} + \frac{1-\sigma^2 C_c^2}{2C_c^2} u_0^2 = \frac{p_1 - p_2}{\rho_0} \tag{1.48}$$

In this approach, the unsteady driving pressure applied to the plate is the sum of two terms:

- The first term in the left hand side of Eq. (1.48) represents the frequency-dependent part of the total pressure drop. It is linked to the oscillating mass of a slug of fluid of length l, and can be associated to the reactance of the orifice.
- The second term in the left hand side of Eq. (1.48) is associated to aerodynamic losses, which are included in the contraction coefficient C_c. The total aerodynamic losses associated to the pressure drop through a perforation are usually represented by the discharge coefficient C_D (see for example Batchelor (1967)). This discharge coefficient can be expressed as the product of losses due to *vena contracta* effects C_c, and viscous losses C_v: $C_D = C_c C_v$. Viscous losses are generally small compared to *vena contracta* effects, and thus we will assume here that $C_D \simeq C_c$.

The contributions of the mean bias flow and the unsteady acoustic perturbation are highlighted by decomposing pressure and velocity as $p(t) = \bar{p} + p'(t)$, $u_0(t) = \bar{u}_0 + u_0'(t)$. Replacing these expressions in Eq. (1.48) and discarding the time-independent terms, Cummings and Eversman (1983) obtained the following expression:

$$l\frac{\partial u_0'}{\partial t} + \frac{1-\sigma^2 C_c^2}{2C_c^2} u_0'^2 + \frac{1-\sigma^2 C_c^2}{C_c^2} \bar{u}_0 u_0' = \frac{p_1' - p_2'}{\rho_0}, \tag{1.49}$$

which is valid when no reverse flow appears in the aperture, i.e. $|u_0'| \leq \bar{u}_0$. By introducing the radiation impedance of the nozzle, they obtained an expression for the total specific impedance of the perforation placed at a duct termination, when it is submitted to an harmonic acoustic perturbation $u_0' = \tilde{u}_0 \exp(-\mathrm{i}\omega t)$:

$$\zeta = \frac{1}{\sigma}\left[\mathrm{M}_c \frac{1-\sigma^2 C_c^2}{C_c^2} + \frac{1-\sigma^2 C_c^2}{2C_c^2}\frac{\tilde{u}_0}{c} + \mathrm{i}k(\delta_1 + \delta_2) + \frac{(ka)^2}{4}\right], \tag{1.50}$$

where $k = \omega/c$ is the acoustic wave number, δ_1 and δ_2 are the inner and outer end correction lengths of the nozzle, respectively.

These authors also noted that, for the case of zero mean flow at high amplitudes, the nonlinear resistance term dominates the nozzle impedance, and Eq. (1.50) reduces to:

$$\tilde{p}_1 - \tilde{p}_2 = \rho_0 \tilde{u}_0^2 \frac{1 - \sigma^2 C_c^2}{2 C_c^2}, \tag{1.51}$$

This expression is similar to Ingard and Ising's empirical expression (1.41).

1.4.3 Bellucci et al.'s model

Bellucci et al. (2004) developed a semi-empirical model describing the impedance of a perforated plate operating in both linear and nonlinear regimes. The complex impedance of the perforate is again described as the sum of a real component, the resistance, and an imaginary component, the reactance. The reactance is related to the additional mass fluctuating in the region near the orifice, and it is taken into account by means of a semi-empirical expression for the mass end correction. The orifice resistance is calculated following the quasi-steady approach presented in section 1.4.2. The total pressure loss for a steady flow can be written:

$$\Delta p = \frac{1}{2} \rho_0 \eta |u_0| u_0, \tag{1.52}$$

where η is the pressure loss coefficient, which is a function of the orifice porosity and Reynolds number [Batchelor (1967)]. Note that here the absolute value of the velocity is introduced to take into account flow reversal in the orifice at high perturbation levels [Cummings (1986)]. By decomposing the pressure and velocity as the sum of a mean value and a fluctuation in Eq. (1.52), and keeping only the terms related to the unsteady perturbation, one obtains:

$$\Delta p' = \frac{1}{2} \rho_0 \eta \left[|\bar{u}_0 + u_0'| (\bar{u}_0 + u_0') - \bar{u}_0^2 \right] \tag{1.53}$$

The time derivative of Eq. (1.53) can be written as:

$$\frac{d\Delta p'}{dt} = \rho_0 \eta |\bar{u}_0 + u_0'| \frac{du_0'}{dt} \tag{1.54}$$

Since Eq. (1.54) is nonlinear, Bellucci et al. (2004) applied a Fourier series expansion to obtain the unsteady pressure drop generated by a sinusoidal acoustic velocity perturbation $u_0' = \tilde{u}_0 \sin(\omega t)$. By keeping only the response at the forcing frequency, they obtained:

$$\frac{d\Delta p'}{dt} = \omega \rho_0 \eta \, g\left(\frac{\bar{u}_0}{\tilde{u}_0'} \right) |\tilde{u}_0|^2 \cos(\omega t), \tag{1.55}$$

where the function g is defined as:

$$g(x) = \begin{cases} \dfrac{2}{\pi} \left[x \arcsin(x) + \dfrac{(1 - x^2)^{1/2}}{3} (2 + x^2) \right] & \text{if } x \leq 1 \\ x & \text{if } x > 1 \end{cases}$$

Finally, the Fourier component of the unsteady pressure drop at the forcing angular frequency ω is given by:

$$\widetilde{\Delta p} = \rho_0 \eta \, g\left(\frac{\bar{u}_0}{\tilde{u}_0}\right) |\tilde{u}_0| \tilde{u}_0 \tag{1.56}$$

Equation (1.56) features a nonlinear behavior for the unsteady pressure loss across the orifice for acoustic velocity amplitudes $\tilde{u}_0$ higher than the mean bias flow velocity $\bar{u}_0$. The pressure drop coefficient η can then be modeled as a function of the operating regime of the perforated plate. In the linear regime, when $\tilde{u}_0 \leq \bar{u}_0$, the pressure loss coefficient η_{lin} is modeled with the vortex-sheet theory from Howe (1979):

$$\eta = \eta_{\text{lin}} = \frac{\pi}{2}\frac{\delta \text{St}}{\gamma^2 + \delta^2}, \tag{1.57}$$

where the functions γ and δ are defined by Eq. (1.18).

In the absence of bias flow $\bar{u}_0 = 0$, the pressure drop across the perforation η_{nobias} is modeled by means of a discharge coefficient C_D with a quasi-steady hypothesis. This condition can be expressed in terms of an acoustic Strouhal number $\text{St}_{\text{ac}} = \omega a/\tilde{u}_0$. For $\text{St}_{\text{ac}} \ll 1$ the quasi-steady assumption is valid, and the pressure loss coefficient is given by:

$$\eta = \eta_{\text{nobias}} = \frac{1}{C_D^2} \tag{1.58}$$

Bellucci et al. (2004) mentioned that $C_D = 0.82$ gave the best agreement between experiments and model predictions. At higher Strouhal numbers, when the flow cannot be considered quasi-steady, they used the Strouhal number St_{ac} model from Disselhorst and Wijngaarden (1980):

$$\eta = \eta_{\text{nobias}} = 0.5\frac{3\pi}{4}\text{St}_{\text{ac}}^{1/3} \tag{1.59}$$

Finally, in the intermediate regime, the pressure loss coefficient is treated by a weighted average:

$$\eta = \frac{\eta_{\text{nobias}}(1-g) + \eta_{\text{lin}}(g - 4/(3\pi))}{1 - 4/(3\pi)} \tag{1.60}$$

A comparison with their measurements shows that this model gives a good agreement with experimental data in the linear ($\tilde{u}_0 \leq \bar{u}_0$) as well as in the zero bias flow regimes ($\bar{u}_0 = 0$). However in the intermediate regime the accuracy of the model worsens. This type of approach is revisited in chapter 5 to make the link with Howe's model in the linear regime for vanishingly small acoustic disturbances and analyze effects of the perturbation amplitude on the transition to nonlinearity.

1.5 Summary and outline

The overview proposed in this chapter shows that the boundaries of a combustor play an important role for the stability of the flame in a gas turbine engine. Passive dampers based on quarter-wave or Helmholtz resonators and perforated plates are widely used in combustion chambers to increase the acoustic dissipation of the system and absorb the acoustic waves generated by heat release rate oscillations in the flame.

Although Helmholtz resonators are more commonly found in industrial applications due to their relatively simple design and integration in an engine, their limited absorption bandwidth is a major drawback when the frequency of the unstable modes varies. Dampers based on perforated screens represent an attractive alternative to the use of quarter-wave or Helmholtz resonators in gas turbines. The present thesis is based on the previous work of Tran (2009) at EM2C, who characterized the upstream acoustic boundary condition and its effect on high-amplitude combustion instabilities in a staged swirled combustor. He developed an impedance control system based on perforated plates to control these instabilities.

The objective of the present thesis is twofold:

- to improve and simplify the design of robust dampers based on perforated plates in order to maximize their acoustic absorption properties;
- to analyze the effect of the sound wave amplitude on the acoustic response and develop models predicting absorption at high forcing amplitudes.

The organization and the contents of this thesis are described in the following sections.

1.5.1 Theoretical, experimental and numerical characterization of the acoustic response of perforates

A considerable amount of work has already been conducted on measuring, simulating and modeling the acoustic response of perforated plates. Different modeling techniques describing the acoustic impedance of a perforated screen in linear and nonlinear regimes have been presented in chapter 1. The vortex-sheet model developed by Howe (1979) has been widely used to characterize the Rayleigh conductivity of an orifice traversed by a mean bias flow and subjected to low-amplitude sound waves. The resulting equations were revisited in section 1.3. General expressions for the impedance of a perforated plate with and without a back cavity were derived as functions of four dimensionless numbers: the Mach number over porosity ratio M_c/σ, the Strouhal number St, the thickness ratio h/a and the Helmholtz number of the back cavity He. The influence of these quantities on the absorption coefficient was also analyzed. It was pointed out that in general it is difficult to optimize their damping properties due to the large number of parameters that must be considered.

When the amplitude of the incident sound wave is increased, transition from the linear to the nonlinear regime occurs. A review of the existing models describing the nonlinear response of perforates was carried out in section 1.4. Three models describing amplitude effects on the orifice impedance developed by Ingard and Ising (1967), Cummings and Eversman (1983) and Bellucci et al. (2004) were analyzed in detail. They are all based on a quasi-steady description of the flow response. These models are difficult to use for impedance prediction over a wide range of amplitudes because the transition from linear to nonlinear regime is only approximated. They also rely on the knowledge of several lumped parameters that need to be specified.

Chapter 2 introduces the experimental setup used in this work to characterize the reflection coefficient of perforates. The acoustic properties of a set of perforated plates are measured in the impedance tube called ITHACA. The test rig, the perforates and the diagnostics are presented. The three microphone method used to measure the impedance is validated on the ideal configuration of a closed-end tube. The effect of air injection through the perforations is also studied. The measurements made with this test rig are presented in the next chapters.

The numerical solver AVBP developed by Cerfacs used to calculate the unsteady flow though an orifice subjected to incident sound waves of increasing amplitudes is presented in chapter 3. Three-dimensional direct simulations are carried out on a single geometrical configuration, for two different forcing frequencies and Sound Pressure Levels (SPL) ranging from 90 dB up to 160 dB. The numerical configuration simulated is presented, together with the description of the modeled boundary conditions. Acoustic forcing is simulated by superposing an incident pressure wave to the mean flow at the outlet of the numerical domain. Two types of inlet conditions can be used to simulate either an infinite length tube or a back cavity situation. Spatial convergence is discussed by comparing the mean flows obtained on three grids with increasing resolution. The simulation made are used in chapter 5 to analyze effects of the amplitude level.

1.5.2 Optimization of acoustic absorption in the linear regime

The acoustic behavior of perforated plates depends in general on:

- geometrical parameters, such as hole shape, size, inter-hole spacing, plate thickness, back cavity size, plate porosity, perforation angle;
- flow parameters, such as bias flow velocity, grazing flow velocity, Mach number, Reynolds number;
- acoustic parameters, such as the forcing frequency, the incident angle and the amplitude of sound waves.

As already mentioned, because of the large number of parameters to examine, the optimization of a damper based on perforated plates is not a simple task.

Chapter 4 aims at closing this gap, by identifying two interesting operating regimes where it is possible to independently choose the optimal bias flow velocity in the perforations and the back cavity depth that maximize acoustic absorption.

First, conditions maximizing absorption in the linear regime are derived. Two asymptotic regimes, where the damper operates at low and high Strouhal numbers respectively, are then analyzed, and simplified expressions for the acoustic properties of perforated screens are inferred. In particular, the absorption bandwidths corresponding to dampers operating in these two regimes are derived to assess the robustness of their designs. Predictions from these models are then compared to measurements made in the impedance tube presented in chapter 2. Finally, the response of perforated plates operating in off-design conditions, when the bias flow velocity shifts away from its optimal value, is discussed for the low and high Strouhal regimes. The impact of this deviation on the reflection and absorption coefficients is modeled and compared to experimental results.

1.5.3 Effect of amplitude on the acoustic response of perforates

Amplitude effects on the acoustic response of a perforated plate are investigated in chapter 5. Direct numerical simulations with the solver presented in chapter 3 are first carried out to analyze the physical mechanisms taking place in the vicinity of the orifice when sound waves of increasing amplitudes impinge onto the perforation. These simulations are first used to confirm hypotheses made on the flow dynamics to determine the acoustic properties of perforates in the linear regime. It is then shown that the transition from linear to nonlinear regimes occurs when the acoustic velocity amplitude in the orifice is comparable to the mean bias flow velocity, and periodic flow reversal takes place. The evolution of the vortex rings swept at the perforation is analyzed and their trajectory and convection velocity are extracted from the calculations.

An analysis of these simulations is then conducted to devise two novel nonlinear models. A Vortex Convection (VC) model is developed by exploiting the analysis of the trajectory of vortices swept from the perforation at low and high perturbation amplitudes. It is shown that it is possible to model to some extent the major nonlinear effects by introducing the mean convection velocity extracted from the calculations in the linear expression of the acoustic impedance. The second model is deduced from a quasi-steady analysis of the flow in the vicinity of the perforation. This approach is an extension of the works of Cummings and Eversman (1983), Morse and Ingard (1986) and Bellucci et al. (2004). By comparing the linearized Bernoulli's equation with Howe's linear model, two original expressions for the contraction coefficient and the end correction length are derived as functions of the Strouhal number and compared to results from the literature. Additionally, a Fourier series expansion of the unsteady pressure drop through the orifice allows the determination of its Rayleigh conductivity as a function of the acoustic velocity amplitude. This is used to derive an Impedance Describing Function (IDF) of the perforated plate.

Predictions of the two nonlinear models VC and IDF are then compared to measurements and simulations. The reflection, transmission and absorption coefficients determined from the models are compared to numerical results and to experimental data for different plate geometries, forcing frequencies and SPL. Both models are demonstrated to capture well the linear and high-amplitude operating regimes. The IDF shows superior performance in the transition region.

Finally, the acoustic power dissipated at the orifice is also inferred from the VC and IDF models, and it is compared to the dissipated power extracted from the numerical simulations. Once again, the IDF model is shown to correctly capture the nonlinear behavior of the acoustic dissipation, while the VC model is only capable of reproducing the behavior at low amplitudes.

Chapter 2

Description of the experimental configuration

The present chapter introduces the experimental setup used in this work to characterize the reflection coefficient of dampers based on perforates. The acoustic properties of a set of perforated plates are measured in an impedance tube. The test rig, the geometries of the perforates and the diagnostic technique are presented. The three microphone method used to measure the impedance is validated on the ideal configuration of a closed-end tube. The effect of air injection through the perforations is also studied.

2.1 The impedance tube ITHACA

All the acoustic measurements were realized in the vertical impedance tube ITHACA (*Impedance Test bench for High ACoustic Amplitudes*), developed at EM2C during the Ph.D. thesis of Tran (2009). This test bench, sketched in Fig. 2.1 and shown in Fig. 2.2, was designed to allow measurements of the acoustic properties of devices introduced at the boundaries of a combustor, such as a perforated plate with a back cavity.

The main element of the test bench is a 50 mm inner diameter tube which is connected at the bottom to a 320 mm diameter high efficiency loudspeaker using a conical adaptation piece. This loudspeaker is driven by an amplifier fed by a signal synthesizer that enables to reach sound pressure levels (SPL) up to 150 dB for harmonic waves generated in a frequency range 100 Hz to 2 kHz. The SPL of a sound wave is expressed in this work in decibels (dB) and is defined as:

$$\mathrm{SPL} = 20 \log \frac{p'_{\mathrm{rms}}}{p_{\mathrm{ref}}} \tag{2.1}$$

where $p_{\mathrm{ref}} = 2 \cdot 10^{-5}$ Pa is a reference pressure, and p'_{rms} is the root-mean-square value of the sound pressure signal. For a monochromatic harmonic wave

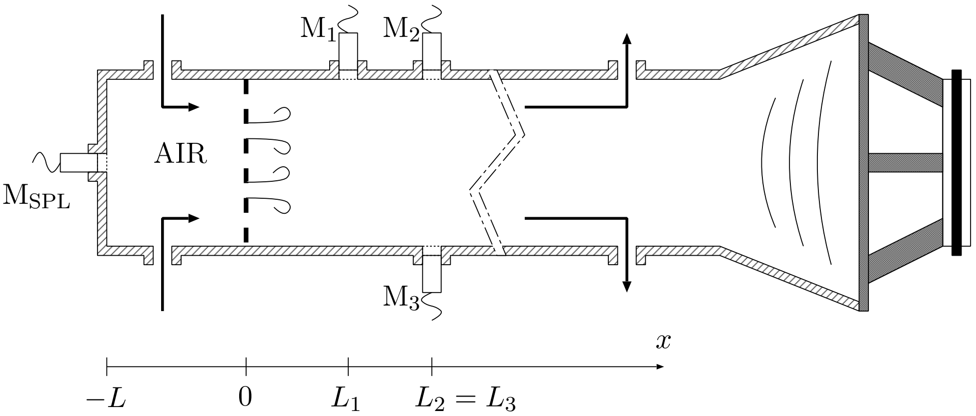

Figure 2.1: *ITHACA impedance tube apparatus schematic, with microphones locations [Tran (2009)]. The flow is injected in the back cavity and leaves the system far away from the microphones and the loudspeaker.*

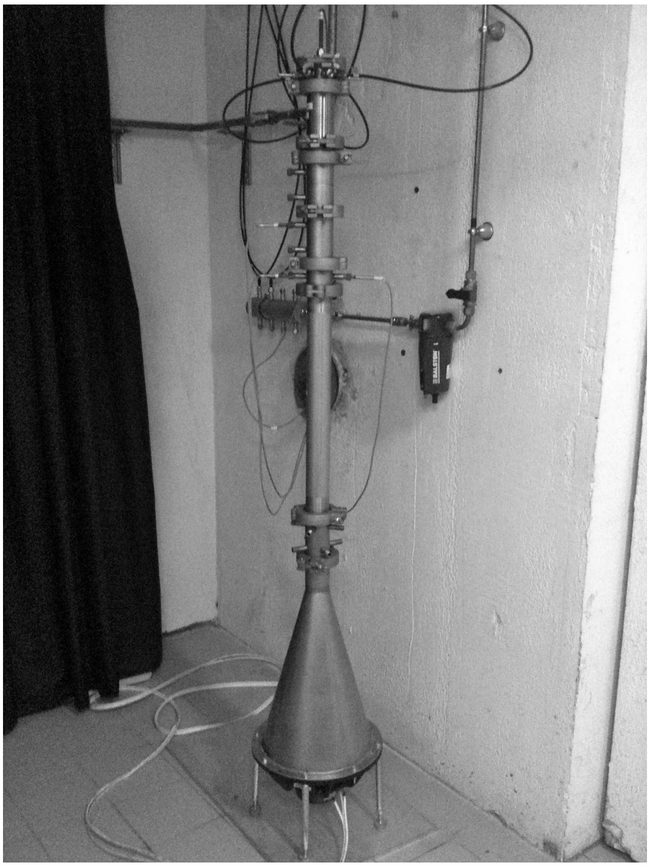

Figure 2.2: *Photography of the experimental setup. The air inlets are connected to a Bronkhorst massflow controller and a Balstom filter.*

of amplitude p'_{amp}, $p'_{\mathrm{rms}} = p'_{\mathrm{amp}}/\sqrt{2}$. The sound level in the system is controlled at the rear side of the back cavity with the microphone $\mathrm{M_{SPL}}$ flush mounted to the top rigid wall.

A particular care has been adopted to redesign the air injection system, located in the back cavity. The main objective was to minimize the fraction of acoustic energy which is dissipated in the air injection tubings. The original air inlet featured eight inlet tubings of 8 mm inner diameter distributed over two rows, as shown in Fig. 2.3(a). The new air injection system, presented in Fig. 2.3(b), is composed by four radial air injection tubes of 6 mm inner diameter, located on a single row. The new inlet is flexible and can be easily modified to inject air from one up to eight tubes by simply obstructing the unsought pipes with flush-mounted rods. Reducing the number of inlet pipes decreases the injection open area and the acoustic flux dissipated, but at the same time increases the injection bulk velocity and thus the turbulence level in the cavity. It was experimentally checked over the whole investigated range of air flow rates that minimum impact on acoustics was reached with four diametrically opposed injection pipes. The modified injection system has the additional advantage of being much more compact, decreasing the minimum possible cavity size from $L = 100$ mm down to $L = 24.5$ mm.

The air injection system is connected to the main impedance tube to supply a regulated air flowrate fixed by a Bronkhorst massflow controller. Two controllers have been used in this work to minimize measurement errors: the first features a maximum mass flowrate of $\dot{m}_{\mathrm{max}} = 10\ \mathrm{Nm^3\,h^{-1}}$, and is used for plates P_3 and P_4, while the second with $\dot{m}_{\mathrm{max}} = 1\ \mathrm{Nm^3\,h^{-1}}$ is used for the other plates. Air flows within the tube and passes through a perforated plate which can be inserted between two air-tight tubes equipped with a pair of diametrically opposed plugs. Air is then evacuated from the impedance tube a long distance away from the perforated plate location by a set of radial holes just upstream the loudspeaker.

The distance between the perforated plate and the loudspeaker membrane is about one meter long. It has been checked that it is long enough to ensure plane wave propagation in the frequency range considered and to have a uniform flow in the test bench. The cavity depth between the perforated plate and the back plane where the microphone $\mathrm{M_{SPL}}$ is installed can be varied from $L = 24.5$ to 500 mm by adding tubing of different sizes to the system.

Three B&K type 4938 microphones with type 2670 preamplifiers are flush mounted at locations $\mathrm{M_1}$ to $\mathrm{M_3}$. These microphones were calibrated upon specific requirements. Their sensitivity differs by less than 0.2 mV/Pa in gain and their phase response by less than one degree in the $50 - 2000$ Hz frequency range. Microphone $\mathrm{M_1}$ is located at a distance L_1 away from the perforated

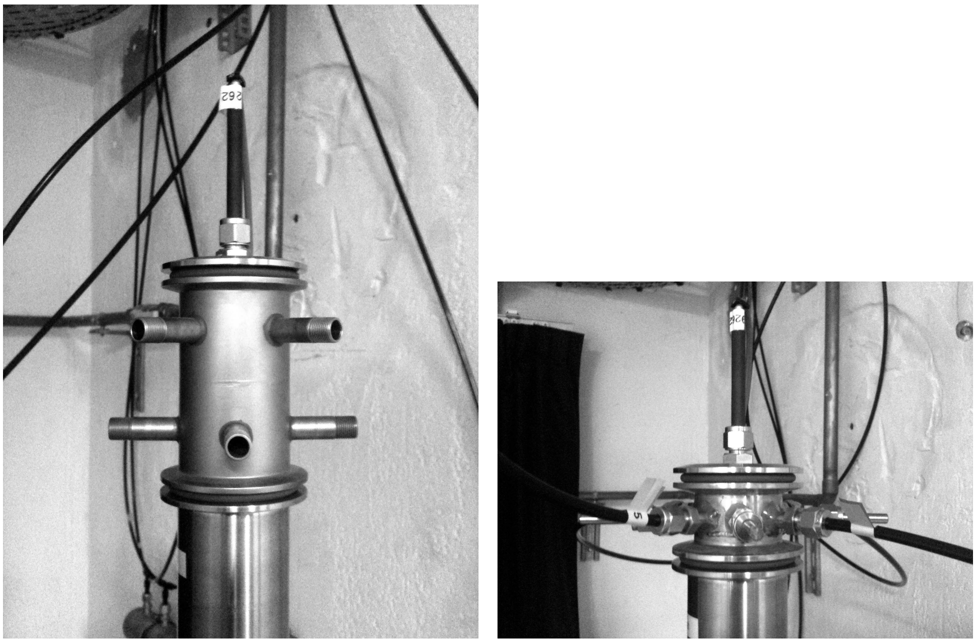

(a) Original air inlet.

(b) Modified air inlet.

Figure 2.3: *Photography of the air injection system. Comparison between the original air inlet (a), characterized by eight inlet tubings of* 8 mm *diameter distributed over two rows, and the new air inlet (b), characterized by four inlet tubings of* 6 mm *diameter, diametrically opposed on a single row.*

plate and is separated by a distance $L_2 - L_1$ from microphone M_2. Microphone M_3 is diametrically facing microphone M_2. These three microphones were used to determine the reflection coefficient R of the perforated plates investigated in this work, as a function of several parameters, such as the plate geometry, the forcing frequency f, the SPL and the back cavity length L, following the procedure described in section 2.2.

2.2 Measuring the acoustic properties

2.2.1 The three microphone method

Assuming plane wave propagation, the impedance ζ at the perforated plate location $x = 0$ can be measured for different forcing frequencies imposed by the loudspeaker using the three microphone measurement technique described by Chung and Blaser (1980a). In the configuration presented in Fig. 2.1, the specific acoustic impedance $\zeta = \tilde{p}/\rho_0 c_0 \tilde{u}$ at the location $x = 0$ can be obtained from the pressure signals measured by microphones M_1 and M_2:

$$\zeta(\omega) = \mathrm{i}\frac{H_{12}(\omega)\sin(\omega L_1/c) - \sin(\omega L_2/c)}{\cos(\omega L_2/c) - H_{12}(\omega)\cos(\omega L_1/c)} \tag{2.2}$$

In this expression $H_{12} = S_{12}/S_{11}$ corresponds to the transfer function between microphones M_1 and M_2, where S_{12} designates the cross power spectral density of pressure signals recorded by microphones M_1 and M_2 examined at the forcing angular frequency ω and S_{11} is the power spectral density of the signal at the same frequency recorded by microphone M_1. The interspace between microphones M_1 and M_2 defines the maximum frequency at which the impedance at the plate location $x = 0$ can be measured. This separation should be chosen such that $L_2 - L_1 \leq c/2f_{\mathrm{max}}$, where f_{max} is the highest frequency of interest, fixed here at $f_{\mathrm{max}} = 2$ kHz. The second spacing constrain is related to the minimum wavelength to be considered. This fixes the position of the first pressure node within the setup from the plate location $x = 0$, and sets a maximum for L_1. In order to meet these requirements, the distance L_1 was fixed to 160 mm, and the separation between M_1 and M_2 was set to $L_2 - L_1 = 105$ mm for measurements in the frequency range $100 \leq f \leq 1000$ Hz. These distances were reduced to $L_1 = 105$ mm and $L_2 - L_1 = 55$ mm in the frequency range $1000 < f \leq 2000$ Hz. Furthermore, the microphone M_1 should be placed far enough from the loudspeaker at a location where the wavefield has a plane wave structure [Durrieu et al. (2001)].

Accurate determination of the transfer function H_{12} requires a suitable calibration in both gain and phase of the sensors and data acquisition system. While calibration in gain is quite straightforward, phase distorsions are less easy to reduce. The difficulty can be overcome with a microphone switching technique, as shown by Chung and Blaser (1980b). A transfer function H_{12}^o is first computed for an experiment conducted with all microphones set at their original location. The same experiment is then repeated in a switched configuration where the microphone M_2 is placed at $x = L_1$ and M_1 is placed at $x = L_2$ (all other parameters remaining fixed). A second transfer function H_{12}^s is computed in the switched configuration. The transfer function H_{12} appearing in Eq. (2.2) is then determined as the geometric mean of these transfer functions:

$$H_{12} = (H_{12}^s H_{12}^o)^{1/2} \tag{2.3}$$

The signal to noise ratio can be further improved using an additional microphone M_3 located at $x = L_2$ in front of microphone M_2, in the original configuration. A coherence factor C is determined between the three microphone signals M_1 to M_3 at the forcing frequency in the original ($n = o$) and switched ($n = s$) configurations:

$$C^n = \frac{C_{23}^n}{C_{12}^n C_{31}^n} \tag{2.4}$$

where C_{xy} is the spectral coherence between the signals x and y, defined as:

$$C_{xy} = \frac{|S_{xy}|^2}{S_{xx} S_{yy}} \tag{2.5}$$

In Eq. (2.5), S_{xy} indicates the cross power spectral density between the signals x and y and S_{xx}, S_{yy} denote the corresponding power spectral densities of the signals x and y. Chung and Blaser (1980b) suggested to replace the transfer function H_{12} in Eq. (2.2) by the following expression:

$$H_{12} = [C^o H_{12}^o C^s H_{12}^s]^{1/2} \tag{2.6}$$

Equation (2.6) is useful for a precise determination of the resistive and reactive components of an impedance in noisy environments, like those found in a turbulent combustor under unstable regimes [Tran et al. (2009a); Tran et al. (2009b); Lamraoui et al. (2011)]. This method enables also to eliminate hydrodynamic pressure fluctuations due to the mean flow which are not synchronized with the acoustic forcing.

Data were sampled in the experiments conducted during this work at $f_s = 16384$ Hz during 4 seconds and digitized with a 12 bit analog to digital converter PCI-MIO-16XE-50 National Instrument card. The signals are divided into 31 segments characterized by a 50 % overlap. Cross and power spectral densities were computed using the Welch periodogram method with Hanning type windows to ensure statistical convergence of the coherent acoustic signals in the noisy environment produced by hydrodynamic pressure fluctuations of the flow. The reflection coefficient is deduced from Eq. (2.2) using the identity:

$$R = \frac{\zeta + 1}{\zeta - 1} = |R| \exp(\mathrm{i}\varphi) \tag{2.7}$$

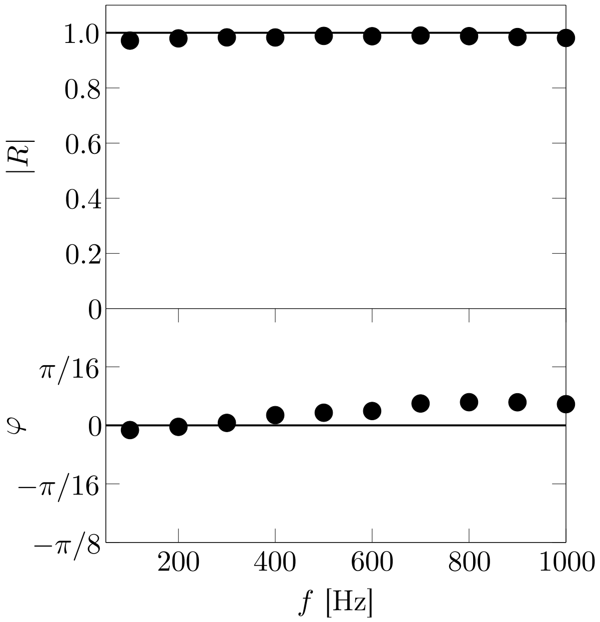

Figure 2.4: *Reflection coefficient modulus $|R|$ (top graph) and phase φ (bottom graph), as a function of frequency, for the closed end configuration with sealed air injections. Measurements (•) are compared to the theoretical predictions (solid line).*

2.2.2 Methodology validation

The three microphone measurement technique presented in section 2.2.1 was tested in a few generic configurations, with a closed end duct and in the absence of perforated plate. Theoretical predictions based on one-dimensional wave propagation show that a unity reflection coefficient modulus $|R| = 1$ is expected, with a zero phase shift $\varphi = 0$ [Pierce (1981); Morse and Ingard (1986)].

In the first experiment, the four air injection holes were sealed, in order to provide proper acoustic boundary conditions near the rigid wall. Microphone M_1 was located at $x = 315$ mm from the wall, and microphones M_2 and M_3 were placed at $x = 415$ mm from the wall. Results are gathered in Fig. 2.4 for both modulus $|R|$ and phase φ of the reflection coefficient. The agreement between measurements and predictions is good over the whole frequency range investigated $100 \leq f \leq 1000$ Hz. The modulus of the reflection coefficient is always higher than $|R| > 0.97$, and the phase deviation from its theoretical value of 0 is always lower than $|\varphi| < \pi/32$.

The influence of the injection holes in the back cavity was examined in a second series of experiments, with and without flow through the setup. In this case slightly higher acoustic losses are expected, since a fraction of the incident acoustic flux may be transmitted and dissipated in the injection pipes. Acoustic

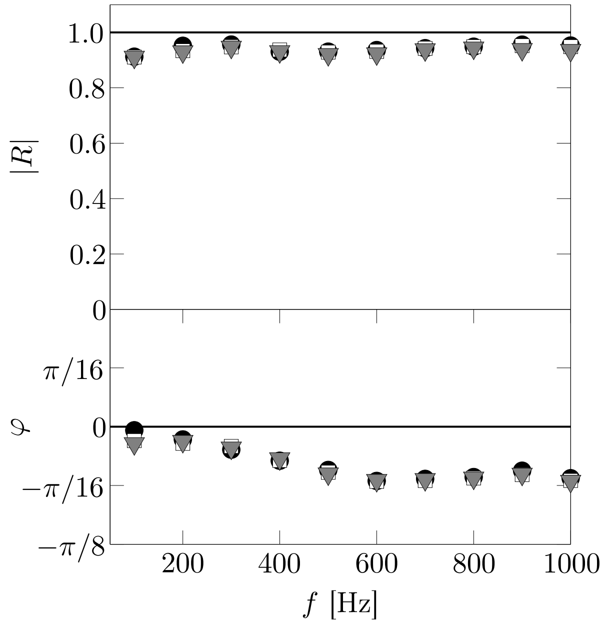

Figure 2.5: *Reflection coefficient modulus* $|R|$ *(top graph) and phase* φ *(bottom graph), as a function of frequency, for the closed end configuration with open air injections. Measurements without mean flow (black circles), for a mass flowrate of* $\dot{m} = 2.80\ \mathrm{nm^3\,h^{-1}}$ *(white squares) and with a mass flowrate of* $\dot{m} = 8.95\ \mathrm{Nm^3\,h^{-1}}$ *(gray triangles) are compared to the theoretical predictions (solid line).*

dissipation may also take place within the boundary layers. The reflection coefficient was measured in the frequency range $100 \leq f \leq 1000$ Hz, and is shown in Fig. 2.5. Measurements were realized for three different flow conditions. In the first configuration, the sealing of the injection air tubes was removed and the reflection coefficient was measured without air injection through the system. In the second and third configurations air was injected in the system, with a mass flowrate of $\dot{m} = 2.80\ \mathrm{Nm^3\,h^{-1}}$ and $\dot{m} = 8.95\ \mathrm{Nm^3\,h^{-1}}$ respectively. The test configuration corresponds to the highest bias flow velocity investigated in the present work. Figure 2.5 shows that there is no difference in modulus and phase of the reflection coefficient for these flow conditions. This suggests that the influence of the air cross-flow jet on the acoustic measurements carried out in this work is weak enough to neglect this phenomenon. It is also interesting to note that the reflection coefficient modulus is always higher than $|R| > 0.93$, and the phase difference between the measured value and the theoretical value of 0 is lower than $|\varphi| < \pi/16$.

In conclusion the air injection setup developed and used in this work has been acoustically characterized and has a minor impact on the acoustic response of the resonant cavity. The perturbation is independent of the air flowrate through

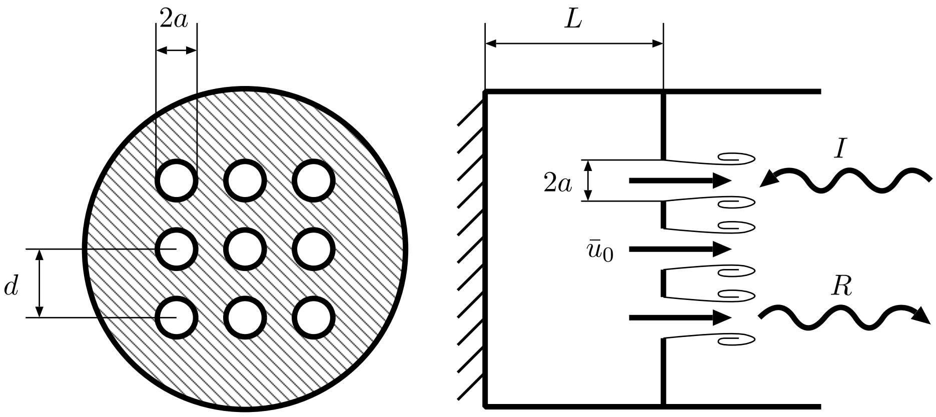

Figure 2.6: *Schematic view of a perforated plate. The circular holes are distributed over a square mesh. The plate is backed by a cavity of size* L*, each hole being traversed by a mean bias flow velocity* $\bar{u}_0$*. This device is subjected to normal incident acoustic waves.*

the injection pipes, and is mainly due to the acoustic losses through the total open area of the injection system. These losses have been significantly reduced with the new air inlet by means of a 70% reduction of the total open area. The perforated plate geometries investigated in this work are presented in the next section.

2.3 The perforated plates investigated

A set of perforated plates was designed based on a regular distribution of circular holes over a square mesh as shown in Fig. 2.6. A particular care has been adopted while perforating the plates with sharp edged holes [Peters et al. (1993)]. All the plates investigated feature a thickness $h = 1$ mm.

The experimental study carried out in this work covers a wide range of operating conditions, corresponding to forcing frequencies ranging from $100 \leq f \leq 1000$ Hz, bias flow velocities $2.18 \leq \bar{u}_0 \leq 15.3$ m s^{-1}, back cavity lengths $24.5 \leq L \leq 300$ mm, and sound pressure levels $90 \leq \mathrm{SPL} \leq 150$ dB. To explore these conditions, a series of seven plates designated as P_d, where the subscript indicates the aperture interspace d in mm, were designed. Their geometrical parameters are gathered in Tab. 2.1.

The hole radius was fixed to $a = 0.3$ mm for plate $P_{2.5}$ and to $a = 0.5$ mm for plates P_3 to P_8, and the aperture interspace was varied from $d = 2.5$ to 8 mm. These plates are characterized by a porosity given by $\sigma = 4Na^2/D^2$, where N is the number of holes and $D = 50$ mm denotes the plate diameter. Considering the perforations as a network of N elementary square patterns, the

Table 2.1: *Perforated plate geometrical parameters. a: aperture radius, d: aperture interspace, N: number of holes, σ: porosity, h: plate thickness*

Plate	a [mm]	d [mm]	N	σ [%]	h/a
$P_{2.5}$	0.3	2.5	325	4.68	3.33
P_3	0.5	3	221	8.84	2
P_4	0.5	4	121	4.84	2
P_5	0.5	5	69	2.76	2
P_6	0.5	6	49	1.96	2
P_7	0.5	7	37	1.48	2
P_8	0.5	8	25	1.00	2

porosity can also be expressed as $\sigma = \pi a^2/d^2$. It is interesting to note that all these plates feature low porosities, ranging from $1.0\% \leq \sigma \leq 8.8\%$.

In order to characterize the aerodynamic and acoustic properties of these perforated plates, it is interesting to estimate the range of values covered by three dimensionless numbers:

- the Reynolds number $\mathrm{Re} = (\bar{u}_0\, 2a)/\nu$, based on the hole diameter $2a$, the mean bias flow velocity $\bar{u}_0$ and the kinematic viscosity ν;
- the bias flow Mach number $\mathrm{M} = \bar{u}_0/c_0$, where c_0 is the sound speed;
- the Strouhal number $\mathrm{St} = (\omega a)/\bar{u}_0$, where $\omega = 2\pi f$ is the angular frequency.

In the configurations explored in the present work, the Reynolds number varied from 138 to 975. It is high enough to ensure flow separation at the hole edges, so that the flow at the outlet of the perforation forms a jet. The Reynolds number is also small enough for the flow to be considered laminar. The Mach number in the perforations ranged from $6.4 \cdot 10^{-3}$ to $4.5 \cdot 10^{-2}$. Since the Mach number remains very low $\mathrm{M} \ll 1$, its effects on the sound wave propagation velocity are neglected in this study [Durrieu et al. (2001); Rienstra and Hirschberg (2003)]. Finally the Strouhal number varied in the range $0.02 \leq \mathrm{St} \leq 2.88$. It will be shown in the following chapters that the Strouhal number can be used to define different interesting absorption regimes of the perforated plate.

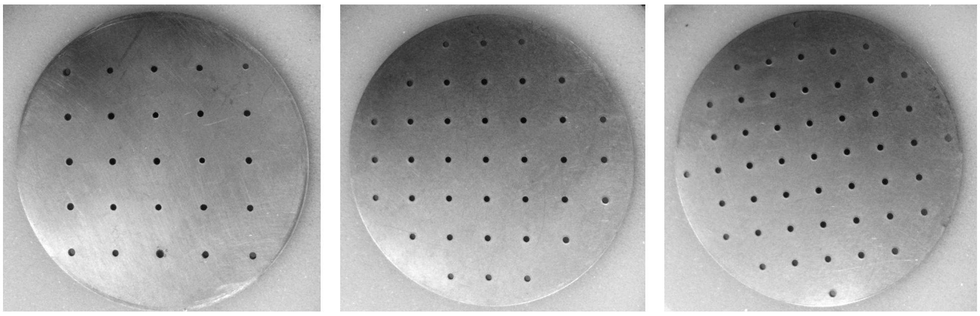

(a) Plate P_8. (b) Plate P_7. (c) Plate P_6.

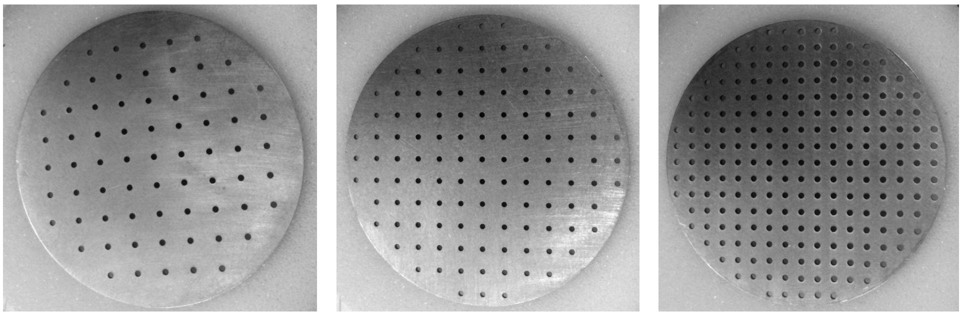

(d) Plate P_5. (e) Plate P_4. (f) Plate P_3.

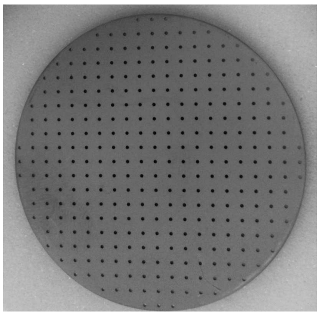

(g) Plate $P_{2.5}$.

Figure 2.7: *The 7 perforated plates* P_d *used in this work. They are characterized by an interhole space* d *ranging from* 2.5 *to* 8 mm, *and a thickness* $h = 1$ mm. *Plates* P_3 *to* P_8 *feature holes of diameter* $2a = 1$ mm, *while the perforations of plate* $P_{2.5}$ *have a smaller diameter* $2a = 0.6$ mm.

Chapter 3

Numerical simulation strategy for the prediction of acoustic absorption through a perforation

The present chapter introduces the numerical techniques and solver that have been used in this work to simulate the aeroacoustic response of a perforated plate traversed by a mean bias flow and subjected to incident sound waves. Section 3.1 gives an overview of the governing equations. In section 3.2 the numerical configuration is presented. Then section 3.3 briefly introduces the AVBP solver used in this study. Finally an analysis of the mean flow fields obtained in the simulations is carried out in section 3.4.

3.1 Overview of the governing equations

The evolution of the flow field describing the unsteady air flow in the vicinity of an orifice subjected to acoustic waves is governed by the unsteady compressible Navier-Stokes equations. In this configuration, the following general hypotheses can be done:

- air can be treated as an ideal gas;
- air is a Newtonian fluid;
- volume forces can be neglected here;
- the mean flow can be considered as isothermal.

Under these assumptions, the governing equations can be expressed as follows in local form (see for example Candel (2001)):

$$\frac{\partial \rho}{\partial t} + \nabla \cdot \rho \mathbf{u} = 0 \tag{3.1}$$

$$\frac{\partial \rho \mathbf{u}}{\partial t} + \nabla \cdot \rho \mathbf{u}\mathbf{u} = -\nabla p + \mu \nabla^2 \mathbf{u} + \frac{\mu}{3} \nabla (\nabla \cdot \mathbf{u}) \tag{3.2}$$

$$\frac{\partial}{\partial t} \rho \left(e + \frac{1}{2} u^2 \right) + \boldsymbol{\nabla} \cdot \rho \left(e + \frac{1}{2} u^2 \right) \boldsymbol{u} = -\boldsymbol{\nabla} \cdot p \boldsymbol{u} + \boldsymbol{\nabla} \cdot (\boldsymbol{\tau} \cdot \boldsymbol{u}) - \boldsymbol{\nabla} \cdot \boldsymbol{q} \tag{3.3}$$

Equations (3.1), (3.2) and (3.3) represent the conservation of mass, momentum and energy respectively, which are numerically integrated by the solver[1]. In these equations ρ is the density of the fluid, μ is the dynamic viscosity, p is the pressure, $\mathbf{u}$ is the velocity vector, characterized by its components u, v and w along the x, y and z directions of space respectively, e is the internal energy, $\boldsymbol{q}$ is the heat flux, and $\boldsymbol{\tau}$ is the viscous tensor. Since the fluid is an ideal gas, its pressure, density and temperature are related by the equation of state:

$$p = \rho r T \tag{3.4}$$

where r is the gas constant of the fluid. If M is the molar mass of the fluid, the gas constant is given by $r = R/M$, where $R = 8.31446\ \mathrm{J\,mol^{-1}\,K^{-1}}$ is the universal gas constant.

In the framework of Large-Eddy Simulations (LES), these equations are filtered in order to solve only the largest scales of the physical flow field. The dynamics of the scales which are smaller than the mesh size are modeled and represented by subgrid terms. An interesting survey of numerical techniques applied to jet noise prediction with LES can be found in Bodony and Lele (2008).
Direct numerical simulations (DNS) have been used in the literature to study the detailed flow through liner resonators subjected to incident acoustic waves. The behavior of an acoustically excited liner in the absence of bias flow was investigated by Tam and Kurbatskii (2000) using DNS. They noted that at low forcing amplitudes, acoustic dissipation was low and came mainly from viscous losses in the acoustic boundary layers in the openings. At larger excitation amplitudes, the dissipation was much higher and related to the vortex shedding at the mouth of the resonator. Tam et al. (2010) then extended their analysis to a three-dimensional array of slit resonators, and were able to predict the acoustic impedance in good agreement with experimental data. More recently, Zhang and Bodony (2012) carried out resolved simulations of the acoustically

---

[1] The AVBP solver can actually solve a much more complex system of equations, including reactive cases, real gas effects and two-phase flows. However with the assumptions made in this chapter the solved equations are equivalent to Eqs. (3.1)-(3.3).

excited flow through an orifice backed by a hexagonal cavity, and analyzed the effect of the acoustic modulation on the orifice boundary layer and the discharge coefficient.

In the present work, low-order direct numerical simulations (DNS) of the interactions between the acoustic waves and the jet generated by the mean bias flow passing through a circular orifice are conducted. The main focus being the analysis of the vortex shedding at the orifice outlet at medium to high forcing amplitudes and low frequencies, the acoustic dissipation due to viscous losses in the orifice are negligible and the acoustic boundary layers are not fully resolved. At an excitation frequency of 400 Hz, the order of magnitude of the acoustic boundary layer thickness is $\delta_V = \sqrt{2\nu/\omega} \simeq 0.11$ mm, approximately one tenth of the orifice diameter. With the very fine mesh used, at least three nodes are located in the acoustic boundary layer.

3.2 Numerical configuration

The configuration simulated in this work aims at modeling the unsteady flow through a perforated plate with a regular distribution of holes. Since the number of apertures can be important (see Tab. 2.1), simulating the whole plate would imply coarse resolutions near the holes. Thus only a single hole is considered here, and periodic conditions are imposed at the lateral boundaries of the numerical domain to take into account the presence of an array of apertures distributed over a square mesh.

This approach is similar to the one adopted by Dassé et al. (2008), who simulated the acoustic response of a perforated plate subjected to low amplitude sound waves with LES. Large-Eddy Simulations were also carried out by Scarpato et al. (2011) to analyze the effect of sound level on the response of the perforate. Several numerical techniques, ranging from 1D network solvers, to Large-Eddy Simulations and Finite Element Models of the wave equations in the frequency domain, were also compared by Simonetti et al. (2011) to assess their applicability in the different design phases of a combustor.

The symmetry of the problem is fixed by lateral periodic conditions and asymmetrical interactions between the orifices are not considered here. Asymmetry would for example be triggered by an oblique sound wave impacting the perforation, or by an instability in the flow within the perforation. Both cases are out of the scope of this work, and were never observed in the experiments conducted here.

3.2.1 Numerical domain

Figure 3.1 shows a schematic view of the numerical domain. The domain has

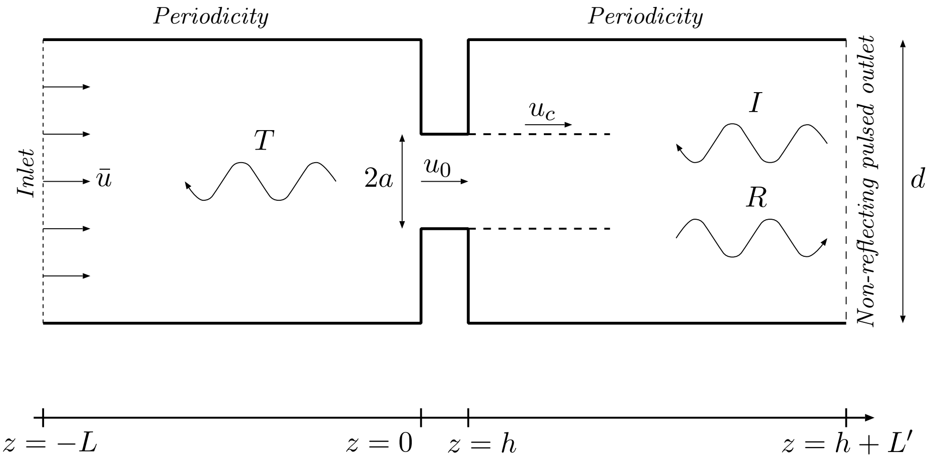

Figure 3.1: *Schematic view of the computational domain. A mean flow passes through the orifice from left to right in this figure. Acoustic modulation is imposed on the right boundary condition.*

a square section with edges of length $d = 6$ mm, and corresponds to the tested plate P_6 described in chapter 2. This distance also represents the separation between two apertures. In the center of the domain, a solid wall of thickness $h = 1$ mm features a circular orifice of diameter $2a = 1$ mm. The porosity of the plate is then given by $\sigma = \pi a^2/d^2 = 2.18\,\%$, as indicated in chapter 2. Note that this porosity is slightly different from the actual plate porosity $\sigma = 4Na^2/D^2 = 1.96\,\%$ (Tab. 2.1), because the tested plate has N holes distributed over a disk with diameter D, as shown in Fig. 2.7.

The inlet and outlet boundaries are located at a large distance $L/a \geq 120$ from the aperture. The ratio $L/d = 10$ is also large enough so that plane acoustic waves can be considered at these boundaries [Peters et al. (1993)]. Non-reflecting acoustic conditions are imposed at the outlet boundary [Poinsot and Lele (1992)]. The inlet boundary can be modeled either with non-reflecting or fully reflecting conditions, corresponding respectively to the case of a perforated plate placed in an infinite duct (no resonant cavity) or to the case of a perforate coupled with a resonant back cavity (rigid wall at the inlet). The orifice walls comprised between $z = 0$ and $z = h$ are treated with a no-slip condition for the velocity.

3.2.2 Grids

The numerical domain was discretized with a tetrahedral grid. Three computational meshes were used in the simulations: a coarse, a fine and a very fine mesh. The main characteristics of these grids are summarized in Tab. 3.1. The very fine mesh is dedicated to the simulation of plate P_6 coupled with a resonant cavity of size $L = 150$ mm.

Table 3.1: *Main characteristics of the computational meshes. N_t: number of tetrahedra, N_p: number of grid points, L: length of the upstream cavity, L': length of the downstream domain (see Fig. 3.1), y^+: dimensionless distance of the first grid point to the orifice wall.*

Mesh type	N_t	N_p	L [m]	L' [m]	y^+
Coarse	0.64×10^6	1.16×10^5	0.060	0.060	2.22
Fine	1.34×10^6	2.39×10^5	0.060	0.060	1.75
Very fine	2.15×10^6	3.82×10^5	0.150	0.060	1.45

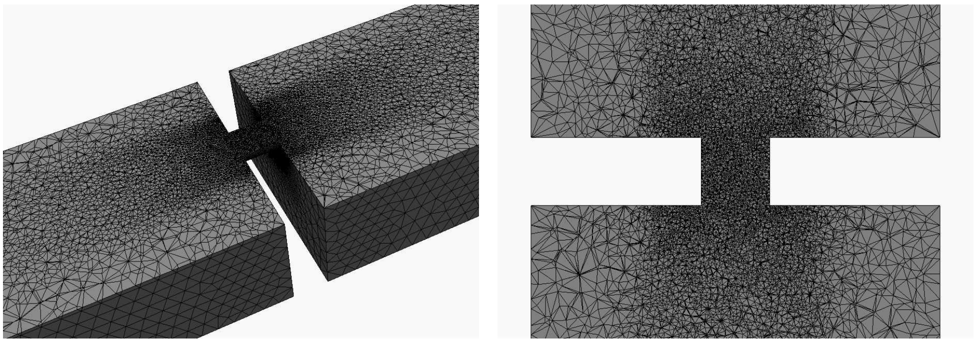

(a) Clip view. (b) Axial cut.

Figure 3.2: *Coarse mesh: clip view (a) and axial cut (b) near the orifice of the simulated numerical domain.*

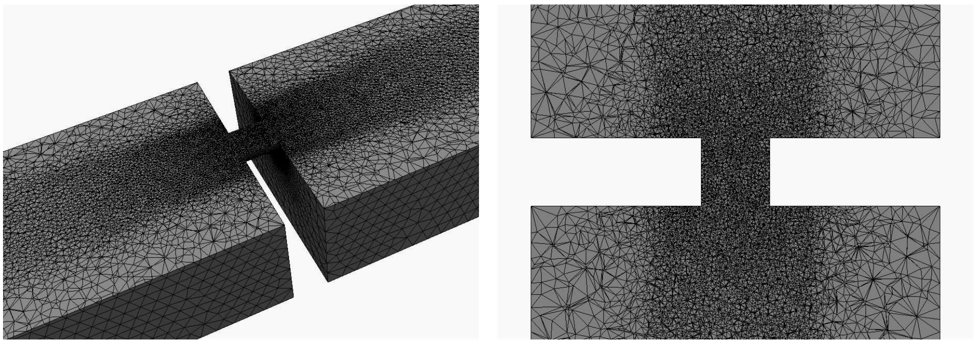

(a) Clip view. (b) Axial cut.

Figure 3.3: *Fine mesh: clip view (a) and axial cut (b) near the orifice of the simulated numerical domain.*

Figures 3.2 to 3.4 show different enlarged views of the meshes near the orifice. To ensure a good numerical resolution of the unsteady flow in the region near the perforation, the orifice channel of diameter $2a$ has been discretized with at least 20 points in the radial direction for the coarse mesh, and at least 30 points for the very fine mesh. This discretization ensures a good resolution of the boundary layers in the orifice, as shown by the low y^+ values in Tab. 3.1. The meshes are also refined near the orifice axis, both upstream and downstream of the perforation. This refinement is necessary to solve with sufficient accuracy the jet formed downstream the orifice, as well as the unsteady vortex rings generated by acoustic waves impinging on the perforation. At high sound pressure levels, these rings are swept both upstream and downstream of the orifice, as it will be shown later.

3.2.3 Operating conditions

In all the simulations conducted in this work, a mean bias flow passes through the aperture from left to right, as shown in Fig. 3.1. The configuration analyzed in this work is motivated by the use of perforated plates backed by a resonant cavity to damp low frequency combustion instabilities at the inlet of an injection system, as studied by Tran et al. (2009a). This type of low frequency thermo-acoustic interaction typically features self-sustained oscillations of a few hundred Hertz. In the envisaged application, incident acoustic waves are normal to the plate and the temperature of the gas remains constant.

The ideal case considered here to mimic the real configuration is an isothermal flow of nitrogen characterized by a density $\rho_0 = 1.18\ \mathrm{kg\,m^{-3}}$ with a temperature $T_0 = 300$ K. Nitrogen is injected at the inlet with a small uniform velocity $\bar{u} = 0.074\ \mathrm{m\,s^{-1}}$. This flow velocity corresponds to a bulk velocity in the aperture $\bar{u}_0 = \bar{u}/\sigma = 3.4\ \mathrm{m\,s^{-1}}$. At this operating point, the Mach number in the orifice is $M_0 = \bar{u}_0/c \simeq 0.01$ and the Reynolds number is $\mathrm{Re}_0 = \bar{u}_0 2a/\nu \simeq 220$.

The mean pressure imposed at the outlet is $p_a = 101300$ Pa. The acoustic forcing is obtained by imposing a harmonic oscillation to the characteristic acoustic wave entering the domain denoted I in Fig. 3.1, with a constant frequency $f = 400$ or 800 Hz. These forcing conditions correspond to two Strouhal numbers, $\mathrm{St} = \omega a/\bar{u}_0 = 0.37$ at 400 Hz and $\mathrm{St} = 0.74$ at 800 Hz respectively. The two forcing frequencies chosen in this study correspond to two different absorption regimes (see chapter 4):

- $f = 400$ Hz: this regime is close to optimal acoustic absorption at small perturbation levels for plate P_6 backed by a resonant cavity of size $L = 150$ mm.
- $f = 800$ Hz: in this regime acoustic absorption is far from optimal at small perturbation levels for plate P_6 backed by a resonant cavity of size $L = 150$ mm.

The amplitude of the incoming pressure wave is then varied from 0.89 to 2828 Pa. This corresponds to SPL ranging from 90 dB up to 160 dB. Eight different simulations were conducted to investigate both the linear (low forcing amplitude) and nonlinear (high forcing amplitude) regimes. These calculations were run over 40 modulation periods and only the last 20 periods were post-processed to examine the acoustic properties, in order to ensure convergence of the simulations.

The hypothesis of plane wave propagation away from the orifice has been verified in the computations. The maximum phase difference between two pressure signals taken at different points in the same cross-section at $z/a = 100$ away from the orifice is less than 1 degree, and the maximum amplitude difference reaches 0.3%. At the forcing frequencies $f = 400$ and 800 Hz considered here, the ratio between the orifice diameter $2a$ and the acoustic wavelength λ is small enough $2a/\lambda = 1.2 \times 10^{-3}$ at 400 Hz and 2.4×10^{-3} at 800 Hz, so that the orifice can be considered compact.

In all the simulations conducted, no higher modes were observed, except the harmonics of the modulation frequency when the SPL is increased. Far from the orifice, the amplitude of the second harmonic of the modulation frequency observed in the pressure spectrum remains lower by at least one order of magnitude than the amplitude of the fundamental peak, as shown in the example in Fig. 3.5.

3.3 The AVBP solver

Simulations in this study were conducted with the AVBP solver, developed at Cerfacs (`www.cerfacs.fr/4-26334-The-AVBP-code.php`). It solves the compressible Navier-Stokes equations on unstructured meshes using explicit methods. The discretization implemented in the solver is of cell-vertex type, where all the variables are stored at mesh nodes and the set of equations is integrated within each cell. A recent overview of the models included in the AVBP solver and a detailed description of the solver can be found in Senoner (2010).

All the simulations in this work are carried out with the finite-volume Lax-Wendroff scheme (see Lax and Wendroff (1964) and Schönfeld and Rudgyard (1999)). It is a one-step numerical scheme, second order accurate in space and time.

3.3.1 Potential effect of the subgrid scales on acoustic coefficients

In Large-Eddy Simulations, a spatial filtering operator is applied to the Navier-Stokes equations to separate the large scales (larger than the filter size) and

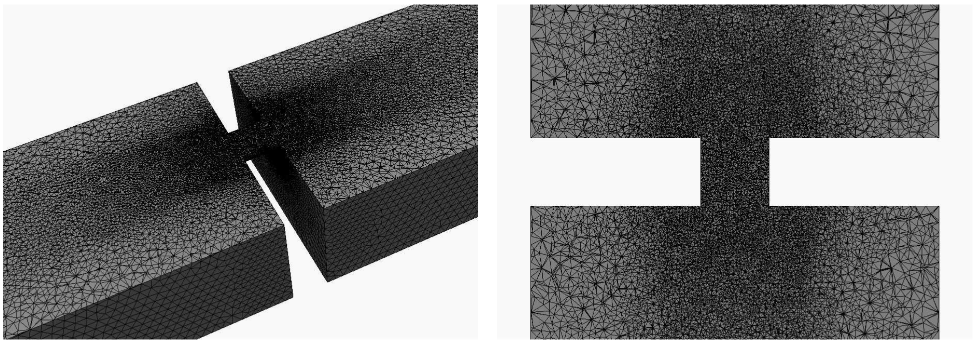

(a) Clip view. (b) Axial cut.

Figure 3.4: *Very fine mesh: clip view (a) and axial cut (b) near the orifice of the simulated numerical domain.*

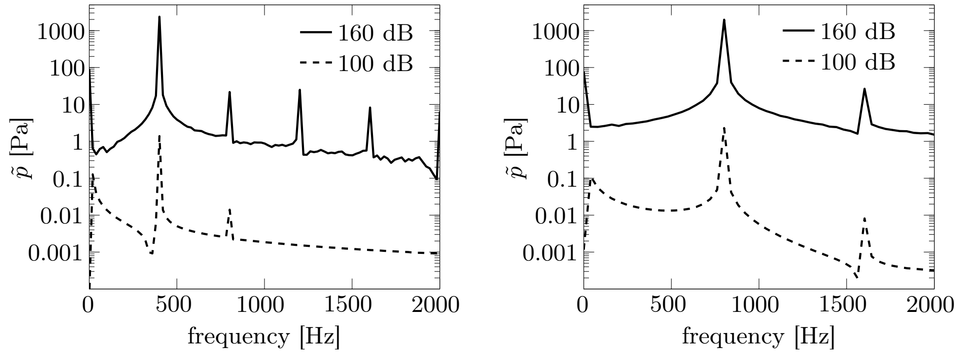

(a) $f = 400$ Hz. (b) $f = 800$ Hz.

Figure 3.5: *Examples of pressure spectra taken downstream of the perforation at* $z/a = 100$ *at the forcing frequencies* $f = 400$ Hz *(a) and* $f = 800$ Hz *(b).*

the small scales (smaller than the filter size) of the flow. The large scales are resolved, but a model is needed for the small scales. The SGS model is based on the introduction of a turbulent viscosity ν_{turb}, assuming that the effect of the SGS stresses on the resolved field is purely dissipative.

In the present work, the Reynolds number based on the orifice diameter and the mean bias flow velocity within the perforation is very small ($\text{Re} \simeq 220$). In this case, the flow is laminar and thus the effect of the subgrid model on the flow and on the acoustic properties of the orifice is negligible. This hypothesis has been verified by analyzing preliminary Large-Eddy Simulations carried out on the coarse grid presented in section 3.2.2. This grid represents the worse case scenario to assess the effect of the subgrid model, since the minimum cell size is larger compared to the fine and very fine meshes. The orifice is simulated without resonant back cavity at a forcing frequency $f = 400$ Hz. Ten simulations were conducted, corresponding to ten values of the SPL ranging from 90 to 160 dB. They cover all the operating regimes of interest analyzed in this work, from linear (small perturbation levels) to nonlinear (high perturbation levels). The SGS model chosen for the simulation is the WALE model from Nicoud and Ducros (1999).

In the axial cut extracted from LES in Fig. 3.6, the evolution of the ratio $\nu_{\text{turb}}/\nu_{\text{lam}}$ is shown over the first half of the forcing cycle, where the orifice is subjected to an incident sound wave at $f = 400$ Hz and SPL = 160 dB. The first instants corresponding to the generation and the advection of a vortex ring due to the incident acoustic wave impinging on the orifice are shown. When the vortex ring is generated ($t/T_p \leq 0.10$, where $T_p = 1/f$ is the modulation period), the effect of the SGS model is negligible, as demonstrated by the low values of the ratio $\nu_{\text{turb}}/\nu_{\text{lam}}$ close to the vortices. The SGS model then increases the turbulent dissipation of the vortex ring only for $t/T_p \geq 0.15$, when the vortices are convected downstream of the orifice during the first half of the forcing cycle. However this increased dissipation occurring relatively far from the perforation has a negligible effect on the acoustic properties of the orifice.

To prove this point, the reflection and transmission coefficients obtained with and without subgrid-scale (SGS) model, i.e. in LES or DNS frameworks respectively, are compared. In Fig. 3.7, the modulus and phase of the reflection and transmission coefficients of the simulated orifice are plotted as functions of the incident SPL on the perforation. These results are compared to simulations carried out without any SGS model (DNS framework) at SPL = 100 dB (linear regime) and 160 dB (nonlinear regime). Excellent agreement is observed for both reflection and transmission coefficients, in modulus and phase, showing the limited influence of SGS contributions on the results.
In the following chapters, all the calculations were obtained without SGS model, i.e. in a DNS framework.

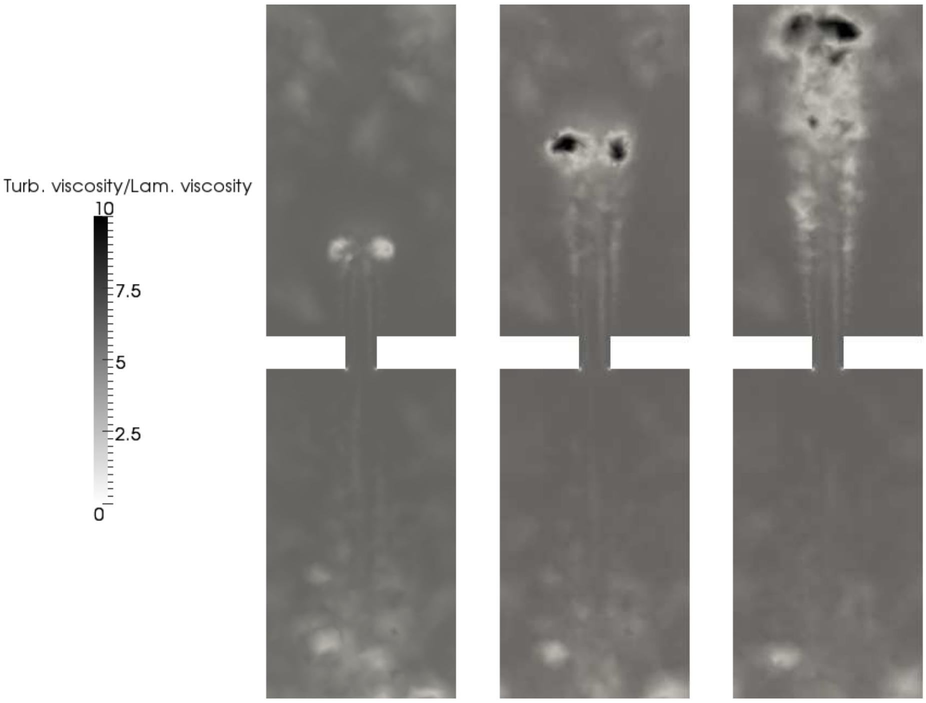

(a) $t/T_p = 0.10$.

(b) $t/T_p = 0.15$.

(c) $t/T_p = 0.20$.

Figure 3.6: *Axial cut of the ratio* $\nu_{\mathrm{turb}}/\nu_{\mathrm{lam}}$*, for several forcing instants. The forcing acoustic wave has a frequency* $f = 400$ Hz *and a* SPL $= 160$ dB.

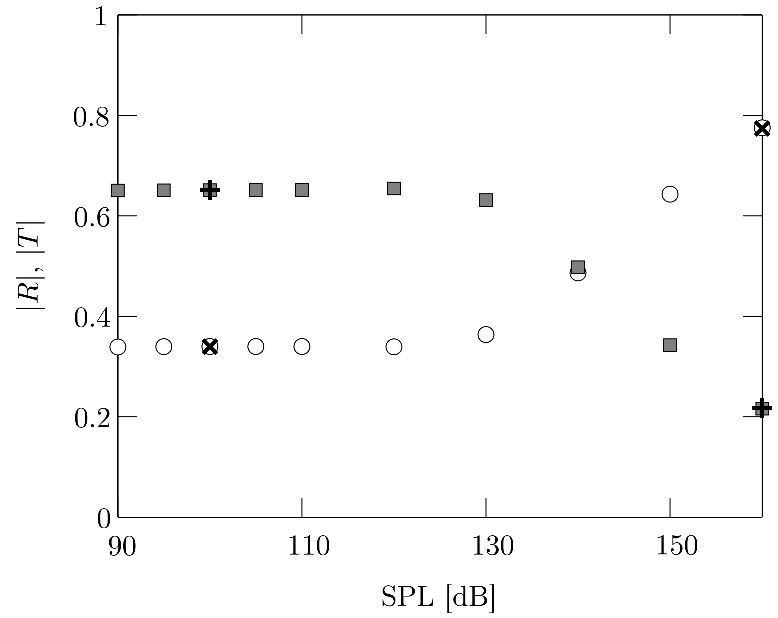

(a) Modulus.

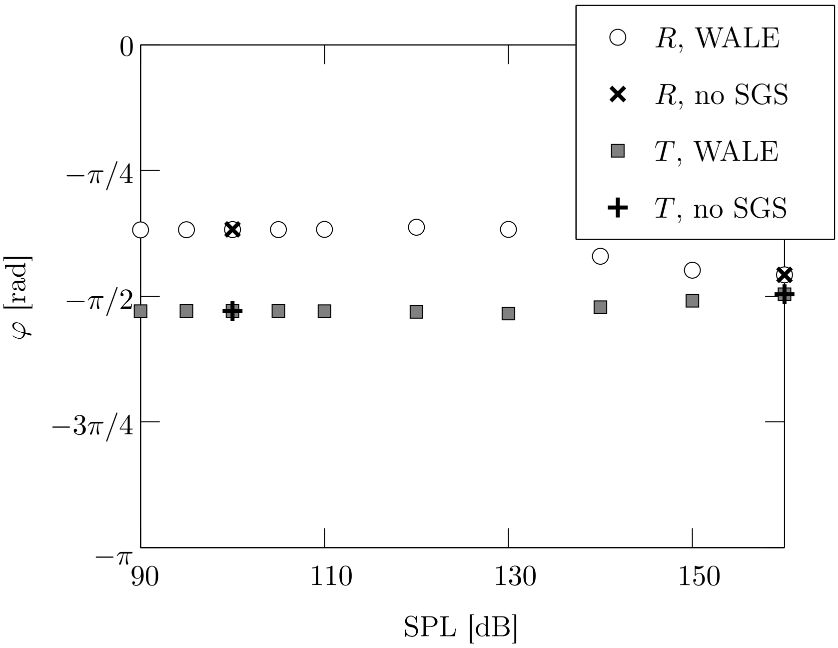

(b) Phase.

Figure 3.7: *Evolution of modulus (a) and phase (b) of the reflection R and transmission T coefficients of an orifice without resonant cavity as a function of the incident SPL, at the forcing frequency $f = 400$ Hz. Comparison between results obtained with the WALE subgrid model and without subgrid (SGS) model.*

3.3.2 Acoustic inlet and outlet boundary conditions

The treatment of acoustic waves near the domain boundaries is an important aspect for aeroacoustic simulations. The key problem is to link information computed from the numerical domain to the conditions imposed at the boundaries. This aspect has been thoroughly analyzed in the recent years, and good overviews can be found for example in Colonius and Lele (2004), Ducruix and Candel (2004) or Bodony and Lele (2008).

In subsonic flows, an additional challenge is present because inlet and outlet conditions must also allow acoustic waves to travel in the opposite direction of the flow. Several types of boundary conditions (BC) have been developed to minimize spurious reflections at the domain boundaries. Radiation BC assume that the boundaries are located far from the sources of disturbances and use asymptotic solutions to describe the propagation of outgoing waves [Tam and Webb (1993)]. Alternatively, a perfectly matched layer can be used to damp waves in the vicinity of the domain boundaries [Hu (1996)]. However, this technique requires some fine tuning of the buffer layer thickness and the absorption profile to optimize the performance of the perfectly matched layer. Another approach is based on nonreflecting BC. This technique exploits the characteristic wave decompositions of hyperbolic systems of equations. In this method, all the waves propagating towards a boundary leave the domain freely at this boundary, while incoming waves are set to zero. The characteristic BC are exact in one-dimensional Eulerian flows, where they are trajectories in the $x - t$ plane, but can also be used in an approximate way for two and three-dimensional flows [Thompson (1987); Thompson (1990); Poinsot and Lele (1992)]. Hixon et al. (1995) show an interesting analysis of the performance of several boundary conditions techniques for computational aeroacoustics.

In the present work, inlet and outlet boundary conditions are treated with the Navier-Stokes Characteristic Boundary Conditions (NSCBC) method proposed by Poinsot and Lele (1992). According to this method, all equations are written in terms of characteristic variables and are projected in a reference frame linked to the domain boundary of interest (with a normal unit vector $\boldsymbol{n}$ and two tangential unit vectors). In general there is no simple method to find an exact expression of the incoming wave amplitude variation at the boundaries in the viscous multi-dimensional case. However, the approach followed in NSCBC is to infer these values by examining a Local One-Dimensional Inviscid (LODI) problem, i.e. by neglecting transverse and viscous terms in the system of characteristic equations.

In the one-dimensional case, it is possible to locally identify and decouple the acoustic characteristic waves propagating in the downstream and upstream directions with velocities of $\lambda_2 = u + c_0$ and $\lambda_1 = u - c_0$: $A_2 = p' + \rho_0 c_0 u'$ and $A_1 = p' - \rho_0 c_0 u'$. Following the analysis of Thompson (1987) and Poinsot and Lele (1992), the amplitude variation of the characteristic waves crossing the boundary can be written as:

$$\mathcal{L}_1 = \lambda_1 \left(\frac{\partial p'}{\partial x} - \rho_0 c_0 \frac{\partial u'}{\partial x} \right) \tag{3.5}$$

$$\mathcal{L}_2 = \lambda_2 \left(\frac{\partial p'}{\partial x} + \rho_0 c_0 \frac{\partial u'}{\partial x} \right) \tag{3.6}$$

In the following, the terms *inlet* and *outlet* refer to the aerodynamic flow (and not to the acoustic propagation). We also recall that *incoming* and *outgoing* refer respectively to waves penetrating into and leaving the computational domain. Forcing the outlet boundary condition (which is the approach taken in the present work) means imposing the amplitude variation of the incoming characteristic wave $\mathcal{L}_1$ propagating into the numerical domain. Let $\bar{p}_0$ be the mean pressure imposed at the outlet, $p'_f = A_f \sin(\omega t)$ the incident forcing pressure fluctuation, and p_s the pressure at the current state. The LODI relations written for a non-reflecting forced outlet of the numerical domain lead to the following expression of the incoming characteristic wave $\mathcal{L}_1$:

$$\mathcal{L}_1 = -2 \frac{\partial p'_f}{\partial t} - 2K(p_s - \bar{p}_0 - p'_f) \tag{3.7}$$

The first term in the right-hand-side of Eq. (3.7) represents the forced part of the incoming acoustic wave. The second term is the condition to ensure convergence to the target pulsed pressure $\bar{p}_0 + p'_f$, using the relaxation factor K. This factor should be carefully chosen so that the outlet boundary remains nonreflecting, meaning that $\mathcal{L}_2$ waves freely leave the domain. Selle et al. (2004) showed that the reflection coefficient of this forced relaxed outlet takes the form:

$$R_{\text{out}} = \frac{1}{2\mathrm{i}\omega/K - 1} \tag{3.8}$$

Equation (3.8) shows that, for a fixed value of K, it is possible to determine the cut-off frequency of the boundary condition:

$$f_c = \frac{K}{4\pi} \tag{3.9}$$

This implies that all the frequencies lower than the cut-off frequency ($f < f_c$) will be strongly reflected, while the frequencies higher than the cut-off frequency ($f > f_c$) will freely leave the numerical domain. For our simulations, $K = 100$, and it was checked that nonreflecting conditions applied for all the forcing frequencies and amplitudes simulated ($R_{\text{out}} \leq 0.03$).

3.4 Analysis of the mean flow

First a comparison of the mean flow fields obtained for the three computational meshes described in paragraph 3.2.2 is carried out. Results for the mean axial velocity are shown in Fig. 3.8. The mean uniform flow upstream of the plate is accelerated at the orifice inlet. At the orifice outlet flow separation takes place and a jet is formed downstream. In these simulations, no acoustic forcing was applied at the domain outlet. The simulations were run for a sufficient long time to ensure that a steady flow is established downstream the perforation.

While hardly any difference can be spotted between the computations with the fine and very fine meshes, the larger width of the jet far from the orifice suggests that the simulation with the coarse mesh is more dissipative. Figure 3.9 shows the mean normal vorticity field, $\bar{\omega}$, in the axial z-cut through the numerical domain. The jet vorticity is quickly dissipated in the coarse mesh simulations.

It is now interesting to analyze the mean axial velocity profiles in the orifice. Figure 3.10 shows a comparison of the velocity profiles at the orifice inlet ($x = 0$ mm), in the center of the channel ($x = 0.5$ mm) and at the orifice outlet ($x = 1$ mm). A typical double hat profile can be observed at the orifice inlet, due to the acceleration of the fluid near the perforation walls. The centerline velocity then increases within the channel while the velocity gradient at the walls decreases. At the orifice outlet, a quasi-paraboloidal shape is reached, except in the vicinity of the centerline where the velocity profile is flat. From the axial velocity profiles it is possible to estimate the contraction ratio (which is approximately the discharge coefficient) of the orifice:

$$C_c = \frac{A_j}{A_0} = \frac{\bar{u}_0}{\bar{u}_j} \tag{3.10}$$

Applying Eq. (3.10) with $\bar{u}_0 = 3.40\ \mathrm{m\,s^{-1}}$ and $\bar{u}_j = 5.6\ \mathrm{m\,s^{-1}}$, one obtains $C_c \simeq 0.61$, which is close to the theoretical value for a thin orifice with sharp edges $C_c = \pi/(\pi + 2)$.
In Fig. 3.11 the mean vorticity profiles in the orifice are plotted for the three simulated meshes. All the mean velocity and vorticity profiles in this region show a very good agreement between the simulations, regardless of the refinement of the mesh.

Figures 3.12 and 3.13 show the mean transverse profiles of axial velocity and vorticity respectively, in the jet generated downstream the perforation outlet, at different distances from the perforation. Once again, a good agreement is observed between the velocity profiles obtained with the fine and very fine meshes, showing that spatial convergence is reached with these discretization grids, except at very large distances $x/a \geq 80$ from the orifice. The coarse mesh being more dissipative, the centerline jet velocity decreases faster and,

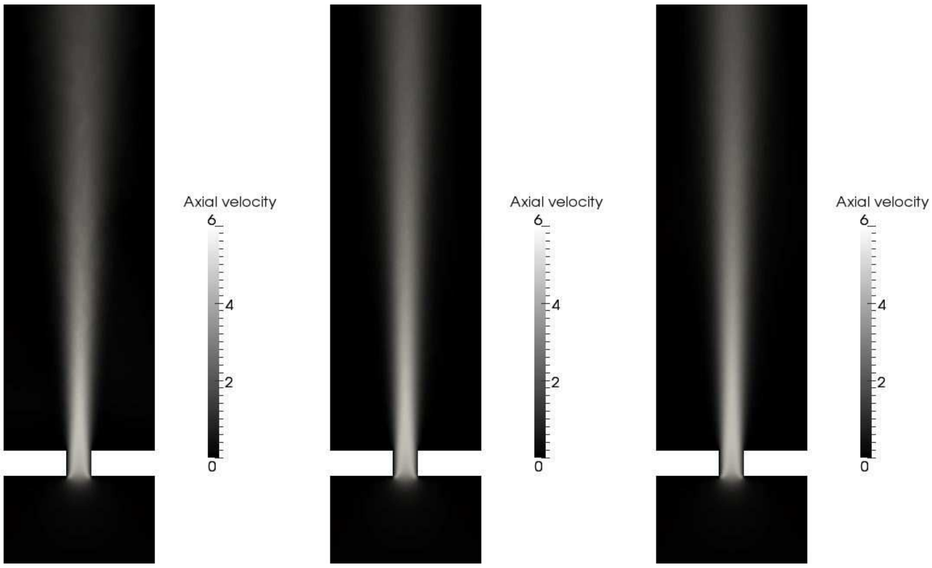

(a) Coarse mesh. (b) Fine mesh. (c) Very fine mesh.

Figure 3.8: *Mean axial velocity field (units in* $[\mathrm{ms}^{-1}]$*). Axial cut.*

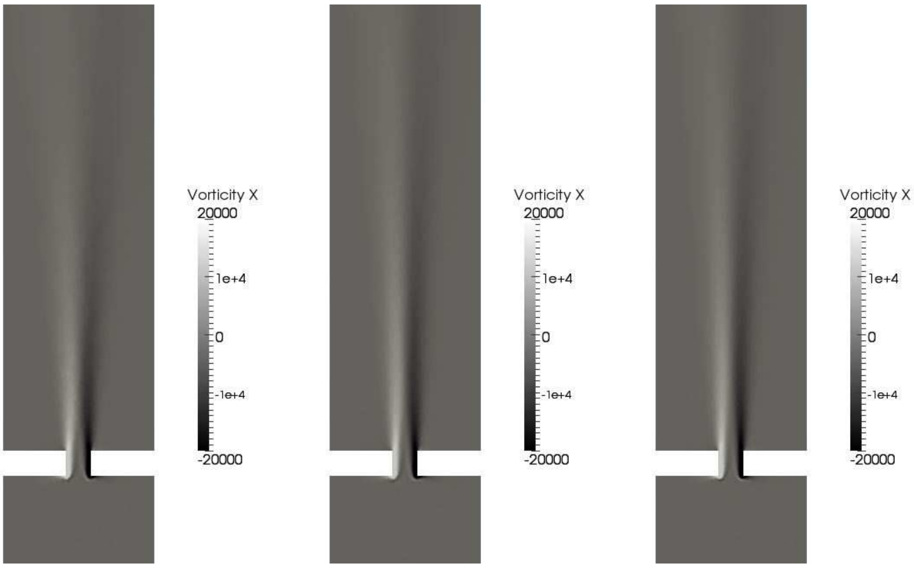

(a) Coarse mesh. (b) Fine mesh. (c) Very fine mesh.

Figure 3.9: *Mean vorticity field (units in* $[\mathrm{s}^{-1}]$*). Axial cut.*

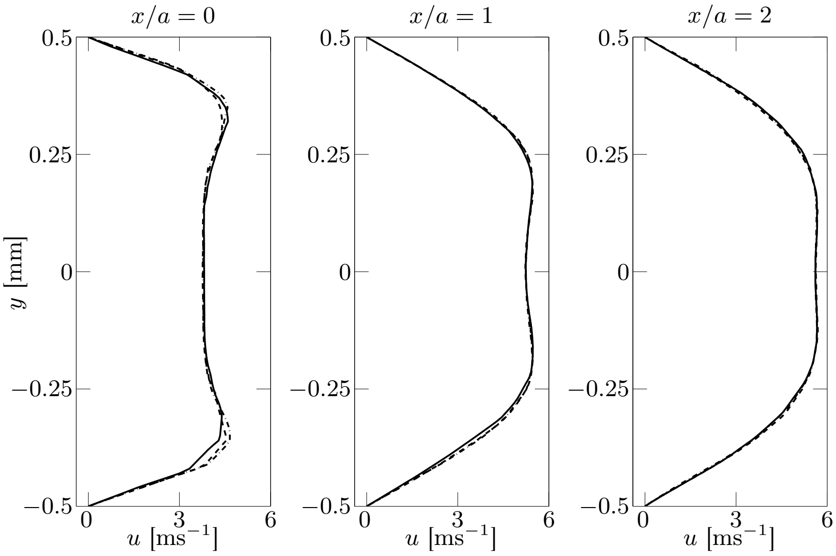

Figure 3.10: *Mean axial velocity profiles in the perforation, at different locations in the orifice ($x/a = 0$, 1 and 2). Comparison between results obtained with the very fine mesh (solid line), the fine mesh (dashed line) and the coarse mesh (dash-dotted line).*

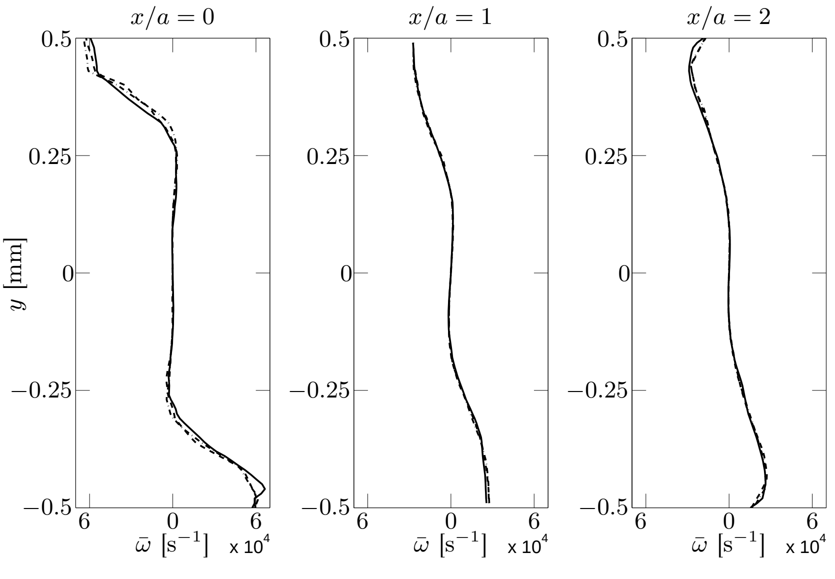

Figure 3.11: *Mean vorticity profiles in the perforation, at different locations in the orifice ($x/a = 0$, 1 and 2). Comparison between results obtained with the very fine mesh (solid line), the fine mesh (dashed line) and the coarse mesh (dash-dotted line).*

approximately 20 diameters downstream the perforation ($x/a = 40$), the jet width increases. It is also interesting to note that vorticity is quickly dissipated downstream in the jet wake. At $x/a = 40$, the peak vorticity (in absolute value) is approximately one order of magnitude lower than at $x/a = 10$, and almost two orders of magnitude lower than its peak value at the orifice outlet. This observation still holds for the fluctuating vorticity generated by the acoustic waves impinging on the perforation. This suggests that most of the acoustic energy dissipation takes place in a region close to the orifice.

This analysis of the mean flow fields enabled to:

- highlight the main features of this confined jet flow without the effects of acoustic forcing;
- ensure that temporal convergence is reached before the orifice is subjected to incident acoustic waves;
- analyze the effect of the mesh refinement on the aerodynamic field.

Results of unsteady simulations, where the perforation is subjected to acoustic waves of increasing amplitude are presented in chapter 5. Several techniques will be applied to extract acoustic coefficients from the simulations, capture the trajectories of the unsteady vortex rings that are swept away from the orifice edges, synchronized with the sound waves, and compare these numerical results to theoretical predictions and measurements.

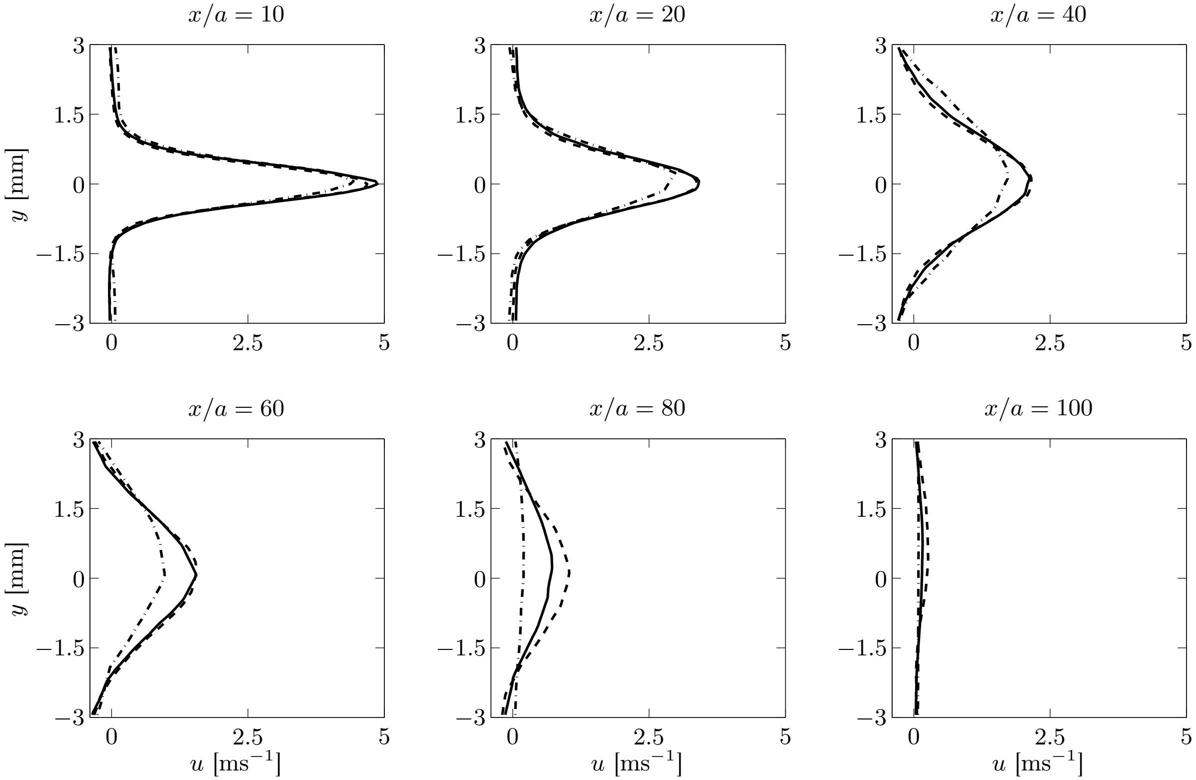

Figure 3.12: *Mean axial velocity profiles in the jet downstream the perforation. Figure captions show the distance from orifice outlet ($x/a = 10$ to 100). Comparison between results obtained with the very fine mesh (solid line), the fine mesh (dashed line) and the coarse mesh (dash-dotted line).*

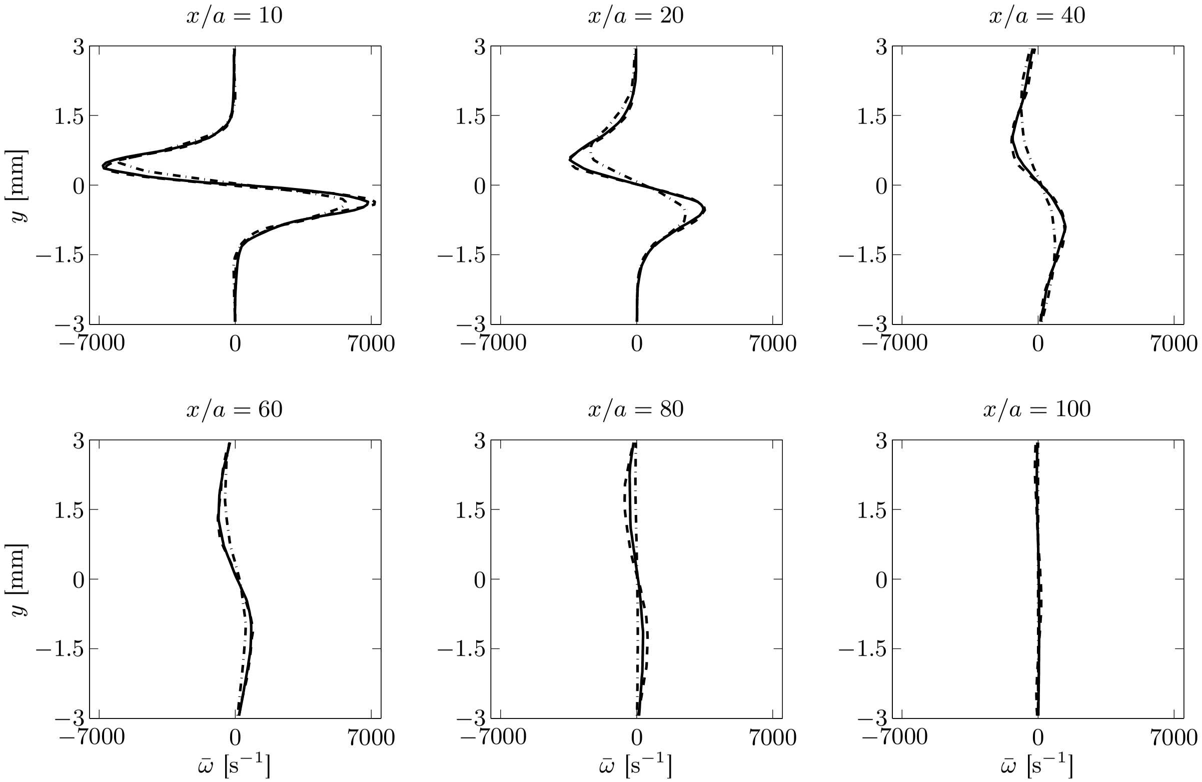

Figure 3.13: *Mean vorticity profiles in the jet downstream the perforation. Figure captions show the distance from orifice outlet ($x/a = 10$ to 100). Comparison between results obtained with the very fine mesh (solid line), the fine mesh (dashed line) and the coarse mesh (dash-dotted line).*

Chapter 4

Maximizing absorption in the linear regime at low and high Strouhal numbers

It was shown in chapter 1 that the design of a perforated plate used to damp incident acoustic waves relies on an optimization procedure, with a relatively large number of geometrical and flow parameters that need to be considered.

There is no simple design rule to fix the optimal bias flow velocity in the perforations maximizing absorption associated to a specific size of the back-cavity. For a given geometry of the perforated plate, these two design parameters are interrelated and the optimal bias flow velocity depends generally on the frequency and size of the back cavity. This problem is tackled in the present work by identifying two asymptotic regimes operating at low and high Strouhal numbers, where it is possible to decouple the choice of the optimal bias flow velocity in the orifices and the back cavity depth to cancel the reflection coefficient at certain frequencies.

This possibility has been identified for dampers operating at low Strouhal numbers [Scarpato et al. (2012)]. A generalization of this method to other regimes where these choices can be decoupled was then presented in a second publication [Scarpato et al. (2013a)]. In these regimes, the bias flow velocity is shown to be related only to the plate porosity, and is independent of frequency. This yields thus flexible solutions to design acoustic dampers where the size of the back cavity controlling the absorption frequency can be chosen separately from the bias flow velocity. An analysis of the absorption bandwidth was then proposed [Scarpato et al. (2013b)], leading to different conclusions regarding their robust behavior when the bias flow velocity deviates from its optimal value or when the frequency to damp varies.

The chapter is organized as follows. In section 4.1, expressions for the reflection coefficient of perforated plates backed by cavities are used to identify the operating conditions that maximize absorption for certain frequencies. Simplified expressions for the reflection coefficient and the optimal geometrical parameters and corresponding flow operating conditions are derived in the limit of high and low Strouhal numbers, in sections 4.2 and 4.3 respectively. The absorption bandwidth in these different regimes is analyzed in order to assess the robustness of the plate designs. Measurements of the absorption coefficient for perforated plates backed by a resonant cavity are also carried out in the two asymptotic regimes under optimal conditions. Expressions are derived to take into account variations of the bias flow velocity during off-design operations, and are presented in section 4.5. Measurements are then shown at off-design conditions when the bias flow velocity is shifted with respect to its optimal value to examine the robustness of their behavior. Predictions in the two optimal regimes identified at low and high Strouhal numbers are finally compared to measurements to validate the proposed analysis.

4.1 Maximization of absorption

In chapter 1, two analytical expressions were derived for the specific impedance ζ (Eq. (1.38)) and the reflection coefficient R (Eq. (1.39)) of a perforated plate backed by a cavity. The notations used in this chapter were introduced in Fig. 1.12, which is reproduced here for convenience in Fig. 4.1.

For small acoustic disturbances, the reflection and absorption coefficients of a perforated plate backed by a cavity and traversed by a bias flow were shown to be a function of four dimensionless numbers:

- the Strouhal number $\mathrm{St} = \omega a/u_c$, based on the orifice radius a and the vortex convection velocity u_c;
- the Helmholtz number $\mathrm{He} = kL$, where $k = \omega/c_0$ is the wavenumber and L the size of the back cavity;
- the ratio M_c/σ, where $\mathrm{M}_c = u_c/c_0$ is the Mach number based on the vortex convection velocity and σ is the plate porosity;
- the thickness-to-radius ratio h/a.

The objective is here to find conditions that maximize absorption. Maximizing absorption is equivalent to set the reflection coefficient to zero $R = 0$. Equation (1.37) shows that this is realized for the roots of $\zeta + 1 = 0$, when:

$$\Re(\zeta) + 1 = 0 \tag{4.1}$$

$$\Im(\zeta) = 0 \tag{4.2}$$

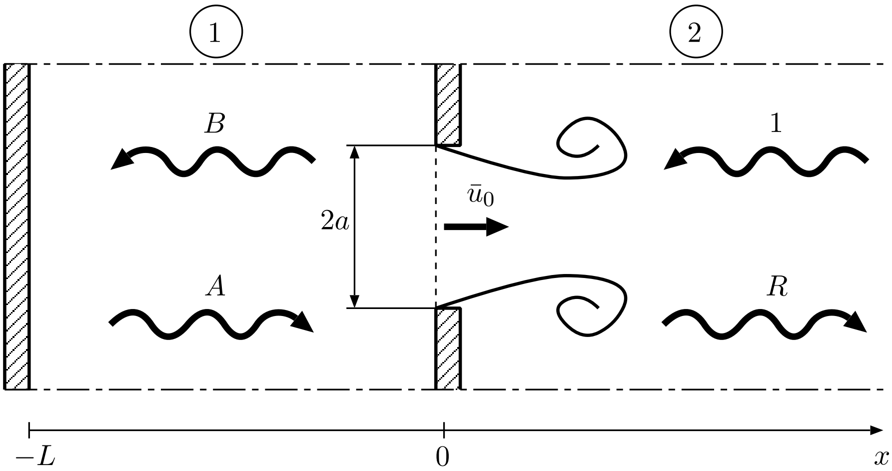

Figure 4.1: *Perforated plate traversed by a bias flow and submitted to normal incident pressure waves. Circular holes of diameter* $2a$ *are regularly spaced with a square pattern of size* d*. The plate is coupled to a resonant back cavity, of size* L*. The complex amplitude of the reflected wave is denoted* R*. The coefficients* A *and* B *denote the pressure wave amplitudes in the back cavity.*

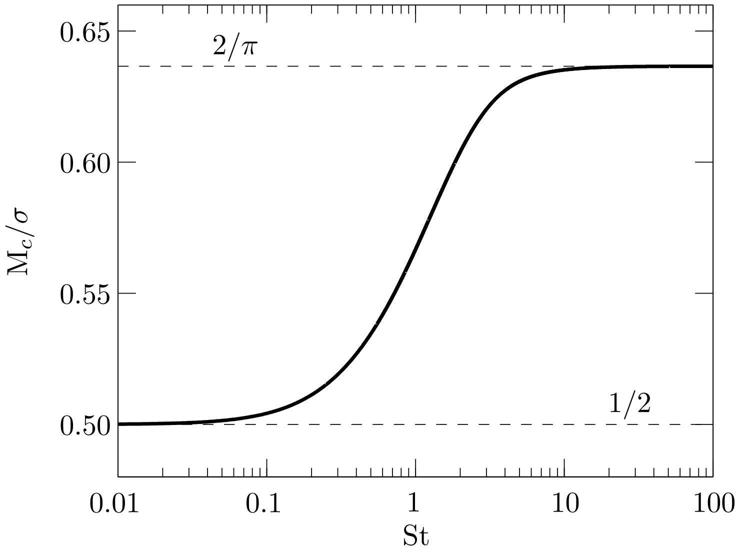

Figure 4.2: *Evolution of the optimal ratio* M_c/σ *as a function of the Strouhal number* St *given by Eq. (4.3). The ratio* M_c/σ *is independent of the plate thickness.*

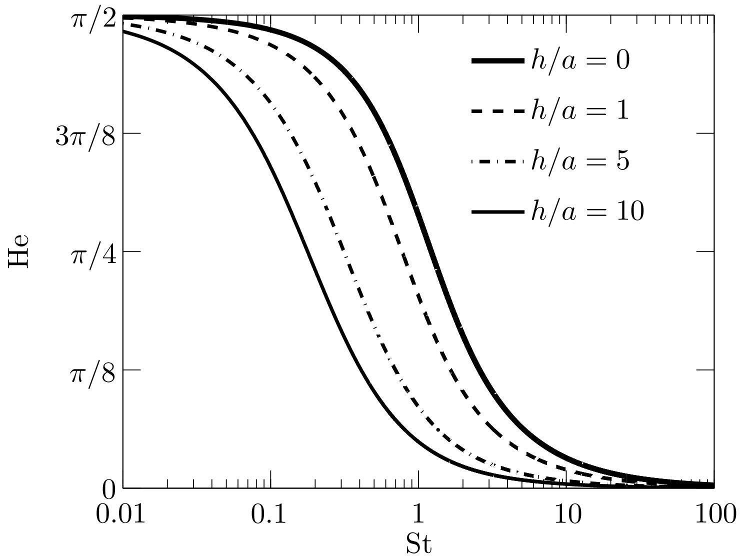

Figure 4.3: *Evolution of the optimal Helmholtz number* He *as a function of the Strouhal number* St, *given by Eq. (4.4) for different values of the thickness ratio* $h/a = 0$, 1, 5 *and* 10.

where $\Re(\zeta)$ and $\Im(\zeta)$ indicate the real and imaginary components of the specific impedance ζ. Replacing the expression for ζ given by Eq. (1.38) in Eqs. (4.1) and (4.2), one obtains the following set of conditions that must be satisfied:

$$\frac{\mathrm{M}_c}{\sigma} = \frac{2}{\pi \mathrm{St}} \frac{\gamma^2 + \delta^2}{\delta} \tag{4.3}$$

$$\frac{1}{\tan(\mathrm{He})} = \frac{\gamma}{\delta} + \frac{2h}{\pi a} \frac{\gamma^2 + \delta^2}{\delta} \tag{4.4}$$

Equation (4.3) fixes the optimal bias flow Mach number to porosity ratio M_c/σ yielding a cancellation of the reflection coefficient. This ratio is a function of the Strouhal number St only and increases monotonically with St, as shown in Fig. 4.2. This figure also shows that values of the ratio M_c/σ are bounded by $1/2 \leq \mathrm{M}_c/\sigma \leq 2/\pi$ for all Strouhal numbers. We will demonstrate in the following sections that these boundaries reached at low and high Strouhal numbers constitute particularly interesting operating regimes to design acoustic dampers.

The optimal Helmholtz number He of the cavity is fixed by Eq. (4.4). For a plate of finite thickness h, this parameter depends on both the Strouhal number and the thickness to orifice radius ratio h/a. Note that for an infinitely thin plate, this expression reduces to $\tan(\mathrm{He}) = \delta/\gamma$, which is a function of the

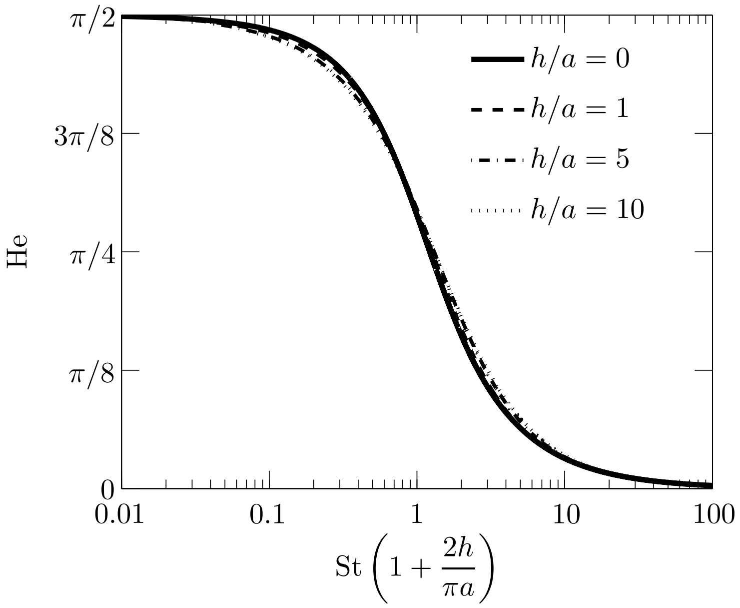

Figure 4.4: *Evolution of the optimal Helmholtz number* He *as a function of the parameter* $\mathrm{St}\,[1+2h/(\pi a)]$*, given by Eq. (4.4) for different values of the thickness ratio* $h/a = 0$*,* 1*,* 5 *and* 10*.*

Strouhal number only. Figure 4.3 shows that the Helmholtz number decreases monotonically when the Strouhal number increases: $\mathrm{He} \to \pi/2$ for $\mathrm{St} \ll 1$, and $\mathrm{He} \to 0$ when $\mathrm{St} \gg 1$. Increasing the plate thickness does not modify these limits, but intermediate values are shifted towards lower Strouhal numbers. This observation can be interpreted as follows. The perforated plate backed by a cavity can be assimilated to a spring-mass system. The spring corresponds to the volume of air comprised in the back cavity, whereas the oscillating volume in the orifice constitutes the mass of the spring-mass system. Increasing the plate thickness increases the oscillating volume in the orifice, leading to a higher inertia of the system, thus all the curves in Fig. 4.3 are shifted towards lower Strouhal numbers. It is also interesting to note that, when plotting the data as a function of the dimensionless product $\mathrm{St}\,[1+2h/(\pi a)]$ in Fig. 4.4, which takes into account the plate thickness, all curves roughly collapse on a single line. The optimal back cavity size or peak absorption frequency in damping systems featuring perforates of different thicknesses can then be easily determined.

The choice of the optimal bias flow velocity and back cavity depth are generally interrelated [Hughes and Dowling (1990); Dowling and Hughes (1992)]. One possibility to ease the design of dampers is to identify regimes where these choices can be decoupled. This problem is examined in the following sections for perforates operating at low and high Strouhal numbers.

4.2 Analysis at high Strouhal number

4.2.1 Optimal conditions maximizing absorption

The γ and δ functions appearing in the set of conditions Eqs. (4.3) and (4.4) that maximize the absorption coefficient are known functions of the Strouhal number (see Eq. (1.18)). Using the asymptotic form Eq. (1.21) to estimate the γ and δ functions at high Strouhal numbers $\mathrm{St} \gg 1$ in Eqs. (4.3) and (4.4), one obtains the following approximations to maximize the absorption coefficient:

$$\frac{\mathrm{M}_c}{\sigma} = \frac{2}{\pi} \tag{4.5}$$

$$\frac{1}{\tan(\mathrm{He})} = \mathrm{St}\left(1 + \frac{2h}{\pi a}\right) \tag{4.6}$$

This set of conditions can be used to design compact acoustic absorbers to damp a particular frequency. Equation (4.5) shows that, at large Strouhal numbers, the bias flow velocity is uniquely fixed by the plate porosity, and is given by $\bar{u}_0 = u_c = (2/\pi)\sigma c_0$. The underlying hypothesis on the convection velocity of vortices is $u_c = \bar{u}_0$, as discussed in chapter 1. Combining this expression with the knowledge of the frequency to damp, Eq. (4.6) defines the optimal Helmholtz number, and consequently determines also the optimal cavity depth L. Note that when $\mathrm{St} \gg 1$, Eq. (4.6) implies that $\tan(\mathrm{He}) \to 0$. The smallest Helmholtz number satisfying this condition is $\mathrm{He} = kL \simeq 0$. This model shows that operating at high Strouhal numbers yields compact damper designs with short cavity depths.

It is now useful to introduce the resonance parameter Q, defined by Hughes and Dowling (1990) as the ratio between the angular frequency ω and the resonance frequency of a Helmholtz resonator $\omega_{\mathrm{He}} = c_0(2a/Ld^2)^{1/2}$ formed by the back cavity volume Ld^2 and the aperture characterized by a Rayleigh conductivity $2a$. It is interesting to rewrite this resonance parameter as a function of the dimensionless numbers appearing in Eqs. (4.5) and (4.6):

$$\mathrm{Q} = \left(\frac{\omega}{\omega_{\mathrm{He}}}\right)^2 = \frac{\pi}{2}\mathrm{St}\frac{\mathrm{M}_c}{\sigma}\mathrm{He} \tag{4.7}$$

Hughes and Dowling (1990) argued that, for infinitely thin plates, improved absorption properties are expected near Helmholtz resonance, and proposed to work at $\mathrm{Q} = 1$. Substituting Eq. (4.5) in Eq. (4.7) leads to $\mathrm{Q} = \mathrm{St}\,\mathrm{He}$. Operating with a Helmholtz resonator $\mathrm{He} \ll 1$ at $\mathrm{Q} = 1$ necessarily implies that the Strouhal number in the perforations takes large values $\mathrm{St} \gg 1$.

Figure 4.5 plots the modulus of the reflection coefficient $|R|$ as a function of the Helmholtz number He, given by Eq. (1.39), at $\mathrm{St} = 5$ for an infinitely thin plate ($h/a = 0$) and for different values of the ratio M_c/σ. It is shown here that

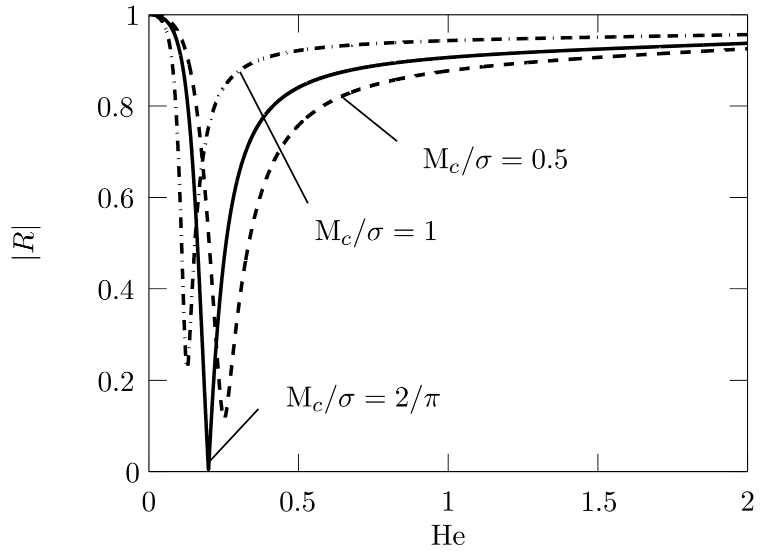

Figure 4.5: *Modulus* $|R|$ *of the reflection coefficient as a function of the back cavity Helmholtz number* He*, for a fixed Strouhal number* St $= 5$ *in the perforations (Eq. (1.39)). Influence of the ratio* M_c/σ *for an infinitely thin plate,* $h/a = 0$*.*

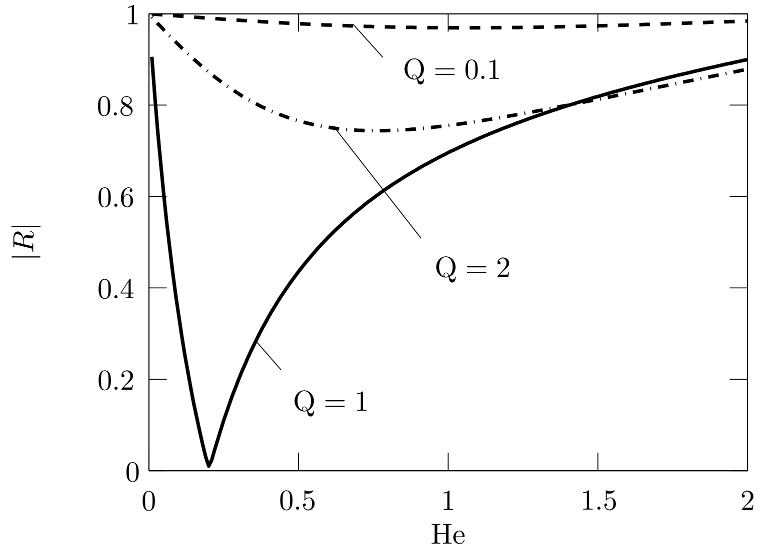

Figure 4.6: *Modulus* $|R|$ *of the reflection coefficient as a function of the back cavity Helmholtz number* He*, for a fixed Strouhal number* St $= 5$ *in the perforations (Eq. (1.39)). Influence of the resonance parameter* Q *for an infinitely thin plate,* $h/a = 0$*.*

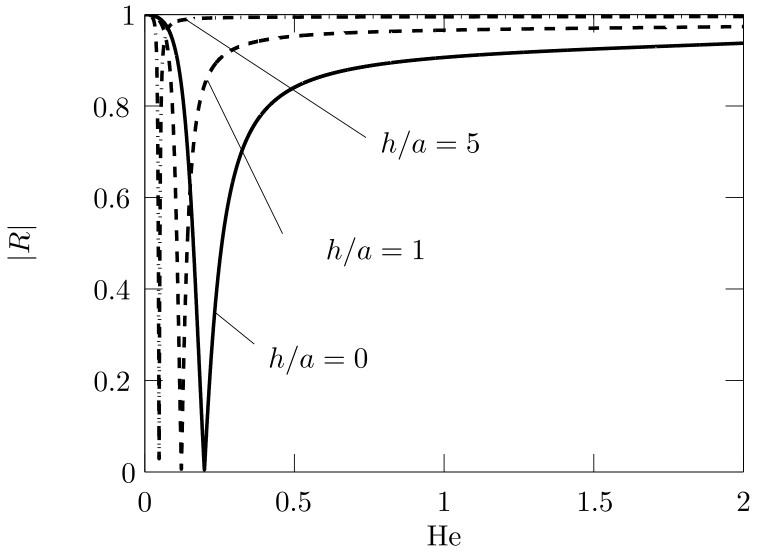

Figure 4.7: *Modulus $|R|$ of the reflection coefficient as a function of the back cavity Helmholtz number* He*, for a fixed Strouhal number* $\mathrm{St} = 5$ *in the perforations. Influence of the plate thickness h when* $\mathrm{M}_c/\sigma = 2/\pi$.

cancellation of the reflection coefficient is reached only for $\mathrm{M}_c/\sigma = 2/\pi$. When this condition is not met, absorption properties are degraded. The smallest value of the reflection coefficient increases, and the point of maximum absorption slightly shifts towards higher Helmholtz numbers when M_c/σ decreases. Conversely, the peak absorption shifts towards lower values of the Helmholtz number when M_c/σ increases. One may also note that maximum absorption always occurs when the resonance condition $\mathrm{Q} = 1$ is met. This is clearly shown in Fig. 4.6, where the evolution of the modulus of the reflection coefficient is plotted as a function of the Helmholtz number, at $\mathrm{St} = 5$ for an infinitely thin plate ($h/a = 0$) and for different values of the resonance parameter Q. In Figs. 4.5 and 4.6, the Strouhal number is fixed to $\mathrm{St} = 5$. For $\mathrm{M}_c/\sigma = 2/\pi$ the resonance parameter $\mathrm{Q} = \mathrm{St}\,\mathrm{He}$ is thus a linear function of the Helmholtz number only. In this case the Helmholtz number corresponding to the peak absorption is equal to $\mathrm{He} = \mathrm{Q}/\mathrm{St} = 1/5$.

Operating at $\mathrm{Q} = 1$ is not the best solution to maximize damping when the plate thickness cannot be neglected. Figure 4.7 shows the evolution of the modulus of the reflection coefficient $|R|$ as a function of the Helmholtz number He when $\mathrm{St} = 5$ and $\mathrm{M}_c/\sigma = 2/\pi$, for different values of the plate thickness. When these parameters are fixed, increasing the plate thickness h degrades the absorption bandwidth of the perforate, and shifts the peak absorption towards lower Helmholtz numbers. It is possible to show this effect analytically.

Replacing the identity $\mathrm{Q} = \mathrm{St}\,\mathrm{He}$ in Eq. (4.6) leads to:

$$\frac{1}{\tan(\mathrm{He})} = \frac{\mathrm{Q}}{\mathrm{He}}\left(1 + \frac{2h}{\pi a}\right) \tag{4.8}$$

At high Strouhal numbers, maximum absorption is reached for $\mathrm{He} \ll 1$, implying that $\tan(\mathrm{He}) \simeq \mathrm{He}$. Thus in the vicinity of optimal absorption, Eq. (4.8) shows that the best absorption properties at high Strouhal numbers are obtained when:

$$\mathrm{Q}\left(1 + \frac{2h}{\pi a}\right) = 1 \tag{4.9}$$

This condition sets the resonance of plates featuring a finite thickness and operating at high Strouhal numbers. Thickening the plate increases the effective length of the orifice, which is the sum of the plate thickness h and the end correction length associated to the oscillating mass of fluid in the vicinity of the perforation [Ingard (1953)]. For a Helmholtz resonator with a plate of finite thickness, the condition $\mathrm{Q} = 1$ is replaced by Eq. (4.9). Increasing the orifice length h leads thus to a reduction of Q, and subsequently to a reduction of the resonance frequency.

4.2.2 Absorption bandwidth at high Strouhal number

It is now worth analyzing the absorption bandwidth around the peak absorption frequency in the high Strouhal regime. This is realized by expanding the expression of the reflection coefficient R in Eq. (1.39) using the approximation Eq. (1.21) valid at high Strouhal numbers and the condition Eq. (4.5) setting the bias flow velocity in the perforations. This procedure yields the following approximation for the reflection coefficient:

$$R = \frac{\mathrm{i}\left[\mathrm{St}\left(1 + \dfrac{2h}{\pi a}\right) - \dfrac{1}{\tan(\mathrm{He})}\right]}{\mathrm{i}\left[\mathrm{St}\left(1 + \dfrac{2h}{\pi a}\right) - \dfrac{1}{\tan(\mathrm{He})}\right] - 2} \tag{4.10}$$

The range of Helmholtz numbers $\Delta\mathrm{He}$ satisfying $|R| \leq \beta$, where $\beta \in [0, 1]$ is an arbitrary threshold level, can be determined from Eq. (4.10). Introducing the dimensionless thickness parameter $\eta_h = 1 + 2h/(\pi a)$ yields:

$$\Delta\mathrm{He} = \arctan\left[\frac{1-\beta^2}{\eta_h \mathrm{St}(1-\beta^2) - 2\beta}\right] - \arctan\left[\frac{1-\beta^2}{\eta_h \mathrm{St}(1-\beta^2) + 2\beta}\right] \tag{4.11}$$

Using the approximation $\tan(\mathrm{He}) \simeq \mathrm{He}$, valid near optimal absorption, one finally obtains the following expression:

$$\Delta\mathrm{He} = \frac{4\beta(1-\beta^2)}{\eta_h^2 \mathrm{St}^2(1-\beta^2)^2 - 4\beta^2} \tag{4.12}$$

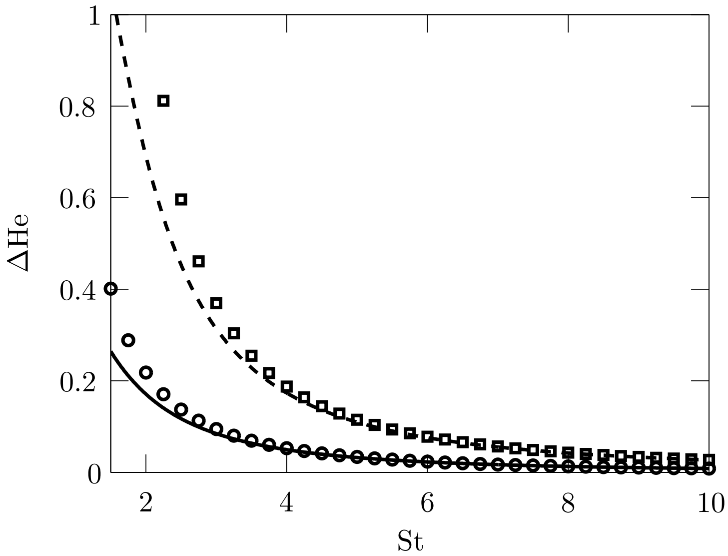

Figure 4.8: *Evolution of the range of Helmholtz numbers* ΔHe *satisfying* $|R| \leq \beta$ *as a function of the Strouhal number* St*, for two values of the threshold level* β *and for an infinitely thin plate* $h/a = 0$. $\beta = 0.2$*: general model Eq. (4.11) (solid line) and first order approximation Eq. (4.12)* ($\circ$). $\beta = 0.5$*: general model Eq. (4.11) (dashed line) and first order approximation Eq. (4.12)* ($\square$).

Equation (4.12) demonstrates that the absorption bandwidth ΔHe where $|R| \leq \beta$ is inversely proportional to the square of the Strouhal number. For a fixed back cavity length L, ΔHe is proportional to the frequency bandwidth Δf where $|R| \leq \beta$: $\Delta\text{He} \sim \Delta f$. In the high Strouhal regime the absorption bandwidth rapidly narrows when St increases. This is shown in Fig. 4.8 for two values of the threshold level $\beta = 0.2$ and 0.5. For the sake of clarity, the absorption bandwidth ΔHe is plotted as a function of the Strouhal number only for an infinitely thin plate. A similar analysis can be carried out for thick plates. Equation (4.12) indicates that increasing the ratio h/a (which is equivalent to increasing the thickness parameter η_h) leads to a reduction of the absorption bandwidth ΔHe. The comparison between the general model Eq. (4.11) and the first order approximation Eq. (4.12) shows a good agreement for $\text{St} \geq 3$.

It has been shown that operating with a Helmholtz resonator leads to a reduction of the size of the back cavity. The optimal bias flow velocity is in this case fixed by $\text{M}_c/\sigma = 2/\pi$, but the damper must work at high Strouhal numbers with a narrow absorption bandwidth around peak absorption. In the next section a similar analysis is conducted when the Strouhal number takes small values. This defines the second absorption regime where the choice of the optimal back cavity length and bias flow velocity can again be decoupled [Scarpato et al. (2012)], but it will be shown that this leads to slightly different flow and geometrical operating conditions.

4.3 Analysis at low Strouhal number

4.3.1 Optimal conditions maximizing absorption

In modern aeronautical engine or gas turbine combustors, the oscillation frequency associated to undesired combustion instabilities ranges from a few tens to a few thousands Hertz, and the diverse orifices present in the combustion chamber have generally a small diameter. The Strouhal number evaluated with the hole diameter and the bias flow velocity reached in these orifices takes then small values. Rupp et al. (2011) mentioned that perforated plates used in gas turbine combustion chambers operate in the range $\mathrm{St} \leq 0.25$. A second important aspect is that the frequency of unstable modes may vary with the operating regime and during unstable conditions, as discussed in chapter 1. Efficient dampers must then feature robust absorption properties over a large range of frequencies to circumvent these problems. The low Strouhal asymptotic regime identified in this section will be shown to fulfill conditions for robust damping at low frequencies.

Starting from Eqs. (4.3) and (4.4), two simplified conditions are derived in the limit of low Strouhal numbers to set the reflection coefficient to zero by replacing the asymptotic form Eq. (1.20) for the functions γ and δ in these expressions. At low Strouhal numbers, the condition $R = 0$ is satisfied when:

$$\frac{\mathrm{M}_c}{\sigma} = \frac{1}{2} \tag{4.13}$$

$$\frac{1}{\tan(\mathrm{He})} = \mathrm{St}\left(\frac{4}{3\pi} + \frac{h}{2a}\right) \tag{4.14}$$

The optimal bias flow velocity $\bar{u}_0$ is in this regime again fixed by the plate porosity only, $\bar{u}_0 = u_c = (1/2)\sigma c_0$, but it takes a lower value than in the high Strouhal regime where $\bar{u}_0 = (2/\pi)\sigma c_0$. Equation (4.14) can then be used to fix the frequency to damp by adjusting the back cavity size L. It is worth noting that when $\mathrm{St} \ll 1$, $\tan(\mathrm{He}) \to \infty$ to satisfy Eq. (4.14), and thus $\mathrm{He} \simeq \pi/2$, corresponding to a wavelength $\lambda = 4L$. At low Strouhal numbers, optimal absorption is reached when the cavity operates as a quarter-wave resonator.

The modulus of the reflection coefficient $|R|$ is plotted in Fig. 4.9 as a function of the Helmholtz number He, when $\mathrm{St} = 0.1$, for different values of the ratio M_c/σ. It is shown that maximum absorption is reached for $\mathrm{M}_c/\sigma = 1/2$. Moving away from this optimal ratio does not change significantly the Helmholtz number corresponding to the peak absorption condition, but the smallest value taken by the reflection coefficient increases. Absorption properties are thus degraded. The influence of plate thickness is shown in Fig. 4.10. In the low Strouhal number regime, the plate thickness barely modifies the acoustic response of the

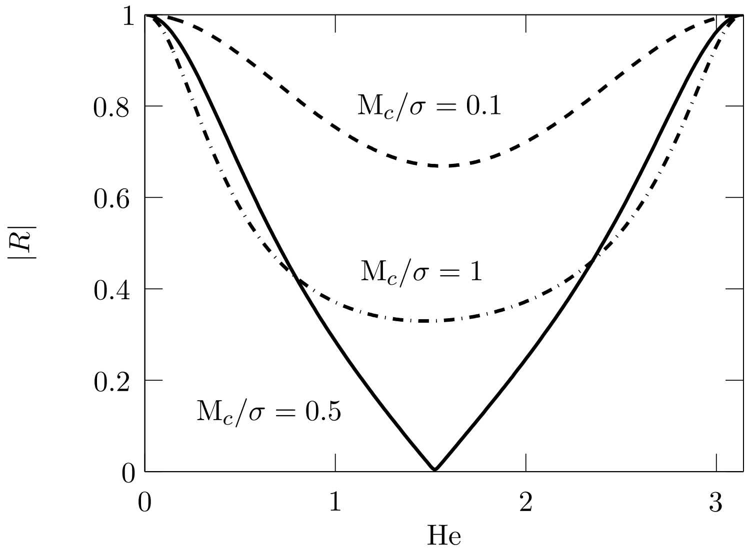

Figure 4.9: *Modulus* $|R|$ *of the reflection coefficient as a function of the back cavity Helmholtz number* He *when* St $= 0.1$ *in the perforations, Eq. (1.39). Influence of the ratio* M_c/σ *for* $h/a = 0$.

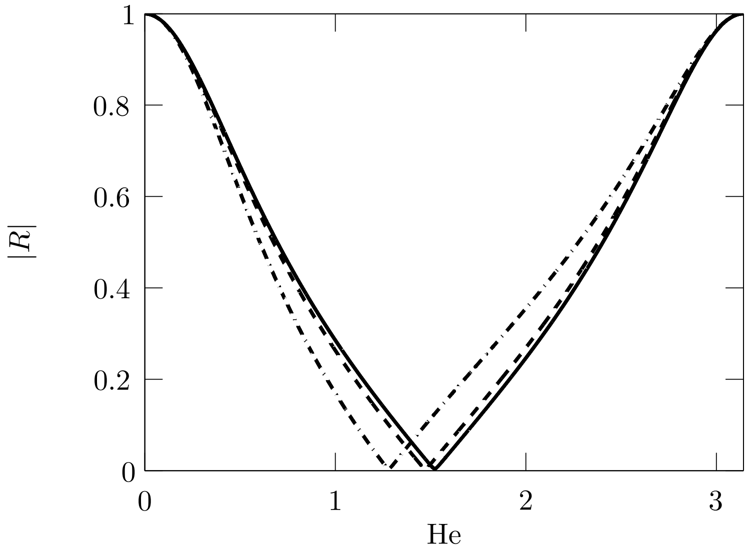

Figure 4.10: *Modulus* $|R|$ *of the reflection coefficient as a function of the back cavity Helmholtz number* He *when* St $= 0.1$ *in the perforations, Eq. (1.39). Influence of the plate thickness* h *for* $\mathrm{M}_c/\sigma = 0.5$. $h/a = 0$ *(solid line),* $h/a = 1$ *(dashed line),* $h/a = 5$ *(dash-dotted line).*

damper, leading to a slight shift of maximal absorption towards lower Helmholtz numbers when it increases. This behavior is in agreement with the observations made by Jing and Sun (2000). They found that at high bias flow velocities, hence when the Strouhal number is reduced, the acoustic response of a thick perforate is unchanged compared to the response of a thin plate featuring the same orifice geometry.

4.3.2 Absorption bandwidth at low Strouhal number

Figure 4.9 suggests that in the low Strouhal regime the absorption bandwidth around the peak absorption frequency is large compared to the one found in the high Strouhal regime. It is possible to demonstrate this result analytically. Starting from Eq. (1.39), taking the limit $\mathrm{St} \ll 1$ and the condition $\mathrm{M}_c/\sigma = 1/2$ defined by Eq. (4.13), one obtains a low Strouhal first order approximation of the reflection coefficient:

$$R = \frac{\mathrm{i}\left[\mathrm{St}\left(\dfrac{4}{3\pi} + \dfrac{h}{2a}\right) - \dfrac{1}{\tan(\mathrm{He})}\right]}{\mathrm{i}\left[\mathrm{St}\left(\dfrac{4}{3\pi} + \dfrac{h}{2a}\right) - \dfrac{1}{\tan(\mathrm{He})}\right] - 2} \tag{4.15}$$

This expression is very similar to Eq. (4.10) obtained for high Strouhal numbers, except that the coefficient multiplying the Strouhal numbers is modified. A rough approximation of the absorption bandwidth $\Delta\mathrm{He}$, again defined as the range of Helmholtz numbers verifying $|R| \leq \beta$, $\beta \leq 1$ being an arbitrary threshold, was derived by Scarpato et al. (2012). This expression was then slightly improved by Scarpato et al. (2013a) and is reproduced here. Starting from Eq. (4.15) and defining now the thickness parameter as $\eta_l = 4/(3\pi) + h/(2a)$, one obtains the following first order approximation for the absorption bandwidth:

$$\Delta\mathrm{He} = \arctan\left[\frac{1-\beta^2}{\eta_l \mathrm{St}(1-\beta^2) - 2\beta}\right] - \arctan\left[\frac{1-\beta^2}{\eta_l \mathrm{St}(1-\beta^2) + 2\beta}\right] \tag{4.16}$$

It is worth noting that Eq. (4.16) is formally identical to Eq. (4.11), only the definitions of the thickness parameters η_l and η_h are different. Taking the limit of low Strouhal numbers, Eq. (4.16) becomes:

$$\Delta\mathrm{He} = \pi - 2\arctan\left[\frac{1-\beta^2}{2\beta}\right] \tag{4.17}$$

Equation (4.17) shows that the absorption bandwidth at low Strouhal number only depends on the threshold level β. A comparison between the absorption bandwidth in the low and high Strouhal regimes is presented in Fig. 4.11. It is interesting to note that the range of Helmholtz numbers over which optimized absorption properties are found is always larger for the low Strouhal regime

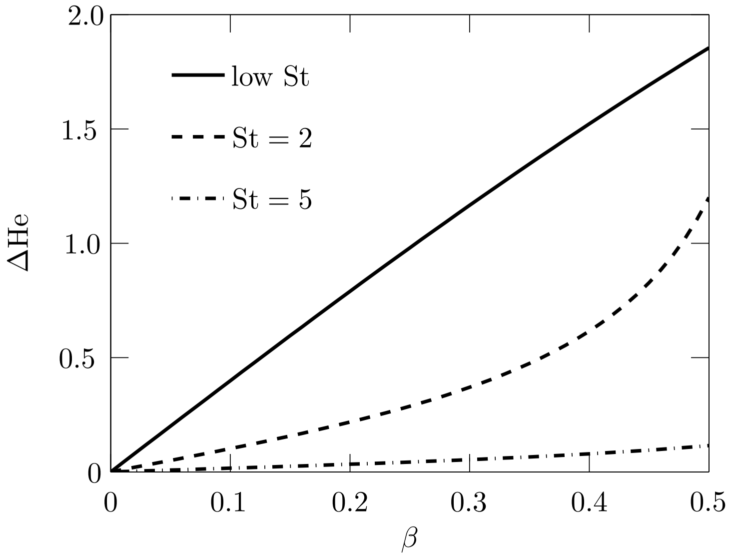

Figure 4.11: *Evolution of the range of Helmholtz numbers* $\Delta\mathrm{He}$ *where* $|R| \leq \beta$ *as a function of the threshold level* β*, in the low Strouhal regime defined by Eq. (4.17) (solid line), and in the high Strouhal regime defined by Eq. (4.12) (dashed and dash-dotted lines), for an infinitely thin plate* $h/a = 0$*.*

than for the high Strouhal one.

In conclusion to this section, the low Strouhal regime features a large absorption bandwidth, which makes it suitable for the design of robust dampers. The optimal bias flow velocity is in this case again only fixed by the plate porosity. However, the back cavity operates as a quarter-wave resonator, thus its depth is larger than for a damper operating at high Strouhal numbers.

4.4 Comparison with measurements

Predictions from the general model presented in chapter 1 and from the asymptotic regimes identified in this chapter are compared to measurements realized in the ITHACA test bench, described in chapter 2. The theoretical models used for comparison are summarized in Tab. 4.1.

The reflection coefficient of the six plates P_3 to P_8 presented in chapter 2 was measured for small to moderate pressure disturbances and for frequencies below 1 kHz. Results are presented here for a sound level fixed to 100 dB which was controlled at the rear side of the back cavity by the microphone $\mathrm{M_{SPL}}$. This level is small enough to consider that the six tested dampers operate in the linear regime. This was verified by conducting measurements at lower sound

Table 4.1: *Theoretical models for the reflection coefficient of a perforated plate backed by a cavity and traversed by a mean bias flow. Model 1 and 2 are the general model introduced in chapter 1, for an infinitely thin plate and a plate of thickenss h respectively. Model 3 and 4 are respectively the high Strouhal and the low Strouhal models presented in this chapter.*

Model	Expression	Remarks
1	$R = \dfrac{\mathrm{i}\left[\dfrac{\pi}{2}\mathrm{St}\dfrac{\mathrm{M}_c}{\sigma}\dfrac{1}{\gamma-\mathrm{i}\delta} - \dfrac{1}{\tan(\mathrm{He})}\right]+1}{\mathrm{i}\left[\dfrac{\pi}{2}\mathrm{St}\dfrac{\mathrm{M}_c}{\sigma}\dfrac{1}{\gamma-\mathrm{i}\delta} - \dfrac{1}{\tan(\mathrm{He})}\right]-1}$	General model Eq. (1.39) with $h=0$
2	$R = \dfrac{\mathrm{i}\left[\dfrac{\pi}{2}\mathrm{St}\dfrac{\mathrm{M}_c}{\sigma}\left(\dfrac{1}{\gamma-\mathrm{i}\delta}+\dfrac{2h}{\pi a}\right) - \dfrac{1}{\tan(\mathrm{He})}\right]+1}{\mathrm{i}\left[\dfrac{\pi}{2}\mathrm{St}\dfrac{\mathrm{M}_c}{\sigma}\left(\dfrac{1}{\gamma-\mathrm{i}\delta}+\dfrac{2h}{\pi a}\right) - \dfrac{1}{\tan(\mathrm{He})}\right]-1}$	General model Eq. (1.39) when $h \neq 0$
3	$R = \dfrac{\mathrm{i}\left[\mathrm{St}\left(1+\dfrac{2h}{\pi a}\right) - \dfrac{1}{\tan(\mathrm{He})}\right]}{\mathrm{i}\left[\mathrm{St}\left(1+\dfrac{2h}{\pi a}\right) - \dfrac{1}{\tan(\mathrm{He})}\right]-2}$	High Strouhal model Eq. (4.10)
4	$R = \dfrac{\mathrm{i}\left[\mathrm{St}\left(\dfrac{4}{3\pi}+\dfrac{h}{2a}\right) - \dfrac{1}{\tan(\mathrm{He})}\right]}{\mathrm{i}\left[\mathrm{St}\left(\dfrac{4}{3\pi}+\dfrac{h}{2a}\right) - \dfrac{1}{\tan(\mathrm{He})}\right]-2}$	Low Strouhal model Eq. (4.15)

levels and results were found identical. More data were however obtained at 100 dB.

4.4.1 Influence of porosity

In the asymptotic regimes developed in sections 4.2 and 4.3, the porosity determines the optimal bias flow velocity $\bar{u}_0$ within the perforations given by Eqs. (4.5) and (4.13). At low Strouhal number, increasing the plate porosity corresponds to higher operating bias flow velocities $\bar{u}_0 = (1/2)\sigma c_0$ and to lower values of Strouhal numbers $\mathrm{St} = 2\omega a/(\sigma c_0)$ for a fixed frequency and hole radius. The influence of the plate porosity on the reflection coefficient modulus and phase was characterized versus frequency, for a fixed cavity depth $L = 150$ mm and the corresponding optimal bias flow velocity $\bar{u}_0$ given by

Table 4.2: *Perforated plate parameters for the six configurations explored here.* a*: aperture radius,* σ*: porosity,* h*: plate thickness,* L*: back cavity depth,* σ*: porosity,* $\bar{u}_0$*: bias flow velocity in the orifices,* $\mathrm{St} = \omega a/\bar{u}_0$*: Strouhal number.*

Plate	a [mm]	σ [%]	h/a	$\bar{u}_0$ [$\mathrm{m\,s^{-1}}$]	L [mm]	Range of St
P_3	0.5	8.84	2	15.3	150	0.021 - 0.205
P_4	0.5	4.84	2	8.40	150	0.037 - 0.374
P_5	0.5	2.76	2	4.79	150	0.066 - 0.656
P_6	0.5	1.96	2	3.40	150	0.092 - 0.924
P_7	0.5	1.48	2	2.57	150	0.122 - 1.222
P_8	0.5	1.00	2	1.74	150	0.181 - 1.806

Eq. (4.13) for each plate at a low constant SPL of 100 dB. Measurements for increasing plate porosities are gathered in Figs. 4.12 to 4.14 for plates P_8 to P_3. They are compared to predictions obtained with different approximations. The dashed line (model 1 in Tab. 4.1) corresponds to the reflection coefficient calculated with the general expression Eq. (1.39), when the optimal bias flow velocity used to evaluate the Rayleigh conductivity is fixed by Eq. (4.13) and the plate thickness is neglected $h/a = 0$. The solid lines (model 2 in Tab. 4.1) include additional effects of the plate thickness in the calculation of the Rayleigh conductivity (Eq. (1.39) with $h/a = 2$). Table 4.2 summarizes the main operating conditions of the six configurations explored here.

Evolutions of the modulus $|R|$ and phase φ of the reflection coefficient for the perforated plates P_8 and P_7 are presented in Figs. 4.12(a) and 4.12(b). In the top graphs of Fig. 4.12 the modulus of the reflection coefficient is plotted versus frequency. It first decreases quasi-linearly with the frequency, reaches a minimum and then increases at higher frequencies. The measured modulus $|R|$ reaches a minimum $|R| = 0.05$ around $f = 350$ Hz for plate P_8 and $|R| = 0.18$ around $f = 400$ Hz for plate P_7. In both cases, predictions of the reflection coefficient with models 1 and 2 are in fairly good agreement with experimental data. Measurements lie within these two limits obtained by neglecting (model 1) or considering the plate thickness (model 2). For plate P_7, data for the modulus of the reflection coefficient match well model 1 for frequencies lower than the peak absorption frequency and then coincide with model 2 at higher frequencies. The opposite is observed for the phase evolution, where experimental data match model 2 at low frequencies and model 1 at higher frequencies.

The same type of analysis is conducted for plates P_5 and P_6. Figure 4.13 shows the evolution of the modulus and phase of the reflection coefficient R as a function of frequency. Both plates are characterized by a similar evolution of the modulus $|R|$, that first decreases quasi-linearly with frequency, reaches a

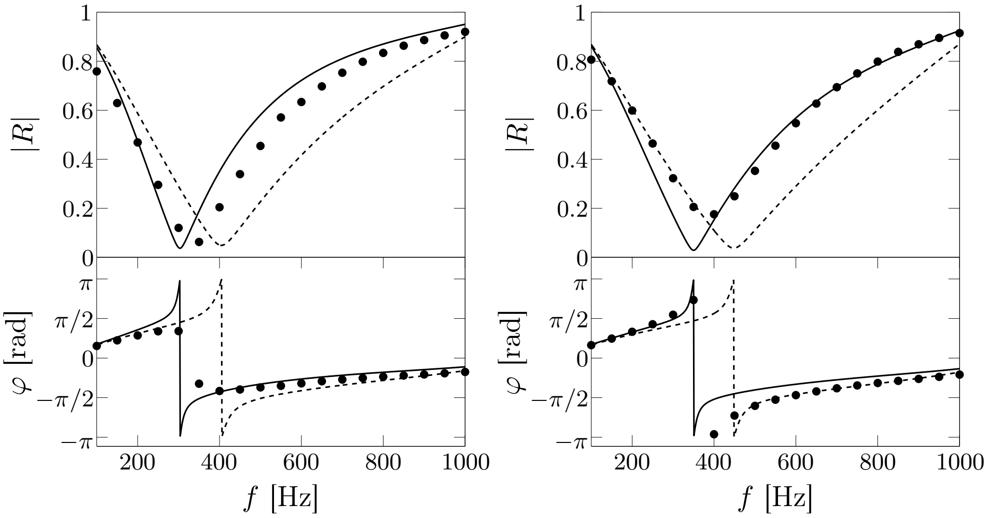

(a) Plate P_8.

(b) Plate P_7.

Figure 4.12: *Evolution of the modulus* $|R|$ *(top) and the phase* φ *(bottom) of the reflection coefficient of plate* P_8 *at* $\bar{u}_0 = 1.74\ \mathrm{m\,s^{-1}}$ *(a), and plate* P_7 *at* $\bar{u}_0 = 2.57\ \mathrm{m\,s^{-1}}$ *(b). The plates are operated at their optimum bias flow velocity for a fixed cavity depth of* $L = 150$ mm *and a constant* SPL *of* 100 dB*. Predictions with model 1 (dashed line) and model 2 (solid line) in Tab. 4.1, are compared to measurements (black circles).*

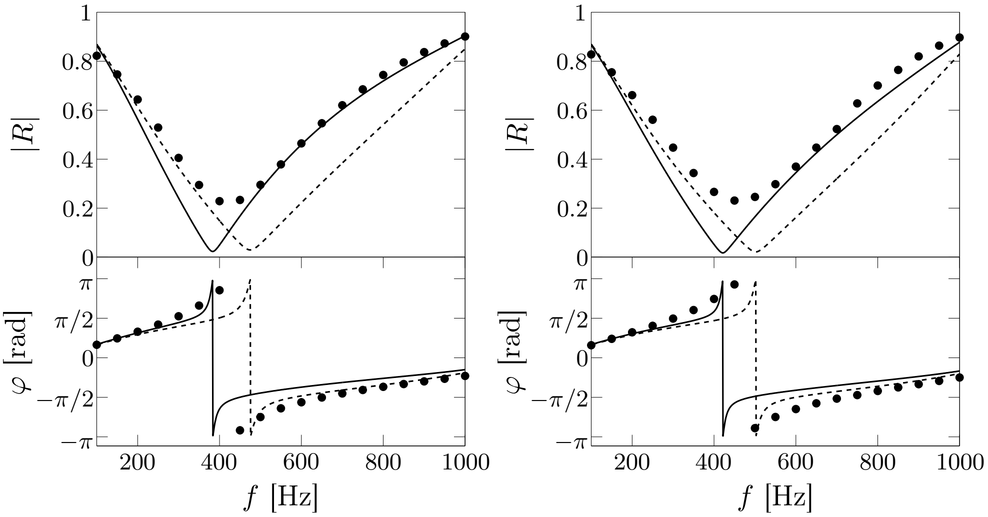

(a) Plate P_6.

(b) Plate P_5.

Figure 4.13: *Evolution of the modulus* $|R|$ *(top) and the phase* φ *(bottom) of the reflection coefficient of plate* P_6 *at* $\bar{u}_0 = 3.40\ \mathrm{m\,s^{-1}}$ *(a), and plate* P_5 *at* $\bar{u}_0 = 4.79\ \mathrm{m\,s^{-1}}$ *(b). The plates are operated at their optimum bias flow velocity for a fixed cavity depth of* $L = 150$ mm *and a constant* SPL *of* 100 dB*. Predictions with model 1 (dashed line) and model 2 (solid line) in Tab. 4.1, are compared to measurements (black circles).*

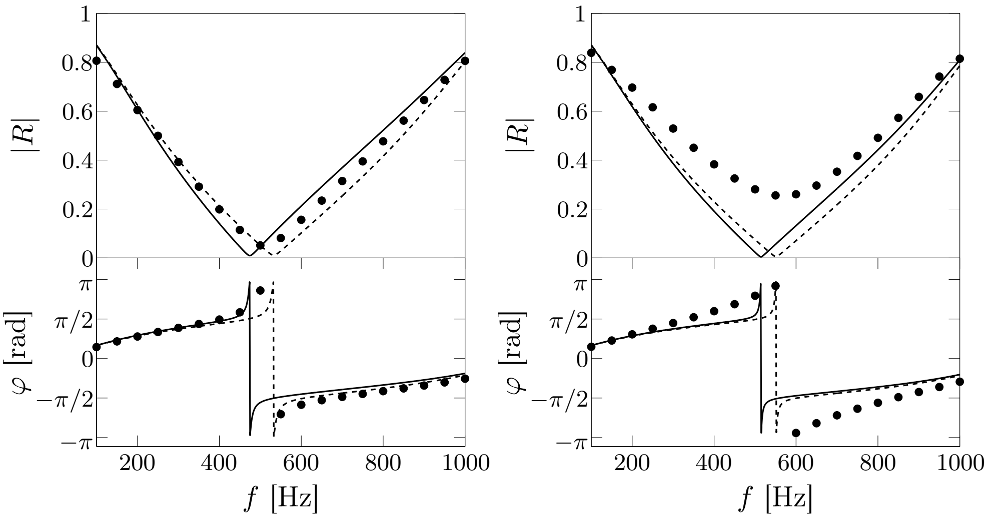

(a) Plate P_4.

(b) Plate P_3.

Figure 4.14: *Evolution of the modulus* $|R|$ *(top) and the phase* φ *(bottom) of the reflection coefficient of plate* P_4 *at* $\bar{u}_0 = 8.40\ \mathrm{m\,s^{-1}}$ *(a), and plate* P_3 *at* $\bar{u}_0 = 15.3\ \mathrm{m\,s^{-1}}$ *(b). The plates are operated at their optimum bias flow velocity for a fixed cavity depth of* $L = 150$ mm *and a constant* SPL *of* 100 dB*. Predictions with model 1 (dashed line) and model 2 (solid line) in Tab. 4.1, are compared to measurements (black circles).*

minimum value of 0.2 at a frequency of 420 Hz for plate P_6 and 450 Hz for plate P_5 and then increases with frequency. As observed for plates P_7 and P_8, the peak absorption frequency lies between model 1 and model 2 predictions. If we focus on the modulus of the reflection coefficient, model 2 taking into account the plate thickness shows the best agreement with experimental data at higher frequencies. At lower frequencies, model 1 is closer to measurements. Results are reversed in terms of the phase of the reflection coefficient.

Plates P_3 and P_4 feature higher porosities and the predictions given by model 1 and 2 nearly collapse for these plates. They are operated at higher bias flow velocities, which are fixed by the plate porosity Eq. (4.13). It was shown by Jing and Sun (2000) that the effect of the plate thickness reduces for high bias flow velocities. Figure 4.14(a) shows an excellent agreement between measurements and both models for plate P_4, in terms of both modulus and phase of the reflection coefficient. This plate features a nearly zero reflection coefficient at $f = 500$ Hz, and a large absorption bandwidth around this frequency. The situation is different for the response of plate P_3 presented in Fig. 4.14(b) where predictions do not improve. While the peak absorption frequency is well predicted by the different models, the minimum value measured for the modulus of the reflection coefficient $|R| \simeq 0.25$ is higher than expected. The general trend is also well predicted but the experimental data remain always larger for the modulus. This plate features the largest porosity explored in this study

Table 4.3: *Absorption bandwidth Δf [Hz] where $|R| \leq 0.5$. Comparison between model 1 (general model), model 2 (general model including the effect of plate thickness) and experimental data extracted from Figs. 4.12 to 4.14.*

Plate	Model 1	Model 2	Exp.
P_3	610	587	486
P_4	594	545	566
P_5	562	472	409
P_6	528	408	362
P_7	493	349	341
P_8	418	266	326

$\sigma = 8.84$ % and the highest tested bias flow velocity $\bar{u}_0 = 15.3$ m s^{-1}. In this case, it is suspected that the absorption properties of the damping system are perturbed by two phenomena which were not included in the models. The first is associated to possible interactions between the holes. It is known that interaction effects between orifices need to be considered for plates featuring a ratio $\xi = a(S_{\text{za}}/\pi)^{-1/2}$ higher than 0.2 [Melling (1973)]. In this expression S_{za} is the influence zone area of each hole which is equal to $S_{\text{za}} = d^2$ in our case due to the symmetry of the perforations. This quantity can be estimated for plate P_4 and P_3. One finds $\xi = 0.2$ and $\xi = 0.3$ respectively. Multiple holes interactions can then be neglected for plate P_4 but probably not for plate P_3 where optimal absorption may be altered by this phenomenon. A second source of perturbations may be linked to the high velocities reached in the air injection holes feeding the back cavity. These injection units generate high speed transverse jets that may interact with the acoustic waves in the back cavity. This can be characterized by the background noise level measured by the microphone M_{SPL} in absence of acoustic forcing which reaches 80 dB for measurements with plate P_4 and 90 dB for plate P_3. The signal to noise ratio between the coherent acoustic signal and the background noise associated to turbulence in the back cavity is then significantly reduced for the measurements conducted with plate P_3.

It is now worth examining the frequency bandwidth around the peak absorption frequency, where the reflection coefficient remains below a certain threshold level. Results are summarized in Tab. 4.3 for the different plates characterized, this bandwidth being defined as the range of frequencies where $|R| \leq 0.5$. The table shows that the absorption bandwidth narrows when plates do not operate in the low Strouhal regime. For plates P_3 and P_4, operating in the low Strouhal regime, a large reduction of $|R|$ over a large frequency span can be achieved. The best performances are obtained with plate P_4 where $|R| \leq 0.5$

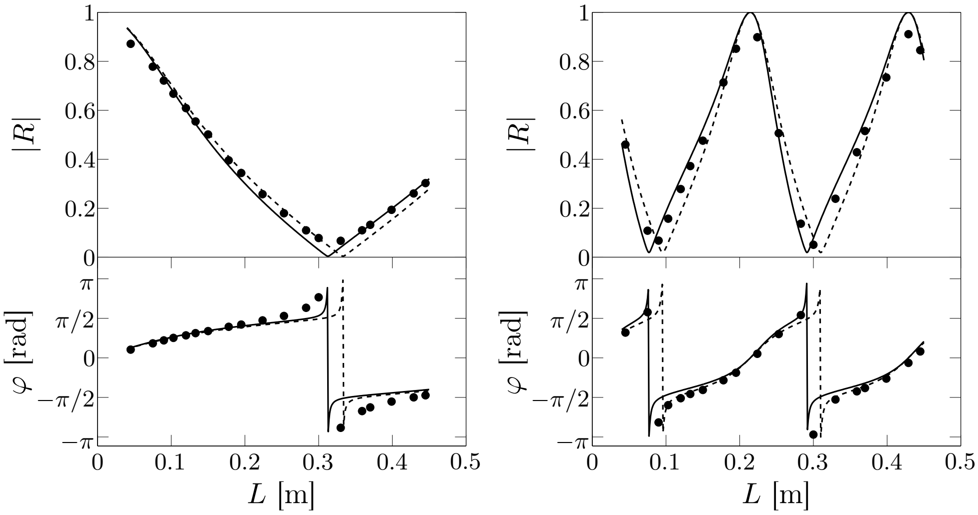

(a) Plate P_4, $f = 250$ Hz.
(b) Plate P_4, $f = 800$ Hz.

Figure 4.15: *Modulus $|R|$ of the reflection coefficient of plate P_4 operated with the bias flow velocity $\bar{u}_0 = 8.40$ m s^{-1} as a function of cavity depth L for two different forcing frequencies: (a) $f = 250$ Hz, (b) $f = 800$ Hz. Predictions with model 1 (dashed line) and model 2 (solid line) in Tab. 4.1 are compared to measurements (black circles).*

over a 550 Hz frequency span and $|R| \leq 0.2$ around a 220 Hz bandwidth. These validations demonstrate that the low Strouhal regime explored in section 4.3 enables to cancel the reflection coefficient at specific low frequencies together with a large absorption bandwidth around this optimal frequency. This regime is then interesting to design low frequency robust dampers for thermo-acoustic modes where the instability frequency may vary significantly. Since the bias flow velocity is only fixed by the plate porosity, a control of the reflection coefficient is then possible by uniquely varying the size of the back cavity [Tran et al. (2009a); Tran et al. (2009b)]. This property is examined in the next section for plate P_4.

4.4.2 Effect of the cavity depth

Predictions obtained with the general model for infinitely thin plates (model 1 in Tab. 4.1) and the general model including the effect of thickness (model 2 in Tab. 4.1) are now compared with measurements for fixed frequencies when the back cavity size is varied. Figures 4.15(a) and 4.15(b) show the modulus and phase of the reflection coefficient as a function of the cavity depth L for plate P_4 at two different frequencies $f = 250$ Hz and $f = 800$ Hz. In Fig. 4.15(a), the modulus of the reflection coefficient decreases with the cavity size to reach a minimum $|R| \simeq 0.06$. Then it increases for larger cavity depths. Optimal absorption is reached for a size $L' \simeq 0.35$ m that corresponds to the first resonant mode of the cavity $fL'/c_0 \simeq 1/4$, in agreement with the predictions

of Eq. (4.14). When $\mathrm{St} = \omega a/\bar{u}_0 = 0.087$, one finds $\mathrm{He} = 1.53$ and $L' = 0.34$ m with model 1, which are close to the measured values. For a higher forcing frequency $f = 800$ Hz, data plotted in Fig. 4.15(b) feature now two minima around $|R| \simeq 0.05$ reached when $L' \simeq 0.09$ m and $L'' \simeq 0.30$ m. These minima correspond to the first and second resonant modes of the cavity $fL'/c_0 \simeq 1/4$ and $fL''/c_0 \simeq 3/4$ respectively. These values are again in agreement with Eq. (4.14). When $\mathrm{St} = \omega a/\bar{u}_0 = 0.28$, Eq. (4.14) yields $\mathrm{He}' = 1.45$, $L' = 0.10$ m and $\mathrm{He}'' = \mathrm{He}' + \pi = 4.59$, $L'' = 0.32$ m.
It is also important to note that at low frequencies ($f = 250$ Hz, Fig. 4.15(a)) the modulus of the reflection coefficient reaches small values over a relatively large range of cavity depths. At higher frequencies ($f = 800$ Hz, Fig. 4.15(b)) the cavity depth must be carefully chosen, because the range of depths leading to valuable absorption is narrower.

These measurements were found in good agreement with predictions and have confirmed the key role of the bias flow through the apertures, which is fixed for a given porosity by Eq. (4.13) at low Strouhal number. The tested design P_4, operating in the low Strouhal regime, shows that it is possible to cancel the reflection coefficient when the back cavity resonates around the 1/4 and 3/4 wave modes. These non-reflecting conditions are robust over certain frequency and cavity size ranges when submitted to low amplitude pressure perturbations. In the next section, comparisons between measurements realized with the ITHACA test bench or with data extracted from the literature, and predictions of the models developed in the present work for plates operating at low and high Strouhal numbers are further presented.

4.4.3 Validation of the low and high Strouhal number models

Experimental data for five different perforated plate configurations are examined here. These plates operate in the low and high Strouhal regimes, and were selected in order to validate the models described in this chapter (respectively model 3 in Tab. 4.1 for the high Strouhal regime, and model 4 in Tab. 4.1 for the low Strouhal regime). By varying the forcing frequency, the response of these dampers is explored over a large range of Strouhal numbers covering the low and high Strouhal limits. Table 4.4 synthesizes the main parameters characterizing these operating regimes. All the results were obtained in the ITHACA test bench, presented in chapter 2, except for configuration 3, where experimental data were extracted from Hughes and Dowling (1990).

In the first configuration the perforated plate P_8 is used with a back cavity L=24.5 mm and is subjected to forcing frequencies lower than 1200 Hz. This damper operates at small to moderate Strouhal numbers ($0.14 \leq \mathrm{St} \leq 1.73$, Tab. 4.4). Measurements of the absorption coefficient $\alpha = 1 - |R|^2$ are plotted as a function of frequency in Fig 4.16, when the bias flow velocity is fixed to

Table 4.4: *Operating parameters for the five configurations examined in the present section. a: orifice radius, σ: plate porosity, L: back cavity depth, h: plate thickness,* M_c*: Mach number in the orifices,* $\mathrm{St} = 2\pi f a/\bar{u}_0$*: Strouhal number. *Data extracted from Hughes and Dowling (1990).*

Config.	Plate	a [mm]	σ [%]	L [mm]	h [mm]	M_c/σ	Range of St
1	P_8	0.5	1.00	24.5	1	0.64	0.14 – 1.73
2	P_8	0.5	1.00	150	1	0.64	1.44 – 2.88
3*	HD	1.5	2.45	10	$\simeq 0$	0.57	0.97 – 5.82
4	$P_{2.5}$	0.3	4.68	150	1	0.50	0.02 – 0.23
5	$P_{2.5}$	0.3	4.68	300	1	0.50	0.02 – 0.23

$\bar{u}_0 = 2.18\ \mathrm{m\,s^{-1}}$ corresponding to the optimal value given by $\mathrm{M}_c/\sigma = 2/\pi$ in the limit of high Strouhal numbers. These data are compared to predictions obtained with the high Strouhal model Eq. (4.10) (model 3 in Tab. 4.1), and with the general model of Eq. (1.39) (model 2 in Tab. 4.1). The thickness ratio for plate P_8 is $h/a = 2$. The general trend is well predicted and the agreement between both models and measurements is fairly good, except at very low frequencies, below 200 Hz. The peak absorption is predicted at 810 Hz, whereas experimental data show maximum absorption at a slightly higher frequency of 870 Hz. This condition coincides with the Helmholtz resonance of the cavity, satisfying Eq. (4.9). It is also worth noting that maximum absorption $\alpha = 1$ or equivalently $|R| = 0$ is achievable in practice.

The response of plate P_8 traversed by the same bias flow velocity $\bar{u}_0 = 2.18\ \mathrm{m\,s^{-1}}$ is now examined in the frequency range 1000 to 2000 Hz when the back cavity length is increased to $L = 150$ mm. This corresponds to configuration 2 in Tab. 4.4 operating at higher Strouhal numbers $1.44 \leq \mathrm{St} \leq 2.88$ than configuration 1. Results for the absorption coefficient are plotted in Fig. 4.17 as a function of frequency. The peak absorption is now found at 1225 Hz in the experiments, corresponding to the Helmholtz number $\mathrm{He}_{\max} \simeq 3.37$. This peak corresponds to the second resonant mode of the back cavity featuring a half-wavelength structure, and is in agreement with predictions of Eq. (4.6), yielding a value $\mathrm{He}_{\max} \simeq 3.38$. One may also note that the absorption bandwidth defined by the range of frequencies Δf around the peak absorption frequency where $\alpha \geq 0.8$ is narrower in configuration 2 ($\Delta f \simeq 50$ Hz in Fig. 4.17) than in configuration 1 ($\Delta f \simeq 330$ Hz in Fig. 4.16). This observation is consistent with Eq. (4.12). The range of Strouhal numbers covered in configuration 2 being higher than in configuration 1, the absorption bandwidth necessarily narrows as shown by Eq. (4.12).

The third configuration examined is the one studied by Hughes and Dowling (1990). In the top graph of Fig. 6 in their paper, the absorption coefficient

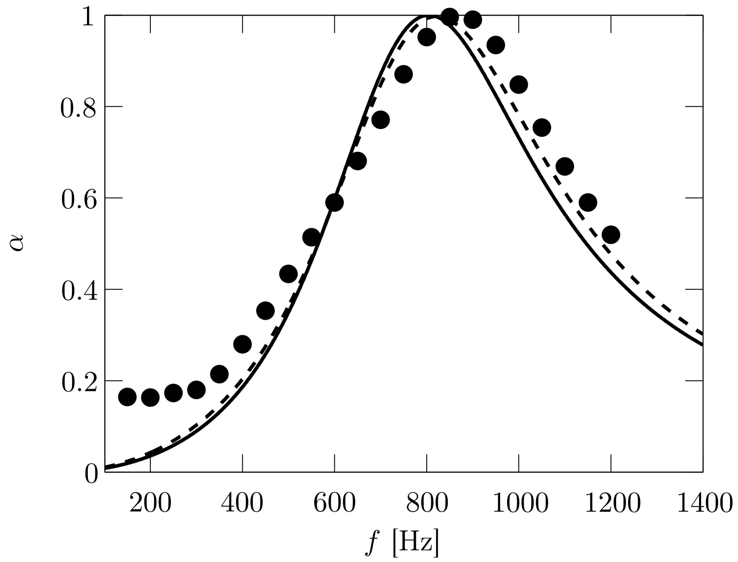

Figure 4.16: *Case 1. Evolution of the absorption coefficient* $\alpha = 1 - |R|^2$ *as a function of frequency* f *(configuration 1 in Tab. 4.4). Measurements (•) are compared to predictions obtained for* $h/a = 2$, $L = 24.5$ mm *and* $\mathrm{M}_c/\sigma = 2/\pi$. *Dashed line: general model (model 2 in Tab. 4.1). Solid line: high Strouhal approximation (model 3 in Tab. 4.1).*

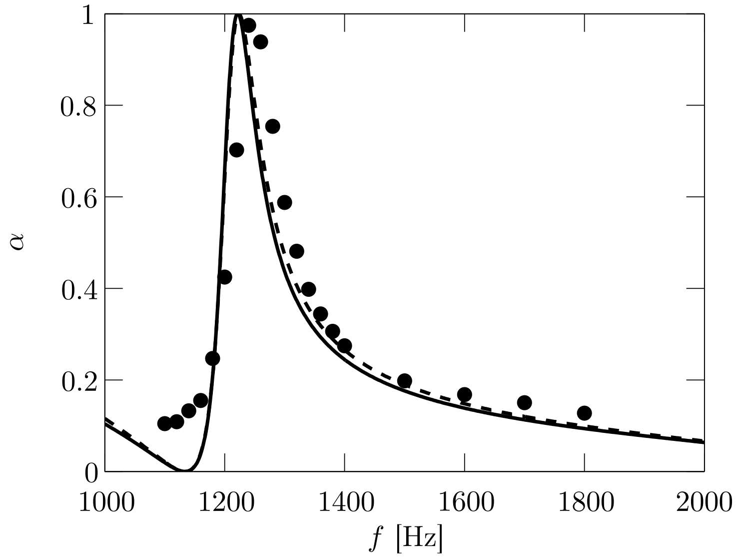

Figure 4.17: *Case 2. Evolution of the absorption coefficient* $\alpha = 1 - |R|^2$ *as a function of frequency* f *(configuration 2 in Tab. 4.4). Measurements (•) are compared to predictions obtained for* $h/a = 2$, $L = 150$ mm *and* $\mathrm{M}_c/\sigma = 2/\pi$. *Dashed line: general model (model 2 in Tab. 4.1). Solid line: high Strouhal approximation (model 2 in Tab. 4.1).*

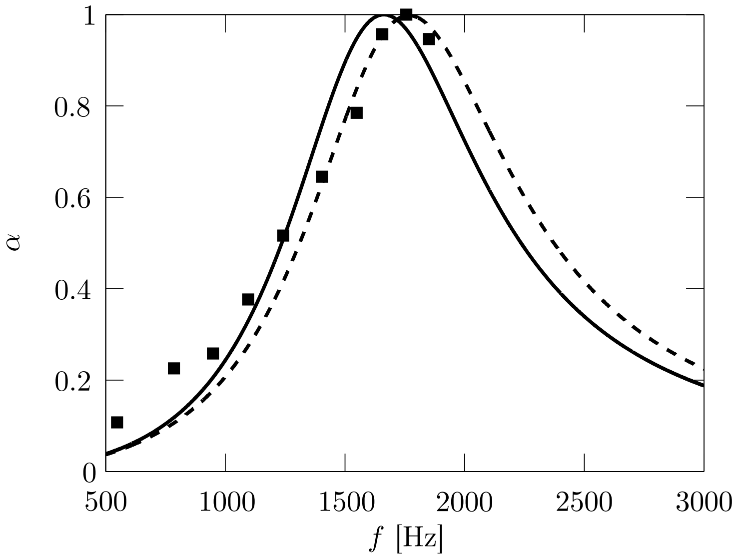

Figure 4.18: *Case 3. Evolution of the absorption coefficient* $\alpha = 1 - |R|^2$ *as a function of frequency* f *(configuration 3 in Tab. 4.4). Data extracted from Hughes and Dowling (1990) (■) are compared to the high Strouhal model (model 3 in Tab. 4.1) with* $h/a = 0$ *(solid line), and to the general model for infinitely thin plates (model 1 in Tab. 4.1, dashed line).*

$\alpha = 1 - |R|^2$ is plotted as a function of the resonance parameter Q, for a constant back cavity depth L and Mach number M_c in the orifice. Note that in this configuration the range of Strouhal numbers investigated is quite large and they take high values ($0.97 \leq \mathrm{St} \leq 5.82$, Tab. 4.4). Experimental data were extracted from Hughes and Dowling (1990) and are plotted in Fig. 4.18. These data are compared to predictions obtained with the high Strouhal approximation (model 3 in Tab. 4.1), and with the general model (model 1 in Tab. 4.1). Hughes and Dowling did not take into account the effect of plate thickness in their study, therefore these theoretical relations are computed by assuming $h/a = 0$. The agreement between both models and measurements is fairly good, although the peak absorption obtained with the high Strouhal approximation is predicted at slightly lower frequencies compared to the general model and experimental data.

In the fourth configuration explored (see Tab. 4.4), plate P_8 is replaced by plate $P_{2.5}$ traversed by a bias flow velocity $\bar{u}_0 = 8.03\ \mathrm{m\,s^{-1}}$. The size of the back cavity is here fixed to $L = 150$ mm and the response is examined between 100 and 1000 Hz. This configuration operates now in the low Strouhal regime where $0.02 \leq \mathrm{St} \leq 0.23$. The thickness ratio is here equal to $h/a = 3.33$. Measurements are presented in Fig. 4.19 for the absorption coefficient as a function of frequency. They are compared to predictions obtained with the low Strouhal

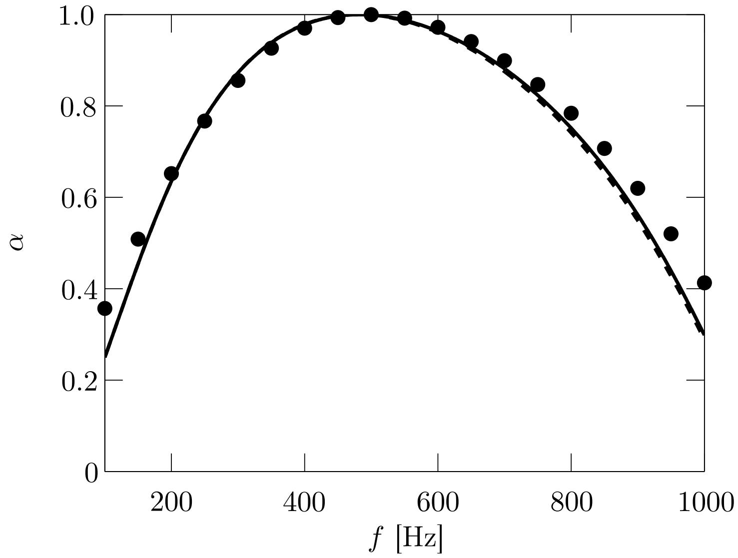

Figure 4.19: *Case 4. Evolution of the absorption coefficient* $\alpha = 1 - |R|^2$ *as a function of frequency* f *(configuration 4 in Tab. 4.4). Measurements (●) are compared to predictions obtained for* $h/a = 3.33$, $L = 150$ mm *and* $\mathrm{M}_c/\sigma = 1/2$*. Dashed line: general model (model 2 in Tab. 4.1). Solid line: low Strouhal approximation (model 4 in Tab. 4.1).*

model (model 4 in Tab. 4.1) and the general model (model 2 in Tab. 4.1). The agreement between predictions with both models and measurements is very good. The peak absorption frequency is predicted at 500 Hz and corresponds to a quarter-wave resonance. Note that in this configuration, the absorption coefficient α takes values larger than 0.8 over a 500 Hz frequency span, whereas in configurations 1 and 2 operating at higher Strouhal numbers this absorption bandwidth reduces to 330 Hz around the first peak frequency (Fig. 4.16) and to 50 Hz around the second peak frequency (Fig. 4.17) respectively.

The response of the same plate traversed by the same bias flow is now examined over the same frequency range but for a larger cavity depth $L = 300$ mm. This defines configuration 5 in Tab. 4.4, operating in the same Strouhal range $0.02 \leq \mathrm{St} \leq 0.23$ as configuration 4. Measurements of the absorption coefficient are shown in Fig. 4.20 as a function of frequency. Again, good agreement is observed between models and measurements. Doubling the back cavity size results in halving the first resonance frequency, corresponding to the first peak absorption $\alpha = 1$ found at 250 Hz. Two absorption peaks appear in this frequency range, corresponding to the quarter-wave and three-quarter-wave resonant modes at $f = 250$ Hz and $f = 800$ Hz respectively.

In conclusion to this section, perforated plates coupled to back cavities designed

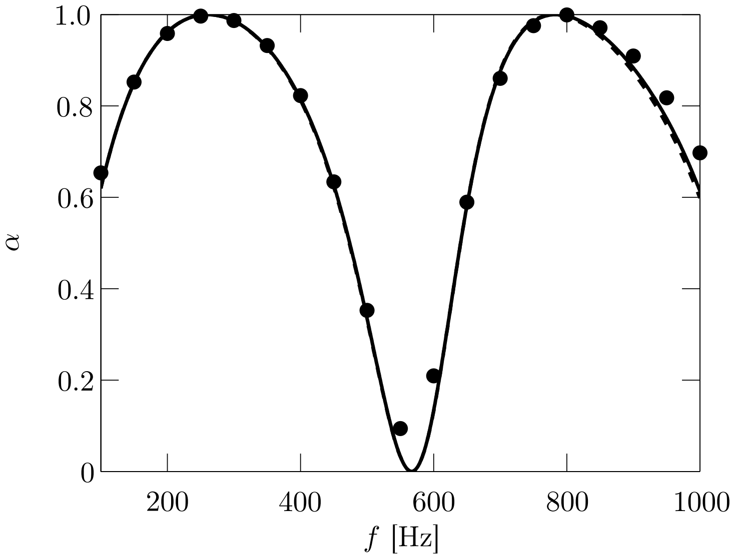

Figure 4.20: *Case 5. Evolution of the absorption coefficient* $\alpha = 1 - |R|^2$ *as a function of frequency* f *(configuration 5 in Tab. 4.4). Measurements (●) are compared to predictions obtained for* $h/a = 3.33$, $L = 300$ mm *and* $\mathrm{M}_c/\sigma = 1/2$. *Dashed line: general model (model 2 in Tab. 4.1). Solid line: low Strouhal approximation (model 4 in Tab. 4.1).*

to operate in the two limit regimes investigated in this study show satisfactory absorption properties. The possibility to achieve total absorption $\alpha = 1$ near resonances of the back cavity is demonstrated in agreement with the simplified expressions derived in the present chapter. Plates designed to work in the low Strouhal regime are, however, more robust to a change in the damping frequency, since they show larger absorption bandwidths than plates operating at high Strouhal numbers. It is now interesting to analyze the acoustic properties of these dampers under off-design conditions, when the velocity within the orifices differs from the optimal one.

4.5 Analysis at off-design flow conditions

The flow velocity within the orifices of perforates placed in a combustor may vary significantly during the operation of a gas turbine, as shown for example by Lörstad et al. (2009). In their work it was reported that the bias flow velocity in the perforations depends on the engine load and the burner pressure drop. The bias flow velocity is fixed by the pressure drop between the casing and the chamber that increases with the air flowrate breathed by the engine. When the engine speed is modified, the bias flow velocity within the perforations is in turn altered. In section 4.1 we showed how to determine the optimal bias flow velocity which maximizes the absorption coefficient. It is now worth analyzing how the damping properties are modified when the velocity within the orifices varies. The analysis is first conducted for dampers operating in the high Strouhal regime. The second regime at low Strouhal numbers is examined next.

4.5.1 Off-design operation at high Strouhal number

At the perforate design point, where $R = 0$, the two conditions Eqs. (4.5) and (4.6) hold, and the optimal bias flow velocity is given by $\bar{u}_{0,\text{opt}} = (2/\pi)\sigma c_0$ for a damper operating at high Strouhal numbers. Let now the velocity within the orifices change, all other parameters remaining constant. At this off-design condition, the actual bias flow velocity is then given by:

$$\bar{u}_{0,\text{off}} = \bar{u}_{0,\text{opt}} + \Delta u, \tag{4.18}$$

where $\bar{u}_{0,\text{opt}}$ is the optimal bias flow velocity and Δu is an additional component, not necessarily small compared to the optimal velocity in the perforations $\bar{u}_{0,\text{opt}}$. The other dimensionless parameters of interest can be written as follows:

$$\text{M}_{c,\text{off}} = \frac{\bar{u}_{0,\text{off}}}{c_0} = \frac{\bar{u}_{0,\text{opt}} + \Delta u}{c_0} = \text{M}_{c,\text{opt}} + \frac{\Delta u}{c_0} \tag{4.19}$$

$$\text{St}_{\text{off}} = \frac{\omega a}{\bar{u}_{0,\text{off}}} \tag{4.20}$$

$$\text{He}_{\text{off}} = kL = \text{He}_{\text{opt}} \tag{4.21}$$

The Helmholtz number remains unchanged since only modifications of the flow within the orifices are considered. It is worth noting that, even if the Mach number and the Strouhal number change, their product at off-design operation remains equal to the product at optimal setting:

$$\text{St}_{\text{off}}\text{M}_{c,\text{off}} = \frac{\omega a}{\bar{u}_{0,\text{off}}}\frac{\bar{u}_{0,\text{off}}}{c_0} = \frac{\omega a}{c_0} = \text{St}_{\text{opt}}\text{M}_{c,\text{opt}} \tag{4.22}$$

It was shown in section 4.2 that taking the high Strouhal limit for the Rayleigh conductivity given by Eq. (1.21), and replacing it in Eq. (1.39), one obtains the following expression for the reflection coefficient of the damper:

$$R = \frac{\left(1 - \frac{\pi}{2}\frac{\text{M}_c}{\sigma}\right) + \text{i}\left[\frac{\pi}{2}\text{St}\frac{\text{M}_c}{\sigma}\left(1 + \frac{2h}{\pi a}\right) - \frac{1}{\tan(\text{He})}\right]}{-\left(1 + \frac{\pi}{2}\frac{\text{M}_c}{\sigma}\right) + \text{i}\left[\frac{\pi}{2}\text{St}\frac{\text{M}_c}{\sigma}\left(1 + \frac{2h}{\pi a}\right) - \frac{1}{\tan(\text{He})}\right]} \tag{4.23}$$

Equations (4.21) and (4.22) imply that the imaginary components of the numerator and denominator in Eq. (4.23) are not modified when the bias flow velocity varies. One can thus write at off-design operation:

$$R_{\text{off}} = \frac{\left(1 - \frac{\pi}{2}\frac{\text{M}_{c,\text{off}}}{\sigma}\right) + \text{i}\left[\frac{\pi}{2}\text{St}_{\text{opt}}\frac{\text{M}_{c,\text{opt}}}{\sigma}\left(1 + \frac{2h}{\pi a}\right) - \frac{1}{\tan(\text{He}_{\text{opt}})}\right]}{-\left(1 + \frac{\pi}{2}\frac{\text{M}_{c,\text{off}}}{\sigma}\right) + \text{i}\left[\frac{\pi}{2}\text{St}_{\text{opt}}\frac{\text{M}_{c,\text{opt}}}{\sigma}\left(1 + \frac{2h}{\pi a}\right) - \frac{1}{\tan(\text{He}_{\text{opt}})}\right]} \tag{4.24}$$

Since at the optimal design point the reflection coefficient is equal to zero, the imaginary component of the numerator cancels out:

$$\frac{\pi}{2}\text{St}_{\text{opt}}\frac{\text{M}_{c,\text{opt}}}{\sigma}\left(1 + \frac{2h}{\pi a}\right) - \frac{1}{\tan(\text{He}_{\text{opt}})} = 0 \tag{4.25}$$

When the bias flow velocity within the orifices varies, the reflection coefficient at maximum absorption can finally be written as:

$$R_{\text{off}} = \frac{\frac{\pi}{2}\frac{\text{M}_{c,\text{off}}}{\sigma} - 1}{\frac{\pi}{2}\frac{\text{M}_{c,\text{off}}}{\sigma} + 1} \tag{4.26}$$

Replacing Eq. (4.19) in Eq. (4.26), and considering that at high Strouhal numbers $\text{M}_{c,\text{opt}} = 2\sigma/\pi$, yields:

$$R_{\text{off}} = \frac{1}{1 + 2\frac{\bar{u}_{0,\text{opt}}}{\Delta u}} \tag{4.27}$$

This relation links the reflection coefficient R_{off}, corresponding to the absorption coefficient $\alpha_{\text{off}} = 1 - |R_{\text{off}}|^2$, to the velocity variation in the orifice Δu during off-design operation. This expression is valid as long as the Strouhal number remains high when the bias flow velocity is modified.

Figure 4.21 shows the evolution of the absorption coefficient as a function of frequency for different bias flow velocities. Data where gathered for perforated plate P_8 operated in configuration 1 (Tab. 4.4) at moderate values of the Strouhal number. Configuration 1 is reached in Fig. 4.21(c) when the bias flow velocity is equal to its optimal value $\bar{u}_{0,\text{opt}} = 2.18\ \text{m}\,\text{s}^{-1}$ and $\Delta u = 0$. In Figs. 4.21(a) and 4.21(b) the velocity within the orifices is decreased by 50 % and 25 % respectively, while in Figs. 4.21(d), 4.21(e) and 4.21(f) the velocity is increased by 25 %, 50 % and 100 % with respect to its optimal value $\bar{u}_{0,\text{opt}}$. Predictions from Eq. (1.39) are superimposed, using $\bar{u}_{0,\text{off}} = \bar{u}_{0,\text{opt}} + \Delta u$. The main difference between predictions from Eq. (1.39) and measurements is that the model does not retrieve the variation of the peak absorption frequency when the bias flow velocity changes.

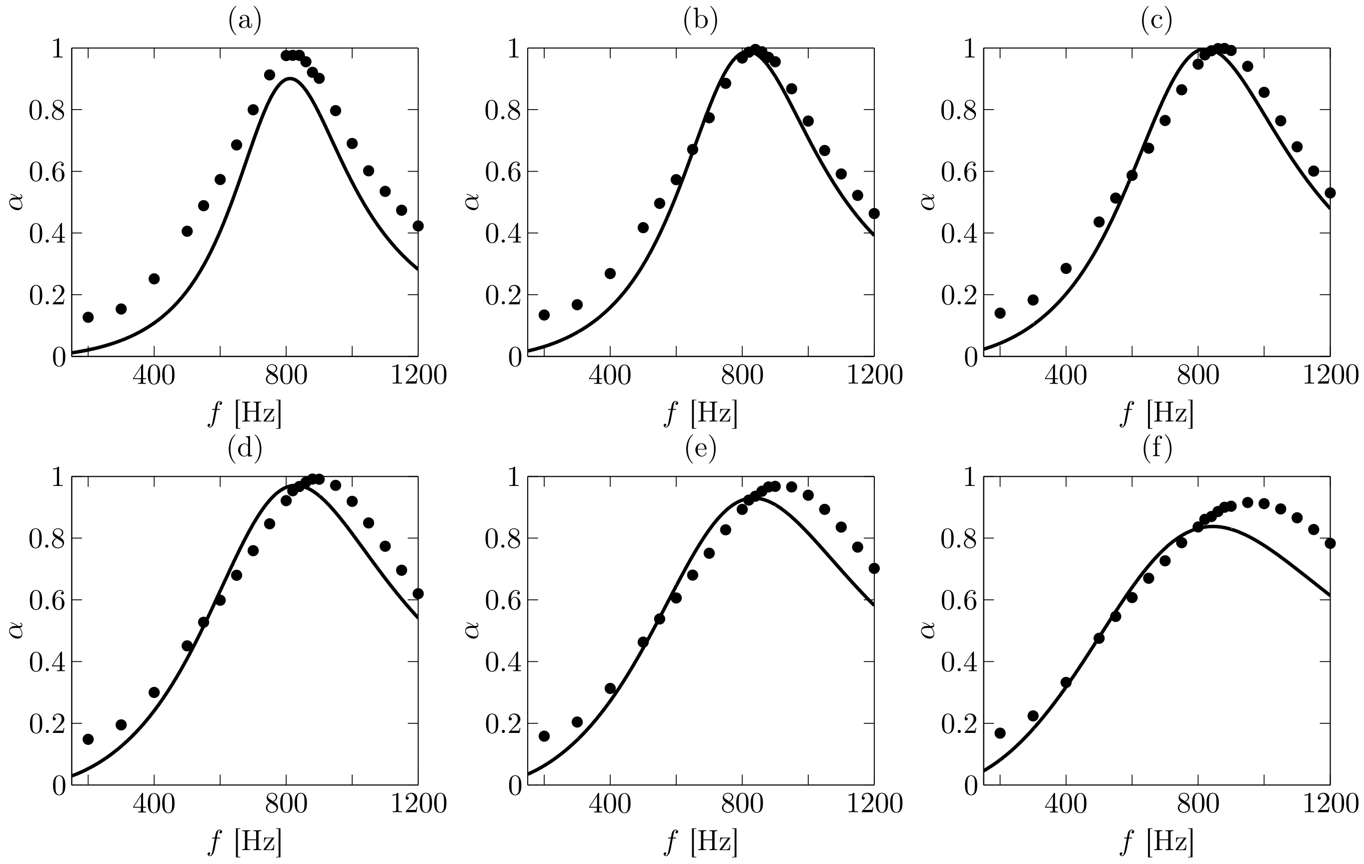

Figure 4.21: *Absorption coefficient* $\alpha = 1 - |R|^2$ *as a function of frequency* f*, for different bias flow velocities (configuration 1 in Tab. 4.4). Measurements (●) are compared to predictions from Eq. (1.39) (solid line). (a)* $\Delta u/\bar{u}_{0,\mathrm{opt}} = -0.50$*. (b)* $\Delta u/\bar{u}_{0,\mathrm{opt}} = -0.25$*. (c)* $\Delta u/\bar{u}_{0,\mathrm{opt}} = 0$*. (d)* $\Delta u/\bar{u}_{0,\mathrm{opt}} = 0.25$*. (e)* $\Delta u/\bar{u}_{0,\mathrm{opt}} = 0.50$*. (f)* $\Delta u/\bar{u}_{0,\mathrm{opt}} = 1.00$*.*

The measurements shown in Fig. 4.21 are represented in Fig. 4.22 in a compact form. The absorption coefficient is plotted as a function of frequency and relative bias flow velocity difference. The peak absorption frequency slightly increases when the bias flow in the orifices increases. Good absorption properties are still achieved over all the off-design conditions explored, however both the peak absorption and the absorption bandwidth are reduced for $\Delta u/\bar{u}_{0,\mathrm{opt}} \geq 0.50$.

It is possible to extract from these measurements values of the maximum absorption coefficient α_{off} and the corresponding peak absorption frequency f_{off}. Figure 4.23(a) shows a comparison between predictions from Eq. (4.27) and measurements of the maximum absorption coefficient α_{off} as a function of the relative bias flow velocity difference $\Delta u/\bar{u}_{0,\mathrm{opt}}$ with respect to the optimal value $\bar{u}_{0,\mathrm{opt}}$. The fairly good agreement between predictions and measurements validates the model enabling to retrieve modifications of maximum absorption even for large differences of the bias flow velocity with respect to its optimal value. For relative differences up to 100 % of the optimal bias flow velocity, the maximum absorption coefficient α_{off} is still larger than 0.9. The model slightly underestimates maximum absorption in off-design operation, particularly when the velocity within the orifices decreases. In Fig. 4.23(b) the peak absorption frequency f_{off} plotted as a function of the relative bias flow velocity difference $\Delta u/\bar{u}_{0,\mathrm{opt}}$ increases by about 100 Hz when the velocity within the orifice increases from its optimal value to twice this value. This behavior is not predicted by the off-design analysis developed in this study, but can be interpreted as follows. The model developed is only valid for high Strouhal numbers, while measurements were conducted here at moderate values of the Strouhal numbers, around configuration 1 where $0.14 \leq \mathrm{St} \leq 1.73$ (Tab. 4.4). It was not possible to operate the setup ITHACA at larger Strouhal values with this configuration. This explains the differences observed between predictions of the peak absorption frequency and measurements in Fig. 4.23(b). This phenomenon is reinforced when the bias flow velocity increases because the Strouhal number is further reduced.

Off-design operation with plate P_8 is now examined at higher frequencies corresponding to a higher range of Strouhal numbers covered around configuration 2 (Tab. 4.4). The absorption coefficient is plotted as a function of frequency in Fig. 4.24, for different bias flow velocities. Figure 4.24(c) shows results for the optimal bias flow velocity $\bar{u}_{0,opt} = 2.18\ \mathrm{m\,s^{-1}}$ when $\Delta u = 0$ defining configuration 2 in Tab. 4.4. The range of Strouhal numbers covered in these experiments is slightly larger than for the previous exploration with plate P_8 around configuration 1. Modification of the bias flow velocity is limited here to $\Delta u/\bar{u}_{0,opt} = \pm 50\,\%$. Predictions for off-design conditions presented in Fig. 4.24(a), 4.24(b), 4.24(d) and 4.24(e), when the bias flow velocity is lower or larger than the optimal value, match well measurements.

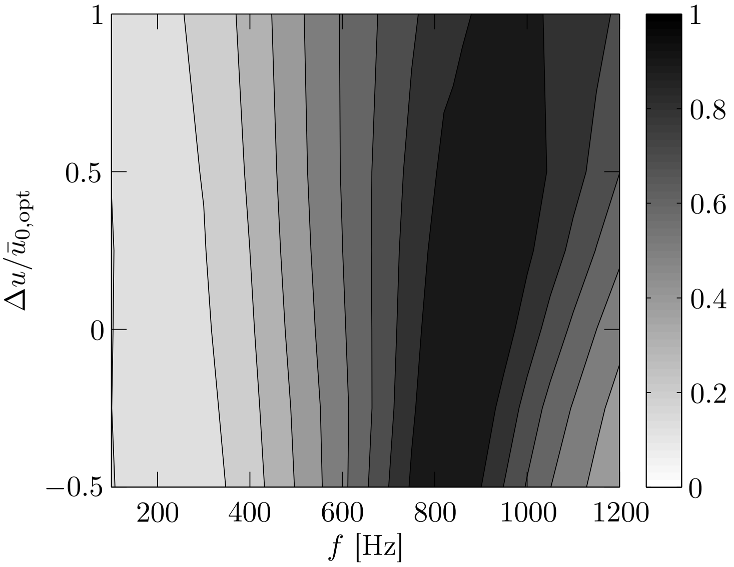

Figure 4.22: *Evolution of the absorption coefficient* $\alpha = 1 - |R|^2$ *as a function of frequency* f *and relative bias flow velocity difference* $\Delta u/\bar{u}_{0,\mathrm{opt}}$ *around configuration 1 in Tab. 4.4. Configuration 1 is reached for* $\Delta u = 0$.

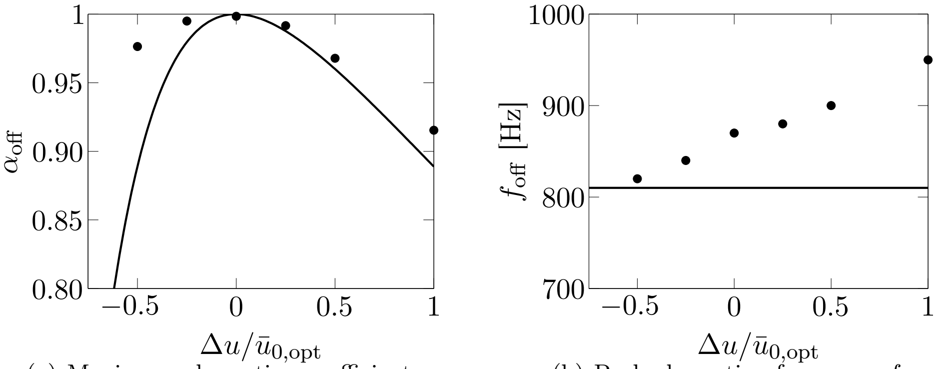

(a) Maximum absorption coefficient α_{off}. (b) Peak absorption frequency f_{off}.

Figure 4.23: *Evolution of the maximum absorption coefficient* $\alpha_{\mathrm{off}} = 1 - |R_{\mathrm{off}}|^2$ *(a) and of the peak absorption frequency* f_{off} *(b) as a function of the relative velocity difference* $\Delta u/\bar{u}_{0,\mathrm{opt}}$ *with respect to the optimal bias flow velocity. Configuration 1 in Tab. 4.4 is reached when* $\Delta u = 0$*. Measurements (●) are compared to predictions from Eq. (4.27) valid in the high Strouhal limit (solid line).*

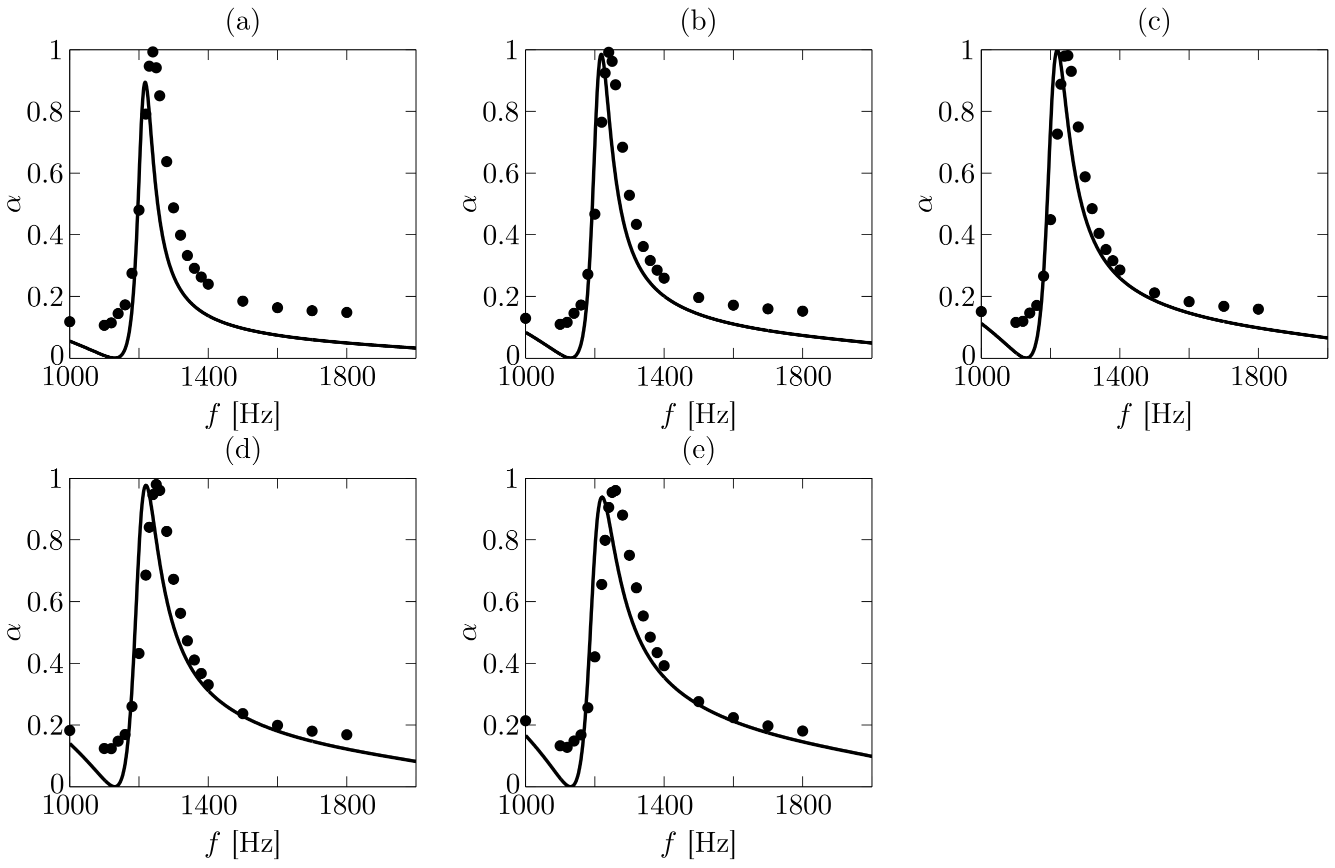

Figure 4.24: *Absorption coefficient* $\alpha = 1 - |R|^2$ *as a function of frequency* f*, for different bias flow velocities (configuration 2 in Tab. 4.4). Measurements (●) are compared to predictions from Eq. (1.39) (solid line). (a)* $\Delta u/\bar{u}_{0,\mathrm{opt}} = -0.50$*. (b)* $\Delta u/\bar{u}_{0,\mathrm{opt}} = -0.25$*. (c)* $\Delta u/\bar{u}_{0,\mathrm{opt}} = 0$*. (d)* $\Delta u/\bar{u}_{0,\mathrm{opt}} = 0.25$*. (e)* $\Delta u/\bar{u}_{0,\mathrm{opt}} = 0.50$*.*

These results are summarized in Fig. 4.25. The absorption coefficient is plotted as a function of frequency and relative bias flow velocity difference. In this case the peak absorption frequency remains constant while the bias flow velocity in the orifices increases. Good absorption properties are still achieved over the whole bias flow velocity range explored.

Figures 4.26(a) and 4.26(b) show respectively the evolution of the maximum absorption coefficient and the peak absorption frequency as a function of $\Delta u/\bar{u}_{0,\mathrm{opt}}$. The maximal value of the absorption coefficient remains larger than $\alpha_{\mathrm{off}} \geq 0.95$ when $\Delta u/\bar{u}_{0,\mathrm{opt}} \leq \pm 50\,\%$. A good agreement between measurements and the model Eq. (4.27) is achieved, especially for bias flow velocities higher than the optimal one. The peak absorption frequency is again slightly shifted with respect to predictions, but the difference is less than 20 Hz for a measured peak frequency of 1240 Hz. The predicted peak frequency at off-design conditions also slightly increases with Δu by less than 20 Hz over the range of Δu explored.

4.5.2 Off-design operation at low Strouhal number

A similar analysis is now carried out for dampers operating in the low Strouhal regime. The reflection coefficient given by Eq. (1.39) can in this case be rewritten using the low Strouhal approximation of the Rayleigh conductivity Eq. (1.20). One finds here:

$$R = \frac{\left(1 - 2\dfrac{\mathrm{M}_c}{\sigma}\right) + \mathrm{i}\left[\dfrac{\pi}{2}\mathrm{St}\dfrac{\mathrm{M}_c}{\sigma}\left(\dfrac{16}{3\pi^2} + \dfrac{2h}{\pi a}\right) - \dfrac{1}{\tan(\mathrm{He})}\right]}{-\left(1 + 2\dfrac{\mathrm{M}_c}{\sigma}\right) + \mathrm{i}\left[\dfrac{\pi}{2}\mathrm{St}\dfrac{\mathrm{M}_c}{\sigma}\left(\dfrac{16}{3\pi^2} + \dfrac{2h}{\pi a}\right) - \dfrac{1}{\tan(\mathrm{He})}\right]} \tag{4.28}$$

This expression is similar to Eq. (4.23). We thus follow here the same procedure developed in section 4.5.1. Noting that, once again, the imaginary components of the numerator and denominator in Eq. (4.28) are independent of the bias flow velocity, one finally obtains:

$$R_{\mathrm{off}} = \frac{2\dfrac{\mathrm{M}_{c,\mathrm{off}}}{\sigma} - 1}{2\dfrac{\mathrm{M}_{c,\mathrm{off}}}{\sigma} + 1} = \frac{1}{1 + 2\dfrac{\bar{u}_{0,\mathrm{opt}}}{\Delta u}} \tag{4.29}$$

Equation (4.29), obtained with the low Strouhal approximation, is formally the same as Eq. (4.27) obtained in the high Strouhal limit. The only difference lies in the value of the optimal velocity, which is now given by $\bar{u}_{0,\mathrm{opt}} = (1/2)\sigma c_0$ at low Strouhal numbers.

Predictions from Eq. (4.29) are examined for plate $P_{2.5}$ operating at off-design conditions around configurations 4 and 5 given by Tab. 4.4. Results are gathered in Figs. 4.27 to 4.32 where the range of bias flow velocities explored was

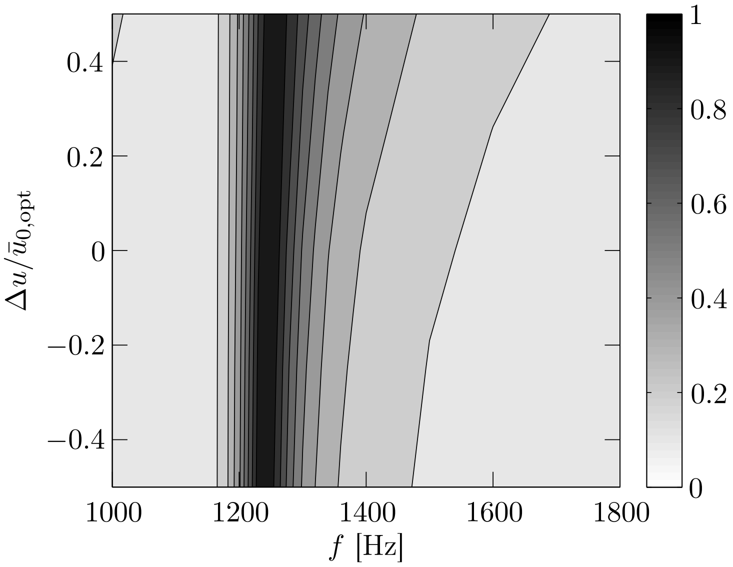

Figure 4.25: *Evolution of the absorption coefficient* $\alpha = 1 - |R|^2$ *as a function of frequency* f *and relative bias flow velocity difference* $\Delta u/\bar{u}_{0,\mathrm{opt}}$ *around configuration 2 in Tab. 4.4. Configuration 2 is reached for* $\Delta u = 0$.

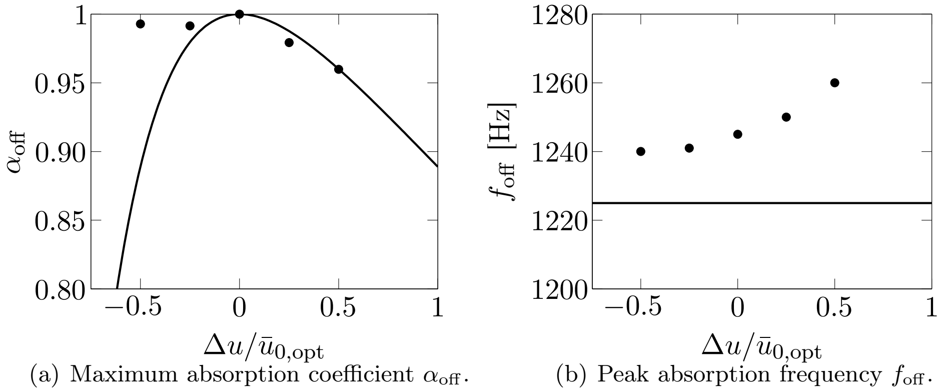

(a) Maximum absorption coefficient α_{off}. (b) Peak absorption frequency f_{off}.

Figure 4.26: *Evolution of the maximum absorption coefficient* $\alpha_{\mathrm{off}} = 1 - |R_{\mathrm{off}}|^2$ *(a) and of the peak absorption frequency* f_{off} *(b) as a function of the relative velocity difference* $\Delta u/\bar{u}_{0,\mathrm{opt}}$ *with respect to the optimal bias flow velocity. Configuration 2 in Tab. 4.4 is reached when* $\Delta u = 0$. *Measurements (●) are compared to predictions from Eq. (4.27) valid in the high Strouhal limit (solid line).*

varied from $\Delta u/\bar{u}_{0,\mathrm{opt}} = -0.5$ to $\Delta u/\bar{u}_{0,\mathrm{opt}} = 1$ around the optimal value $\bar{u}_{0,\mathrm{opt}} = (1/2)\sigma c_0 = 8.03\ \mathrm{m\,s^{-1}}$, all other parameters remaining unchanged.

Measurements match always well predictions from Eq. (4.29), even when the perforated plate is operated with a bias flow velocity far from its optimal value, except that in all the configurations explored, the maximum absorption coefficient was always slightly underestimated by the model. Measurements also show that the peak value of the absorption coefficient takes values higher than 0.9 for bias flow velocities varying from -50 % to +100 % from its optimum, with negligible variation of the peak absorption frequency. It is interesting to examine the variation of the absorption bandwidth around the peak absorption frequency when the bias flow velocity in the orifices varies. Figures 4.28 and 4.31 show the evolution of the absorption coefficient as a function of both the frequency and the relative bias flow velocity difference $\Delta u/\bar{u}_{0,\mathrm{opt}}$. From these contour plots it is possible to observe that the absorption bandwidth increases for increasing bias flow velocities, in the range $-0.50 \leq \Delta u/\bar{u}_{0,\mathrm{opt}} \leq 0$. The peak absorption also increases, in agreement with predictions from Eq. (4.29) and measurements (Figs. 4.29(a), 4.32(a) and 4.32(a)). It then reaches its maximal value for velocities close to the optimal bias flow velocity, corresponding to $\Delta u/\bar{u}_{0,\mathrm{opt}} = 0$, and remains constant for $0 \leq \Delta u/\bar{u}_{0,\mathrm{opt}} \leq 0.50$. At higher velocities, the absorption bandwidth slightly decreases.

These observations and predictions confirm that operating at low Strouhal numbers with a quarter-wave resonator as a back cavity not only enables to obtain a wide absorption bandwidth around the peak frequency, but also offers robust absorption properties when the bias flow velocity varies around its optimum value. These devices constitute thus attractive and flexible solutions to design robust dampers for combustion instabilities even though their use in combustion chambers was yet limited to generic combustor test rigs [Tran et al. (2009a); Tran et al. (2009b)].

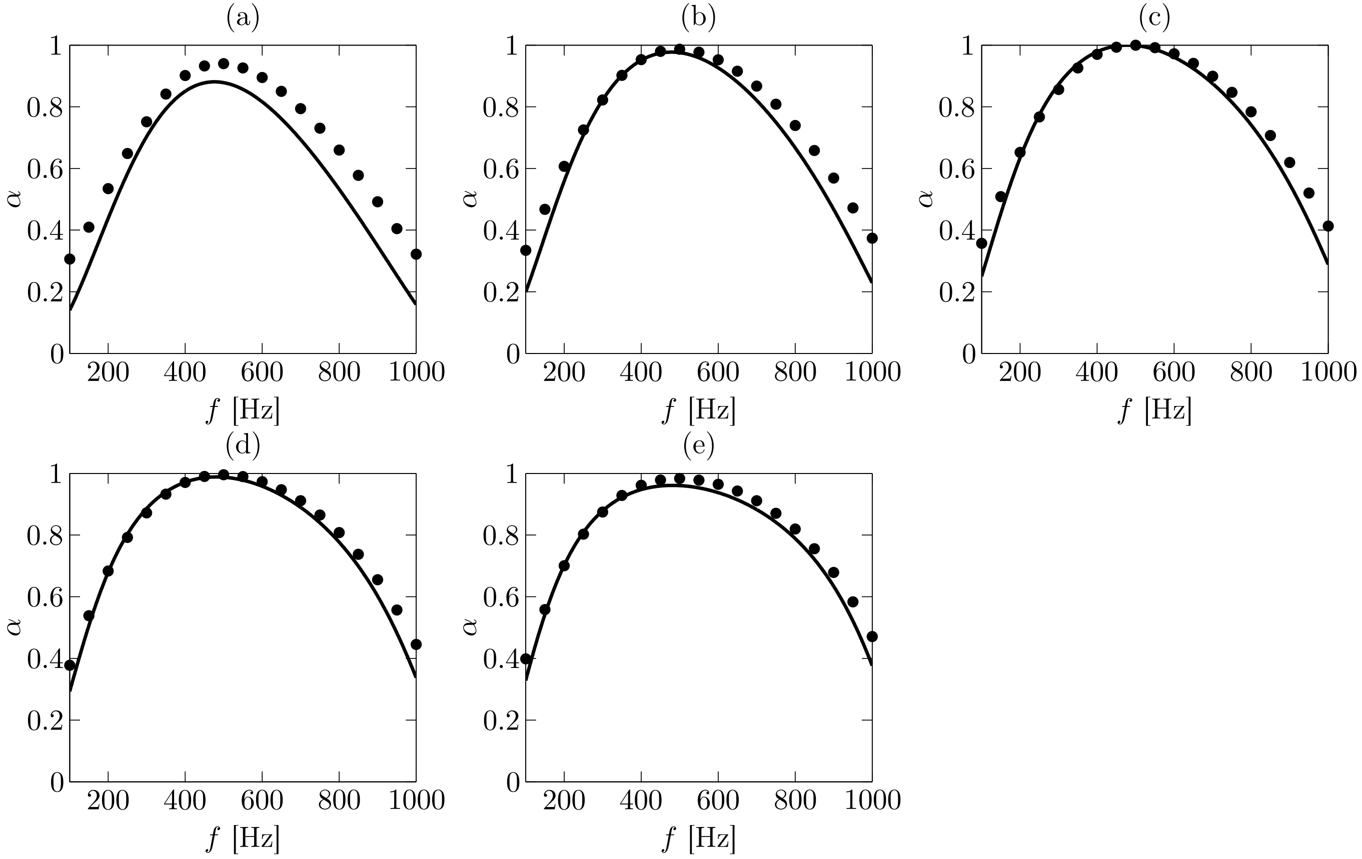

Figure 4.27: *Absorption coefficient* $\alpha = 1 - |R|^2$ *as a function of frequency* f*, for different bias flow velocities (configuration 4 in Tab. 4.4). Measurements (●) are compared to predictions from Eq. (1.39) (solid line). (a)* $\Delta u/\bar{u}_{0,\mathrm{opt}} = -0.50$*. (b)* $\Delta u/\bar{u}_{0,\mathrm{opt}} = -0.25$*. (c)* $\Delta u/\bar{u}_{0,\mathrm{opt}} = 0$*. (d)* $\Delta u/\bar{u}_{0,\mathrm{opt}} = 0.25$*. (e)* $\Delta u/\bar{u}_{0,\mathrm{opt}} = 0.50$*.*

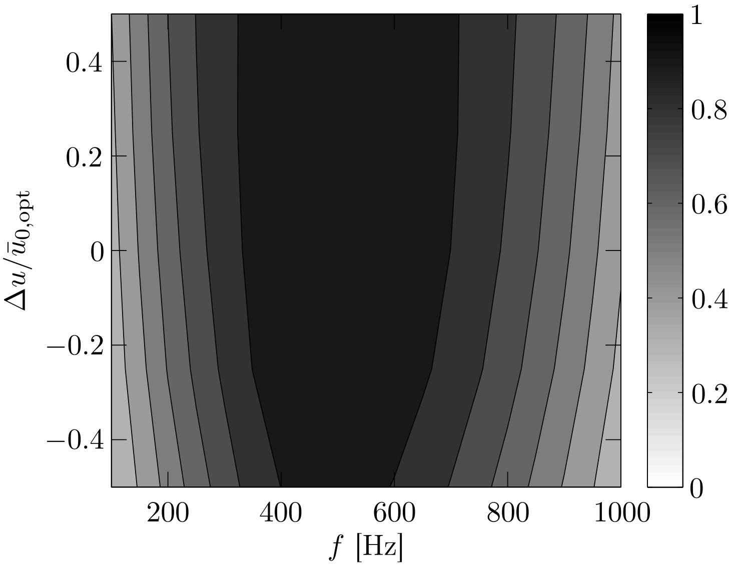

Figure 4.28: *Evolution of the absorption coefficient* $\alpha = 1 - |R|^2$ *as a function of frequency* f *and relative bias flow velocity difference* $\Delta u/\bar{u}_{0,\mathrm{opt}}$ *around configuration 4 in Tab. 4.4. Configuration 4 is reached for* $\Delta u = 0$.

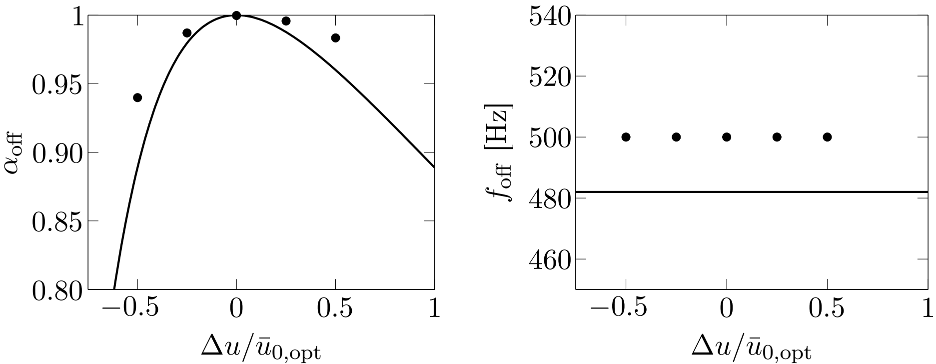

(a) Maximum absorption coefficient α_{off}.

(b) Peak absorption frequency f_{off}.

Figure 4.29: *Evolution of the maximum absorption coefficient* $\alpha_{\mathrm{off}} = 1 - |R_{\mathrm{off}}|^2$ *(a) and of the peak absorption frequency* f_{off} *(b) as a function of the relative velocity difference* $\Delta u/\bar{u}_{0,\mathrm{opt}}$ *with respect to the optimal bias flow velocity. Configuration 4 in Tab. 4.4 is reached when* $\Delta u = 0$*. Measurements (●) are compared to predictions from Eq. (4.29) valid in the low Strouhal limit (solid line).*

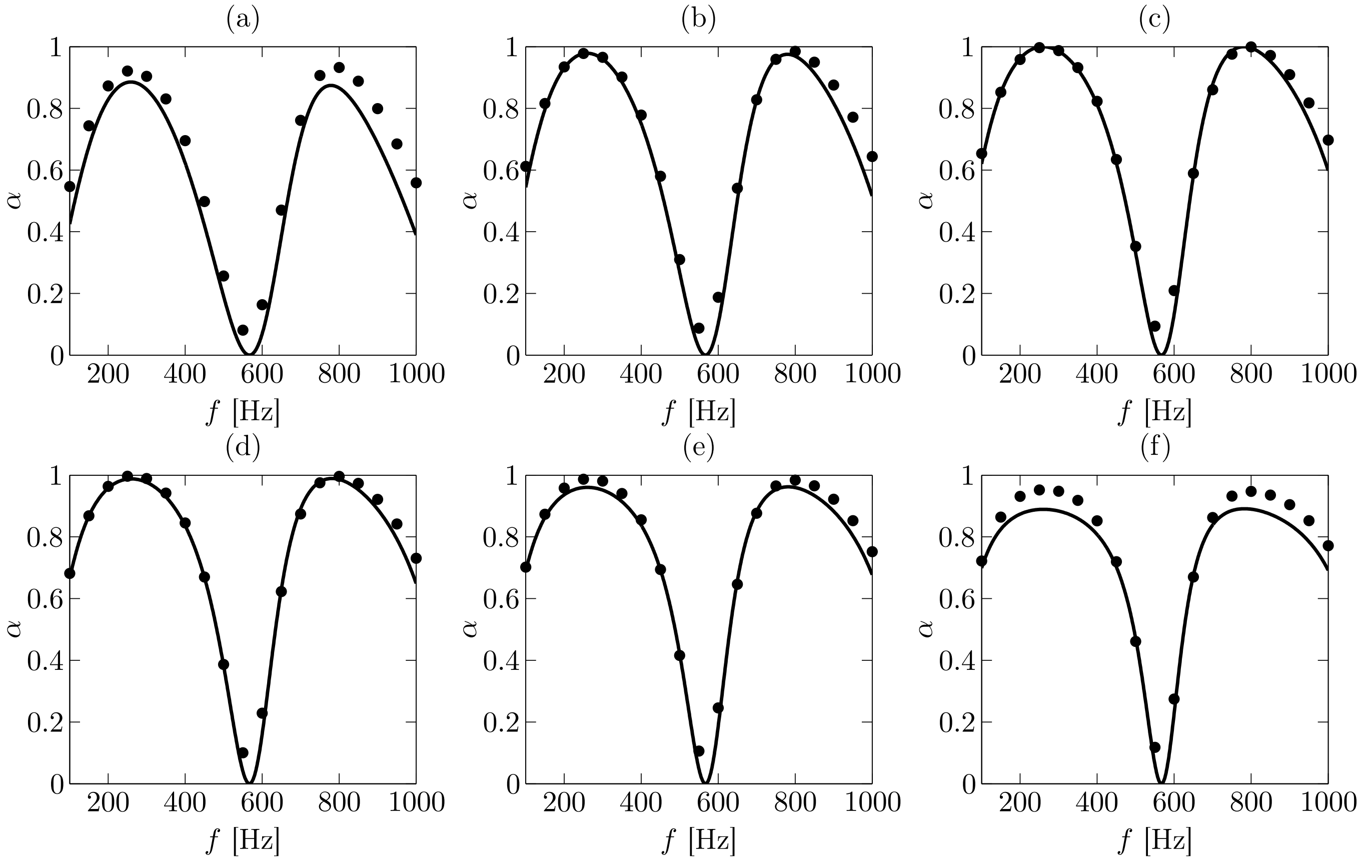

Figure 4.30: *Absorption coefficient* $\alpha = 1 - |R|^2$ *as a function of frequency* f*, for different bias flow velocities (configuration 5 in Tab. 4.4). Measurements (●) are compared to predictions from Eq. (1.39) (solid line). (a)* $\Delta u/\bar{u}_{0,\mathrm{opt}} = -0.50$*. (b)* $\Delta u/\bar{u}_{0,\mathrm{opt}} = -0.25$*. (c)* $\Delta u/\bar{u}_{0,\mathrm{opt}} = 0$*. (d)* $\Delta u/\bar{u}_{0,\mathrm{opt}} = 0.25$*. (e)* $\Delta u/\bar{u}_{0,\mathrm{opt}} = 0.50$*. (f)* $\Delta u/\bar{u}_{0,\mathrm{opt}} = 1.00$*.*

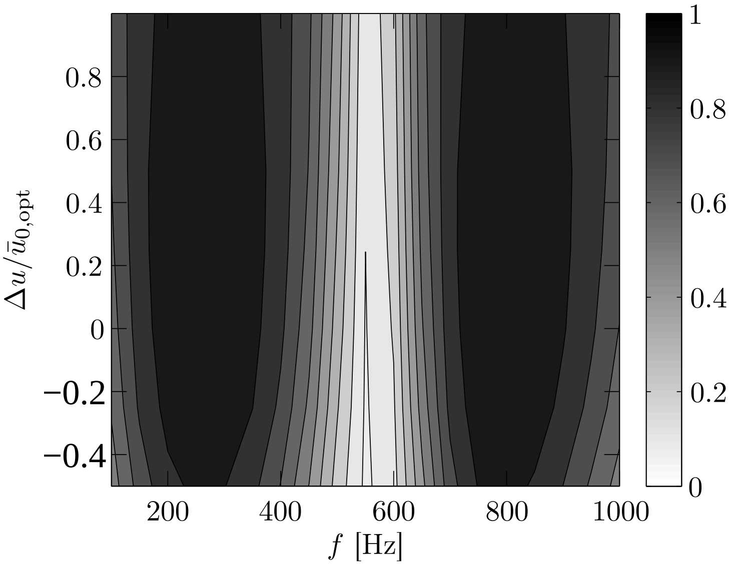

Figure 4.31: *Evolution of the absorption coefficient* $\alpha = 1 - |R|^2$ *as a function of frequency* f *and relative bias flow velocity difference* $\Delta u/\bar{u}_{0,\mathrm{opt}}$ *around configuration 5 in Tab. 4.4. Configuration 5 is reached for* $\Delta u = 0$*.*

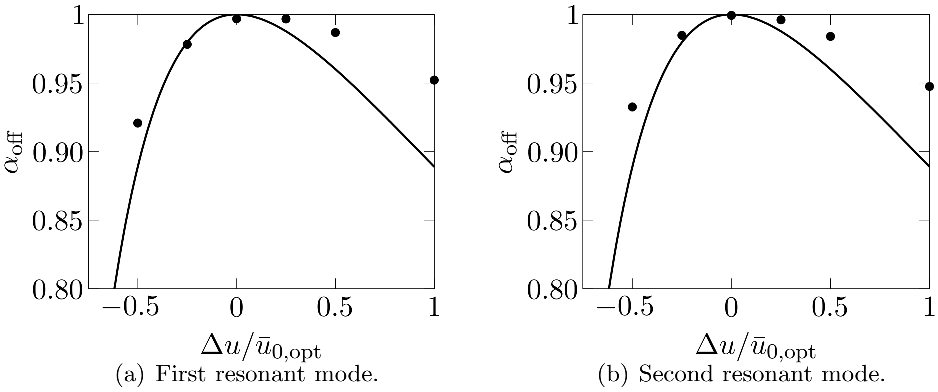

(a) First resonant mode. (b) Second resonant mode.

Figure 4.32: *Evolution of the maximum absorption coefficient* $\alpha_{\mathrm{off}} = 1 - |R_{\mathrm{off}}|^2$ *as a function of the relative velocity difference* $\Delta u/\bar{u}_{0,\mathrm{opt}}$ *with respect to the optimal bias flow velocity. Configuration 5 in Tab. 4.4 is reached when* $\Delta u = 0$*. Measurements (●) are compared to predictions from Eq. (4.29) valid in the low Strouhal limit (solid line). (a) First resonant mode. (b) Second resonant mode.*

4.6 Conclusion

Two different asymptotic absorption regimes for perforates backed by a cavity were analyzed as a function of the Strouhal number reached by the bias flow in the orifices when the damper is submitted to acoustic disturbances. In both low and high Strouhal limits, it was demonstrated that the optimal bias flow velocity leading to a cancellation of the reflection coefficient is solely fixed by the plate porosity. Analytical expressions were derived in these cases for the optimal bias flow velocity. It is possible in these regimes to separately adjust the back cavity depth to minimize the reflection coefficient at a certain frequency without changing the bias flow velocity. The expressions derived in this analysis take also into account the finite thickness of the plate.

Optimal absorption is reached for a Helmholtz resonance of the back cavity at high Strouhal numbers. It is possible with such device featuring a very short back cavity to cancel the reflection coefficient at a specific frequency, but the absorption bandwidth around the peak absorption frequency is narrow, and its width reduces drastically as the Strouhal number increases.

In applications where a large absorption frequency bandwidth is desirable, it can be interesting to work in the low Strouhal regime. This regime features a wider absorption bandwidth, making it an attractive choice for the design of robust dampers. In this case, optimal absorption is reached when the back cavity operates as a quarter-wave resonator, and the damper requires a larger size compared to a Helmholtz resonator.

The acoustic response of these dampers was also investigated at off-design conditions, when the bias flow velocity deviates from its optimum value for which it was designed. The maximal value of the absorption coefficient was shown to remain higher than 0.9, for bias flow velocity variations of up to 100 % of the nominal value. When the velocity within the orifices increases, it was observed that the peak absorption frequency slightly increases. Comparisons between predictions and measurements at both low and high Strouhal regimes validate the expressions proposed in this chapter, which offer a simple theoretical framework to ease the design of robust and flexible dampers for small pressure perturbation levels.

It is now worth analyzing the absorption properties when the sound level increases. These conditions can be found for instance during thermo-acoustic oscillations in gas turbines.

Chapter 5

Amplitude effects on the acoustic properties of perforates

When the amplitude of acoustic velocity fluctuations in the perforation becomes comparable to the mean bias flow velocity, or exceeds it, $u_0' \geq \bar{u}_0$, the response of the perforated plate deviates from its linear response. In this case the amplitude of the acoustic perturbations must be taken into account when attempting to model the acoustic behavior of the orifice. The plate operates in the nonlinear regime.

In the previous chapters, the response of perforated plates traversed by a bias flow and subjected to incident acoustic waves of low to moderate acoustic amplitudes has been analyzed. The objective of the present chapter is to analyze the transition between linear and nonlinear regimes in the sound absorption process and to improve theoretical models in the nonlinear regime for the design of robust damping systems at high sound pressure levels.

This difficult problem is first addressed with direct simulations, that are used to analyze the flow field through the aperture as a function of the perturbation level in section 5.1. It is shown that the velocity fluctuation level u_0' within the perforation plays a key role in the dissipation process linked to flow dynamics and acoustics. A transition occurs when u_0' exceeds the mean bias flow velocity within the orifice $u_0' > \bar{u}_0$ and periodical reverse flow is observed. Based on observations made on the numerical results, two analytical models taking into account nonlinear effects are developed and analyzed in section 5.2. The reflection, transmission and absorption coefficients of the configuration examined in the simulations are inferred and compared to theoretical predictions and to experimental results in section 5.3.

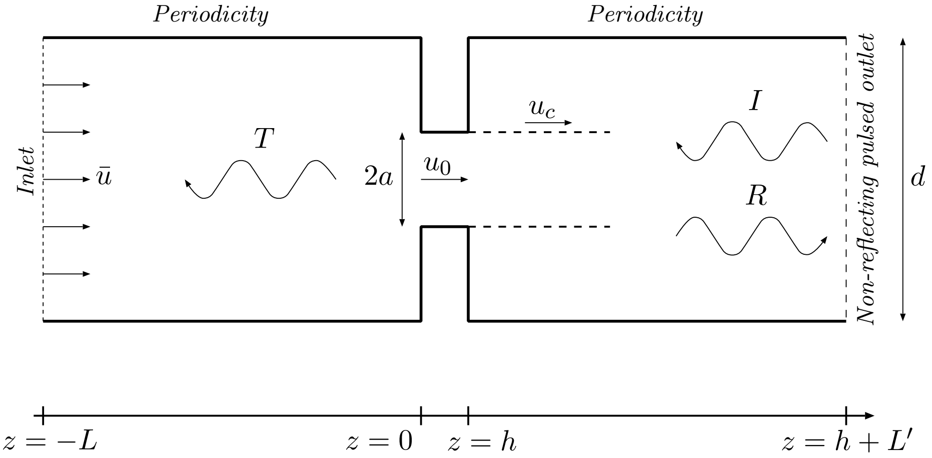

Figure 5.1: *Schematic view of the computational domain. A mean flow passes through the orifice from left to right in this figure. Acoustic modulation is imposed on the right boundary condition.*

5.1 Analysis of numerical simulations

The present section aims at describing the change in the response of a perforated plate from linear to nonlinear regime, when it is subjected to incident acoustic waves of increasing amplitudes at a given forcing frequency. Three-dimensional direct simulations are used to explore the unsteady flow through an orifice at isothermal ambient conditions, allowing a detailed analysis of the flow dynamics near the orifice, which is difficult to obtain with simplified models.

The simulations carried out have been introduced in chapter 3, and only a brief description of the calculated configuration is presented here. A single circular aperture of diameter $2a = 1$ mm in a square-section of size $d = 6$ mm and thickness $h = 1$ mm is considered. The numerical domain is sketched in Fig. 5.1. This solid wall geometry corresponds to plate P_6, introduced in chapter 2. A steady flow passes through the orifice with a mean bias velocity $\bar{u}_0 = 3.40\ \mathrm{m\,s^{-1}}$ at ambient temperature and pressure.

A uniform flow is injected through the inlet boundary condition. The impedance of this boundary condition can be modified. It is set to a non-reflecting condition to simulate the response of an orifice to sound waves in an infinite length duct. It can also be set to a velocity node to simulate the presence of a back cavity with a solid rigid wall. This velocity node simulating the presence of a rigid wall closing the back cavity modifies the sound field upstream the perforation, and results in a modification of the specific impedance of the perforated plate, and thus in a variation of the reflection, transmission and absorption coefficients, as shown in chapter 1. However, this boundary condition being located very far from the orifice at a distance $L/a = 300$ upstream of the perforation,

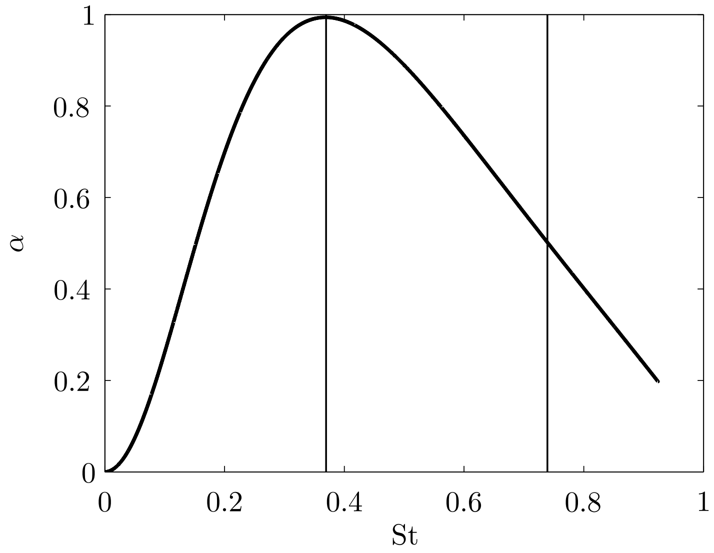

Figure 5.2: *Absorption coefficient of perforated plate P_6 backed by a cavity of size $L = 150$ mm, as predicted by the linear theory at the conditions calculated in the numerical simulations. The Strouhal numbers corresponding to the forcing frequencies chosen for the numerical simulations are highlighted by vertical lines.*

its effect on the unsteady flow field through the aperture is negligible. In the following sections, we will differentiate the simulations by indicating "with back cavity" and "without back cavity" when calculating the acoustic coefficients.

The incident pressure wave at the outlet of the numerical domain is imposed with harmonic modulations of increasing amplitudes. Eight modulation levels have been simulated, ranging from SPL = 90 to 160 dB, corresponding to acoustic pressure amplitudes varying from 0.89 to 2828 Pa. Two forcing frequencies $f = 400$ Hz and $f = 800$ Hz have been chosen to simulate the response of plate P_6 backed by a cavity of size $L = 150$ mm. Figure 5.2 indicates that at $f = 400$ Hz, corresponding to $\mathrm{St} = \omega a/\bar{u}_0 = 0.37$, the system operates close to optimal absorption in the linear regime. At $f = 800$ Hz, $\mathrm{St} = \omega a/\bar{u}_0 = 0.74$, the absorption coefficient is reduced to approximately $\alpha \simeq 0.5$. The lateral boundaries of the numerical domain are modeled as periodic conditions to simulate an array of perforations on a plate.

Figures 5.3 to 5.6 show the temporal evolution of the axial velocity field in the vicinity of the perforation during a forcing cycle, for different excitation conditions. Note that in these figures, only a fraction of the numerical domain is represented upstream and downstream of the orifice over a distance $x/a = 30$. The numerical domain extends up to $L'/a = 120$ downstream the aperture, and up to $L/a = 300$ in the upstream direction. In these images, the mean flow is oriented from the bottom to the top. Flow separation takes place at the edges of the aperture, and a jet is formed in the downstream direction. A three-dimensional isocontour of the Q-criterion [Jeong and Hussain (1995)] is also superposed to the velocity field to highlight a vortex ring swept away from the orifice when the acoustic perturbation impinges on the plate.

5.1.1 Flow description in the linear regime

Before examining any high amplitude modulation case, it is necessary (and interesting) to verify the code ability to properly simulate low amplitude situations. In Fig. 5.3 a moderate perturbation level is applied at the outlet of the domain, corresponding to an incident sound level SPL = 110 dB at this location, at a fixed frequency of $f = 400$ Hz. The acoustic perturbation incident on the jet generates a convective modulation of the velocity field in the direction of the flow synchronized by the forcing frequency. These fluctuations are only visible on the jet flowing through the aperture downstream of the perforation. The flow field upstream of the plate is not affected by these perturbations during the modulation cycle and remains constant. The flow remains axisymmetric during the forcing cycle.

The velocity wave is swept away by the mean flow downstream of the plate and is then dissipated by turbulence at large distance from the orifice. We will show later that, by following the instantaneous position of the maximal vorticity magnitude $x_{\text{vort}}(t)$ in the vortex ring at the different phases during a forcing cycle, these vorticity disturbances triggered by the acoustic waves are convected at an average velocity $\bar{u}_c$ approaching that of the mean flow $\bar{u}_0$:

$$\bar{u}_c = \overline{\left(\frac{\Delta x_{\text{vort}}}{\Delta t}\right)} \simeq \bar{u}_0 \tag{5.1}$$

This behavior is in agreement with the scenario proposed to model the response of an orifice in the linear regime [Howe (1979); Howe (1998)], which was used throughout this work to derive different analytical models (see chapter 4).

Figure 5.4 shows the velocity field when the perforation is subjected to an acoustic wave of the same amplitude SPL = 110 dB, but at a higher frequency $f = 800$ Hz. The situation is similar to the one observed at $f = 400$ Hz, and the sound wave impinging on the plate generates a vortex ring, which is convected downstream of the aperture at a constant velocity $\bar{u}_c \simeq \bar{u}_0$. Note that the distance traveled by the vortex ring during the forcing cycle at $f = 800$ Hz is approximately half the distance traveled at $f = 400$ Hz, but since the acoustic period is also halved, the convection velocity u_c is the same. The higher forcing frequency implies that the train of vortex rings generated during successive acoustic cycles is more compact, and the coherent structures are dissipated closer to the perforation compared to the previous case at $f = 400$ Hz shown in Fig. 5.3.

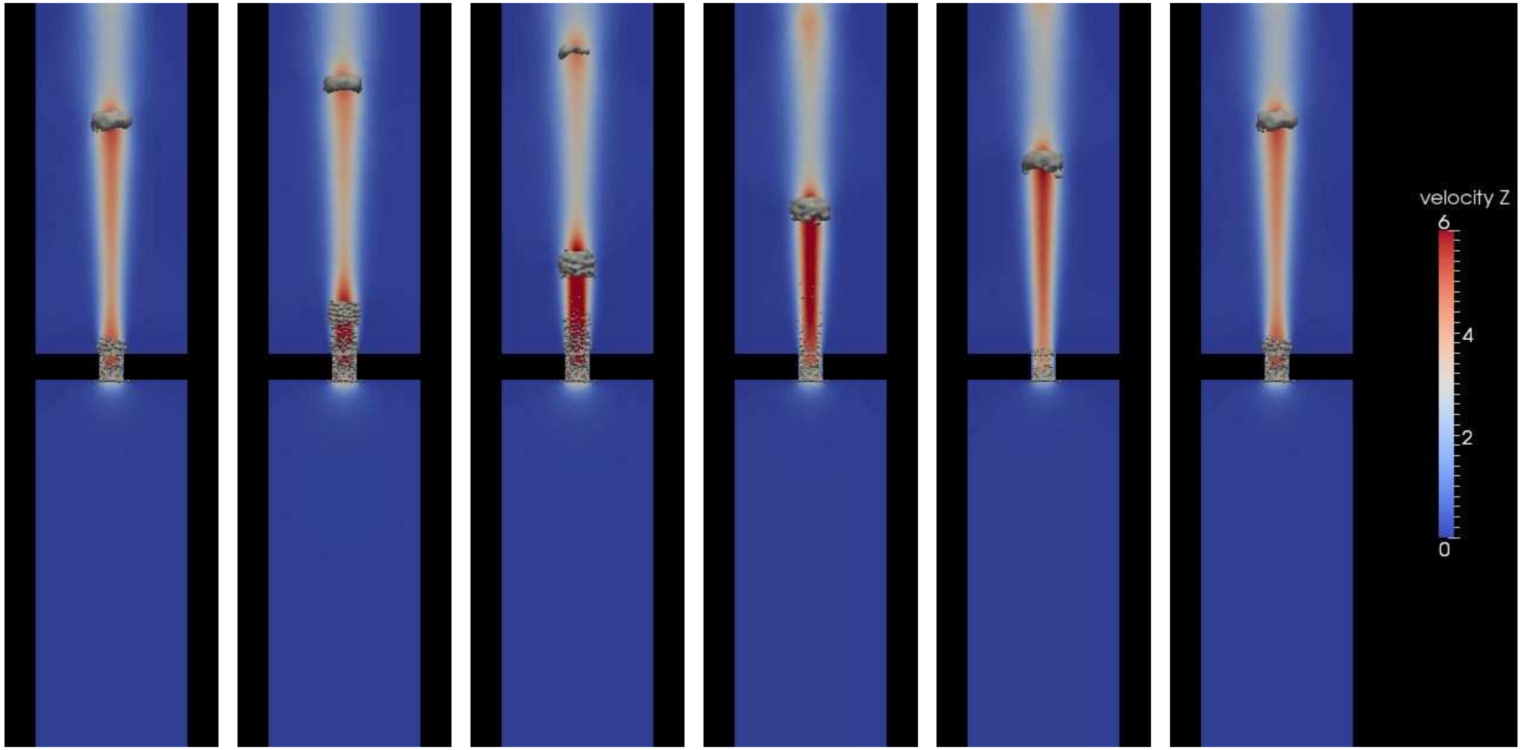

(a) $t/T_p = 0$ (b) $t/T_p = 0.2$ (c) $t/T_p = 0.4$ (d) $t/T_p = 0.6$ (e) $t/T_p = 0.8$ (f) $t/T_p = 1$

Figure 5.3: *Axial slice extracted from simulations, presenting the unsteady flow in the vicinity of the perforation, traversed by a mean bias flow* $\bar{u}_0 = 3.40\ \mathrm{m\,s^{-1}}$ *(directed from the bottom to the top) and subjected to acoustic waves at the forcing frequency* $f = 400$ Hz *and at a moderate* SPL $= 110$ dB. *The slice is colored by axial velocity* u *in* $\mathrm{m\,s^{-1}}$. *The vortex ring swept away from the orifice by the acoustic perturbation is represented by gray three-dimensional isocontours, corresponding to a value of the Q-criterion equal to* $5 \cdot 10^6$. *Figures (a) to (f) show the temporal evolution of the flow field over a period* $T_p = 1/f = 2.5 \cdot 10^{-3}$ s.

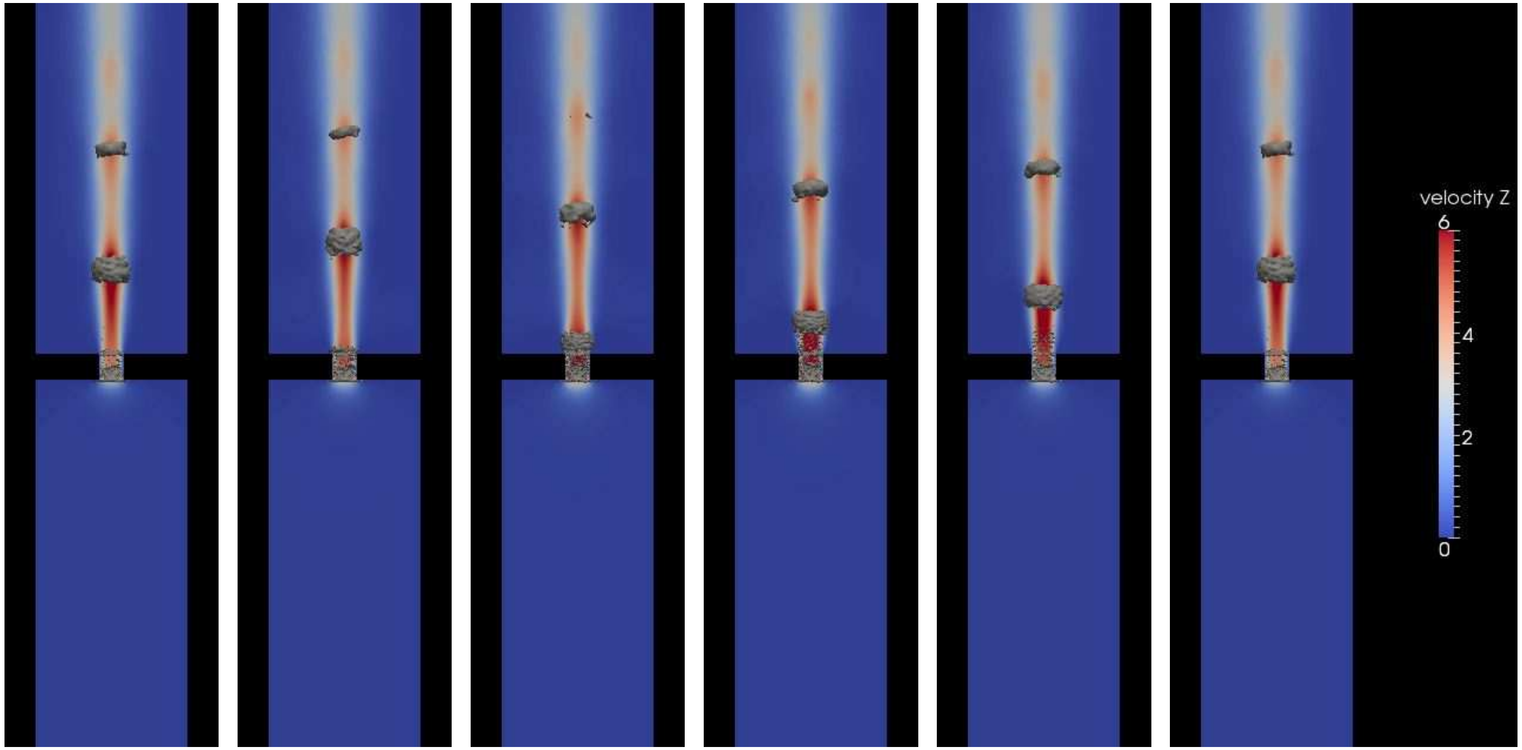

(a) $t/T_p = 0$ (b) $t/T_p = 0.2$ (c) $t/T_p = 0.4$ (d) $t/T_p = 0.6$ (e) $t/T_p = 0.8$ (f) $t/T_p = 1$

Figure 5.4: *Axial slice extracted from simulations, presenting the unsteady flow in the vicinity of the perforation, traversed by a mean bias flow* $\bar{u}_0 = 3.40\ \mathrm{m\,s^{-1}}$ *(directed from the bottom to the top) and subjected to acoustic waves at the forcing frequency* $f = 800$ Hz *and at a moderate* $\mathrm{SPL} = 110$ dB*. The slice is colored by axial velocity* u *in* $\mathrm{m\,s^{-1}}$*. The vortex ring swept away from the orifice by the acoustic perturbation is represented by gray three-dimensional isocontours, corresponding to a value of the Q-criterion equal to* $5 \cdot 10^6$*. Figures (a) to (f) show the temporal evolution of the flow field over a period* $T_p = 1/f = 1.25 \cdot 10^{-3}$ s.

5.1.2 Flow description in the nonlinear regime

At a higher forcing amplitude, the structure of the unsteady flow through the perforation changes drastically. Figure 5.5 shows the axial velocity field for an incident SPL of 140 dB and a forcing frequency $f = 400$ Hz. The velocity field now features large fluctuations on both sides of the perforation with a change of sign during the modulation cycle. The flow within the perforation generates vortex rings, characterized by a higher vorticity, which are alternatively convected downstream and upstream of the plate. These large coherent structures go deeper within the flow, at a larger distance from the perforation, before being dissipated by turbulence and viscous processes. The unsteady flow remains axisymmetric only in the vicinity of the orifice. A similar scenario is repeated in Fig. 5.6, showing the axial velocity field calculated at SPL = 140 dB and $f = 800$ Hz. It will be shown that the convection speed of the vortices before reverse flow occurs now scales with the fluctuating velocity in the orifice. These changes in the flow deeply impact the acoustic properties of the aperture.

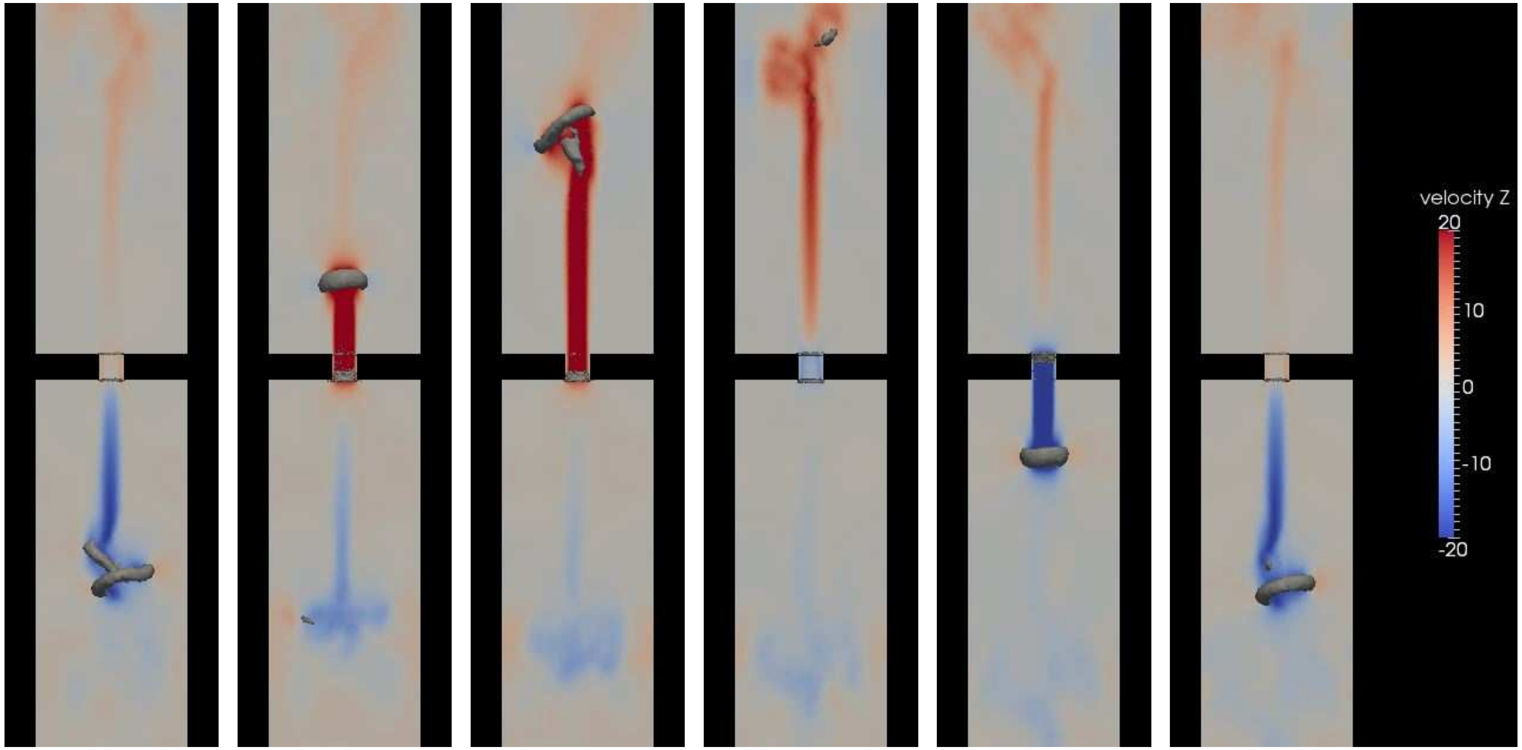

(a) $t/T_p = 0$ (b) $t/T_p = 0.2$ (c) $t/T_p = 0.4$ (d) $t/T_p = 0.6$ (e) $t/T_p = 0.8$ (f) $t/T_p = 1$

Figure 5.5: *Axial slice extracted from simulations, presenting the unsteady flow in the vicinity of the perforation, traversed by a mean bias flow* $\bar{u}_0 = 3.40\ \mathrm{m\,s^{-1}}$ *(directed from the bottom to the top) and subjected to acoustic waves at the forcing frequency* $f = 400$ Hz *and at a high* SPL = 140 dB. *The slice is colored by axial velocity* u *in* $\mathrm{m\,s^{-1}}$. *The vortex ring swept away from the orifice by the acoustic perturbation is represented by gray three-dimensional isocontours, corresponding to a value of the Q-criterion equal to* $1 \cdot 10^8$. *Figures (a) to (f) show the temporal evolution of the flow field over a period* $T_p = 1/f = 2.5 \cdot 10^{-3}$ s.

(a) $t/T_p = 0$ (b) $t/T_p = 0.2$ (c) $t/T_p = 0.4$ (d) $t/T_p = 0.6$ (e) $t/T_p = 0.8$ (f) $t/T_p = 1$

Figure 5.6: *Axial slice extracted from simulations, presenting the unsteady flow in the vicinity of the perforation, traversed by a mean bias flow* $\bar{u}_0 = 3.40\ \mathrm{m\,s^{-1}}$ *(directed from the bottom to the top) and subjected to acoustic waves at the forcing frequency* $f = 800$ Hz *and at a high* SPL = 140 dB. *The slice is colored by axial velocity* u *in* $\mathrm{m\,s^{-1}}$. *The vortex ring swept away from the orifice by the acoustic perturbation is represented by gray three-dimensional isocontours, corresponding to a value of the Q-criterion equal to* $1 \cdot 10^8$. *Figures (a) to (f) show the temporal evolution of the flow field over a period* $T_p = 1/f = 1.25 \cdot 10^{-3}$ s.

5.1.3 Acoustic velocity in the orifice

It is now possible to compute the unsteady volume flowrate in the perforation during the forcing cycle, and therefore calculate the acoustic velocity u_0' averaged over the cross section of the orifice. This quantity is a key parameter to analyze the nonlinear response of the perforated plate at high perturbation levels. The temporal evolution of the acoustic velocity ratio in the orifice $u_0'/\bar{u}_0$ deduced from the simulations is plotted in Figs. 5.7 and 5.8 during two oscillation periods, for the forcing frequencies $f = 400$ Hz and $f = 800$ Hz and for increasing values of the SPL.

Over the two oscillation periods, the velocity signal remains periodic, showing that the simulations are successfully converged. It is interesting to observe that the velocity signal in the orifice is sinusoidal at low to moderate oscillation amplitudes. This signal is then slightly distorted when reverse flow appears due to nonlinear effects, at higher forcing amplitudes. The distortion is more pronounced at $f = 800$ Hz (Fig. 5.8), however the signal still keeps a shape close to a sinusoid, suggesting that the amplitudes of higher order harmonics are much lower than the amplitude at the forcing frequency.

The lines $u_0'/\bar{u}_0 = \pm 1$ are also shown in these figures. For sound pressure levels SPL ≤ 120 dB, the velocity signal does not cross the $u_0'/\bar{u}_0 = -1$ line, and no reverse flow occurs. This is not the case for higher sound levels. When the SPL is higher than 120 dB, the amplitude of the velocity fluctuation u_0' becomes higher than the mean bias flow velocity $\bar{u}_0$. When the temporal signal crosses the $u_0'/\bar{u}_0 = -1$ line, reverse flow is observed during part of the excitation cycle. Vortex rings are then released alternatively from both sides of the aperture, as shown in Figs. 5.5 and 5.6, changing the way acoustic waves are dissipated.

The temporal signal u_0' is used to extract the amplitude of the Fourier component $\tilde{u}_0$ at the forcing frequency. Results are plotted in Fig. 5.9 as a function of the SPL of the incident pressure wave for the two forcing frequencies investigated. This figure confirms that the transition from linear to nonlinear regime occurs at a SPL close to 120 dB, where $\tilde{u}_0/\bar{u}_0 = 1$. Note that the threshold level seems independent of the frequency for the two cases simulated.

5.1.4 Unsteady vorticity fields

The simulations carried out in this work are post-processed to analyze the vortex rings trajectory and the velocity at which they are convected away from the perforation when the sound waves impinge on the perforation. This analysis allows to examine Howe's vortex-sheet model, which assumes that, at low acoustic amplitudes, a thin cylindrical vortex sheet is swept away from the orifice at a constant velocity u_c when sound waves impinge on an orifice traversed by a mean bias flow velocity $\bar{u}_0$ [Howe (1979); Howe (1998)].

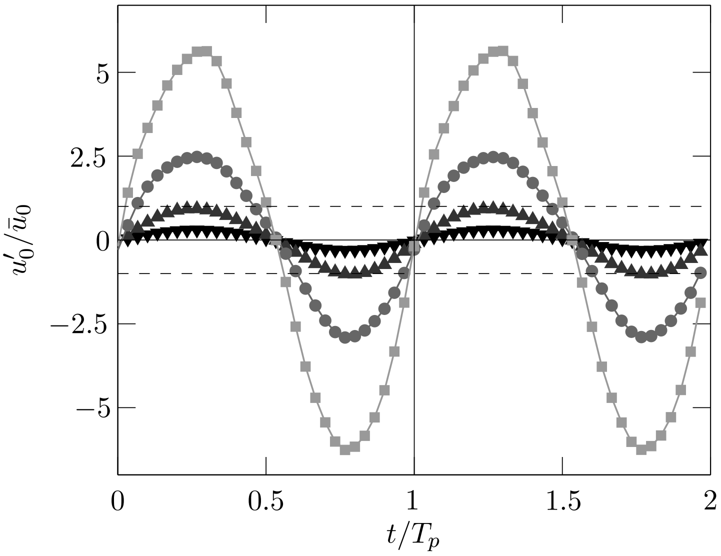

Figure 5.7: *Temporal evolution of the acoustic velocity ratio in the orifice* $u'_0/\bar{u}_0$ *during two forcing periods* $T_p = 1/f = 2.5 \cdot 10^{-3}$ s, *at* $f = 400$ Hz. *Results are shown for* SPL *of* 110 dB *(black triangles),* 120 dB *(dark gray triangles),* 130 dB *(medium gray circles) and* 140 dB *(light gray squares). The black dashed lines* $u'_0/\bar{u}_0 = \pm 1$ *are also drawn.*

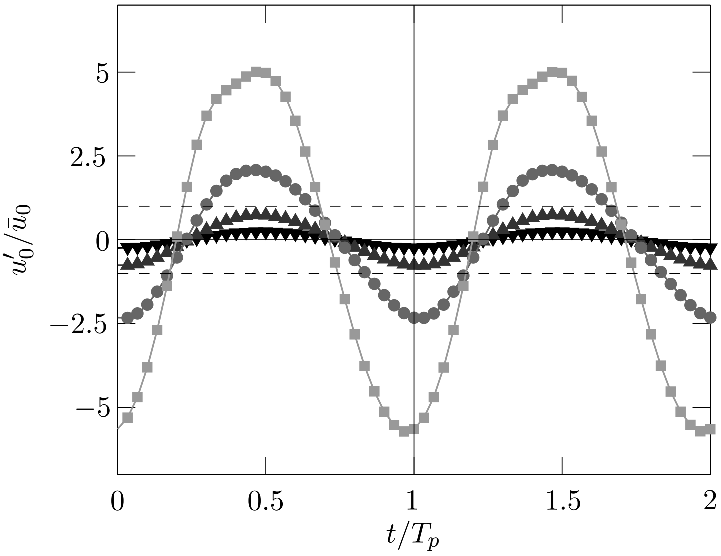

Figure 5.8: *Temporal evolution of the acoustic velocity ratio in the orifice* $u'_0/\bar{u}_0$ *during two forcing periods* $T_p = 1/f = 1.25 \cdot 10^{-3}$ s, *at* $f = 800$ Hz. *Results are shown for* SPL *of* 110 dB *(black triangles),* 120 dB *(dark gray triangles),* 130 dB *(medium gray circles) and* 140 dB *(light gray squares). The black dashed lines* $u'_0/\bar{u}_0 = \pm 1$ *are also drawn.*

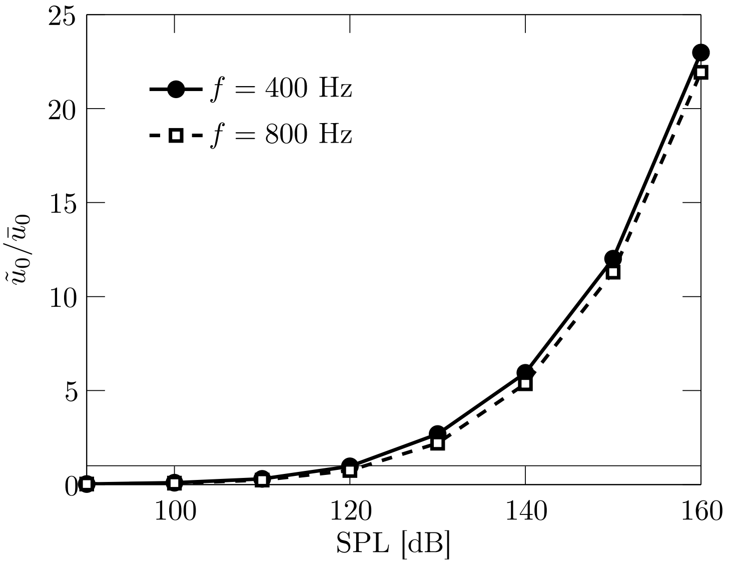

Figure 5.9: *Evolution of the amplitude of the acoustic velocity in the orifice* $\tilde{u}_0/\bar{u}_0$ *as a function of the* SPL *of the incident pressure wave, at* $f = 400$ Hz *and* $f = 800$ Hz. *The horizontal solid line drawn in the figure corresponds to* $\tilde{u}_0/\bar{u}_0 = 1$.

Jeong and Hussain (1995) showed that the λ_2-criterion best represents the topology and geometry of vortex cores in a wide variety of flows. This identification criterion is based on a splitting of the velocity gradient tensor $\boldsymbol{\nabla u}$ in its symmetric $\boldsymbol{S}$ and antisymmetric $\boldsymbol{\Omega}$ components. The eigenvalues of the real symmetric tensor $\boldsymbol{S}^2 + \boldsymbol{\Omega}^2$, $\lambda_1 \geq \lambda_2 \geq \lambda_3$, are then calculated. The region of the flow satisfying the criterion $\lambda_2 \leq 0$ identifies the vortex core.

Using the λ_2-criterion, it is possible to extract the vortex trajectory and the convection velocity from the simulations, following this procedure:

- Instantaneous fields are extracted over the first part of the acoustic period, where the vortex ring is swept downstream of the perforation.
- Only the unsteady components of the flow field are kept: $\boldsymbol{u}' = \boldsymbol{u} - \bar{\boldsymbol{u}}$, $\boldsymbol{\omega}' = \boldsymbol{\omega} - \bar{\boldsymbol{\omega}}$.
- The unsteady component of the velocity gradient tensor $\boldsymbol{\nabla u}'$ is used to calculate the λ_2-criterion.
- Isocontours of $\lambda_2 = 0$ identifying a vortex are plotted and superposed to the unsteady vorticity field $\boldsymbol{\omega}'$.
- The center of the vortex is determined as the point of maximum vorticity within the contour $\lambda_2 = 0$ delimiting the vortex.
- This procedure is repeated for each time step of the time interval investigated.

Figures 5.10 to 5.13 show the evolution of the fluctuating vorticity field ω_z' in the longitudinal plane xy over the first half of the forcing cycle, for the two forcing frequencies $f = 400$ Hz and $f = 800$ Hz, and for the two SPL of 110 and 140 dB investigated in the linear and nonlinear regimes. Only the region downstream of the perforated plate is shown in these figures. Isocontours of $\lambda_2 = 0$ are superposed to the images. These figures emphasize the necessity of always superposing the vorticity field to the $\lambda_2 = 0$ isocontour, to eliminate useless vorticity zones and to properly identify the vortex ring produced by the acoustic waves. It is also vital to use the fluctuating fields to avoid the background noise caused by the vorticity field associated to the jet shear layer, which is not linked to the acoustic excitation but to the mean flow.

The response of the perforated plate in the linear regime is presented in Fig. 5.10 for $f = 400$ Hz and in Fig. 5.11 for $f = 800$ Hz. The evolution of the unsteady vortex ring is examined over the half period when $u_0' \geq 0$. A vortex ring is created at the orifice outlet due to the oscillating flow in the perforation, and it is swept downstream of the perforation with a convection velocity that is determined below. At $f = 800$ Hz, the characteristic size of the vortices is smaller than at $f = 400$ Hz, since the wavelength of the train of vortex rings is also smaller. The flow is symmetric, and very few spurious vortical structures are detected, besides the coherent vortex rings.

At a higher sound level SPL = 140 dB, results in Fig. 5.12 for $f = 400$ Hz and in Fig. 5.13 for $f = 800$ Hz show the evolution of the unsteady vortex ring, again over the half period when $u_0' \geq 0$. Note that the isocontours corresponding to $\lambda_2 = 0$ are not shown here because they do not ease the understanding of the vortex evolution. The flow is more turbulent for these large oscillations, and secondary vorticity zones which are not synchronized with the acoustic forcing appear, generating spurious vortices which are detected by the λ_2-criterion. The symmetry of the flow is only preserved in the region close to the perforation. A vortex ring is still created at the orifice outlet, but a comparison of Figs. 5.12 and 5.13 with Figs. 5.10 and 5.11 indicates that the velocity at which the vortex rings are convected downstream is higher in the nonlinear regime. At higher amplitude, the λ_2-criterion alone is not sufficient to univocally determine the position of the vortices, and thus it must be coupled to the analysis of the unsteady vorticity component ω_z'.

5.1.5 Analysis of the vortex trajectory

The algorithm presented in the previous paragraph is then applied to the vorticity fields calculated for each forcing amplitude. The instantaneous position of the vortex ring $(x_{\text{vort}}, y_{\text{vort}})$ in the xy plane can thus be determined. By tracking the evolution of this position over the half period when $u_0' \geq 0$, the vortex ring trajectory is obtained and shown in Fig. 5.14 for an excitation frequency of 400 Hz, and in Fig. 5.15 for an excitation at 800 Hz. One may first observe that the trajectory slightly widens when the forcing amplitude increases. However

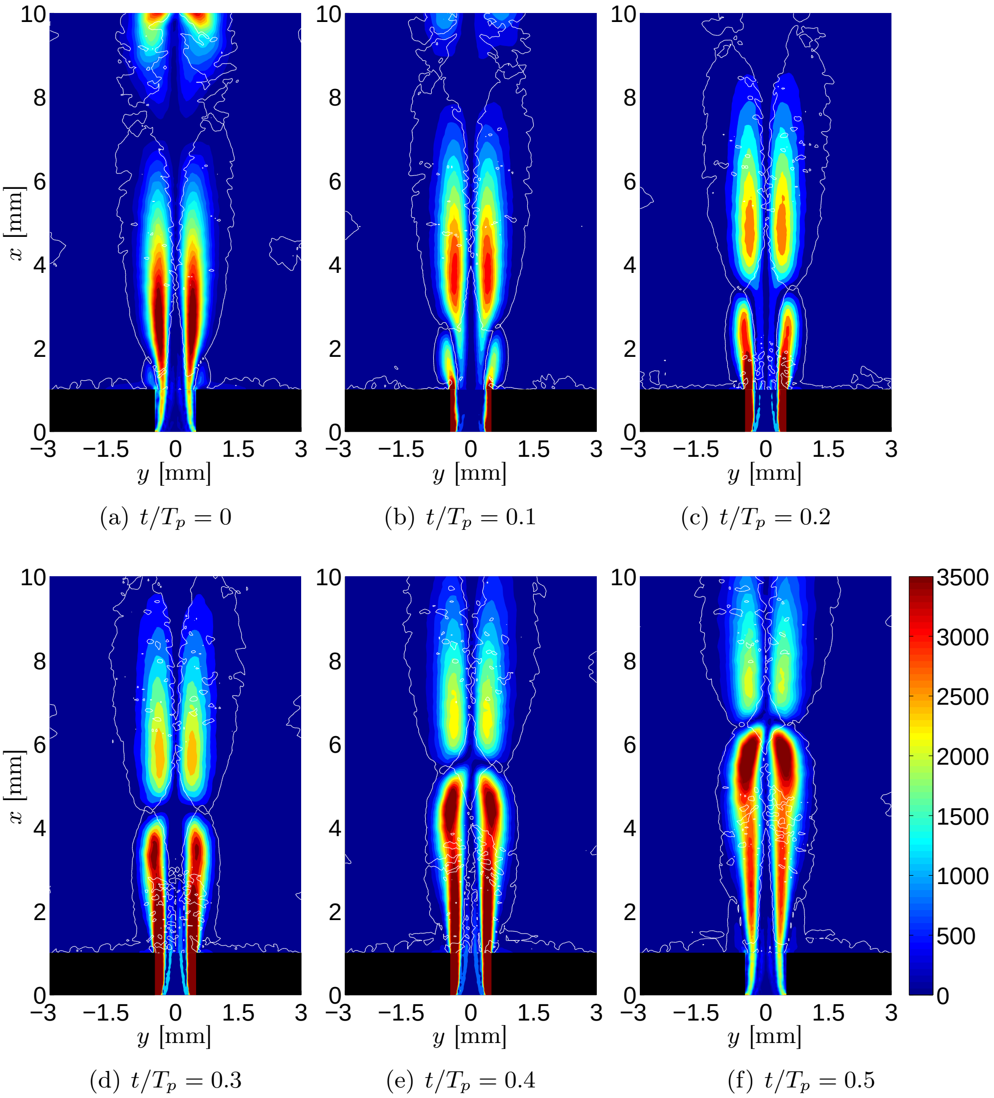

(a) $t/T_p = 0$ (b) $t/T_p = 0.1$ (c) $t/T_p = 0.2$

(d) $t/T_p = 0.3$ (e) $t/T_p = 0.4$ (f) $t/T_p = 0.5$

Figure 5.10: *Axial slices extracted from simulations, presenting the unsteady vorticity field downstream of the perforation, traversed by a mean bias flow* $\bar{u}_0 = 3.40\ \mathrm{m\,s^{-1}}$ *(directed from the bottom to the top) and subjected to acoustic waves at the forcing frequency* $f = 400$ Hz *and at a moderate* SPL $= 110$ dB*. The slice is colored by the vorticity component* ω'_z *in* s^{-1}*. The vortex ring swept away from the orifice by the acoustic perturbation is represented by white isocontours of* $\lambda_2 = 0$*. Figures (a) to (f) show the temporal evolution of the flow field over the half period when* $u'_0 \geq 0$*.*

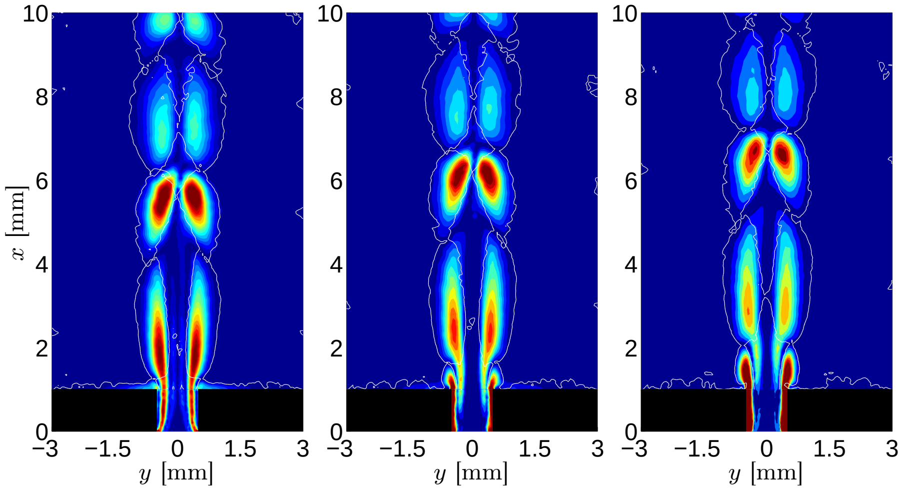

(a) $t/T_p = 0$ (b) $t/T_p = 0.1$ (c) $t/T_p = 0.2$

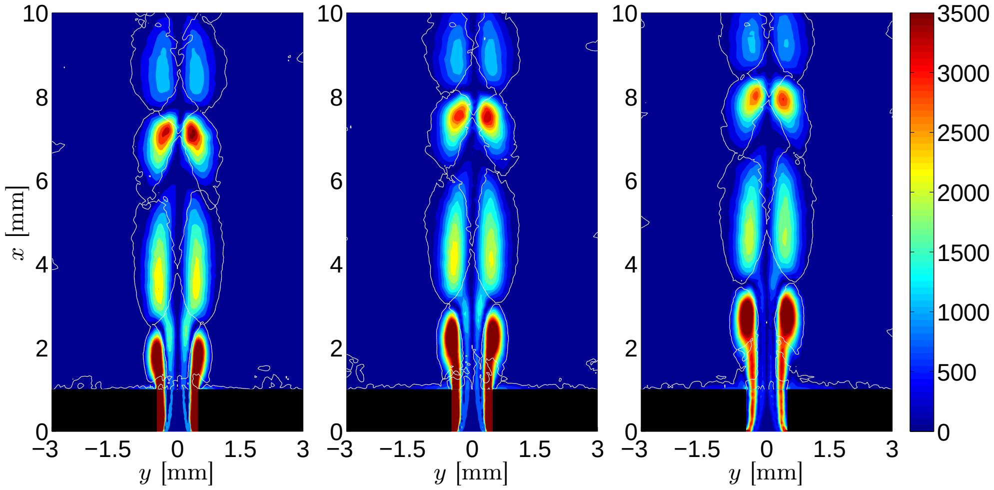

(d) $t/T_p = 0.3$ (e) $t/T_p = 0.4$ (f) $t/T_p = 0.5$

Figure 5.11: *Axial slices extracted from simulations, representing the unsteady vorticity field downstream of the perforation, traversed by a mean bias flow* $\bar{u}_0 = 3.40\ \mathrm{m\,s^{-1}}$ *(directed from the bottom to the top) and subjected to acoustic waves at the forcing frequency* $f = 400$ Hz *and at a moderate* SPL $= 110$ dB. *The slice is colored by the vorticity component* ω'_z *in* $\mathrm{s^{-1}}$. *The vortex ring swept away from the orifice by the acoustic perturbation is represented by white isocontours of* $\lambda_2 = 0$. *Figures (a) to (f) show the temporal evolution of the flow field over the half period when* $u'_0 \geq 0$.

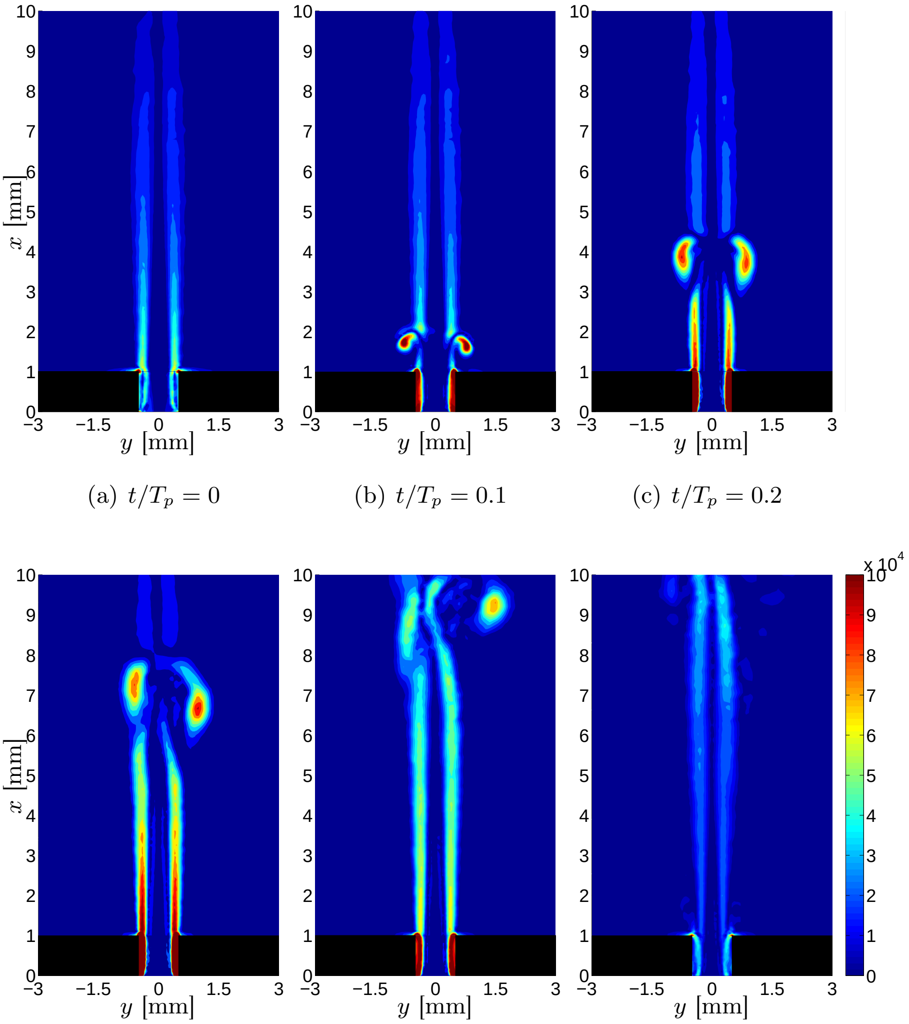

(a) $t/T_p = 0$ (b) $t/T_p = 0.1$ (c) $t/T_p = 0.2$

(d) $t/T_p = 0.3$ (e) $t/T_p = 0.4$ (f) $t/T_p = 0.5$

Figure 5.12: *Axial slices extracted from simulations, presenting the unsteady vorticity field downstream of the perforation, traversed by a mean bias flow* $\bar{u}_0 = 3.40\ \mathrm{m\,s^{-1}}$ *(directed from the bottom to the top) and subjected to acoustic waves at the forcing frequency* $f = 400$ Hz *and at a high* SPL = 140 dB*. The slice is colored by the vorticity component* ω'_z *in* $\mathrm{s^{-1}}$*. Figures (a) to (f) show the temporal evolution of the flow field over the half period when* $u'_0 \geq 0$*.*

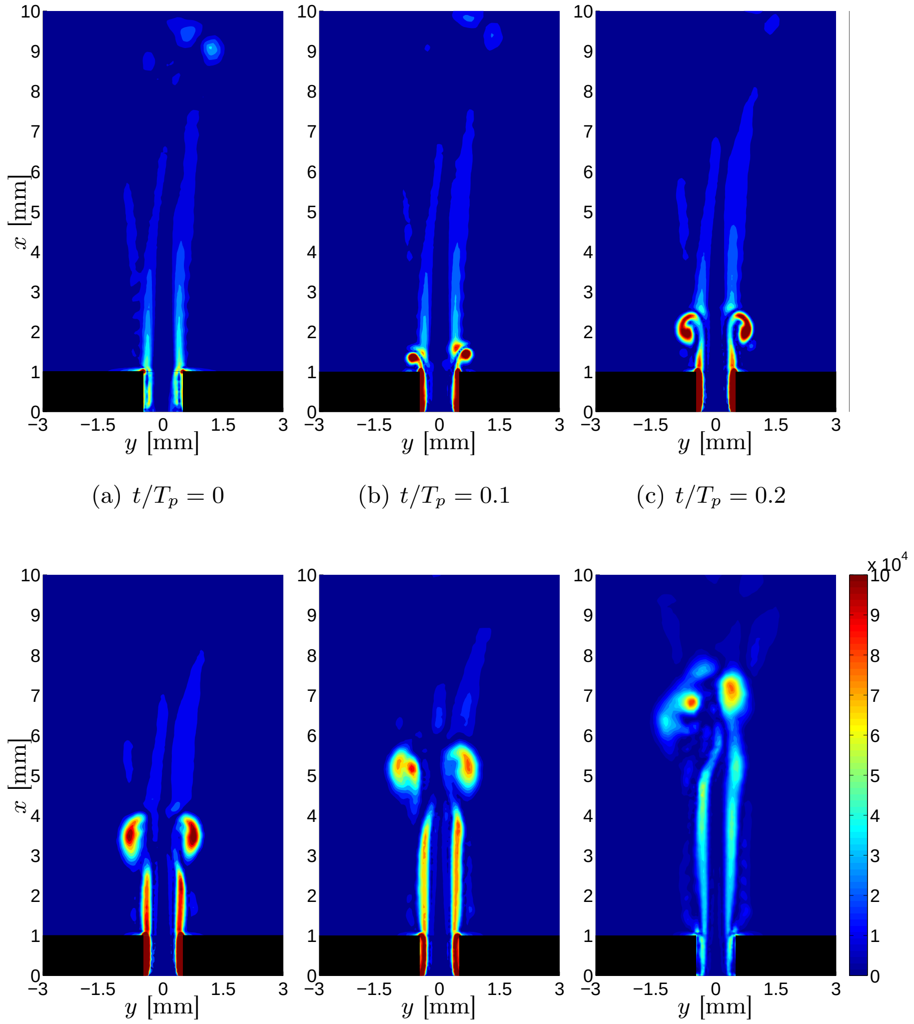

(a) $t/T_p = 0$ (b) $t/T_p = 0.1$ (c) $t/T_p = 0.2$

(d) $t/T_p = 0.3$ (e) $t/T_p = 0.4$ (f) $t/T_p = 0.5$

Figure 5.13: *Axial slices extracted from simulations, presenting the unsteady vorticity field downstream of the perforation, traversed by a mean bias flow* $\bar{u}_0 = 3.40\ \mathrm{m\,s^{-1}}$ *(directed from the bottom to the top) and subjected to acoustic waves at the forcing frequency* $f = 800$ Hz *and at a high* SPL = 140 dB*. The slice is colored by the vorticity component* ω_z' *in* $\mathrm{s^{-1}}$*. Figures (a) to (f) show the temporal evolution of the flow field over the half period when* $u_0' \geq 0$*.*

it remains essentially a straight line, forming a vortex tube of diameter $2a$, thus confirming Howe's hypothesis for his linear model at small amplitudes [Howe (1979)]. This observation remains also true for large forcing amplitudes.

The vortex rings are generated at the outlet of the perforation, before being convected downstream at an average velocity $\bar{u}_c$, which increases when the amplitude of the acoustic oscillation increases. It is worth noting that the time scales are different in Figs. 5.14 and 5.15, since the oscillation periods are different. At higher amplitudes, the vortex position can only be reconstructed up to less than half period, since the symmetry of the flow is broken afterwards and the coherent structures are scattered and dissipated by the strong forcing.

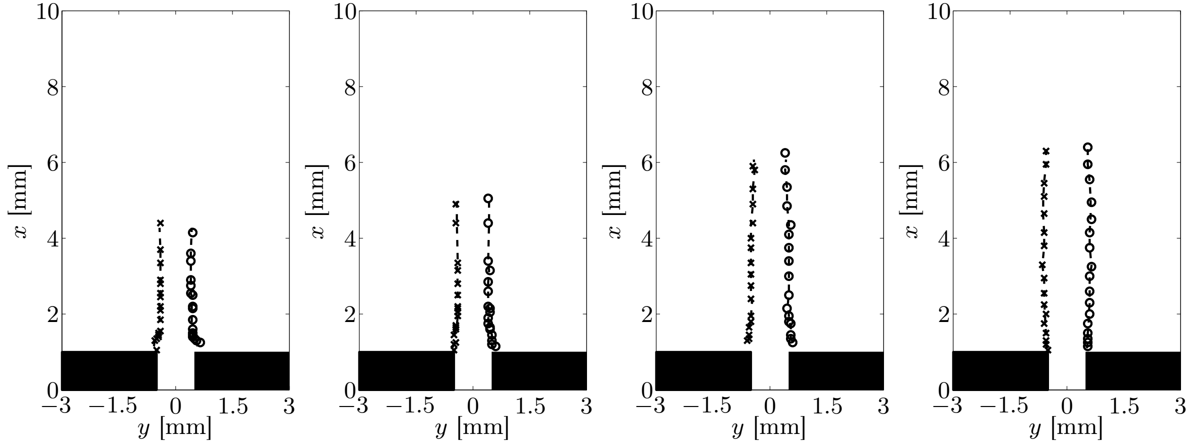

(a) SPL = 90 dB (b) SPL = 100 dB (c) SPL = 110 dB (d) SPL = 120 dB

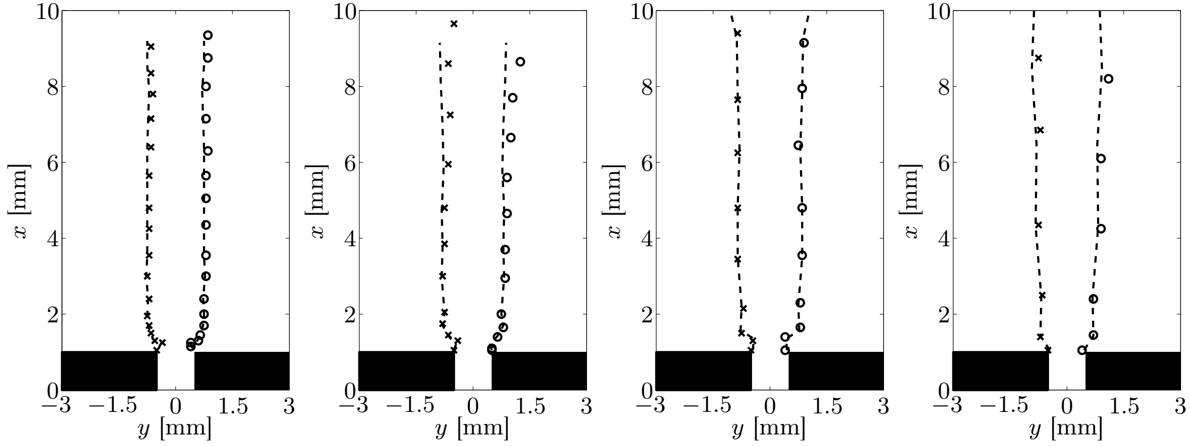

(e) SPL = 130 dB (f) SPL = 140 dB (g) SPL = 150 dB (h) SPL = 160 dB

Figure 5.14: *Reconstruction of vortex trajectories at* $f = 400$ *Hz and for increasing sound levels. The vortex ring is tracked over half a period, when* $u'_0 \geq 0$. *The mean flow direction is from bottom to top.*

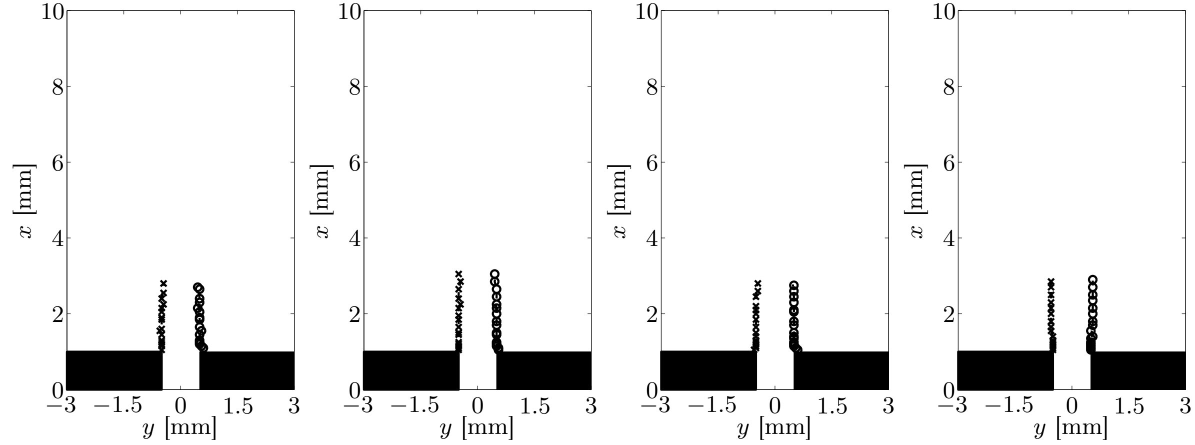

(a) SPL = 90 dB (b) SPL = 100 dB (c) SPL = 110 dB (d) SPL = 120 dB

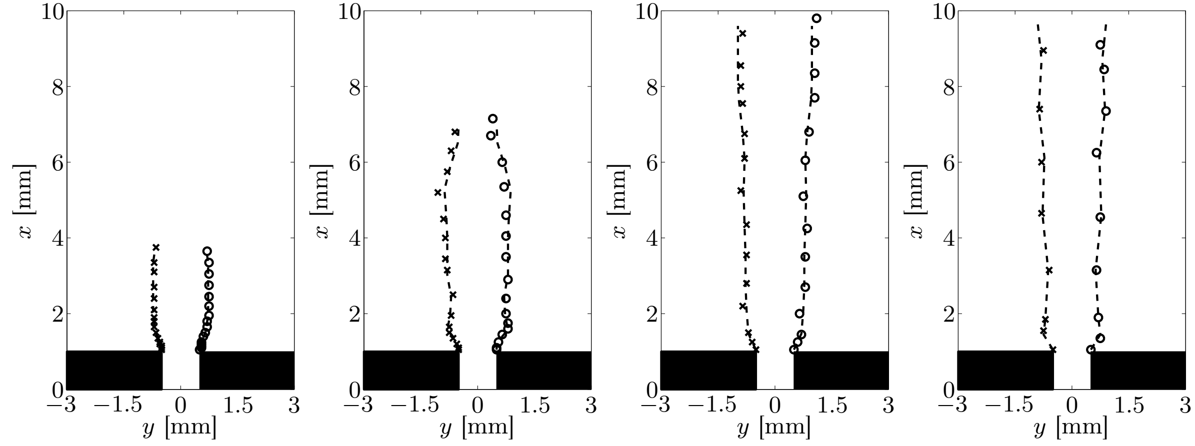

(e) SPL = 130 dB (f) SPL = 140 dB (g) SPL = 150 dB (h) SPL = 160 dB

Figure 5.15: *Reconstruction of vortex trajectories at* $f = 800$ *Hz and for increasing sound levels. The vortex ring is tracked over half a period, when* $u'_0 \geq 0$*. The mean flow direction is from bottom to top.*

5.1.6 Analysis of the convection velocity

The average convection velocity of the vortex ring along its trajectory can be deduced from the simulations. This velocity is plotted in Fig. 5.16 for $f = 400$ Hz and in Fig. 5.17 for $f = 800$ Hz as a function of the acoustic level $\tilde{u}_0/\bar{u}_0$ reached in the perforation. First, the convection velocity does not appear to depend on the acoustic forcing frequency, since very little differences can be observed between results at $f = 400$ Hz and at $f = 800$ Hz. There is a slight difference for the point corresponding to the highest acoustic amplitude SPL $= 160$ dB ($\tilde{u}_0/\bar{u}_0 \simeq 23$) at $f = 400$ Hz, which is due to the fact that the vortex ring is dissipated more rapidly at this frequency and amplitude. This structure cannot be tracked during a sufficiently long time to obtain a correct determination of the convection velocity.

In the linear regime, when $\tilde{u}_0/\bar{u}_0 \leq 1$, the average convection velocity $\bar{u}_c$ is approximately constant and it satisfies the identity $\bar{u}_c = \bar{u}_0$. This observation confirms again Howe's vortex-sheet linear theory [Howe (1979)], and is coherent with the empirical value found by Hughes and Dowling (1990) in their experiments or in the present study [Scarpato et al. (2012); Scarpato et al. (2013b)]. In the nonlinear regime this behavior ceases and $\bar{u}_c$ increases as the excitation amplitude increases.

The evolution of the velocity ratio $(\bar{u}_0 + \tilde{u}_0)/\bar{u}_0$ is also plotted in Figs. 5.16 and 5.17. A comparison between data extracted from direct numerical simulations for the convection velocity $\bar{u}_c$ and the ratio $(\bar{u}_0 + \tilde{u}_0)/\bar{u}_0$ shows that the slope of $\bar{u}_c/\bar{u}_0$ is actually lower. Therefore we propose the following approximation for the convection velocity:

$$\bar{u}_c = \overline{\left(\frac{\Delta x_{\text{vort}}}{\Delta t}\right)} \simeq \bar{u}_0 + C\tilde{u}_0 \quad \text{for} \quad \frac{t}{T_p} \leq 0.5 \tag{5.2}$$

where C is a real positive constant. In our case, the best agreement between the model presented in Eq. (5.2) and data extracted from the simulations is obtained for $C = 1/3$.

This model is used in section 5.2.1 to explore nonlinear effects of the perturbation level on the acoustic response of the perforated plate.

5.1.7 Analysis of the reflection coefficient

The acoustic properties of the perforation, such as the specific impedance, the reflection and the absorption coefficients, can be deduced from the direct numerical simulations presented by post-processing numerical data far from the perforation. It is interesting to compare the values of the reflection coefficient computed from the numerical simulations with the predictions of the linear model Eq. (1.39) when the modulation level is increased.

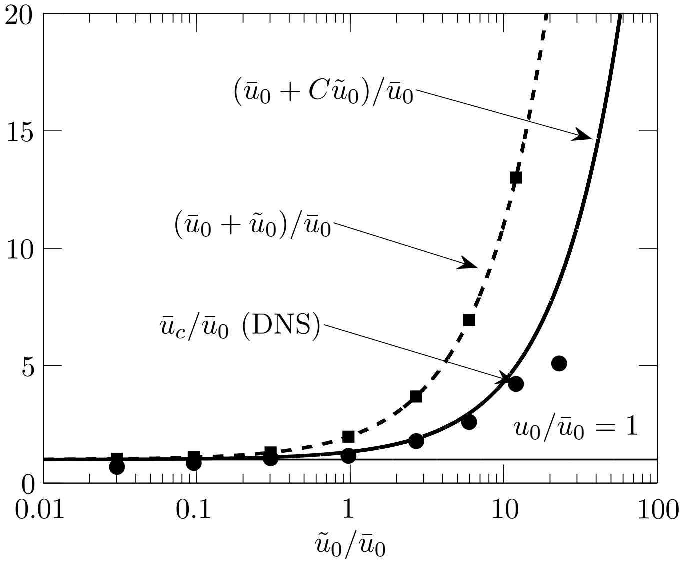

Figure 5.16: *Evolution of characteristic velocities as functions of the acoustic velocity ratio in the orifice* $\tilde{u}_0/\bar{u}_0$*, at* $f = 400$ Hz*. The average convection velocity* $\bar{u}_c$ *deduced from simulations (●) for each forcing amplitude is compared to the velocity ratio in the orifice* $(\bar{u}_0 + \tilde{u}_0)/\bar{u}_0$ *(dashed line and black squares), and to the model* $(\bar{u}_0 + C\tilde{u}_0)/\bar{u}_0$*, with* $C = 1/3$ *(solid line). Also the line* $u_0/\bar{u}_0 = 1$ *is shown (thin solid line).*

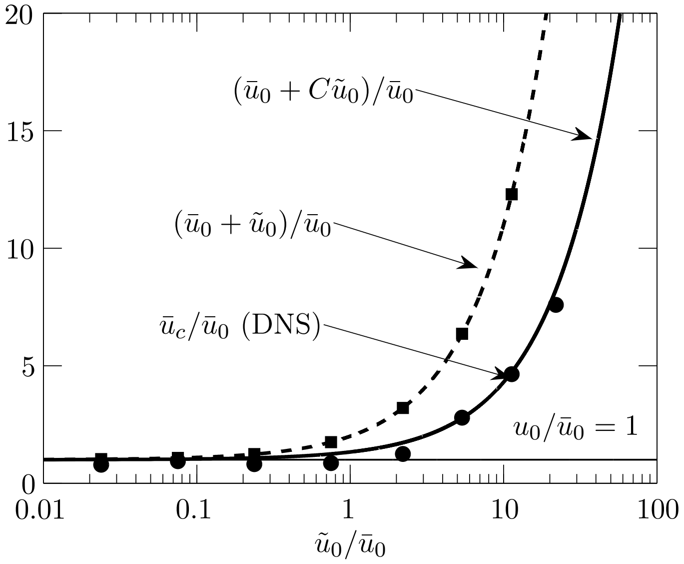

Figure 5.17: *Evolution of characteristic velocities as functions of the acoustic velocity ratio in the orifice* $\tilde{u}_0/\bar{u}_0$*, at* $f = 800$ Hz*. The average convection velocity* $\bar{u}_c$ *deduced from simulations (●) for each forcing amplitude is compared to the velocity ratio in the orifice* $(\bar{u}_0 + \tilde{u}_0)/\bar{u}_0$ *(dashed line and black squares), and to the model* $(\bar{u}_0 + C\tilde{u}_0)/\bar{u}_0$*, with* $C = 1/3$ *(solid line). Also the line* $u_0/\bar{u}_0 = 1$ *is shown (thin solid line).*

The reflection coefficient R is determined in the simulations by computing the specific impedance of the orifice, which is defined as follows (see also Fig. 1.8):

$$\zeta = \frac{\tilde{p}_2}{\rho_0 c_0 \tilde{u}_2}, \tag{5.3}$$

where the pressure fluctuation $\tilde{p}_2$ and the corresponding axial velocity disturbance $\tilde{u}_2$ are taken here at a distance $l/a = 100$ downstream of the orifice, in a region where the flow is uniform away from the jet. The pressure and velocity signals are first averaged over the cross section area of the numerical domain. In nonlinear regimes, $\tilde{p}$ and $\tilde{u}$ represent the harmonic components of pressure and velocity fluctuations, taken at the forcing frequency f.

The reflection coefficient R is then obtained with the expression (1.37), which is reproduced here:

$$R = \frac{\zeta + 1}{\zeta - 1}$$

Figures 5.18 and 5.19 show the modulus of the reflection coefficient extracted from the simulations, which is compared to the predictions from Eq. (1.39), at $f = 400$ Hz and $f = 800$ Hz respectively. As expected, the agreement is good at low to moderate excitation levels when $\tilde{u}_0/\bar{u}_0 \leq 1$, thus validating the methodology. The reflection coefficient is constant, showing excellent absorption properties at $f = 400$ Hz ($|R| \simeq 0$) and a higher value $|R| \simeq 0.65$ at $f = 800$ Hz.

In the nonlinear regime, the velocity fluctuation is higher than the mean bias flow velocity in the orifice $\tilde{u}_0/\bar{u}_0 > 1$, and the modulus $|R|$ depends now on the acoustic perturbation amplitude. At $f = 400$ Hz, the reflected wave amplitude increases and the absorption coefficient $\alpha = 1 - |R|^2$ decreases. At $f = 800$ Hz, the modulus of the reflection coefficient first decreases, reaching a minimum when $\tilde{u}_0/\bar{u}_0 \simeq 5$ (corresponding to an incident SPL $= 140$ dB), before increasing again.

From this first comparison it is clear that the linear model from Howe (1979) captures the correct behavior for small acoustic disturbances, as long as $\tilde{u}_0/\bar{u}_0 \leq 1$. There are some small differences which are mainly due to practical difficulties of obtaining temporal signals over a sufficiently long time interval in the simulations conducted at low forcing frequencies. Figures 5.18 and 5.19 also show that Howe's model does not reproduce the acoustic response of a perforated plate subjected to high forcing amplitudes and operating in the nonlinear regime. Two nonlinear models are investigated in the following section to describe the response of the perforate at high amplitudes.

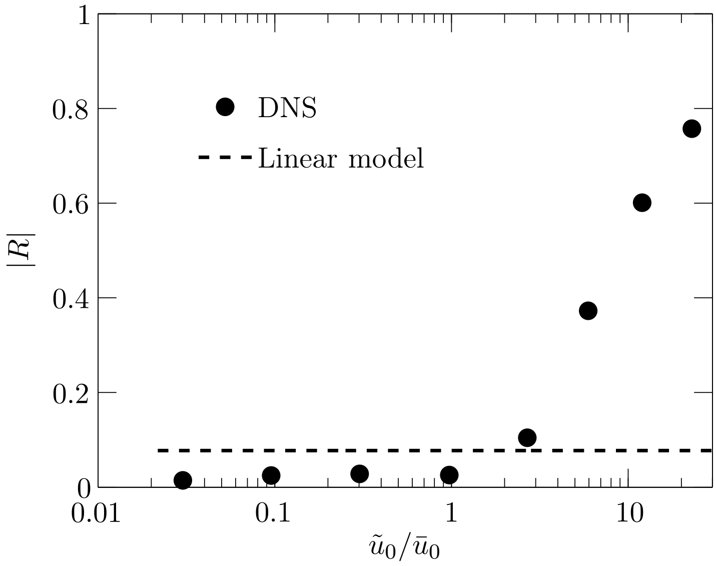

Figure 5.18: *Modulus of the reflection coefficient $|R|$ as a function of the velocity amplitude ratio in the orifice $\tilde{u}_0/\bar{u}_0$, at the forcing frequency $f = 400$ Hz. Results from simulations (●) are compared to the linear model given by Eq. (1.39).*

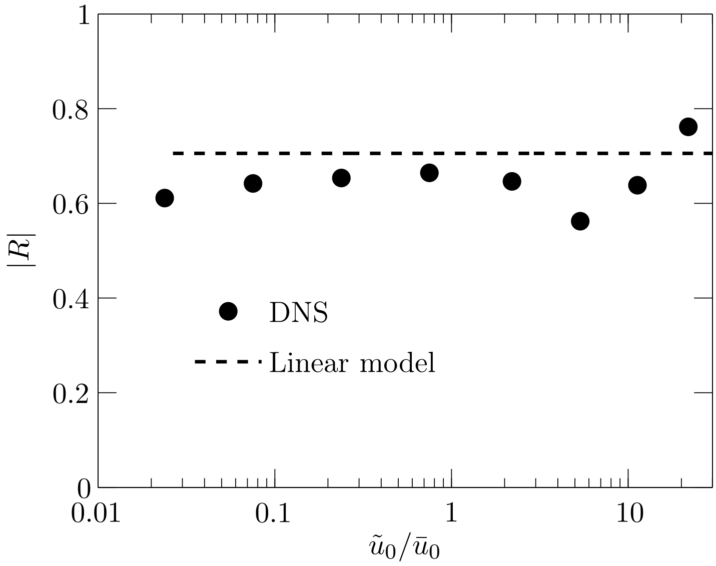

Figure 5.19: *Modulus of the reflection coefficient $|R|$ as a function of the velocity amplitude ratio in the orifice $\tilde{u}_0/\bar{u}_0$, at the forcing frequency $f = 800$ Hz. Results from simulations (●) are compared to the linear model given by Eq. (1.39).*

5.2 Modeling the effect of amplitude on the impedance of a perforate

Two models are analyzed in the present section, taking into account effects of nonlinearity at high acoustic amplitudes. The first model uses the vortex convection velocity extracted from the simulations, combined with the vortex-sheet model from Howe (1979). The second one is based on the unsteady Bernoulli's equation. Using a principal component analysis, a new expression for the specific impedance of the perforated plate is proposed.

5.2.1 The vortex convection model VC

The simulations presented in section 5.1 have revealed the unsteady behavior of the vortex ring that is detached from the orifice when the sound wave impinges on the perforation. Its convection velocity u_c remains constant in the linear regime, when $\tilde{u}_0 \leq \bar{u}_0$, and satisfies the identity $u_c = \bar{u}_0$. In the nonlinear regime, the calculations show that the convection velocity is given by $u_c = \bar{u}_0 + C\tilde{u}_0$ (Eq. (5.2)), with $C = 1/3$ giving the best agreement with numerical data. This last expression gives also good results when $\tilde{u}_0/\bar{u}_0 \leq 1$ and is used in the following to represent the vortex convection velocity for all perturbation levels.

The basic idea of the model presented in this section, called VC for Vortex Convection, is to use the actual convection velocity u_c, determined in Eq. (5.2), in the original expressions of Howe for the Strouhal number appearing in the Rayleigh conductivity. In this model we neglect all interactions taking place when reverse flow appears in the orifice, and we assume that the effects of nonlinearity can be represented by considering only the correct convection velocity of the vortex rings.

First we introduce Eq. (5.2) in the definitions of the Mach number and Strouhal number:

$$\mathrm{M}_{c,\mathrm{VC}} = \frac{u_c}{c_0} = \frac{\bar{u}_0 + C\tilde{u}_0}{c_0} \tag{5.4}$$

$$\mathrm{St}_{\mathrm{VC}} = \frac{\omega a}{u_c} = \frac{\omega a}{\bar{u}_0 + C\tilde{u}_0} \tag{5.5}$$

These dimensionless numbers depend now on the perturbation level. The new expression for the Strouhal number is then used in the linear model for the Rayleigh conductivity Eq. (1.18) to obtain the nonlinear expression:

$$K_{R,\mathrm{VC}} = 2a(\gamma_{\mathrm{VC}} + \mathrm{i}\delta_{\mathrm{VC}}) = 2a[\gamma(\mathrm{St}_{\mathrm{VC}}) + \mathrm{i}\delta(\mathrm{St}_{\mathrm{VC}})], \tag{5.6}$$

where the function γ and δ are given by Eq. (1.18). Figure 5.20 shows the real and imaginary components of the Rayleigh conductivity obtained with

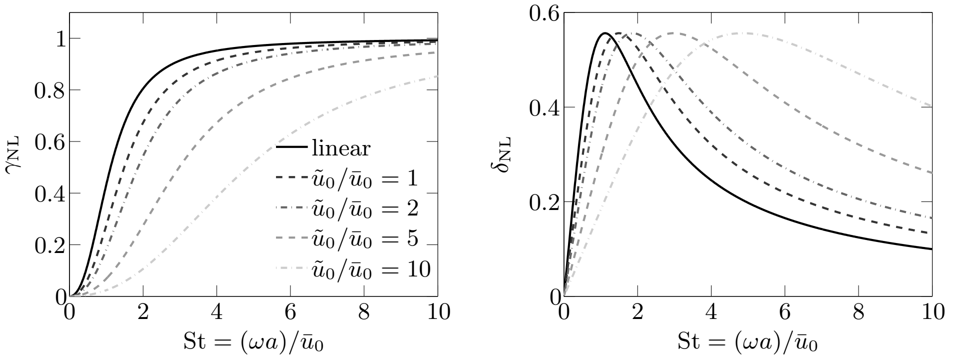

(a) Real component of $K_{R,\mathrm{VC}}/(2a)$. (b) Imaginary component of $K_{R,\mathrm{VC}}/(2a)$.

Figure 5.20: *Evolutions of the real component* γ_{VC} *(a) and of the imaginary component* δ_{VC} *(b) of the nonlinear Rayleigh conductivity* K_R*, given by Eq. (5.6), as a function of the Strouhal number* $\mathrm{St} = (\omega a)/\bar{u}_0$ *for different values of the acoustic perturbation level* $\tilde{u}_0/\bar{u}_0$*.*

Eq. (5.6). Note that, according to this model, when the acoustic amplitude increases the functions γ_{VC} and δ_{VC} are simply shifted towards higher Strouhal numbers. Equation (5.6), together with Eqs. (5.4) and (5.5), are then used in the linear expression of the specific impedance of the perforate coupled to a back cavity Eq. (1.38) to obtain an expression for its nonlinear impedance:

$$\zeta_{\mathrm{VC}} = \mathrm{i}\left[\frac{\pi}{2}\mathrm{St}\frac{\mathrm{M}_c}{\sigma}\left(\frac{1}{\gamma_{\mathrm{VC}} - \mathrm{i}\delta_{\mathrm{VC}}} + \frac{2h}{\pi a}\right) - \frac{1}{\tan(\mathrm{He})}\right] \tag{5.7}$$

Note that in this expression the product of Mach and Strouhal numbers use the linear definition based on $u_c = \bar{u}_0$, because the identity $\mathrm{St}\,\mathrm{M}_c = \mathrm{St}_{\mathrm{VC}}\,\mathrm{M}_{c,\mathrm{VC}}$ holds. Predictions with Eq. (5.7) are compared later to results from simulations, experiments and to predictions from other models.

5.2.2 Quasi-steady analysis

In section 5.1, the analysis of the unsteady flow field in the vicinity of the perforation showed that a vortex ring is swept away from the plate in the direction of the local jet velocity. Linear models, such as the vortex-sheet theory proposed by Howe (1979) fail to correctly predict the acoustic properties of the perforated plate at high acoustic amplitudes. However, there is evidence from the previous works of Ingard and Ising (1967), Cummings and Eversman (1983) and Bellucci et al. (2004) that a quasi-steady approach based on Bernoulli's equation can be promisingly adapted to describe the perforated plate response at high SPL.

A quasi-steady approach can be applied to our problem if the wavelength λ is much larger than the dimension of the orifice $\lambda/2a \gg 1$, or equivalently if

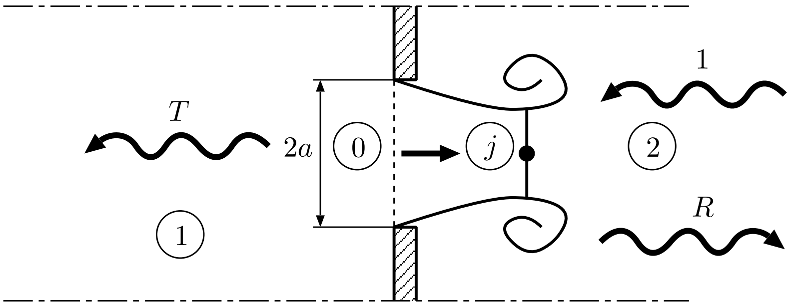

Figure 5.21: *Single orifice traversed by a mean bias flow and subjected to normal incident sound waves. The different zones considered for the application of Bernoulli's theorem are highlighted in the schematic. The* vena contracta *section is denoted by* j.

the acoustic particle displacement $\tilde{u}_0/\omega$ and the mean flow displacement $\bar{u}_0/\omega$ are much larger than the characteristic orifice size $2a$: $\tilde{u}_0/\omega \gg 2a$, $\bar{u}_0/\omega \gg 2a$ [Rienstra and Hirschberg (2003)]. In this case we will show that it is possible to determine the Rayleigh conductivity of the perforate using the analysis developed by Morse and Ingard (1986) for an aperture and by Cummings and Eversman (1983) for nozzles.

The notations were introduced in chapter 1, and are recalled in Fig. 5.21. The unsteady Bernoulli's theorem Eq. (1.47) is applied to a streamline starting upstream the orifice (denoted 1 in Fig. 5.21) and ending at the *vena contracta* section (denoted j in Fig. 5.21). After discarding the time-independent terms and normalizing Eq. (1.49), one can rewrite Bernoulli's theorem as follows:

$$\frac{p_1' - p_2'}{\frac{1}{2}\rho_0 \bar{u}_0^2} = \frac{2l}{\bar{u}_0}\frac{\partial}{\partial t}\left(\frac{u_0'}{\bar{u}_0}\right) + \frac{1-\sigma^2 C_c^2}{C_c^2}\left[\left(1+\frac{u_0'}{\bar{u}_0}\right)\left|1+\frac{u_0'}{\bar{u}_0}\right| - 1\right] \tag{5.8}$$

where l is the end correction length, σ is the plate porosity and $C_c = A_j/A_0$ is the contraction coefficient between the *vena contracta* section and the orifice.

Equation (5.8) links the unsteady pressure drop across the perforation to the evolution of the ratio $u_0'/\bar{u}_0$. The absolute value has been introduced in the nonlinear term to take into account reverse flow in the orifice at high amplitudes, when $u_0'/\bar{u}_0 \geq 1$. Note that, in the limit of small porosities $\sigma \ll 1$, where $(1-\sigma^2 C_c^2)/C_c^2 \simeq 1/C_c^2$, Eq. (5.8) can be simplified as follows:

$$\frac{p_1' - p_2'}{\frac{1}{2}\rho_0 \bar{u}_0^2} = \frac{2l}{\bar{u}_0}\frac{\partial}{\partial t}\left(\frac{u_0'}{\bar{u}_0}\right) + \frac{1}{C_c^2}\left[\left(1+\frac{u_0'}{\bar{u}_0}\right)\left|1+\frac{u_0'}{\bar{u}_0}\right| - 1\right] \tag{5.9}$$

When the pressure modulation $p_1' - p_2'$ is fixed, this differential equation can be numerically solved in the time domain with well-known Runge-Kutta methods to obtain the unsteady acoustic velocity in the perforation. This approach is useful for arbitrary (also non-periodic) driving pressures, such as during transient pressure conditions, or complex periodic forcing signals [Cummings (1986)]. However, a time domain expression is difficult to implement in thermoacoustic solvers, which usually solves the Helmholtz equation in the frequency domain [Nicoud et al. (2007); Silva et al. (2013)].

5.2.2.1 Analysis in the linear regime

When acoustic velocity perturbations in the orifice are much smaller than the mean bias flow velocity $\tilde{u}_0/\bar{u}_0 \ll 1$, Eq. (5.9) can be simplified by neglecting the nonlinear terms which are of second order. Therefore, keeping only unsteady terms of first order, one obtains the linearized expression [Luong et al. (2005)]:

$$\frac{p_1' - p_2'}{\frac{1}{2}\rho_0 \bar{u}_0^2} = \frac{2l}{\bar{u}_0}\frac{\partial}{\partial t}\left(\frac{u_0'}{\bar{u}_0}\right) + \frac{2}{C_c^2}\frac{u_0'}{\bar{u}_0} \tag{5.10}$$

It is now possible to apply the Fourier transform to Eq. (5.10), using the identities $u_0'(t) = \Re\{\tilde{u}_0 e^{-\mathrm{i}\omega t}\}$ and $p_i'(t) = \Re\{\tilde{p}_i e^{-\mathrm{i}\omega t}\}$, with $i = 1$ or 2. The following expression for the unsteady pressure drop in the frequency domain is then obtained:

$$\tilde{p}_2 - \tilde{p}_1 = \rho_0 \bar{u}_0 \tilde{u}_0 \left(\frac{\mathrm{i}\omega l}{\bar{u}_0} - \frac{1}{C_c^2}\right) \tag{5.11}$$

The unsteady pressure drop in Eq. (5.11) can be introduced in the definition of the Rayleigh conductivity K_R given by Eq. (1.13), yielding a new expression valid in the linear regime:

$$\frac{K_R}{2a} = \frac{\pi \mathrm{St}}{2\mathrm{St}\dfrac{l}{a} + \dfrac{2\mathrm{i}}{C_c^2}} \tag{5.12}$$

The unknown parameters in Eq. (5.12) are the mass end correction length l and the contraction coefficient C_c, which have not been made explicit yet. Luong et al. (2005) found this result with the same approach, using $l = \pi a/2 + h$, where h is the orifice thickness, and $\pi a/2$ is the end correction of a circular orifice in a thin plate with irrotational flow on both sides of the plate [Pierce (1981); Howe (1998); Rienstra and Hirschberg (2003)]. By comparing Eq. (5.12) with the asymptotic limits of the linear theory from Howe (1979) (i.e. for St $\ll 1$ and St $\gg 1$), they also showed that the empirical value $C_c = 0.75$ for the contraction coefficient gives a good agreement between the two models at high frequencies, but at low frequencies the agreement is only approximate.

The identification method proposed here is slightly different. There is *a priori* no reason for the end correction length l and the contraction coefficient C_c to be independent of the forcing frequency [Cummings and Eversman (1983)]. It is interesting to compare Eq. (5.12) to the expression obtained using Howe's model

Table 5.1: *Asymptotic values of the end correction length l/a given by Eq. (5.13), and the contraction coefficient C_c given by Eq. (5.14), at low and high Strouhal numbers.*

Regime	l/a	C_c
$\mathrm{St} \ll 1$	$\dfrac{8}{3\pi} \simeq 0.849$	$\dfrac{1}{\sqrt{2}} \simeq 0.707$
$\mathrm{St} \gg 1$	$\dfrac{\pi}{2} \simeq 1.571$	$\sqrt{\dfrac{2}{\pi}} \simeq 0.798$

for the Rayleigh conductivity Eq. (1.17) for an infinitely thin plate ($h = 0$). The effect of the plate thickness h is neglected here, but it will be re-introduced later in the study. By identification of the different terms, these expressions are equal when the contraction coefficient C_c and the mass end correction l are given by:

$$\frac{l}{a} = \frac{\pi}{2}\frac{\gamma}{\gamma^2 + \delta^2} \tag{5.13}$$

$$\frac{1}{C_c^2} = \frac{\pi}{2}\mathrm{St}\frac{\delta}{\gamma^2 + \delta^2} \tag{5.14}$$

The corresponding evolution of l/a and C_c are plotted in Fig. 5.22. They are both monotonic functions of the Strouhal number only, bounded by two asymptotic limits at low and high Strouhal numbers. Using the asymptotic values of the Rayleigh conductivity given by Eqs. (1.20) and (1.21), one obtains the values summarized in Tab. 5.1.

The value found for the contraction coefficient at low Strouhal numbers $C_c \simeq 0.707$ is higher than the theoretical value $C_c \simeq 0.61$ predicted for a steady jet issued from a circular aperture in an infinitely large flanged space (see Batchelor (1967), Durrieu et al. (2001) and Hofmans et al. (2001) for a detailed discussion). However, there is *a priori* no obvious reason why the contraction coefficient of a jet flowing through an orifice subjected to harmonic modulations at low Strouhal numbers should be the same as the one of a steady jet. As St increases, C_c varies between 0.707 and 0.798, close to the optimal empirical values $C_c \simeq 0.75$ found by Cummings (1986), $C_c \simeq 0.76$ found by Hersh and Rogers (1975) or $C_c \simeq 0.82$ found by Bellucci et al. (2004). Simulations of the unsteady flow through an orifice subjected to harmonic modulations were also conducted in this work [Scarpato et al. (2011)]. By post-processing the numerical data, a contraction coefficient $C_c = 0.71$ was found for small perturbation amplitudes and moderate Strouhal numbers ($\mathrm{St} = 0.37$), in agreement with the theoretical values found here.

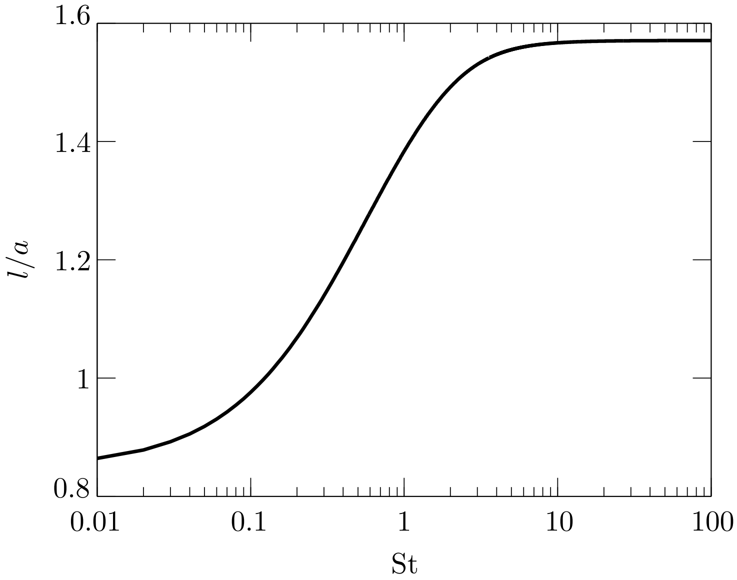

(a) l/a.

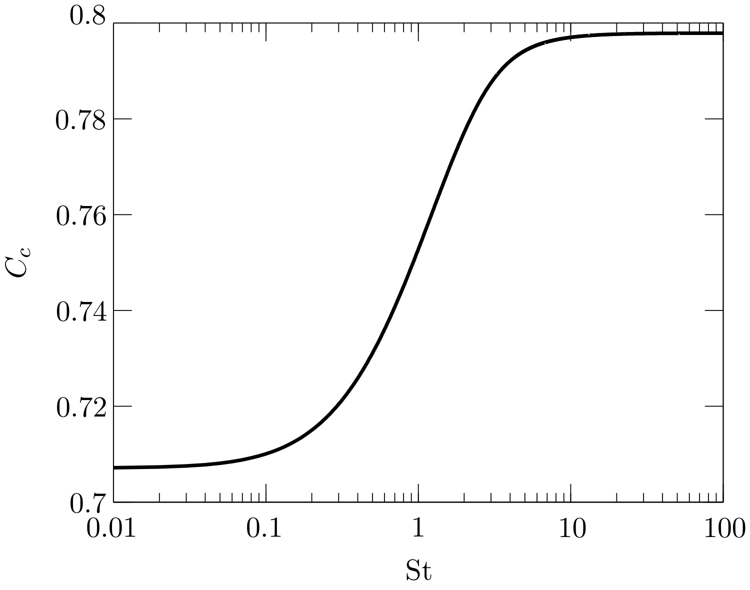

(b) C_c.

Figure 5.22: *Evolutions of the dimensionless mass end correction length* l/a *(a) and the contraction coefficient* C_c *(b) as functions of the Strouhal number* St*, as predicted by the linear theory Eqs. (5.13) and (5.14).*

The low Strouhal expression $l = 8a/(3\pi)$ for the end correction length is consistent with theoretical predictions from Ingard (1953). At high Strouhal numbers, the end correction length increases to $\pi a/2$, which is the end correction for a circular orifice in a thin plate [Pierce (1981); Howe (1998); Rienstra and Hirschberg (2003)]. This value is however always much higher than the end correction for an unflanged pipe determined by Rayleigh (1896) and Levine and Schwinger (1948), which is approximately $l = 0.61a$.

The low and high Strouhal models presented in chapter 4 can be seen as particular cases of the quasi-steady model presented here, when the contraction coefficient C_c and the end correction length l are equal to their respective asymptotic values shown in Tab. 5.1. Equation (5.12) provides an interesting expression for the Rayleigh conductivity that can be used to analyze effects of the contraction coefficient C_c and mass end correction l, which are also function of the aperture geometry and flow in the orifice.

5.2.2.2 Analysis in the nonlinear regime

For harmonic perturbations, the nonlinear expression Eq. (5.8) shows that even when the acoustic velocity in the orifice remains sinusoidal, the pressure drop does not. Introducing $u_0'(t) = \Re\{\tilde{u}_0 e^{-\mathrm{i}\omega t}\} = \tilde{u}_0 \cos(\omega t)$ in the nonlinear term of Eq. (5.8), one obtains the following time-dependent function:

$$f(t) = \left(1 + \frac{\tilde{u}_0}{\bar{u}_0}\cos(\omega t)\right)\left|1 + \frac{\tilde{u}_0}{\bar{u}_0}\cos(\omega t)\right| - 1 \tag{5.15}$$

The function f represents the general form of the (nonlinear) convection term in Bernoulli's equation. The linearized form of this expression yields a linear differential equation which can be easily solved. At moderate to high amplitudes, however, this function must be first expanded in a Fourier series. By considering a new variable $\phi = \omega t$, the Fourier series expansion of f is given by:

$$f(\phi) = \frac{a_0}{2} + \sum_{n=1}^{\infty}\left[a_n \cos(n\phi) + b_n \sin(n\phi)\right] \tag{5.16}$$

where the coefficient a_0, a_n and b_n are defined as follows:

$$a_0 = \frac{1}{\pi}\int_{-\pi}^{\pi} f(\phi)\, d\phi \tag{5.17}$$

$$a_n = \frac{1}{\pi}\int_{-\pi}^{\pi} f(\phi)\cos(n\phi)\, d\phi \tag{5.18}$$

$$b_n = \frac{1}{\pi}\int_{-\pi}^{\pi} f(\phi)\sin(n\phi)\, d\phi \tag{5.19}$$

Three cases must be considered. In the linear regime, when $\tilde{u}_0/\bar{u}_0 \ll 1$, the linearized Bernoulli's equation Eq. (5.10) shows that $f(t) = 2u'_0/\bar{u}_0 = 2(\tilde{u}_0/\bar{u}_0)\cos(\omega t)$.

At moderate amplitudes $\tilde{u}_0/\bar{u}_0 \simeq 1$, when the acoustic velocity cannot be neglected compared to the mean bias flow velocity, but its amplitude is still small enough to avoid reversed flow in the orifice $\tilde{u}_0/\bar{u}_0 \leq 1$, the absolute value in Eq. (5.15) vanishes and a simple calculation gives the following zeroth and first order Fourier coefficients:

$$a'_0 = \left(\frac{\tilde{u}_0}{\bar{u}_0}\right)^2 \tag{5.20}$$

$$a'_1 = 2\frac{\tilde{u}_0}{\bar{u}_0} \tag{5.21}$$

$$b'_1 = 0 \tag{5.22}$$

In the nonlinear regime with reversed flow in the perforation, when $\tilde{u}_0/\bar{u}_0 \geq 1$, a calculation of the zeroth and first order coefficients obtained by using Eq. (5.15) in Eqs. (5.17) to (5.19) gives:

$$a_0 = \left(\frac{\tilde{u}_0}{\bar{u}_0}\right)^2 + \frac{6}{\pi}\left[\left(\frac{\tilde{u}_0}{\bar{u}_0}\right)^2 - 1\right]^{1/2} - \frac{1}{\pi}\left[4 + 2\left(\frac{\tilde{u}_0}{\bar{u}_0}\right)^2\right]\arccos\left(\frac{\bar{u}_0}{\tilde{u}_0}\right) \tag{5.23}$$

$$a_1 = 2\frac{\tilde{u}_0}{\bar{u}_0}\left(1 - \frac{2}{\pi}\arccos\left(\frac{\bar{u}_0}{\tilde{u}_0}\right) + \frac{2}{3\pi}\left[2 + \left(\frac{\bar{u}_0}{\tilde{u}_0}\right)^2\right]\left[\left(\frac{\tilde{u}_0}{\bar{u}_0}\right)^2 - 1\right]^{1/2}\right) \tag{5.24}$$

$$b_1 = 0 \tag{5.25}$$

Figure 5.23 shows the evolution of the Fourier coefficients a_0, a_1, a'_0 and a'_1 as functions of the velocity ratio $\tilde{u}_0/\bar{u}_0$ in the intermediate ($\tilde{u}_0/\bar{u}_0 \leq 1$) and nonlinear regimes ($\tilde{u}_0/\bar{u}_0 > 1$). These functions increase monotonically with the acoustic amplitude. It is interesting to note the continuity of their values when $\tilde{u}_0/\bar{u}_0 = 1$: $a_0(1) = a'_0(1) = 1$, $a_1(1) = a'_1(1) = 2$.

It is now possible to provide a unified model for the function f appearing in Eq. (5.15). Keeping only the zeroth and first order terms of the Fourier series, the nonlinear term f can then be written in the three operating regimes (linear,

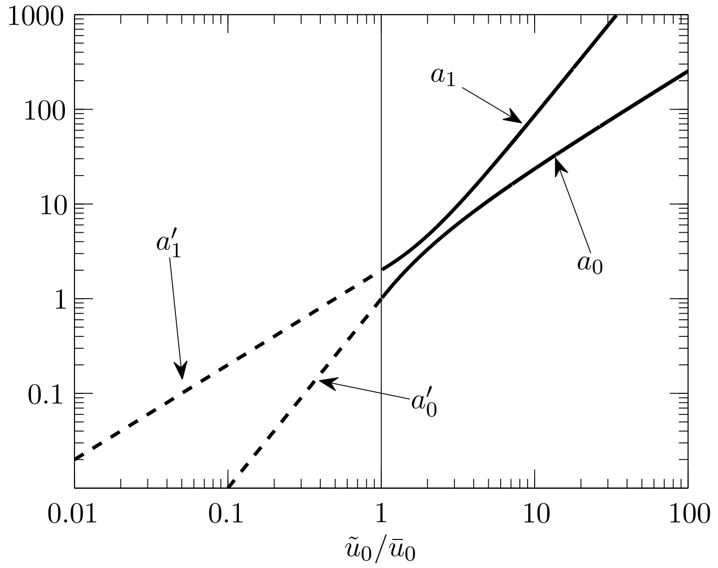

Figure 5.23: *Evolutions of the Fourier coefficients* a_0 *and* a_1 *in the nonlinear regime* $\tilde{u}_0/\bar{u}_0 > 1$*, and* a'_0 *and* a'_1 *in the intermediate regime* $\tilde{u}_0/\bar{u}_0 \leq 1$*, as a function of the velocity ratio* $\tilde{u}_0/\bar{u}_0$ *in the orifice.*

intermediate and nonlinear):

$$f(t) = \begin{cases} 2\dfrac{\tilde{u}_0}{\bar{u}_0}\cos(\omega t) & \text{for } \dfrac{\tilde{u}_0}{\bar{u}_0} \ll 1 \\ \dfrac{a'_0}{2} + a'_1\cos(\omega t) & \text{for } \dfrac{\tilde{u}_0}{\bar{u}_0} \leq 1 \\ \dfrac{a_0}{2} + a_1\cos(\omega t) & \text{for } \dfrac{\tilde{u}_0}{\bar{u}_0} > 1 \end{cases} \tag{5.26}$$

where a_0 and a_1 are defined by Eqs. (5.23) and (5.24), and a'_0 and a'_1 are defined by Eqs. (5.20) and (5.21). With this expansion the nonlinearity of f has been shifted to these coefficients, which depend on the velocity ratio $\tilde{u}_0/\bar{u}_0$.

In the linear regime $\tilde{u}_0/\bar{u}_0 \ll 1$, the expression for $f(t)$ is exact, i.e. the only contribution of the convective term is at the forcing frequency ω. In the intermediate and nonlinear regimes, these expressions correspond to an approximation to the first order, and higher harmonics due to nonlinear effects exist. However they are discarded in the present approach, since we only analyze the response of the perforated plate at the forcing frequency ω. Note also that the coefficients a_0 and a'_0 represent a reduction in the mean volume flowrate passing through the perforation produced by the unsteady acoustic perturbation [Luong et al. (2005)]. The effect is however small, and will be neglected in this study.

5.2.3 Impedance Describing Function

Keeping only the first order terms, and taking advantage of the fact that the first order Fourier coefficients remain unchanged in the linear and intermediate regimes, it is then possible to further simplify the system of equations (5.26):

$$f(t) = 2\frac{\tilde{u}_0}{\bar{u}_0}\xi\left(\frac{\tilde{u}_0}{\bar{u}_0}\right)\cos(\omega t) \tag{5.27}$$

where ξ is given by:

$$\xi(\psi) = \begin{cases} 1 & \text{for} \quad \psi \leq 1 \\ 1 - \dfrac{2}{\pi}\arccos\left(\dfrac{1}{\psi}\right) + \dfrac{2}{3\pi}\left[2 + \left(\dfrac{1}{\psi}\right)^2\right]\left(\psi^2 - 1\right)^{1/2} & \text{for} \quad \psi > 1 \end{cases}$$

Introducing Eq. (5.27) in Bernoulli's equation Eq. (5.9) and converting this expression in the frequency domain, one obtains:

$$\tilde{p}_2 - \tilde{p}_1 = \rho_0\bar{u}_0\tilde{u}_0\left[\frac{\mathrm{i}\omega l}{\bar{u}_0} - \frac{1}{C_c^2}\xi\left(\frac{\tilde{u}_0}{\bar{u}_0}\right)\right] \tag{5.28}$$

Note the similarity of this expression for the nonlinear unsteady pressure drop with its expression Eq. (5.11) in the linear regime, where $\xi(\tilde{u}_0/\bar{u}_0) = 1$.
It is now possible to use Eq. (5.28) to determine the Rayleigh conductivity of the perforated plate in the nonlinear regime, defined by Eq. (1.13). The nonlinear Rayleigh conductivity K_R is thus given by:

$$\frac{K_R}{2a} = \frac{\pi\mathrm{St}}{2\mathrm{St}\dfrac{l}{a} + \dfrac{2\mathrm{i}}{C_c^2}\xi\left(\dfrac{\tilde{u}_0}{\bar{u}_0}\right)} = \gamma_{\mathrm{NL}} - \mathrm{i}\delta_{\mathrm{NL}} \tag{5.29}$$

where we also introduced the functions $\gamma_{\mathrm{NL}}(\mathrm{St}, \tilde{u}_0/\bar{u}_0)$ and $\delta_{\mathrm{NL}}(\mathrm{St}, \tilde{u}_0/\bar{u}_0)$, which are formally equivalent to the $\gamma(\mathrm{St})$ and $\delta(\mathrm{St})$ functions defined by Eq. (1.17) and introduced by Howe (1979) in the framework of his linear theory. This expression is also valid in the linear regime, since when $\tilde{u}_0/\bar{u}_0 \leq 1$, $\xi = 1$, Eq. (5.29) is equivalent to the linear expression Eq. (5.12), and $\gamma_{\mathrm{NL}} - \mathrm{i}\delta_{\mathrm{NL}} = \gamma - \mathrm{i}\delta$.

In this approach the end correction length l and the contraction coefficient C_c have been supposed to be independent of the sound level. They are defined by the expressions Eqs. (5.13) and (5.14) obtained in the linear regime, and they depend here only on the Strouhal number St.

The real and imaginary components of the normalized Rayleigh conductivity $K_R/(2a)$ are plotted in Fig. 5.24 as a function of the Strouhal number St for increasing values of the acoustic perturbation level $\tilde{u}_0/\bar{u}_0$. The main effect of the

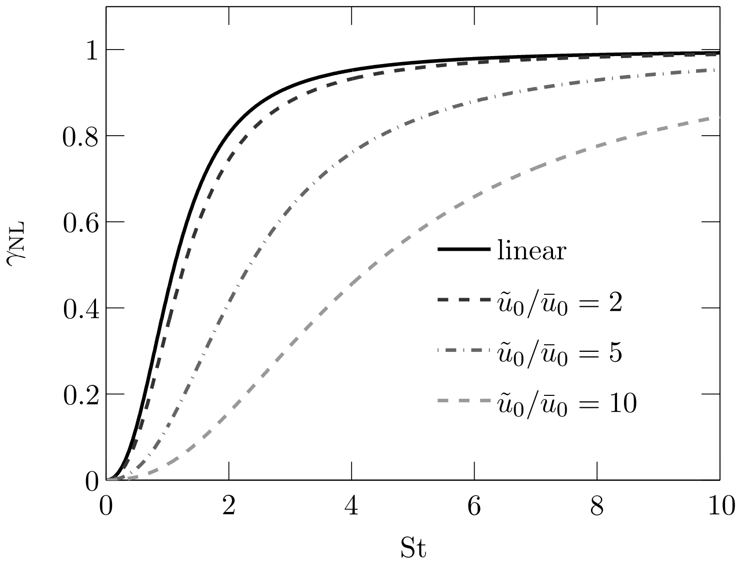

(a) Real component of $K_R/(2a)$.

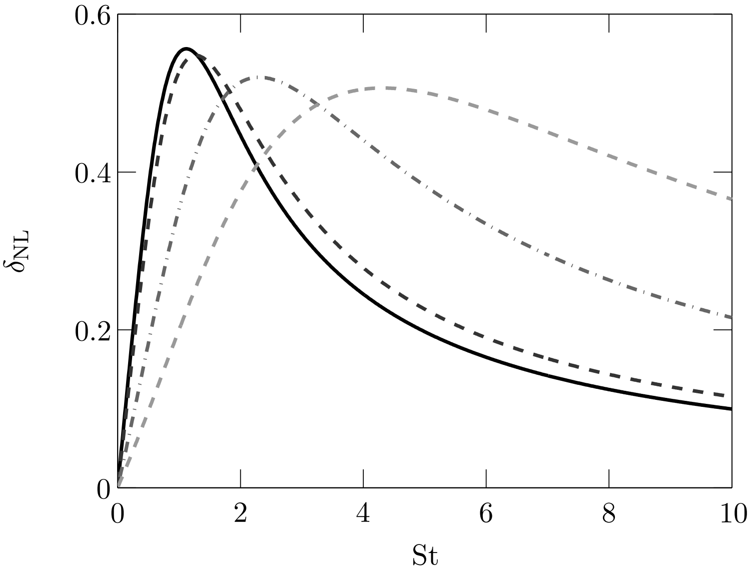

(b) Imaginary component of $K_R/(2a)$.

Figure 5.24: *Evolution of the real component* $\gamma_{\rm NL}$ *(a) and of the imaginary component* $\delta_{\rm NL}$ *(b) of the nonlinear Rayleigh conductivity* K_R*, given by Eq. (5.29), as functions of the Strouhal number* St *and for different acoustic perturbation amplitudes* $\tilde{u}_0/\bar{u}_0$*.*

perturbation level is to shift both the real and imaginary components towards higher Strouhal numbers. However the peak value of the imaginary component δ_{NL} decreases when the acoustic amplitude increases. This particular behavior has consequences on the acoustic power dissipated at the perforation. Indeed Howe (1998) showed that, at low Mach numbers, the power Π dissipated at the aperture, i.e. the power extracted from the fluctuating pressure difference across the plate $\tilde{p}_1 - \tilde{p}_2$ and converted into vorticity, is directly proportional to the imaginary component of the Rayleigh conductivity δ_{NL}:

$$\Pi = \rho_0 \int_{\mathcal{V}} \boldsymbol{\omega} \wedge \boldsymbol{u} \cdot \boldsymbol{u}'_{\mathrm{ac}} d\mathcal{V} = \frac{|\tilde{p}_1 - \tilde{p}_2|^2 a \delta_{\mathrm{NL}}}{\rho_0 \omega} \tag{5.30}$$

Introducing Eq. (5.28) in Eq. (5.30), one obtains the following expression for the average normalized acoustic power dissipated at the perforation:

$$\frac{\Pi}{\rho_0 \bar{u}_0^3 A_0} = \frac{\xi}{2C_c^2} \left(\frac{\tilde{u}_0}{\bar{u}_0} \right)^2 \tag{5.31}$$

where $A_0 = \pi a^2$ is the orifice surface area. The acoustic power Π is thus a function of the acoustic perturbation level $\tilde{u}_0/\bar{u}_0$, and depends only weakly on the Strouhal number St. According to Eq. (5.14), the contraction ratio C_c is approximately independent of St, and Tab. 5.1 shows that $2C_c^2 \simeq 1$. This is confirmed by Fig. 5.25, where the normalized acoustic power $\Pi/(\rho_0 \bar{u}_0^3 A_0)$ is plotted with a log scale as a function of $\tilde{u}_0/\bar{u}_0$, for different values of the Strouhal number. In the linear regime, when $\tilde{u}_0/\bar{u}_0 \leq 1$, $\xi = 1$ and the acoustic power dissipated increases as the square of the acoustic perturbation level. In the nonlinear regime, the dependence is approximately cubic. This is in agreement with the analysis of the orders of magnitude performed by Howe (1998) and Luong et al. (2005). Let the acoustic perturbation $\boldsymbol{u}'_{\mathrm{ac}}$ be $\mathcal{O}(\varepsilon)$. At low acoustic amplitudes, both the shed vorticity $\boldsymbol{\omega}$ and the local flow velocity $\boldsymbol{u}$ have large mean components, so that the term $\boldsymbol{\omega} \wedge \boldsymbol{u}$ appearing in Eq. (5.30) is $\mathcal{O}(\varepsilon)$, and the dissipated power is second order in the acoustic amplitude $\Pi \sim \mathcal{O}(\varepsilon^2)$. In the nonlinear regime, $\boldsymbol{\omega}$, $\boldsymbol{u}$ and $\boldsymbol{u}'_{\mathrm{ac}}$ are all $\mathcal{O}(\varepsilon)$, implying that the acoustic power scales with the third order in acoustic amplitude $\Pi \sim \mathcal{O}(\varepsilon^3)$.

5.2.4 IDF model with a back cavity

Let us consider now the case of a perforated plate backed by a resonant cavity and subjected to acoustic waves of increasing amplitude. In chapter 1 we found an expression Eq. (1.38) for the specific impedance of this system in the linear regime, as function of the dimensionless parameters St, h/a, He and M_c/σ. Assuming that at high acoustic amplitudes, nonlinear effects are confined in the region near the perforation, and that the wave propagation can still be described by linear acoustics far from the orifice, introducing the nonlinear

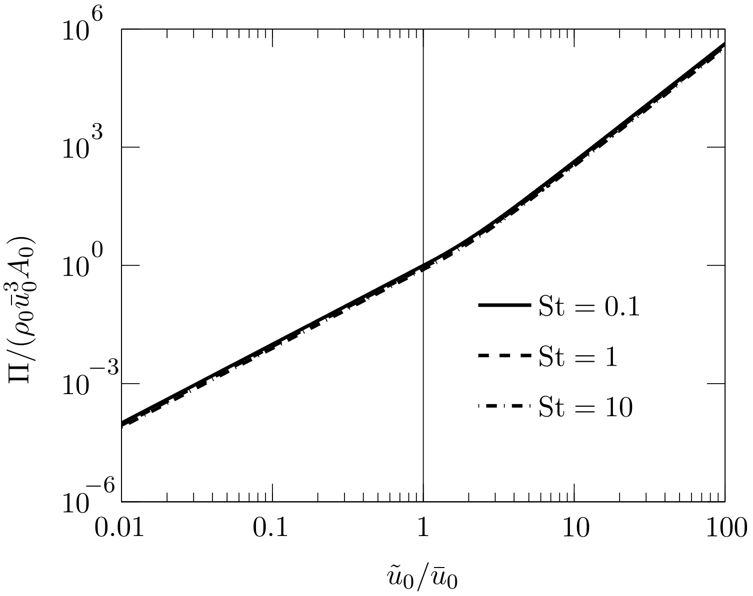

Figure 5.25: *Evolution of the average normalized acoustic power dissipated at the aperture* $\Pi/(\rho_0 \bar{u}_0^3 A_0)$ *as a function of the acoustic perturbation level* $\tilde{u}_0/\bar{u}_0$*, given by Eq. (5.31), for different values of the Strouhal number* St.

expression for the Rayleigh conductivity Eq. (5.29) in Eq. (1.38) yields:

$$\zeta = \mathrm{i}\left[\frac{\pi}{2}\mathrm{St}\frac{\mathrm{M}_c}{\sigma}\left(\frac{1}{\chi(\mathrm{St}, \tilde{u}_0/\bar{u}_0)} + \frac{2h}{\pi a}\right) - \frac{1}{\tan(\mathrm{He})}\right] \tag{5.32}$$

where

$$\chi(\mathrm{St}, \tilde{u}_0/\bar{u}_0) = \frac{K_R}{2a} = \gamma_{\mathrm{NL}} - \mathrm{i}\delta_{\mathrm{NL}} \tag{5.33}$$

and the function γ_{NL} and δ_{NL} are given by Eq. (5.29). The expression Eq. (5.32) defines an Impedance Describing Function (IDF), which takes into account the effect of amplitude at the forcing frequency on the response of the perforate backed by a cavity. In the linear regime, for $\tilde{u}_0 \leq \bar{u}_0$, Eq. (5.32) is strictly equivalent to Eq. (1.38). Note that the effect of plate thickness is taken into account with the model from Jing and Sun (2000).

It is now possible to introduce Eq. (5.29) in Eq. (5.32), and separate the real and imaginary components of the specific impedance, yielding:

$$\zeta = \mathrm{i}\left[\mathrm{St}\frac{\mathrm{M}_c}{\sigma}\frac{l+h}{a} - \frac{1}{\tan(\mathrm{He})}\right] - \frac{\mathrm{M}_c}{\sigma}\frac{\xi(\tilde{u}_0/\bar{u}_0)}{C_c^2} \tag{5.34}$$

The term $l_{\mathrm{eff}} = l + h$ is the *effective* length of the oscillating mass of fluid in the orifice, which takes into account the plate thickness h and the end correction length l. Equation (5.34) also shows that, in the framework of the IDF model, the acoustic amplitude has only an effect on the real component (the resistance) of the specific impedance, and that the imaginary component (the reactance) is independent of the forcing sound pressure level. In their experimental work, Ingard and Ising (1967) showed that the reactance of the investigated orifice decreased slightly at high acoustic amplitudes. However, very rapidly after the onset of nonlinearity, the increasing resistance becomes the dominant contribution to the impedance, thus making the variation of the reactance negligible. At high acoustic velocities, measurements carried out by Ingard and Ising (1967) indicate that $|\zeta| \simeq \Re(\zeta)$.

5.2.5 Effect of amplitude on maximum absorption

The knowledge of the specific impedance in the linear and nonlinear regimes allows the determination of the absorption properties of the perforated plate. It is thus possible, following the approach presented in chapter 4, to analyze the conditions maximizing acoustic absorption $\alpha = 1 - |R|^2$ at high forcing amplitudes.

The reflection coefficient R being given by Eq. (1.37) $R = (\zeta+1)/(\zeta-1)$, using Eq. (5.34) one obtains in the nonlinear regime:

$$R = \frac{\mathrm{i}\left[\mathrm{St}\dfrac{\mathrm{M}_c}{\sigma}\dfrac{l+h}{a} - \dfrac{1}{\tan(\mathrm{He})}\right] + \left(1 - \dfrac{\mathrm{M}_c}{\sigma}\dfrac{\xi}{C_c^2}\right)}{\mathrm{i}\left[\mathrm{St}\dfrac{\mathrm{M}_c}{\sigma}\dfrac{l+h}{a} - \dfrac{1}{\tan(\mathrm{He})}\right] - \left(1 + \dfrac{\mathrm{M}_c}{\sigma}\dfrac{\xi}{C_c^2}\right)} \tag{5.35}$$

The set of conditions Eqs. (4.1) and (4.2) maximizing absorption examined in chapter 4 still holds. Using Eq. (5.35), and introducing the expressions Eq. (5.13) found for the end correction length l and Eq. (5.14) for the contraction coefficient C_c, the conditions that set the reflection coefficient to zero $R = 0$ are:

$$\frac{\mathrm{M}_c}{\sigma} = \frac{2}{\pi \mathrm{St}}\frac{\gamma^2+\delta^2}{\delta}\frac{1}{\xi} \tag{5.36}$$

$$\frac{1}{\tan(\mathrm{He})} = \left[\frac{\gamma}{\delta} + \frac{2h}{\pi a}\frac{\gamma^2+\delta^2}{\delta}\right]\frac{1}{\xi} \tag{5.37}$$

The evolutions of the optimal ratio M_c/σ and of the optimal Helmholtz number He are shown in Fig. 5.26, for an infinitely thin plate, when $h = 0$. The effect of nonlinearity for the set of parameters maximizing absorption is twofold. When the perturbation level increases, the value for the optimal ratio M_c/σ decreases, and the influence of the Strouhal number weakens, whereas the optimal Helmholtz number is shifted towards higher Strouhal numbers.

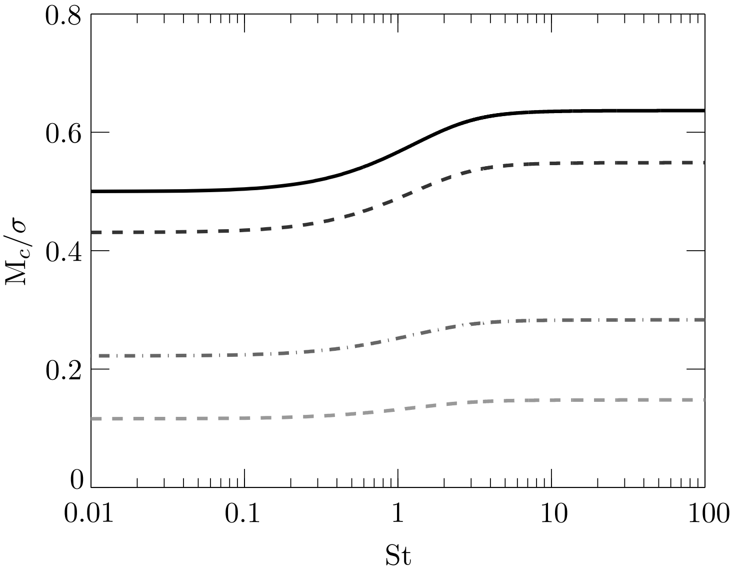

(a)

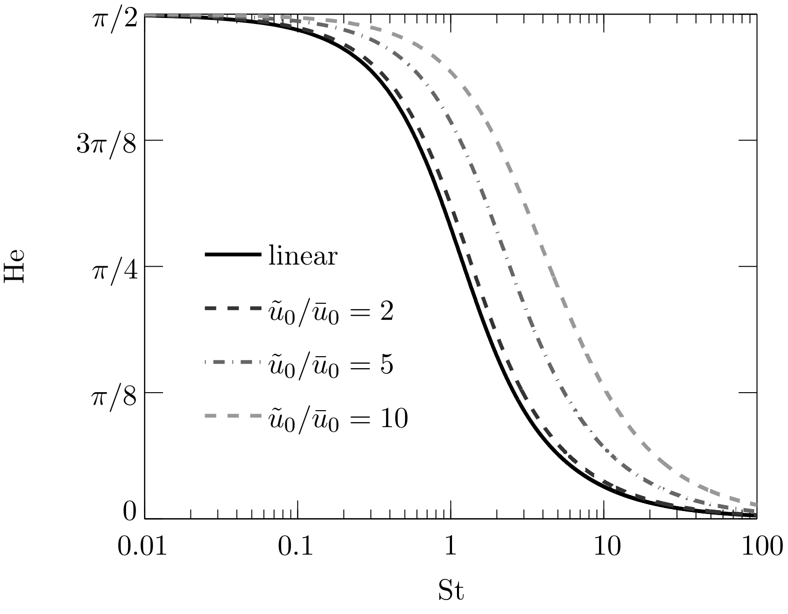

(b)

Figure 5.26: *Evolution of the ratio* M_c/σ *(a) and of the Helmholtz number* He *(b) maximizing acoustic absorption, as functions of the Strouhal number* St, *for an infinitely thin plate* $h = 0$ *and for increasing values of the perturbation level* $\tilde{u}_0/\bar{u}_0$.

5.3 Comparison with measurements and simulations

In the present section, different models from the literature and those developed in this work are used to compare results for the reflection, transmission and absorption coefficients with direct numerical simulations and measurements. These models are summarized in Tab. 5.2 for the case of a perforated plate without back cavity, and in Tab. 5.3 for the case with a back cavity.
The reflection, transmission and absorption coefficients are first calculated for increasing sound levels in section 5.3.1, at different forcing frequencies and for different perforated plates with and without back cavity (Tab. 5.4). From an acoustic energy balance, the power dissipated by these systems is deduced from direct calculations, and compared with predictions from nonlinear models.

Table 5.2: *Models for the reflection R and transmission T coefficients of a perforated plate without a back cavity. The absorption coefficient is given by $\alpha = 1 - |R|^2 - |T|^2$.*

Model	R	T
Howe (linear)	$R = \dfrac{\mathrm{i}\dfrac{\pi}{4}\mathrm{St}\dfrac{\mathrm{M}_c}{\sigma}}{\mathrm{i}\dfrac{\pi}{4}\mathrm{St}\dfrac{\mathrm{M}_c}{\sigma} - (\gamma - \mathrm{i}\delta)}$	$T = \dfrac{\gamma - \mathrm{i}\delta}{\gamma - \mathrm{i}\delta - \mathrm{i}\dfrac{\pi}{4}\mathrm{St}\dfrac{\mathrm{M}_c}{\sigma}}$
Vortex Convection (nonlinear)	$R = \dfrac{\mathrm{i}\dfrac{\pi}{4}\mathrm{St}\dfrac{\mathrm{M}_c}{\sigma}}{\mathrm{i}\dfrac{\pi}{4}\mathrm{St}\dfrac{\mathrm{M}_c}{\sigma} - (\gamma_{\mathrm{VC}} - \mathrm{i}\delta_{\mathrm{VC}})}$	$T = \dfrac{\gamma_{\mathrm{VC}} - \mathrm{i}\delta_{\mathrm{VC}}}{\gamma_{\mathrm{VC}} - \mathrm{i}\delta_{\mathrm{VC}} - \mathrm{i}\dfrac{\pi}{4}\mathrm{St}\dfrac{\mathrm{M}_c}{\sigma}}$
Impedance Describing Function (nonlinear)	$R = \dfrac{\mathrm{i}\dfrac{\pi}{4}\mathrm{St}\dfrac{\mathrm{M}_c}{\sigma}}{\mathrm{i}\dfrac{\pi}{4}\mathrm{St}\dfrac{\mathrm{M}_c}{\sigma} - (\gamma_{\mathrm{NL}} - \mathrm{i}\delta_{\mathrm{NL}})}$	$T = \dfrac{\gamma_{\mathrm{NL}} - \mathrm{i}\delta_{\mathrm{NL}}}{\gamma_{\mathrm{NL}} - \mathrm{i}\delta_{\mathrm{NL}} - \mathrm{i}\dfrac{\pi}{4}\mathrm{St}\dfrac{\mathrm{M}_c}{\sigma}}$

Table 5.3: *Models for the reflection coefficient R of a perforated plate with a back cavity. The absorption coefficient is given by* $\alpha = 1-|R|^2$.

Model	$\lvert R\rvert$
Howe (linear)	$R = \dfrac{\mathrm{i}\left[\dfrac{\pi}{2}\mathrm{St}\dfrac{\mathrm{M}_c}{\sigma}\left(\dfrac{1}{\gamma-\mathrm{i}\delta}+\dfrac{2h}{\pi a}\right)-\dfrac{1}{\tan(\mathrm{He})}\right]+1}{\mathrm{i}\left[\dfrac{\pi}{2}\mathrm{St}\dfrac{\mathrm{M}_c}{\sigma}\left(\dfrac{1}{\gamma-\mathrm{i}\delta}+\dfrac{2h}{\pi a}\right)-\dfrac{1}{\tan(\mathrm{He})}\right]-1}$
Ingard and Ising (nonlinear)	$R = \dfrac{\dfrac{\tilde{u}_0}{\bar{u}_0}\dfrac{\mathrm{M}_c}{\sigma}-1}{\dfrac{\tilde{u}_0}{\bar{u}_0}\dfrac{\mathrm{M}_c}{\sigma}+1}$
Vortex Convection (nonlinear)	$R = \dfrac{\mathrm{i}\left[\dfrac{\pi}{2}\mathrm{St}\dfrac{\mathrm{M}_c}{\sigma}\left(\dfrac{1}{\gamma_{\mathrm{VC}}-\mathrm{i}\delta_{\mathrm{VC}}}+\dfrac{2h}{\pi a}\right)-\dfrac{1}{\tan(\mathrm{He})}\right]+1}{\mathrm{i}\left[\dfrac{\pi}{2}\mathrm{St}\dfrac{\mathrm{M}_c}{\sigma}\left(\dfrac{1}{\gamma_{\mathrm{VC}}-\mathrm{i}\delta_{\mathrm{VC}}}+\dfrac{2h}{\pi a}\right)-\dfrac{1}{\tan(\mathrm{He})}\right]-1}$
Impedance Describing Function (nonlinear)	$R = \dfrac{\mathrm{i}\left[\mathrm{St}\dfrac{\mathrm{M}_c}{\sigma}\dfrac{l+h}{a}-\dfrac{1}{\tan(\mathrm{He})}\right]+\left(1-\dfrac{\mathrm{M}_c}{\sigma}\dfrac{\xi}{C_c^2}\right)}{\mathrm{i}\left[\mathrm{St}\dfrac{\mathrm{M}_c}{\sigma}\dfrac{l+h}{a}-\dfrac{1}{\tan(\mathrm{He})}\right]-\left(1+\dfrac{\mathrm{M}_c}{\sigma}\dfrac{\xi}{C_c^2}\right)}$

Table 5.4: *Configurations used for comparison of the acoustic properties.*

Case	Plate	Back cavity	f [Hz]	DNS	Experiments	Models
1	P_6	None	400	✓	X	✓
2	P_6	$L = 150$ mm	400	✓	✓	✓
3	P_6	$L = 150$ mm	800	✓	✓	✓
4	P_8	$L = 150$ mm	400	X	✓	✓
5	P_8	$L = 150$ mm	800	X	✓	✓

5.3.1 Reflection, transmission and absorption coefficients

The acoustic coefficients are determined for several configurations, which are summarized in Tab. 5.4. Two different plate geometries are investigated here: plate P_6 and plate P_8. For the former, results from numerical simulations are examined at the two forcing frequencies of $f = 400$ Hz and $f = 800$ Hz, with and without a resonant back cavity. These numerical results are compared to theoretical predictions and experiments from the ITHACA test bench. Simulations were not carried out for plate P_8. Predictions from the different models are compared to measurements at $f = 400$ Hz and $f = 800$ Hz.

Both plates P_6 and P_8 have been tested at incident sound pressure levels up to 150 dB, corresponding to acoustic velocity fluctuations in the orifice $\tilde{u}_0$ of up to 8 times the mean bias flow velocity in the perforation $\bar{u}_0$. Additionally, plate P_6 has been simulated with acoustic perturbations up to 160 dB, corresponding to $\tilde{u}_0/\bar{u}_0 = 23$.

5.3.1.1 Analysis without back cavity

The response of plate P_6 has been simulated without resonant back cavity by imposing non-reflecting inlet boundary conditions (case 1 in Tab. 5.4). The simulated system represents then the response of a perforated plate in an infinite length duct. This kind of configuration is frequently encountered in ducts, where flow restrictions or grids are used to generate isotropic turbulence to correct non-homogeneities of the flow, or diaphragms are set to measure the flowrate. A schematic view of this configuration is presented in Fig. 5.27.

The reflection coefficient of this damper and its transmission properties are analyzed. The evolution of the reflection and transmission coefficients is shown in Fig. 5.28(a) as a function of the velocity fluctuation in the orifice $\tilde{u}_0/\bar{u}_0$, for a forcing frequency $f = 400$ Hz. The modulus of the reflection and transmission coefficients deduced from the simulations are compared to predictions from Howe's linear model, the Vortex Convection and the Impedance Describing

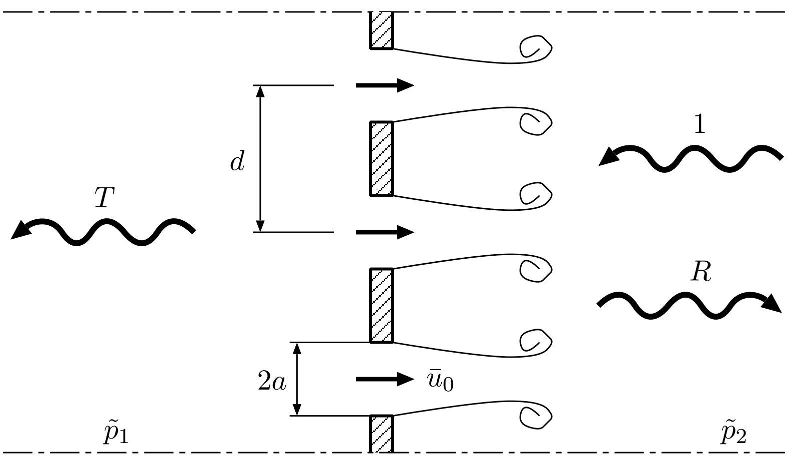

Figure 5.27: *Perforated plate without back cavity traversed by a bias flow and subjected to normal incident pressure waves. Circular holes of diameter* $2a$ *are regularly spaced with a square pattern of size* d*. The complex amplitudes of the reflected and transmitted wave are denoted* R *and* T*, respectively.*

Function nonlinear models, summarized in Tab. 5.2. As expected, the agreement with the linear model is good at low to moderate excitation levels when $\tilde{u}_0/\bar{u}_0 \leq 1$ (corresponding to incident SPL up to 120 dB), thus validating the methodology.

The scenario changes in the nonlinear regime. For sound levels larger than 130 dB ($\tilde{u}_0/\bar{u}_0 > 1$), $|R|$ and $|T|$ depend on the acoustic perturbation amplitude. The reflected wave amplitude increases, whereas the amplitude of the transmitted wave decreases when the sound level increases. The linear model does not capture these modifications. Results from the simulations are also compared to the new nonlinear models developed in the present work. Both the IDF and the VC models show a reasonably good agreement with the simulations. At very low acoustic amplitudes, the two models collapse on the linear model, demonstrating their consistency in the linear regime. At $\tilde{u}_0/\bar{u}_0 \simeq 0.1$, the VC model starts to deviate from the linear values of $|R|$ and $|T|$. This behavior is not observed in the IDF model and the simulations, where nonlinear effects only appear when $\tilde{u}_0/\bar{u}_0 > 1$. The agreement between numerical results and the IDF and VC models is good in the nonlinear regime, when $\tilde{u}_0/\bar{u}_0 \geq 3$. The main differences between direct simulations and nonlinear models are observed for intermediate perturbation levels when $\tilde{u}_0/\bar{u}_0 \simeq 1$.

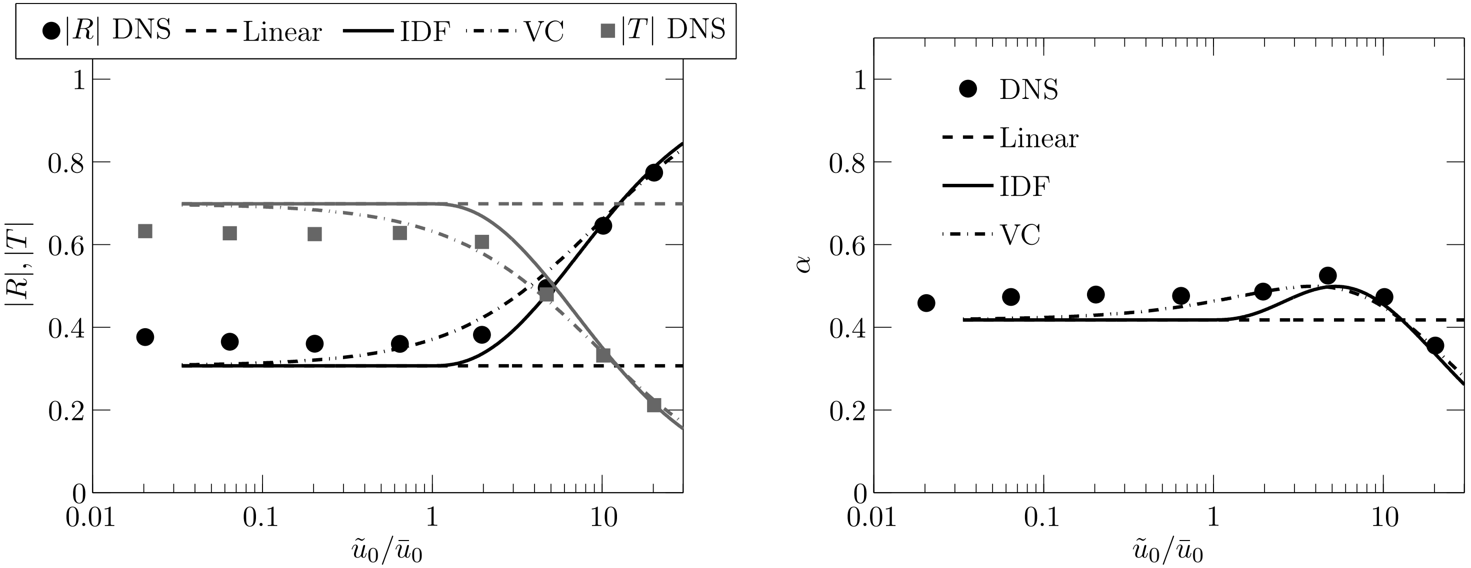

(a) $|R|, |T|$.

(b) $\alpha = 1 - |R|^2 - |T|^2$.

Figure 5.28: *Results for plate P_6 without resonant cavity (Case 1 in Tab. 5.4). Evolution of the modulus of the reflection $|R|$ and transmission $|T|$ coefficients (a), and of the absorption coefficient α (b), as a function of the velocity fluctuation in the orifice $\tilde{u}_0/\bar{u}_0$. The forcing frequency is $f = 400$ Hz. DNS results for $|R|$ (black circles) and $|T|$ (gray squares) are compared to predictions from Howe's linear model (dashed lines), the Vortex Convection model (dash-dotted lines) and the Impedance Describing Function model (solid lines).*

Figure 5.28(b) plots the evolution of the absorption coefficient $\alpha = 1-|R|^2-|T|^2$ as a function of $\tilde{u}_0/\bar{u}_0$ in the orifice calculated by DNS and by the different models. Again, the results from simulations match well with the linear predictions of the absorption coefficient α for perturbation levels lower than $\tilde{u}_0/\bar{u}_0 = 1$. Absorption remains roughly constant over the linear range of perturbation levels explored, before increasing up to a maximum value reached when $\tilde{u}_0/\bar{u}_0 \simeq 5$, and finally decreasing at very high perturbation amplitudes. Both the IDF and the VC models predict well the nonlinear behavior at high amplitudes.

It is worth noting that the way incident acoustic energy is dissipated differs at low and high amplitudes. This can be highlighted by comparing Figs. 5.28(a) and 5.28(b). The contributions of the reflected and the transmitted waves to absorption $\alpha = 1-|R|^2-|T|^2$ are examined. As long as the velocity fluctuation within the orifice $\tilde{u}_0$ remains smaller than the mean bias flow velocity $\bar{u}_0$, the reflection and transmission coefficients remain independent of the sound level. Sound absorption within this orifice at a forcing frequency of 400 Hz nearly reaches the maximal theoretical value $\alpha_{\max} = 0.5$ [Howe (1998)]. This is mainly due to the low amplitude of the reflected wave. When the velocity fluctuation $\tilde{u}_0$ exceeds the mean bias flow velocity, the modulus of the reflection coefficient begins to increase with increasing amplitude and its contribution to absorption drops correspondingly. This loss is however balanced by the increasing contribution of the transmitted wave, because its modulus $|T|$ decreases with the forcing amplitude. Globally, the energy transfer process taking place between the acoustic field and the unsteady flow leads to approximately the same fraction of acoustic energy dissipated for velocity perturbation levels lower than $\tilde{u}_0 \simeq 10\bar{u}_0$. This is an interesting result indicating that dampers traversed by a mean bias flow $\bar{u}_0$ designed and optimized with linear models maintain their absorption properties near their optimal operating conditions even when flow reversal takes place within the orifices, as long as $\tilde{u}_0/\bar{u}_0 \leq 10$.

5.3.1.2 Analysis with back cavity

Effects of the presence of a back cavity coupled to a perforated plate are investigated in this section. This configuration is sketched in Fig. 5.29. Simulation results are compared in Fig. 5.30 to measurements carried out in the ITHACA test bench and to predictions of the different theoretical models summarized in Tab. 5.3. Plate P_6 is subjected to harmonic perturbations at a forcing frequency $f = 400$ Hz and backed by a cavity of size $L = 150$ mm. Measurements were obtained by keeping a constant excitation frequency and varying the amplitude of the incident acoustic waves. Figure 5.30(a) shows the modulus of the reflection coefficient $|R|$, and Fig. 5.30(b) plots the absorption coefficient $\alpha = 1-|R|^2$.

In the linear regime when $\tilde{u}_0/\bar{u}_0 \leq 1$, the agreement between the simulations

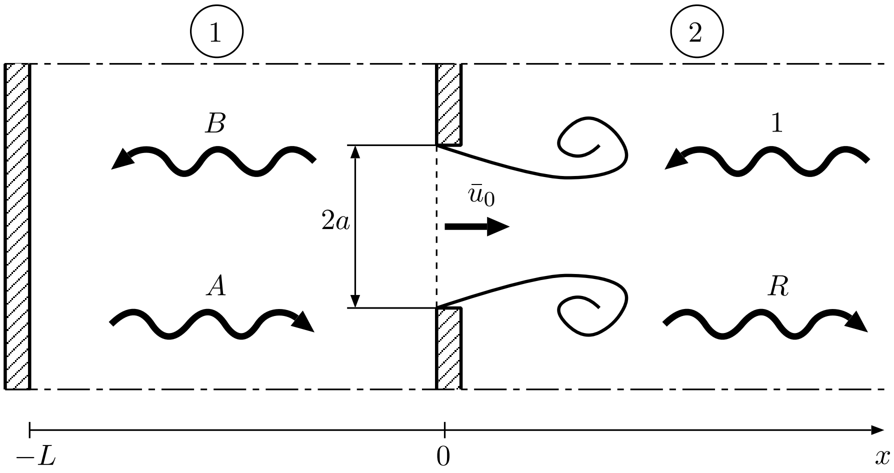

Figure 5.29: *Perforated plate traversed by a bias flow and subjected to normal incident pressure waves. Circular holes of diameter $2a$ are regularly spaced with a square pattern of size d. The plate is coupled to a resonant back cavity, of size L. The complex amplitude of the reflected wave is denoted R.*

and the IDF and VC models is good. At $f = 400$ Hz, the damper operates close to optimal conditions, with maximum acoustic absorption $\alpha \simeq 1$. The measured absorption coefficient is slightly lower than unity in Fig. 5.30(b), but this may be due to experimental uncertainties. Interaction of the sound field with the flow in the air injection units in the back cavity probably also takes place, artificially increasing the back cavity reflection coefficient amplitude. A specific work on reducing this contribution is left for future studies. These differences were already noted in the measurements shown in chapter 4. It is also interesting to note that the nonlinear model proposed by Ingard and Ising (1967) does not capture the observed absorption in the linear regime, since it does not take into account the effect of the mean flow.

For higher acoustic amplitudes $\tilde{u}_0/\bar{u}_0 > 1$, the reflection coefficient decreases and reaches a minimum $|R| = 0$ at $\tilde{u}_0/\bar{u}_0 \simeq 2$. The IDF model, as well as the empirical model from Ingard and Ising (1967), satisfactorily capture this transition, while in the VC model the transition takes place at lower acoustic amplitudes. Then the reflection coefficient increases again and the absorption properties are deteriorated at very high amplitudes. The agreement between all the models, experiments and simulations is good again for $\tilde{u}_0/\bar{u}_0 \geq 5$.

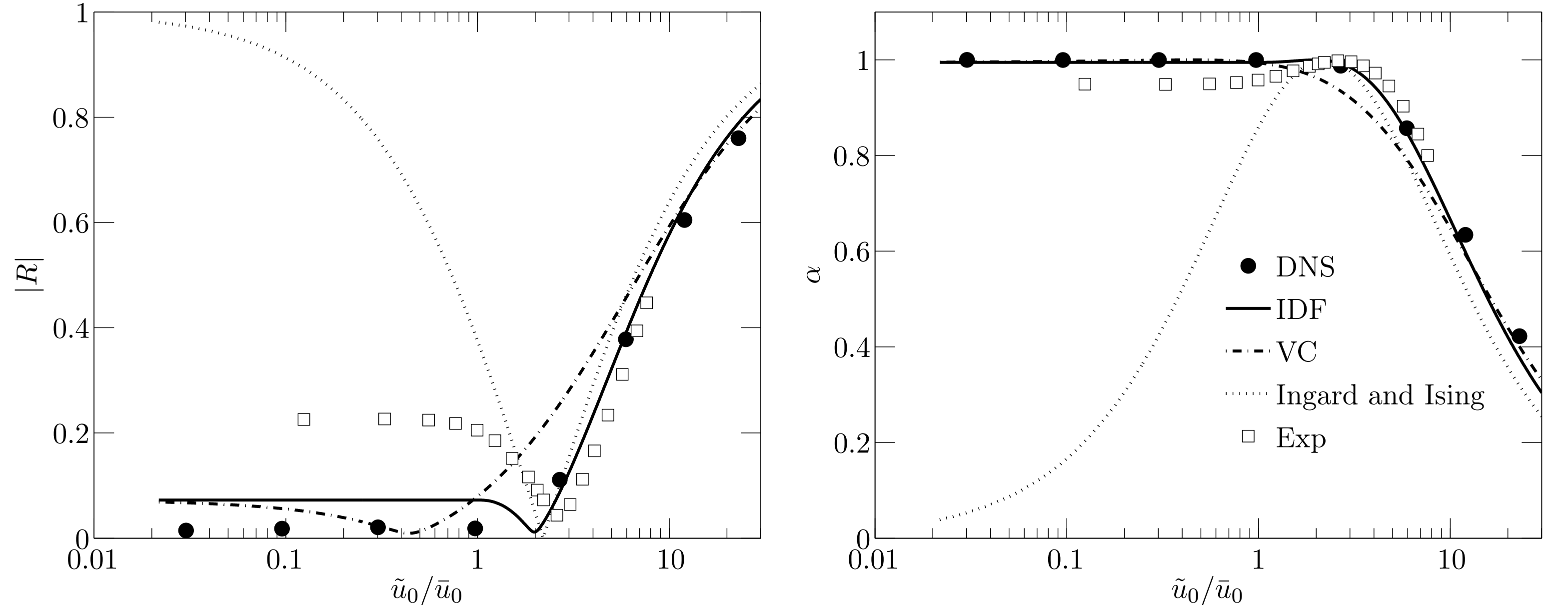

(a) $|R|$.

(b) $\alpha = 1 - |R|^2$.

Figure 5.30: *Results for plate P_6 with a resonant cavity of size $L = 150$ mm (Case 2 in Tab. 5.4). Evolution of the modulus of the reflection coefficient $|R|$ (a), and of the absorption coefficient α (b), as a function of the velocity fluctuation in the orifice $\tilde{u}_0/\bar{u}_0$. The forcing frequency is $f = 400$ Hz. DNS results (black circles) and ITHACA measurements (white squares) are compared to predictions from Ingard and Ising's model (dotted lines), the Vortex Convection model (dash-dotted lines) and the Impedance Describing Function model (solid lines).*

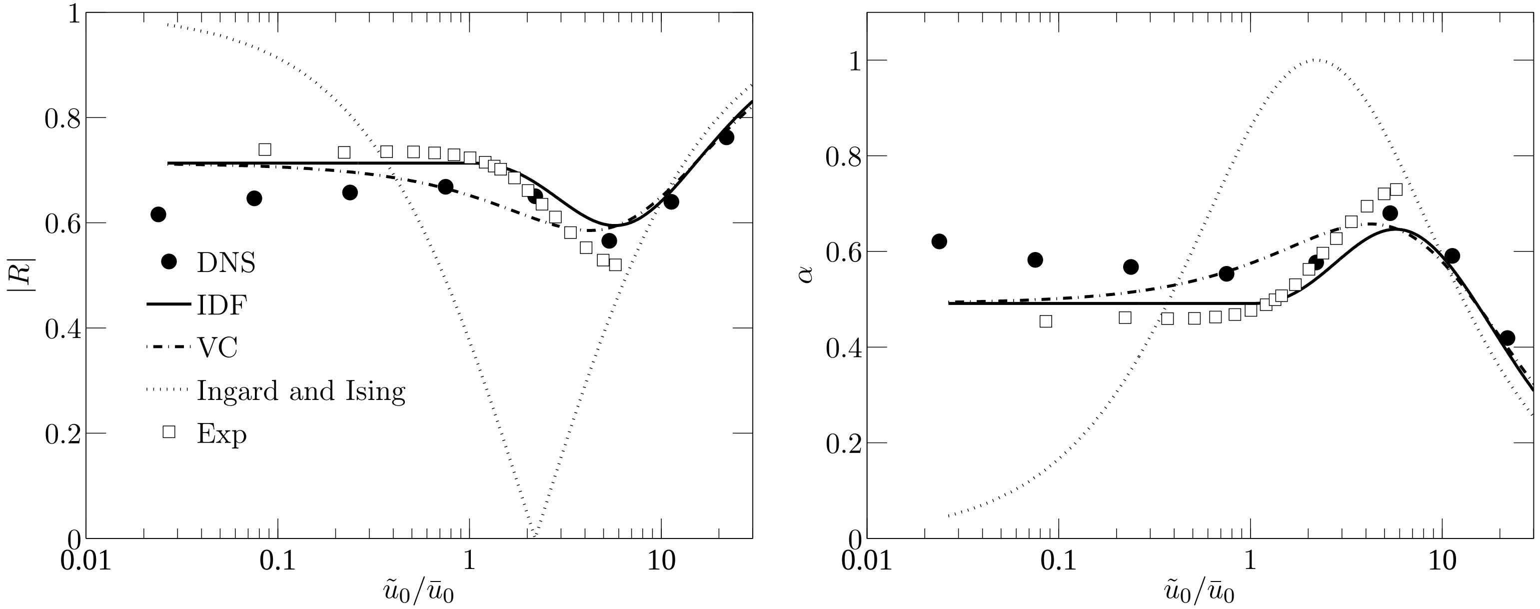

(a) $|R|$.

(b) $\alpha = 1 - |R|^2$.

Figure 5.31: *Results for plate* P_6 *with a resonant cavity of size* $L = 150$ mm *(Case 3 in Tab. 5.4). Evolution of the modulus of the reflection coefficient* $|R|$ *(a), and of the absorption coefficient* α *(b), as a function of the velocity fluctuation in the orifice* $\tilde{u}_0/\bar{u}_0$*. The forcing frequency is* $f = 800$ *Hz. DNS results (black circles) and ITHACA measurements (white squares) are compared to predictions from Ingard and Ising's model (dotted lines), the Vortex Convection model (dash-dotted lines) and the Impedance Describing Function model (solid lines).*

The response of plate P_6 backed by a cavity of size $L = 150$ mm is now analyzed at a forcing frequency $f = 800$ Hz. Once again, results from DNS are compared to measurements carried out in the ITHACA test bench and to the different theoretical models summarized in Tab. 5.3. The comparison is shown in Fig. 5.31(a) for the reflection coefficient $|R|$ and in Fig. 5.31(b) for the absorption coefficient α.

At this frequency, the plate operates far from the resonance conditions, and thus the modulus of the reflection coefficient is higher than the values taken at $f = 400$ Hz. Generally a good agreement is observed between models, experiments and DNS at low to moderate amplitudes $\tilde{u}_0/\bar{u}_0 \leq 1$. The reflection coefficient decreases to a minimum value when $\tilde{u}_0/\bar{u}_0 \simeq 5$, before increasing again at higher amplitudes. The model from Ingard and Ising (1967) fails at predicting the reflection and absorption coefficients, except at very high acoustic amplitudes $\tilde{u}_0/\bar{u}_0 > 10$. This behavior can be explained by the fact that this model is only valid near resonance, which takes place at $f = 400$ Hz for plate P_6 with a cavity of size $L = 150$ mm. Far from these conditions, the reactance of the perforated plate is not correctly predicted.

Results obtained for plate P_6, for which both experiments and simulations have been conducted, demonstrate that the IDF and VC models developed in this work show good agreements with measurements and numerical calculations. The VC and IDF models capture well the linear and high-amplitude responses of the perforated plate with and without a back cavity, even if the IDF model performs better in the transition regime when $\tilde{u}_0/\bar{u}_0 \simeq 1$.

A further validation is proposed in Figs. 5.32(a) and 5.32(b), where experiments carried out on plate P_8 backed by a cavity of size $L = 150$ mm are compared to predictions from the nonlinear models, for the same forcing frequencies $f = 400$ Hz and $f = 800$ Hz respectively. The agreement is again good for both modulus $|R|$ and phase φ of the reflection coefficient $R = |R| \exp(\mathrm{i}\varphi)$ between the IDF and VC models and experiments. As expected, the linear model correctly predict the acoustic properties of the perforated plate only up to $\tilde{u}_0/\bar{u}_0 \simeq 1$. It is also interesting to note that at high amplitudes, the phase of the reflection coefficient changes and converges to zero. This behavior is observed at all forcing frequencies and shows that, at very high amplitudes, the reflected wave tends to be in phase with the acoustic excitation. These results for plate P_8 again demonstrate that the IDF model performs better for the intermediate range of perturbation levels when $\tilde{u}_0/\bar{u}_0 \simeq 1$.

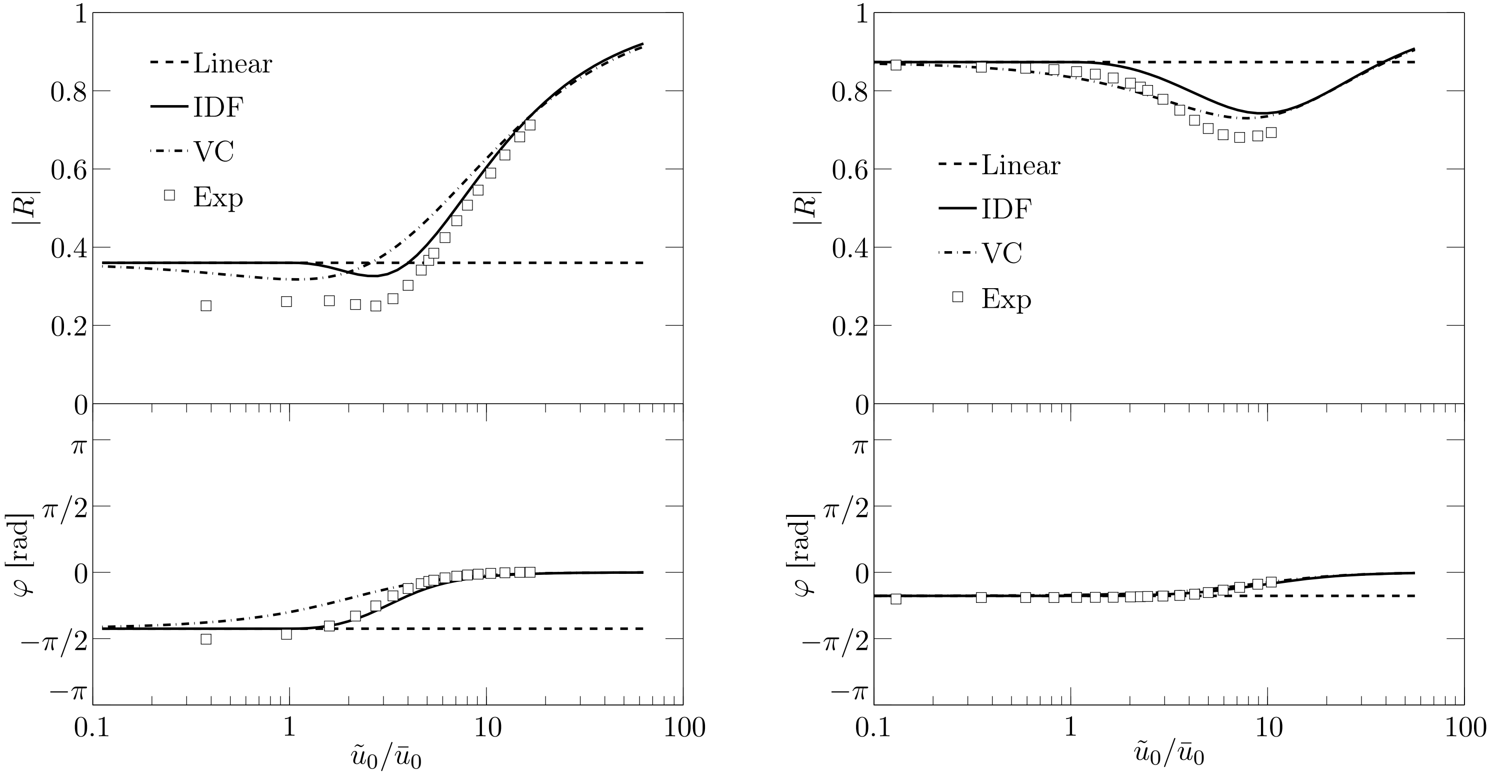

(a) $f = 400$ Hz.

(b) $f = 800$ Hz.

Figure 5.32: *Results for plate* P_8 *with a resonant cavity of size* $L = 150$ mm *(Cases 4 and 5 in Tab. 5.4). Evolution of the modulus* $|R|$ *and phase* φ *of the reflection coefficient as a function of the velocity fluctuation in the orifice* $\tilde{u}_0/\bar{u}_0$*. The forcing frequencies are* $f = 400$ Hz *(a) and* $f = 800$ Hz *(b). ITHACA measurements (white squares) are compared to predictions from Howe's linear model (dashed lines), the Vortex Convection model (dash-dotted lines) and the Impedance Describing Function model (solid lines).*

5.3.2 Acoustic power dissipation

It is finally worth examining the acoustic power dissipated by these dampers when the SPL increases. To do so the starting point is to establish an acoustic energy balance in the system.

One of the first expressions for the acoustic energy in a moving medium can be found in the work of Cantrell and Hart (1964). They showed that there is no production or dissipation of acoustic energy (except from viscous effects) in an irrotational homentropic flow. Morfey (1971) proposed a formulation to extend the concept of acoustic energy to non-uniform flows. Generalized expressions of an exact energy corollary were later established by Myers for perturbations in homentropic flows [Myers (1986)] and in more general non-uniform flows [Myers (1991)]. More recently Rienstra and Hirschberg (2003) gave an extensive overview on this topic.

Following Myers (1986), the acoustic energy balance writes:

$$\frac{\partial E}{\partial t} + \nabla \cdot \boldsymbol{I} = -\mathcal{D}, \tag{5.38}$$

where E is the generalized acoustic energy density, $\boldsymbol{I}$ is the acoustic intensity flux, and $\mathcal{D}$ is the production term representing acoustic dissipation.

Starting from Eq. (5.38), integrating over a fixed reference volume $\mathcal{V}$ bounded by a surface S, and using the Gauss theorem, one obtains:

$$\frac{d}{dt}\int_{\mathcal{V}} E \, d\mathcal{V} + \int_S \boldsymbol{I} \cdot \boldsymbol{n} \, dS = -\int_{\mathcal{V}} \mathcal{D} \, d\mathcal{V} \tag{5.39}$$

Equation (5.39) represents the integral energy balance for acoustic energy. For a system subjected to periodic acoustic waves, such as a perforated plate backed by a cavity, the average acoustic energy integrated over a period T remains constant. Defining the time averaging operator:

$$\langle A \rangle = \frac{1}{T}\int_{t_0}^{t_0+T} A \, dt, \tag{5.40}$$

and noting that:

$$\frac{d}{dt}\left\langle \int_{\mathcal{V}} E \, d\mathcal{V} \right\rangle = 0, \tag{5.41}$$

one finally obtains an expression for the acoustic power Π dissipated:

$$\Pi = -\int_{\mathcal{V}} \langle \mathcal{D} \rangle \, d\mathcal{V} = \int_S \langle \boldsymbol{I} \cdot \boldsymbol{n} \rangle \, dS \tag{5.42}$$

Equation (5.42) shows that the acoustic power dissipated in the control volume comprising a perforated plate can be inferred from the acoustic fluxes calculated at the volume boundaries far from the plate, if there is no additional dissipation taking place within the control volume. By choosing a control volume embedding the perforated plate, whose boundaries correspond to the solid wall of the numerical domain, the lateral boundaries and two surfaces normal to the orifice far away from the perforated plate, this method is used in our work to calculate Π from the simulations. The acoustic fluxes $\boldsymbol{I}_1$ and $\boldsymbol{I}_2$ are calculated and averaged in two transversal planes located upstream (S_1) and downstream (S_2) of the perforation, respectively. The planes represent the only acoustic boundaries of the orifice that have non-zero contribution to the energy balance, since periodic conditions are imposed on the lateral boundaries of the numerical domain. The S_1 and S_2 planes are taken far enough from the orifice, at a distance of $x_1/a = x_2/a = 100$, to ensure uniform flow conditions.

Figures 5.33 and 5.34 show the comparison of the normalized acoustic dissipation deduced from the numerical simulations and predictions from the nonlinear models IDF and VC, for plate P_6 at two different frequencies $f = 400$ Hz and $f = 800$ Hz. The agreement between simulations and both models is excellent in the linear regime, for $\tilde{u}_0/\bar{u}_0 \leq 1$. The dissipation Π increases quadratically with the amplitude of the velocity disturbances. This is consistent with Eq. (5.31) and in agreement with the analysis of the orders of magnitude carried out by Howe (1998). For higher acoustic amplitudes, in the nonlinear regime, the acoustic power Π increases as the cubic power of the velocity perturbation level. The IDF model predicts this change of slope, while the VC model fails to correctly predict the nonlinear behavior of the acoustic dissipation.

This can be explained as follows. In the framework of the VC model, the normalized acoustic power dissipated at the perforation is given by:

$$\frac{\Pi}{\rho_0 \bar{u}_0^3 A_0} = \frac{1}{2C_c^2(\mathrm{St_{VC}})} \left(\frac{\tilde{u}_0}{\bar{u}_0}\right)^2 \tag{5.43}$$

This expression indicates that the nonlinear contribution of the VC model is only included in the Strouhal number calculated with the convection velocity $u_c = \bar{u}_0 + C\tilde{u}_0$. Changes of u_c only influence the value of the contraction coefficient C_c. However we showed that variations of this contraction coefficient are bounded by $0.71 \leq C_C \leq 0.80$. The contraction coefficient thus only weakly depends on $\mathrm{St_{VC}}$. The VC model behaves essentially as a linear model at higher amplitudes, and does not reproduce the correct physics at high oscillation amplitudes.

Before concluding this chapter, it is worth discussing an apparent contradiction highlighted by Figs. 5.33 and 5.34. These figures show that the acoustic power dissipated at the orifice increases with the perturbation level. However, we have

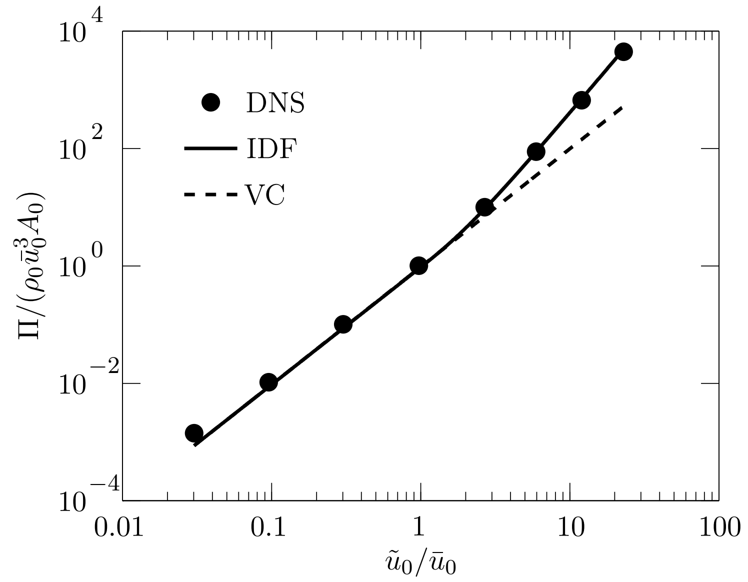

Figure 5.33: *Evolution of the average normalized acoustic power* $\Pi/(\rho_0\bar{u}_0^3A_0)$ *dissipated in the control volume* $\mathcal{V}$ *as a function of the acoustic perturbation level* $\tilde{u}_0/\bar{u}_0$*, at* $f = 400$ *Hz. Simulation results (•) are compared to the value predicted by the IDF model, given by Eq. (5.31).*

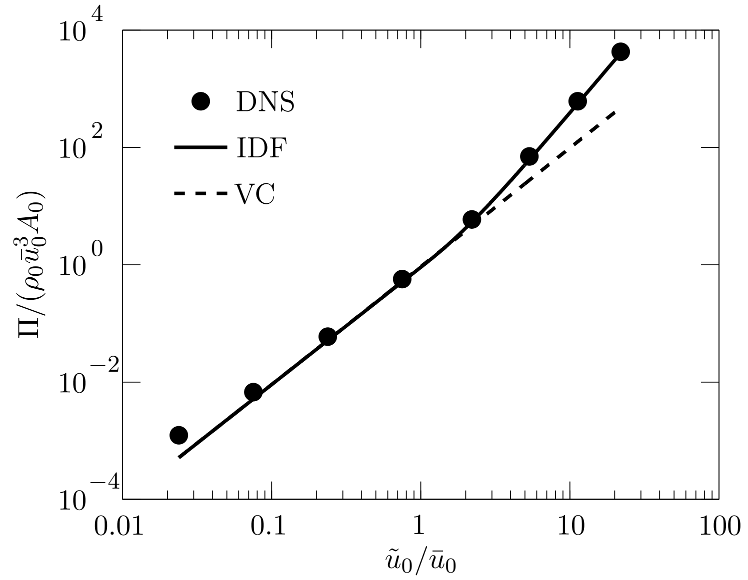

Figure 5.34: *Evolution of the average normalized acoustic power* $\Pi/(\rho_0\bar{u}_0^3A_0)$ *dissipated in the control volume* $\mathcal{V}$ *as a function of the acoustic perturbation* $\tilde{u}_0/\bar{u}_0$*, at* $f = 800$ *Hz. Simulation results (•) are compared to the value predicted by the IDF model, given by Eq. (5.31).*

also shown that the absorption coefficient decreases with the perturbation level. This can be explained by the fact that the absorption coefficient represents the fraction of acoustic energy dissipated, which decreases with the perturbation level. Thus when the SPL increases in the system, the incident acoustic energy impinging on the perforations increases more rapidly than the fraction which is dissipated. This must be kept in mind when designing a damper based on perforated plates.

5.4 Conclusion

The present chapter has addressed the difficult problem of the effect of the perturbation level on the response of a damper based on perforated plates with or without a resonant back cavity. Our objective was twofold: (i) describing the physical phenomena taking place when the velocity fluctuation level u'_0 exceeds the mean bias flow velocity $\bar{u}_0$ in the perforations, and (ii) developing and validating theoretical models capable of capturing the response of the system in the linear and nonlinear regimes.

Direct numerical simulations have been used to analyze the unsteady flow field through the aperture as a function of the perturbation level. Results show that:

- In the linear regime when $\tilde{u}_0/\bar{u}_0 \leq 1$, vortex rings are swept away downstream of the perforation at a constant convection velocity $u_c = \bar{u}_0$. Their trajectory is a straight line, in agreement with the hypothesis made by Howe in his linear model.
- In the nonlinear regime when $\tilde{u}_0/\bar{u}_0 > 1$, vortex rings are swept away alternatively upstream and downstream of the perforation. The analysis of the forcing cycle during which vortices are convected downstream of the perforation revealed that the trajectory remained approximately straight, but their convection velocity increases linearly with the perturbation level $u_c = \bar{u}_0 + C\tilde{u}_0$, where $C = 1/3$ is a constant determined in our simulations.

Based on observations made on the numerical results, two analytical models for the acoustic impedance of the perforated plate taking into account nonlinear effects have been developed and analyzed. The VC model takes into account the actual convection velocity of the vortex rings swept at the aperture when a sound wave impinges on the plate, but it does not consider effects related to flow reversal within the orifice. The IDF model is based on a quasi-steady approach, following Cummings and Eversman (1983), Morse and Ingard (1986) and Bellucci et al. (2004). A comparison with Howe's linear model allowed the determination of important physical parameters such as the contraction coefficient C_c and the end correction length l, which were found to be functions of the Strouhal number only. Analytical expressions were derived for these two quantities which yield predictions at high and low Strouhal numbers in agreement with results from the literature. In the nonlinear regime, a Fourier expansion keeping only the response at the forcing frequency was used to derive expressions for the impedance of the perforated plate as functions of frequency and amplitude.

The reflection, transmission and absorption coefficients of the configurations examined in the simulations have been determined and compared to theoretical predictions and to experimental results. Both the VC and the IDF models capture well the linear and high-amplitude regimes of the response of the perforated plate with and without a back cavity, but the IDF model performs better in the transition regime when $\tilde{u}_0/\bar{u}_0 \simeq 1$. The IDF model also correctly predicts the correct nonlinear behavior of the acoustic power dissipated by the perforated plate, while the VC model fails when $\tilde{u}_0/\bar{u}_0 > 1$.

These results are useful when designing robust dampers that need to operate in environments with very high sound levels, such as the ones developed, for example, in industrial gas turbines or in aeronautical engines. The expressions obtained for the VC and IDF models can be implemented in an acoustic Helmholtz solver to simulate the effect of nonlinear acoustic boundaries. This approach is very useful when estimating the limit-cycle oscillation amplitudes during a thermo-acoustic instability [Noiray et al. (2008); Boudy et al. (2011); Palies et al. (2011)].

Conclusion

The acoustic response of perforated plates traversed by a bias flow combined or not with a resonant back cavity has been investigated analytically, experimentally and with direct simulations of the Navier-Stokes equations. It has been shown that these systems feature interesting damping properties that may eventually be used to control low-frequency thermo-acoustic instabilities.

The optimal set of operating parameters capable of maximizing absorption over the widest possible range of low frequencies has first been determined analytically in the linear regime, when the acoustic velocity amplitude $\tilde{u}_0$ in the orifices remains smaller than the mean bias flow velocity $\tilde{u}_0 \leq \bar{u}_0$ through the perforations. The problem becomes more complex at higher acoustic amplitudes, when nonlinear effects appear and periodic reverse flow takes place within the perforations as $\tilde{u}_0 > \bar{u}_0$. Effects of amplitude were first examined with numerical simulations. These investigations allowed the development and validation of two nonlinear models for the acoustic impedance of the perforated plate. Experiments conducted in the impedance test bench ITHACA showed good agreement between predictions of the models developed in the present work and measurements, thus validating our approach.

The following two sections summarize the principal contributions of the present work to the knowledge of the acoustic properties of perforated plates in the linear and nonlinear regimes. The final section illustrates some further steps and perspectives which would be worth examining based on our findings.

Maximizing the absorption in the linear regime

The design of a perforated plate used to damp incident acoustic waves relies on an optimization procedure involving a large number of geometrical and flow parameters. In the present work, this problem has been drastically simplified by identifying two asymptotic regimes where it is possible to decouple the choice of the optimal bias flow velocity in the perforations and the back cavity size to maximize acoustic absorption. These regimes depend on the Strouhal number of the unsteady flow through the perforations, which is here defined by $\mathrm{St} = \omega a/\bar{u}_0$, where $\bar{u}_0$ denotes the mean bias flow velocity through the perforation

Table 5.5: *Expressions for the optimal bias flow velocity* $\bar{u}_0$ *and back cavity size* L *maximizing absorption in the two asymptotic regimes identified in this work.* $\mathrm{St} = \omega a/\bar{u}_0$, $\mathrm{M}_c = \bar{u}_0/c_0$, $\mathrm{He} = \omega L/c_0$, *where* c_0 *is the speed of sound,* h *denotes the plate thickness and* a *the perforation radius.*

Regime	Bias flow velocity	Back cavity size
$\mathrm{St} \gg 1$	$\dfrac{\mathrm{M}_c}{\sigma} = \dfrac{2}{\pi}$	$\dfrac{1}{\tan(\mathrm{He})} = \mathrm{St}\left(1 + \dfrac{2h}{\pi a}\right)$
$\mathrm{St} \ll 1$	$\dfrac{\mathrm{M}_c}{\sigma} = \dfrac{1}{2}$	$\dfrac{1}{\tan(\mathrm{He})} = \mathrm{St}\left(\dfrac{4}{3\pi} + \dfrac{h}{2a}\right)$

of radius a and ω is the angular frequency of the sound wave:

- At high Strouhal numbers, maximum absorption is reached for a Helmholtz resonance of the back cavity. It is possible with such device featuring a very short back cavity to cancel the reflection coefficient at a specific frequency, but the absorption bandwidth around the peak absorption frequency is narrow, and its width reduces as the Strouhal number increases.
- At low Strouhal numbers, a wider absorption bandwidth can be reached, making it an attractive choice for the design of low frequency robust dampers. In this case, maximum absorption is reached when the back cavity operates as a quarter-wave resonator. This damper requires thus a larger size compared to a Helmholtz resonator.

In these two operating regimes, it was demonstrated that the optimal bias flow velocity $\bar{u}_0$ and the back cavity size L are given by the expressions summarized in Tab. 5.5. They show that the optimal bias flow Mach number $\mathrm{M}_c = \bar{u}_0/c_0$ is solely fixed by the plate porosity σ, whereas the back cavity size L can be chosen as a function of the angular frequency ω that needs to be damped but also slightly depends on the ratio h/a of the plate thickness to perforation radius.

The absorption properties of these dampers were also investigated at off-design conditions, when the bias flow velocity deviates from its optimum value for which it was designed. It was shown that the absorption coefficient remains higher than 0.9, for bias flow velocity variations of up to 100 % of the nominal optimal value. When the velocity within the orifices increases, experiments conducted in the ITHACA impedance tube show that the peak absorption frequency is slightly shifted to higher frequencies.

Effect of amplitude on the acoustic response of perforates

The effect of amplitude on the acoustic response of perforates has been first addressed with direct simulations of the Navier-Stokes equations. These simulations have been carried out to analyze the unsteady flow field through the aperture as a function of the perturbation level for different forcing frequencies. When the amplitude of the acoustic velocity in the perforations remained lower than the mean bias flow velocity, it was found that the perforate operates in the linear regime. When this fluctuation velocity exceeds the mean bias flow velocity, $\tilde{u}_0 > \bar{u}_0$, the response of the perforated plate deviates from its linear response. In this case the plate operates in the nonlinear regime, and the amplitude of the acoustic perturbations must be taken into account when attempting to model the acoustic behavior of the orifice.

In the linear regime when $\tilde{u}_0/\bar{u}_0 \leq 1$, simulations show that vortex rings are swept away from the perforation at a constant convection velocity equal to the mean bias flow velocity through the perforation $u_c = \bar{u}_0$ and that the trajectory of these vortex rings is a straight tube that has the same radius a as the perforation. These observations confirm hypothesis made in modeling the response of perforated plates for small acoustic disturbances. A transition occurs when the velocity amplitude $\tilde{u}_0$ exceeds the mean bias flow velocity within the orifice $\tilde{u}_0 > \bar{u}_0$ and reverse flow is observed. In the nonlinear regime, vortex rings are swept away alternatively upstream and downstream of the perforation. The analysis of the forcing cycle during which vortices are convected downstream of the perforation revealed that the trajectory of these vortices remained approximately a straight tube with the same radius a as in the linear regime, but that their convection velocity u_c is a function of the perturbation level. Vortices are convected at a speed that increases linearly with the perturbation level $u_c = \bar{u}_0 + C\tilde{u}_0$, where C is a constant that was found in our simulations approximatively equal to $C = 1/3$.

The analysis of these simulations also allowed to estimate the acoustic power dissipated by these dampers when the perturbation amplitude increases. An acoustic energy budget across the perforated plated was carried out to infer the dissipated power from the knowledge of the acoustic fluxes far from the orifices. The acoustic power dissipated was shown to have a quadratic dependence on the acoustic perturbation level in the linear regime, and a cubic dependence at high amplitudes, in agreement with the the order of magnitude analysis proposed by Howe (1998).

These observations were used to develop two analytical models taking into account some of the nonlinear effects observed. They both only consider the response of the perforated plate at the same frequency as the harmonic excitation, and higher harmonics due to nonlinearities were not examined in this study.

- The first model is designated as the Vortex Convection (VC) model. It is an extension of Howe's linear model Howe (1979) for the Rayleigh conductivity of an aperture that takes into account changes in the convection velocity of vortex rings swept at the aperture when a sound wave impinges on the plate. This model does not consider effects related to flow reversal within the orifice.
- The second model is designated as the Impedance Describing Function (IDF) model. It is based on a quasi-steady approach that follows the work of Cummings and Eversman (1983), Morse and Ingard (1986) and Bellucci et al. (2004). The coefficients of this model were chosen to match Howe's linear model Howe (1979) for the Rayleigh conductivity of an aperture in the linear regime. This allowed the determination of key physical parameters such as the contraction coefficient C_c of the flow through the orifice and the end correction length l of the perforation, which were shown to be functions of the Strouhal number. By further assuming that these coefficients are independent of the sound level, a Fourier expansion keeping only the response of the damper at the forcing frequency yields an expression for the IDF of the perforated plate. This expression is an extension of the classical impedance in the frequency domain, parametrized with the oscillation level $\tilde{u}_0/\bar{u}_0$ through the perforations.

Both the VC and the IDF models capture well the linear and high-amplitude regimes of the perforated plate response at the forcing frequency with and without a back cavity. The IDF model performs better in the transition regime when the velocity oscillation is of the order of the mean bias flow velocity $\tilde{u}_0/\bar{u}_0 \simeq 1$. The IDF model also correctly predicts the nonlinear behavior of the acoustic power dissipated by the perforated plate, while the VC model fails when $\tilde{u}_0/\bar{u}_0 > 1$.

Perspectives

The results obtained during this work can ease the design of robust dampers that are operated in harsh environments with very high sound levels, such as the ones encountered, for example, in industrial gas turbines or in aeronautical engines. The low Strouhal asymptotic regime coupled to a quarter-wave resonator identified in this study seems particularly suited for these applications thanks to its robustness when the mean bias flow velocity deviates from the optimal one, and thanks to its large absorption bandwidth. These characteristics are crucial to design dampers for gas turbine combustors subjected to variations of the operating conditions. The bias flow, determined by the pressure drop through the perforations, changes when the engine load is varied, and the frequencies to damp can change due to ambient conditions, hot gas ingestion, or operating conditions. When a limited back cavity volume is available and the frequencies to damp are higher and well defined, it is worth considering the high Strouhal regime for the design of the perforated plate in combination with a Helmholtz resonator.

In the work conducted here only isothermal flow conditions have been assumed in the damping system. A further step would be to analyze the acoustic response of these dampers at conditions closer to those typically encountered in gas turbine combustors, by taking into account the temperature difference across the perforated plate, i.e. between the back cavity at relatively low temperatures and the combustion chamber at high temperatures. In addition, at high acoustic oscillation amplitudes, hot gas may be periodically ingested in the back cavity during reverse flow. The subsequent increase of temperature in the cavity will have an effect on the acoustic response of the system, in particular on the damping frequency, which would be worth examining, as initiated by Ćosić et al. (2012).

It would also be of interest to conduct a global acoustic energy budget of a combustor equipped with perforated plate dampers. Such analysis has already been conducted by Tran et al. (2009a) during self-sustained combustion oscillations in a generic gas turbine combustor open to the atmosphere when the size of the back cavity coupled to a perforated plate placed within the premixing unit of the combustor was varied. It was found that this type of damper can be used to efficiently reduce low frequency high-amplitude thermo-acoustic oscillations observed in the combustor when the back cavity length is well tuned, but the nonlinear response of the perforated plate was not precisely understood. It was also found that some high amplitude unstable regimes could not be attenuated with this type of system [Tran et al. (2009b)]. The progress made in understanding the optimal linear and nonlinear responses of these systems could probably be used in a future work to determine the optimal placement of the orifices to damp longitudinal unstable modes of combustors, and to determine the minimum open area and air mass flowrate capable of absorbing the acoustic energy produced during the instability.

Models based on the flame describing function (FDF) framework [Noiray et al. (2008)] accounting for nonlinear effects of the acoustic response of flames, have recently been successfully applied to different configurations and were shown to be capable of retrieving the nonlinear dynamics observed in experiments conducted in generic laminar and swirled combustors [Boudy et al. (2011); Palies et al. (2011); Silva et al. (2013)]. These models consider that the flame is the main nonlinear element of the system. Acoustic boundary conditions and the acoustic dissipation taking place in the vicinity of perforated plates also play a key role in the determination of the stability margin of a combustor. These elements may eventually reach the nonlinear regime as shown in this work and nonlinearly interact with the combustion dynamics [Schuller et al. (2009)]. To go further into this problem, the expressions obtained for the VC and IDF models can be implemented in acoustic analysis combined with a FDF to simulate the effect of nonlinear acoustic boundaries. This approach might help in better delineating the stability margins of combustor and improve the estimation of limit cycle oscillation amplitudes during a thermo-acoustic instability.

It is also worth noting that all the developments proposed in this study concern perforated plates with circular holes traversed by a bias flow in the absence of grazing flow. Another interesting open question is related to the applicability of the models developed in this work to perforated plates equipped with orifices of different shapes and sizes. Orifices in gas turbine perforated walls are often inclined for film cooling to protect the combustor walls from the hot combustion products. The inclination of these holes is an additional parameter of interest and it is not clear how the interactions of sound waves and vorticity will be altered in these cases with respect to the situation studied in the present work with holes at 90^o normal to the plate and aligned with the bias flow main stream. Direct numerical simulations may be envisaged in these cases to infer the response of such perforations in the linear and nonlinear regimes. The observations made on these calculations might help in guiding the development of improved analytical models taking the effects of these inclinations into consideration.

Finally, it is worth exploring the following academic question. It was found by combining the quasi-steady equations of motion in the orifice and Howe's vortex sheet model that the end correction length and the discharge coefficient of the unsteady flow through a perforation are functions of the Strouhal number in the linear regime. This assumption was kept for the nonlinear regime modeling. It would be of interest to make a detailed study of these quantities in order to challenge this assumption. This analysis might be conducted by examining the unsteady velocity field in the vicinity of the perforation using direct numerical simulations, or by means of micro-particle imaging velocimetry measurements for example.

References

Barbosa, S., P. Scouflaire, and S. Ducruix (2009). Time resolved flowfield, flame structure and acoustic characterization of a staged multi-injection burner. *Proceedings of the Combustion Institute 32*(2), 2965–2972. *(p. 6, 8)*

Batchelor, G. K. (1967). *An Introduction to Fluid Dynamics*. Cambridge University Press, Cambridge. *(p. 27, 28, 135)*

Bechert, D. W. (1980). Sound absorption caused by vorticity shedding, demonstrated with a jet flow. *Journal of Sound and Vibration 70*(3), 389–405. *(p. 9, 12)*

Bellucci, V., P. Flohr, and C. Paschereit (2004). Numerical and experimental study of acoustic damping generated by perforated screens. *AIAA Journal 42*(8), 1543–1549. *(p. 10, 22, 28, 29, 31, 32, 132, 135, 161, 166)*

Bellucci, V., P. Flohr, C. O. Paschereit, and F. Magni (2004). On the use of Helmholtz resonators for damping acoustic pulsations in industrial gas turbines. *Journal of Engineering for Gas Turbines and Power 126*(2), 271–275. *(p. 7)*

Bodony, D. and S. K. Lele (2008). Current status of jet noise predictions using large-eddy simulation. *AIAA Journal 46*(2), 364–380. *(p. 48, 58)*

Bothien, M. R., J. P. Moeck, and C. Oliver Paschereit (2008). Active control of the acoustic boundary conditions of combustion test rigs. *Journal of Sound and Vibration 318*(4–5), 678–701. *(p. 6, 7)*

Bothien, M. R., N. Noiray, and B. Schuermans (2013). A novel damping device for broadband attenuation of low-frequency combustion pulsations in gas turbines. *Journal of Engineering for Gas Turbines and Power 136*(4), 041504–041504. *(p. 6, 7, 8, 9)*

Boudy, F., D. Durox, T. Schuller, and S. Candel (2011). Nonlinear mode triggering in a multiple flame combustor. *Proceedings of the Combustion Institute 33*(1), 1121–1128. *(p. 8, 162, 167)*

Bulat, G., K. Liu, G. Brickwood, V. Sanderson, and B. Igoe (2011). Intelligent operation of Siemens (SGT-300) DLE gas turbine combustion system over an extended fuel range with low emissions. In *Proceedings of ASME Turbo Expo 2011, GT2011-46103*. *(p. 6, 8)*

Candel, S. (1992). Combustion instabilities coupled by pressure waves and their active control. *Proceedings of the Combustion Institute 24*, 1277–

1296. *(p. 7)*

Candel, S. (2001). *Mécanique des Fluides.* Dunod. *(p. 48)*

Candel, S. (2002). Combustion dynamics and control: Progress and challenges. *Proceedings of the Combustion Institute 29*(1), 1–28. *(p. 3)*

Candel, S., D. Durox, T. Schuller, J.-F. Bourgouin, and J. P. Moeck (2014). Dynamics of swirling flames. *Annual Review of Fluid Mechanics 46*(1), 147–173. *(p. 4)*

Cantrell, R. H. and R. W. Hart (1964). Interaction between sound and flow in acoustic cavities : mass, momentum and energy considerations. *Journal of the Acoustical Society of America 56*(4). *(p. 5, 158)*

Chung, J. Y. and D. A. Blaser (1980a). Transfer function method of measuring in-duct acoustic properties. I. Theory. *Journal of the Acoustical Society of America 68*(3), 907–913. *(p. 39)*

Chung, J. Y. and D. A. Blaser (1980b). Transfer function method of measuring in-duct acoustic properties. II. Experiment. *Journal of the Acoustical Society of America 68*(3), 914–921. *(p. 40)*

Colonius, T. and S. K. Lele (2004). Computational aeroacoustics: progress on nonlinear problems of sound generation. *Progress in Aerospace Sciences 40*(6), 345–416. *(p. 58)*

Correa, S. M. (1998). Power generation and aeropropulsion gas turbines: From combustion science to combustion technology. *Symposium (International) on Combustion 27*(2), 1793–1807. *(p. 1)*

Ćosić, B., T. G. Reichel, and C. O. Paschereit (2012). Acoustic response of a helmholtz resonator exposed to hot-gas penetration and high amplitude oscillations. *Journal of Engineering for Gas Turbines and Power 134*(10), 101503–101503. *(p. 8, 167)*

Crighton, D. G., A. P. Dowling, J. E. Ffowcs Williams, M. Heckl, and F. G. Leppington (1992). *Modern methods in analytical acoustics.* Springer-Verlag. *(p. 5)*

Crocco, L. and S.-I. Cheng (1956). *Theory of combustion instability in liquid propellant rocket motors.* Buttersworth Scientific Publications, London. *(p. 3)*

Culick, F. E. C. (2006). Unsteady motions in combustion chambers for propulsion systems. Technical report, Technical Report RTO-AG-AVT-039, NATO Research and Technology Organisation. *(p. 3)*

Cummings, A. (1984). Acoustic nonlinearities and power losses at orifices. *AIAA Journal 22*(6), 786–792. *(p. 11)*

Cummings, A. (1986). Transient and multiple frequency sound transmission through perforated plates at high amplitude. *Journal of the Acoustical Society of America 79*(4), 942–951. *(p. 10, 22, 28, 134, 135)*

Cummings, A. and W. Eversman (1983). High amplitude acoustic transmission through duct terminations: Theory. *Journal of Sound and Vibration 91*(4), 503–518. *(p. 10, 22, 24, 25, 26, 27, 31, 32, 132, 133, 134, 161, 166)*

Dassé, J., S. Mendez, and F. Nicoud (2008). Large-eddy simulation of the acoustic response of a perforated plate. In *14th AIAA/CEAS Aeroacoustics Conference, AIAA Paper 2008-3007*. *(p. 10, 49)*

Disselhorst, J. H. M. and L. V. Wijngaarden (1980). Flow in the exit of open pipes during acoustic resonance. *Journal of Fluid Mechanics 99*(02), 293–319. *(p. 29)*

Döbbeling, K., H. Koch, and J. Hellat (2005). 25years of bbc/abb/alstom lean premix combustion technologies. *Journal of Engineering for Gas Turbines and Power 129*(1), 2–12. *(p. 1, 3)*

Dowling, A. P. and I. J. Hughes (1992). Sound absorption by a screen with a regular array of slits. *Journal of Sound and Vibration 156*(3), 387–405. *(p. 15, 18, 19, 71)*

Dowling, A. P. and A. S. Morgans (2005). Feedback control of combustion oscillations. *Annual Review of Fluid Mechanics 37*(1), 151–182. *(p. 3)*

Dragan, S. P. and I. V. Lebedeva (1998). Absorption of high-intensity sound by a perforated panel. *Acoustical Physics 44*, 167–172. *(p. 10)*

Ducruix, S. and S. Candel (2004). External flow modulation in computational fluid dynamics. *AIAA Journal 42*(8), 1550–1558. *(p. 58)*

Ducruix, S., T. Schuller, D. Durox, and S. Candel (2003). Combustion dynamics and instabilities: elementary coupling and driving mechanisms. *Journal of Propulsion and Power 19*(5), 722–734. *(p. 4)*

Dupère, I. D. J. and A. P. Dowling (2001). The absorption of sound near abrupt axisymmetric area expansions. *Journal of Sound and Vibration 239*, 709–730. *(p. 10)*

Dupere, I. D. J. and A. P. Dowling (2005). The use of Helmholtz resonators in a practical combustor. *Journal of Engineering for Gas Turbines and Power 127*(2), 268–275. *(p. 7)*

Durox, D., J. P. Moeck, J.-F. Bourgouin, P. Morenton, M. Viallon, T. Schuller, and S. Candel (2013). Flame dynamics of a variable swirl number system and instability control. *Combustion and Flame 160*(9), 1729–1742. *(p. 6)*

Durrieu, P., G. Hofmans, G. Ajello, R. Boot, Y. Auregan, A. Hirschberg, and M. C. A. M. Peters (2001). Quasisteady aero-acoustic response of orifices. *Journal of the Acoustical Society of America 110*(4), 1859–1872. *(p. 11, 39, 44, 135)*

Eldredge, J., D. Bodony, and M. Shoeybi (2007). Numerical investigation of the acoustic behavior of a multi-perforated liner. In *13th AIAA/CEAS Aeroacoustics Conference, AIAA Paper 2007-3683*. *(p. 11)*

Eldredge, J. D. and A. P. Dowling (2003). The absorption of axial acoustic waves by a perforated liner with bias flow. *Journal of Fluid Mechanics 485*, 307–335. *(p. 10)*

Grace, S. M., K. P. Horan, and M. S. Howe (1998). The influence of shape on the Rayleigh conductivity of a wall aperture in the presence of grazing flow. *Journal of Fluids and Structures 12*(3), 335–351. *(p. 10)*

Griffin, S., S. A. Lane, and S. Huybrechts (2000). Coupled helmholtz resonators for acoustic attenuation. *Journal of Vibration and Acoustics 123*(1), 11–17. *(p. 9)*

Hermann, J., J. R. Seume, A. Orthmann, N. Vortmeyer, C. C. Hantschk, P. Zangl, W. Krause, S. Gleis, and D. Vortmeyer (1998). Application of active combustion instability control to a heavy duty gas turbine. *Journal of Engineering for Gas Turbines and Power 120*(4), 721–726. *(p. 7)*

Hersh, A. S. and T. Rogers (1975). Fluid mechanical model of the acoustic impedance of small orifices. In *AIAA Second Aeroacoustic Conference, AIAA Paper 75-495*. *(p. 135)*

Hersh, A. S., B. E. Walker, and J. W. Celano (2003). Helmholtz resonator impedance model, part 1: Nonlinear behavior. *AIAA Journal 41*(5), 795–808. *(p. 8)*

Hirschberg, A. (2001). Introduction to aero-acoustics of internal flow. In *Advances in aeroacoustics, Lecture series, March 12-16*. Von Karman Institute for Fluid Dynamics. *(p. 17)*

Hixon, R., S. H. Shih, and R. R. Mankbadi (1995). Evaluation of boundary conditions for computational aeroacoustics. In *33rd AIAA Aerospace Sciences Meeting*. *(p. 58)*

Hofmans, G. C. J., R. J. J. Boot, P. P. J. M. Durrieu, Y. Auregan, and A. Hirschberg (2001). Aeroacoustic response of a slit-shaped diaphragm in a pipe at low Helmholtz number, 1: quasi-steady results. *Journal of Sound and Vibration 244*(1), 35–56. *(p. 135)*

Howe, M. S. (1979). On the theory of unsteady high Reynolds number flow through a circular aperture. *Proceeding of the Royal Society 366*, 205–223. *(p. 10, 12, 14, 15, 22, 29, 30, 110, 116, 124, 127, 129, 131, 132, 134, 140, 166)*

Howe, M. S. (1998). *Acoustics of fluid-structure interactions*. Cambridge University Press, Cambridge. *(p. 9, 10, 11, 12, 13, 17, 18, 110, 116, 134, 137, 142, 152, 159, 165)*

Hu, F. Q. (1996). On absorbing boundary conditions for linearized euler equations by a perfectly matched layer. *Journal of Computational Physics 129*(1), 201–219. *(p. 58)*

Huang, Y. and V. Yang (2009). Dynamics and stability of lean-premixed swirl-stabilized combustion. *Progress in Energy and Combustion Science 35*(4), 293–364. *(p. 3, 4)*

Hughes, I. J. and A. P. Dowling (1990). The absorption of sound by perforated linings. *Journal of Fluid Mechanics 218*, 299–335. *(p. 9, 10, 15, 19, 71, 72, 87, 88, 90, 127)*

IEA (2012). *Key World Energy Statistics*. International Energy Agency (IEA). *(p. 1)*

Ingard, U. (1953). On the theory and design of acoustic resonators. *Journal of the acoustical society of America 25*, 1037–1061. *(p. 26, 75, 137)*

Ingard, U. and H. Ising (1967). Acoustic nonlinearity of an orifice. *Journal* *of the Acoustical Society of America 41*(6), 1582–1583. *(p. 9, 10, 11, 22, 23, 24, 31, 132, 144, 153, 156)*

Jeong, J. and F. Hussain (1995). On the identification of a vortex. *Journal of Fluid Mechanics 285*, 69–94. *(p. 110, 118)*

Jing, X. and X. Sun (1999). Experimental investigation of perforated liners with bias flow. *Journal of the Acoustical Society of America 106*(5), 2436–1441. *(p. 15)*

Jing, X. and X. Sun (2000). Effect of plate thickness on impedance of perforated plates with bias flow. *AIAA Journal 38*(9), 1573–1578. *(p. 10, 11, 15, 79, 84, 143)*

Jing, X. and X. Sun (2002). Sound-excited flow and acoustic nonlinearity at an orifice. *Physics of Fluids 14*(1), 268–276. *(p. 10)*

Keller, J. J. (1995). Thermoacoustic oscillations in combustion chambers of gas turbines. *AIAA Journal 33*(12), 2280–2287. *(p. 3)*

Kirby, R. and A. Cummings (1998). The impedance of perforated plates subjected to grazing gas flow and backed by porous media. *Journal of Sound and Vibration 217*(4), 619–636. *(p. 10)*

Krebs, W., P. Flohr, B. Prade, and S. Hoffmann (2002). Thermoacoustic stability chart for high-intensity gas turbine combustion systems. *Combustion Science and Technology 174*(7), 99–128. *(p. 6)*

Lamraoui, A., F. Richecoeur, T. Schuller, and S. Ducruix (2011). A methodology for on the fly acoustic characterization of the feeding line impedances in a turbulent swirled combustor. *Journal of Engineering for Gas Turbines and Power 133*(1), 011504–7. *(p. 40)*

Langhorne, P. J., A. P. Dowling, and N. Hooper (1990). Practical active control system for combustion oscillations. *Journal of Propulsion and Power 6*(3), 324–333. *(p. 6)*

Lax, P. D. and B. Wendroff (1964). Difference schemes for hyperbolic equations with high order of accuracy. *Communications on Pure and Applied Mathematics 17*, 381–398. *(p. 53)*

Lee, S.-H., J.-G. Ih, and K. S. Peat (2007). A model of acoustic impedance of perforated plates with bias flow considering the interaction effect. *Journal of Sound and Vibration 303*(3-5), 741–752. *(p. 10)*

Lefebvre, A. H. and D. R. Ballal (2010). *Gas Turbine Combustion: Alternative Fuels and Emissions, Third Edition.* CRC Press. *(p. 3)*

Leung, R. C. K., R. M. C. So, M. H. Wang, and X. M. Li (2007). In-duct orifice and its effect on sound absorption. *Journal of Sound and Vibration 299*(4-5), 990–1004. *(p. 22)*

Levine, H. and J. Schwinger (1948). On the radiation of sound from an unflanged circular pipe. *Physical Review 73*(4). *(p. 137)*

Lieuwen, T. and K. McManus (2003). Introduction: Combustion dynamics in lean-premixed prevaporized (lpp) gas turbines. *Journal of Propulsion and Power 19*(5), 721–721. *(p. 3)*

Lieuwen, T. and V. Yang (2005). Combustion instabilities in gas turbine engines, operational experience, fundamental mechanisms and modeling. *Progress in Astronautics and Aeronautics AIAA 210. (p. 3)*

Lörstad, D., J. Pettersson, and A. Lindholm (2009). Emission reduction and cooling improvements due to the introduction of passive acoustic damping in an existing SGT-800 combustor. In *Proceedings of ASME Turbo Expo 2009, GT2009-59313. (p. 92)*

Luong, T., M. S. Howe, and R. S. McGowan (2005). On the Rayleigh conductivity of a bias-flow aperture. *Journal of Fluids and Structures 21*(8), 769–778. *(p. 15, 134, 139, 142)*

McManus, K. R., T. Poinsot, and S. Candel (1993). A review of active control of combustion instabilities. *Progress in Energy and Combustion Science 19*(1), 1–29. *(p. 7)*

Melling, T. H. (1973). The acoustic impendance of perforates at medium and high sound pressure levels. *Journal of Sound and Vibration 29*(1), 1–65. *(p. 7, 9, 11, 16, 85)*

Mendez, S. and J. D. Eldredge (2009). Acoustic modeling of perforated plates with bias flow for large-eddy simulations. *Journal of Computational Physics 228*(13), 4757–4772. *(p. 22)*

Mongia, H. C., T. J. Held, G. C. Hsiao, and R. P. Pandalai (2003). Challenges and progress in controlling dynamics in gas turbine combustors. *Journal of Propulsion and Power 19*(5), 822–829. *(p. 3)*

Morfey, C. L. (1971). Acoustic energy in non-uniform flows. *Journal of Sound and Vibration 14*(2), 159–170. *(p. 12, 158)*

Morse, P. M. and U. Ingard (1986). *Theoretical acoustics.* Princeton University Press. *(p. 26, 32, 41, 133, 161, 166)*

Motheau, E., L. Selle, and F. Nicoud (2014). Accounting for convective effects in zero-mach-number thermoacoustic models. *Journal of Sound and Vibration 333*(1), 246–262. *(p. 5)*

Munjal, M. L. (1987). *Acoustics of Ducts and Mufflers.* Wiley-Interscience. *(p. 9)*

Myers, M. K. (1986). An exact energy corollary for homentropic flow. *Journal of Sound and Vibration 109*(2), 277–284. *(p. 5, 158)*

Myers, M. K. (1991). Transport of energy by disturbances in arbitrary steady flows. *Journal of Fluid Mechanics 226*, 383–400. *(p. 5, 158)*

Narayana Rao, K. and M. L. Munjal (1986). Experimental evaluation of impedance of perforates with grazing flow. *Journal of Sound and Vibration 108*(2), 283–295. *(p. 10)*

Nicoud, F., L. Benoit, C. Sensiau, and T. Poinsot (2007). Acoustic modes in combustors with complex impedances and multidimensional active flames. *AIAA Journal 45*(2), 426–441. *(p. 134)*

Nicoud, F. and F. Ducros (1999). Subgrid-scale stress modelling based on the square of the velocity gradient tensor. *Flow, Turbulence and Combustion 62*, 183–200. *(p. 55)*

Nicoud, F. and K. Wieczorek (2009). About the zero Mach number assumption in the calculation of thermoacoustic instabilities. *International Journal of Spray and Combustion Dynamics 1*(1), 67–111. *(p. 5)*

Noiray, N., D. Durox, T. Schuller, and S. Candel (2008). A unified framework for nonlinear combustion instability analysis based on the flame describing function. *Journal of Fluid Mechanics 615*, 139–167. *(p. 5, 162, 167)*

Noiray, N., D. Durox, T. Schuller, and S. Candel (2009). Dynamic phase converter for passive control of combustion instabilities. *Proceedings of the Combustion Institute 32*(2), 3163–3170. *(p. 6)*

Oschwald, M., Z. Farago, G. Searby, and F. Cheuret (2008). Resonance frequencies and damping of a combustor acoustically coupled to an absorber. *Journal of Propulsion and Power 24*(3), 524–533. *(p. 8)*

Palies, P., D. Durox, T. Schuller, and S. Candel (2011). Nonlinear combustion instability analysis based on the flame describing function applied to turbulent premixed swirling flames. *Combustion and Flame 158*(10), 1980–1991. *(p. 162, 167)*

Peat, K. S., R. Sugimoto, and J. L. Horner (2006). The effects of thickness on the impedance of a rectangular aperture in the presence of a grazing flow. *Journal of Sound and Vibration 292*(3-5), 610–625. *(p. 10)*

Peters, M. C. A. M., A. Hirschberg, A. J. Reijnen, and A. P. J. Wijnands (1993). Damping and reflection coefficient measurements for an open pipe at low Mach and low Helmholtz numbers. *Journal of Fluid Mechanics 256*, 499–534. *(p. 18, 43, 50)*

Pierce, A. D. (1981). *Acoustics: an Introduction to its Physical Principles and Applications*. McGraw-Hill Book Company, Inc., New York. *(p. 41, 134, 137)*

Poinsot, T. and S. K. Lele (1992). Boundary conditions for direct simulations of compressible viscous flows. *Journal of Computational Physics 101*(1), 104–129. *(p. 50, 58)*

Poinsot, T. and D. Veynante (2012). *Theoretical and Numerical Combustion, Third Edition*. T. Poinsot. *(p. 3)*

Providakis, T., L. Zimmer, P. Scouflaire, and S. Ducruix (2012). Characterization of the acoustic interactions in a two-staged multi-injection combustor fed with liquid fuel. *Journal of Engineering for Gas Turbines and Power 134*(11). *(p. 6, 8)*

Putnam, A. A. (1971). *Combustion-driven oscillations in industry*. Americal Elsevier Pub. Co. *(p. 5)*

Rayleigh, J. W. S. (1896). *The Theory of Sound*. London: MacMillan. *(p. 3, 5, 11, 13, 17, 137)*

Richards, G. A. and E. H. Robey (2008). Effect of fuel system impedance mismatch on combustion dynamics. *Journal of Engineering for Gas Turbines and Power 130*(1), 011510–011510. *(p. 7, 8)*

Richards, G. A., D. L. Straub, and E. H. Robey (2003). Passive control of combustion dynamics in stationary gas turbines. *Journal of Propulsion and Power 19*(5), 795–810. *(p. 4, 7, 8)*

Rienstra, S. W. and A. Hirschberg (2003). *An Introduction to Acoustics.* Eindhoven University of Technology. *(p. 7, 12, 44, 133, 134, 137, 158)*

Rupp, J., J. Carrotte, and M. Macquisten (2011). The use of perforated damping liners in aero gas turbine combustion systems. In *Proceedings of ASME Turbo Expo 2011, GT2011-45488.* *(p. 77)*

Rupp, J., J. Carrotte, and A. Spencer (2010). Interaction between the acoustic pressure fluctuations and the unsteady flow field through circular holes. *Journal of Engineering for Gas Turbines and Power 132*(6), 061501–9. *(p. 22)*

Salikuddin, M., A. A. Syed, and P. Mungur (1994). Acoustic characteristics of perforated sheets with throughflow in a high intensity noise environment. *Journal of Sound and Vibration 169*(2), 145–177. *(p. 10, 11)*

Scarpato, A., S. Ducruix, and T. Schuller (2011). A LES based sound absorption analysis of high-amplitude waves through an orifice with bias flow. In *Proceedings of ASME Turbo Expo 2011, GT2011-45639.* *(p. 49, 135)*

Scarpato, A., S. Ducruix, and T. Schuller (2013a). A comparison of the damping properties of perforated plates backed by a cavity operating at low and high strouhal numbers. *Comptes Rendus Mécanique 341*(1–2), 161–170. *(p. 67, 79)*

Scarpato, A., S. Ducruix, and T. Schuller (2013b). Optimal and off-design operations of acoustic dampers using perforated plates backed by a cavity. *Journal of Sound and Vibration 332*(20), 4856–4875. *(p. 67, 127)*

Scarpato, A., N. Tran, S. Ducruix, and T. Schuller (2012). Modeling the damping properties of perforated screens traversed by a bias flow and backed by a cavity at low Strouhal number. *Journal of Sound and Vibration 331*, 276–290. *(p. 67, 76, 79, 127)*

Schluter, J. U. (2004). Static control of combustion oscillations by coaxial flows: A large-eddy-simulations investigation. *Journal of Propulsion and Power 20*(3), 460–467. *(p. 6)*

Schönfeld, T. and M. Rudgyard (1999). Steady and unsteady flows simulations using the hybrid flow solver AVBP. *AIAA Journal 37*(11), 1378–1385. *(p. 53)*

Schuller, T., N. Tran, N. Noiray, D. Durox, S. Ducruix, and S. Candel (2009). The role of nonlinear acoustic boundary conditions in combustion/acoustic coupled instabilities. In *Proceedings of ASME Turbo Expo 2009, GT2009-48838*, pp. 325–339. ASME. *(p. 168)*

Selle, L., F. Nicoud, and T. Poinsot (2004). Actual impedance of nonreflecting boundary conditions: Implications for computation of resonators. *AIAA Journal 42*(5). *(p. 59)*

Senoner, J.-M. (2010). *Simulation aux grandes échelles de l'écoulement diphasique dans un brûleur aéronautique par une approche Euler-Lagrange.* Ph. D. thesis, Institut National Polytechnique de Toulouse. *(p. 53)*

Silva, C. F., F. Nicoud, T. Schuller, D. Durox, and S. Candel (2013). Combining a helmholtz solver with the flame describing function to assess combustion instability in a premixed swirled combustor. *Combustion and Flame 160*(9), 1743–1754. *(p. 134, 167)*

Simonetti, F., A. Andreini, C. Bianchini, B. Facchini, and A. Peschiulli (2011). Assessment of numerical tools for the evaluation of the acoustic impedance of multi-perforated plates. In *Proceedings of ASME Turbo Expo 2011, GT2011-46303*. *(p. 49)*

Strahle, W. C. (1978). Combustion noise. *Progress in Energy and Combustion Science 4*(3), 157–176. *(p. 5)*

Tam, C. K. W., H. Ju, M. G. Jones, W. R. Watson, and T. L. Parrott (2010). A computational and experimental study of resonators in three dimensions. *Journal of Sound and Vibration In Press, Corrected Proof*, –. *(p. 48)*

Tam, C. K. W. and K. A. Kurbatskii (2000). Microfluid dynamics and acoustics of resonant liners. *AIAA Journal 38*(8), 1331–1339. *(p. 48)*

Tam, C. K. W. and J. C. Webb (1993). Dispersion-relation-preserving finite difference schemes for computational acoustics. *Journal of Computational Physics 107*(2), 262–281. *(p. 58)*

Tayong, R., T. Dupont, and P. Leclaire (2011). Experimental investigation of holes interaction effect on the sound absorption coefficient of microperforated panels under high and medium sound levels. *Applied Acoustics 72*(10), 777–784. *(p. 10)*

Thompson, K. W. (1987). Time dependent boundary conditions for hyperbolic systems. *Journal of Computational Physics 68*(1), 1–24. *(p. 58)*

Thompson, K. W. (1990). Time-dependent boundary conditions for hyperbolic systems, ii. *Journal of Computational Physics 89*(2), 439–461. *(p. 58)*

Tonon, D., E. M. T. Moers, and A. Hirschberg (2013). Quasi-steady acoustic response of wall perforations subject to a grazing-bias flow combination. *Journal of Sound and Vibration 332*(7), 1654–1673. *(p. 10, 11)*

Tran, N. (2009). *Influence de la condition limite acoustique amont sur les instabilités de combustion de grande amplitude : conception d'un système robuste de contrôle d'impédance (Analysis of the effect of the upstream acoustic boundary condition on high amplitude combustion instabilities: design of a robust impedance control system)*. Ph. D. thesis, Ecole Centrale Paris. *(p. 6, 30, 35, 36)*

Tran, N., S. Ducruix, and T. Schuller (2009a). Damping combustion instabilities with perforates at the premixer inlet of a swirled burner. *Proceedings of the Combustion Institute 32*(2), 2917–2924. *(p. 5, 10, 40, 52, 86, 101, 167)*

Tran, N., S. Ducruix, and T. Schuller (2009b). Passive control of the inlet acoustic boundary of a swirled burner at high amplitude combustion instabilities. *Journal of Engineering for Gas Turbines and Power 131*(5), 051502–7. *(p. 10, 40, 86, 101, 167)*

Wendoloski, J. C. (1998). Sound absorption by an orifice plate in a flow duct. *Journal of the Acoustical Society of America 104*(1), 122–132. *(p. 10, 15)*

Yang, V. and W. E. Anderson (1995). *Liquid rocket engine combustion instability*. American Institute of Aeronautics and Astronautics. *(p. 3)*

Zhang, Q. and D. J. Bodony (2012). Numerical investigation and modelling of acoustically excited flow through a circular orifice backed by a hexagonal cavity. *Journal of Fluid Mechanics 693*, 367–401. *(p. 22, 48)*

Zhao, D. and A. S. Morgans (2009). Tuned passive control of combustion instabilities using multiple Helmholtz resonators. *Journal of Sound and Vibration 320*(4–5), 744–757. *(p. 7, 8)*

Zinn, B. T. (1970). A theoretical study of non-linear damping by Helmholtz resonators. *Journal of Sound and Vibration 13*(3), 347–356. *(p. 8)*